Title	Theoretical Study on Two-Photon Absorption Properties of Open-Shell π-Conjugated Molecules and Molecular Aggregates
Author(s)	横山, 麻紗子
Citation	大阪大学, 2025, 博士論文
Version Type	VoR
URL	https://doi.org/10.18910/101698
rights	
Note	

Theoretical Study on Two-Photon Absorption Properties of Open-Shell π-Conjugated Molecules and Molecular Aggregates

Masako YOKOYAMA

MARCH 2025

Theoretical Study on Two-Photon Absorption Properties of Open-Shell π-Conjugated Molecules and Molecular Aggregates

A dissertation submitted to
THE GRADUATE SCHOOL OF ENGINEERING SCIENCE
OSAKA UNIVERSITY
in partial fulfillment of the requirements for the degree of
DOCTOR OF PHILOSOPHY IN ENGINEERING

BY

Masako YOKOYAMA
MARCH 2025

ABSTRACT

This dissertation provides a theoretical elucidation of the structure-property correlation on two-photon absorption (TPA) in open-shell electron systems, aiming to establish materials design guidelines for controlling these properties. TPA, a third-order nonlinear optical (NLO) phenomenon, has attracted significant attention due to its potential applications. Open-shell molecular systems are expected to be promising candidates for high-efficiency NLO materials. Our research focuses on neutral π-conjugated radicals and their π-stacked molecular aggregates. In such aggregates, tuning the interactions between the radicals is crucial to delocalizing the electrons along the stacking direction, giving unique optical properties. In addition, the NLO responses, including the TPA cross-sections (a measure of the efficiency of TPA), are expected to exhibit a nonlinear enhancement for the number of molecules, potentially surpassing the performance of conventional closed-shell NLO systems. Previous theoretical studies for open-shell systems have primarily focused on the structure-property correlations for the static second hyperpolarizability (γ), which characterizes the third-order NLO response to the static electric field. However, theoretical analysis of TPA properties of open-shell molecules and their aggregates remains limited due to the complexity of their electronic states. The TPA cross-section, which is an incident light frequency-dependent quantity, reflects the ground and excited state electronic structures that are still challenging to treat by quantum chemical calculations. This dissertation analyzes the static γ and TPA properties of monomers, dimers, and multimers of π-conjugated open-shell molecules using high-precision electronic structure theories and computational methods. The correlation between these properties and the diradical character y, which quantifies the degree of open-shell character in the singlet state, is elucidated. Based on the results of calculations and analyses, design guidelines for enhancing the TPA properties of molecular aggregates composed of open-shell π-conjugated molecules are proposed, providing new insights into the development of advanced NLO materials.

This dissertation consists of three parts. PART I introduces the theory, computation, and analysis methods for the electronic states of open-shell systems. In PART I-1, the fundamentals of quantum chemical theory are described. Analytical expressions for the energies and wavefunctions of the ground and excited states of open-shell systems are introduced, derived using the valence configuration interaction (VCI) method for the simplest symmetric two-site diradical model. A fundamental definition of the diradical character y for diradical systems is then presented, along with its extension to N-site multiradical systems, where multiple diradical characters (y_i) can be defined. The theoretical framework of NLO responses is discussed in PART I-2, which includes the derivation of sum-over-states (SOS) and energy derivative expressions for the static and dynamic third-order nonlinear optical susceptibility (γ), with the latter being closely related to the TPA cross-section. Additionally, the correlation between y and static γ (y-γ correlation) is examined. PART I-3 presents the theoretical aspects of TPA, introducing a calculation scheme for evaluating TPA cross-sections and

explaining the differences between TPA and one-photon absorption (OPA).

In PART II, the static γ of one-dimensional (1D) π-stacked aggregate models of phenalenyl molecules is investigated. The dependence of the static γ on the stacking distances (d) and the number of molecules (N) is examined. A new y-based index is introduced to characterize the open-shell electronic structures of such 1D aggregates, comprising the standard deviation (y_{SD}) of y_i, and the averaged diradical character (y_{av}). Additionally, to predict the NLO response of 1D crystalline systems, the static γ per dimer unit is computed in the limit of $N \to \infty$. The theoretical and computational analyses have revealed a range of d where the static γ increases by more than one order of magnitude. These findings provide valuable insights and contribute to developing design principles for open-shell molecular aggregates that exhibit exceptional third-order NLO properties.

PART III discusses the TPA properties of realistic open-shell molecular aggregates. In PART III-1, the ground and excited electronic states of π-dimer models of phenalenyl radicals are analyzed using the multi-configurational quasi-degenerate second-order perturbation theory. Detailed examination of the OPA and TPA spectra has revealed that significant intermolecular electronic transitions occur when the π-dimer is formed with a specific short stacking distance. The mechanism of such electronic transitions is analyzed in terms of y. The analysis reveals a significant enhancement in the intensity of the first TPA peak in the dimer with intermediate y. In PART III-2, the relationship between the open-shell electronic structures and the TPA cross-section at the first peak is examined in the 1D π-stacked multimer models of phenalenyl radicals. The effects of d and N on the open-shell characters, evaluated with y_{av} and y_{SD}, and on the position and intensity of the first TPA peak, are elucidated. It is found that a significant increase in the TPA peak is observed at a similar range of d with those obtained for the static γ case. This work represents the first detailed elucidation of the TPA properties of realistic π-conjugated molecule aggregates, considering their frequency dispersion. These findings are expected to contribute to further developing novel open-shell TPA materials with performance surpassing conventional systems.

Throughout the dissertation, the influence of several structural parameters in the open-shell π-conjugated molecular aggregates on the positions and intensities of the TPA peaks is elucidated through the analysis of open-shell characters of diradical and multiradical systems. The obtained results are expected to construct a theoretical basis for elucidating the fundamental structure-property correlations for TPA in open-shell systems, which has not been established so far, and to contribute to accelerating the future development and applications of novel open-shell NLO materials such as organic crystals.

PREFACE

Experimental results are undeniably factual. However, they are invariably influenced by environmental and human factors. Even with extensive experimentation, it is often challenging to fully discern the underlying causes of the observed results. In such cases, a computational approach based on quantum mechanics offer a robust framework for uncovering the microscopic mechanisms behind physical and chemical phenomena and for establishing foundational principles for material design.

Having begun my academic journey as an experimental researcher, I later resolved to study the theoretical foundations of quantum chemistry. I believed that by integrating experimental and theoretical methodologies, a deeper understanding of fundamental phenomena could be achieved. This dissertation represents a significant milestone in my pursuit of an ideal approach to the development of novel photo-functional materials by combining theoretical and experimental approaches. Throughout this research, I focused on comparing my computational findings with previously reported experimental results to ensure coherence and accuracy.

Quantum chemistry has proven to be far more intricate and profound than I initially anticipated, and I do not claim to have mastered its entirety. Nevertheless, the research mindset I have developed to unravel phenomena through the synergy of theory and experimentation will undoubtedly serve as a cornerstone for my future endeavors. I hope that this dissertation contributes to the advancement of knowledge through the integration of experimental and theoretical perspectives. Moreover, I am deeply grateful for the invaluable growth I have experienced as a researcher through this study.

This dissertation study was carried out under the supervision of Professor Dr. Masayoshi Nakano, Professor Dr. Yasutaka Kitagawa and Dr. Ryohei Kishi at Division of Chemical Engineering, Department of Materials Engineering Science, Graduate School of Engineering Science, Osaka University from October 2020 to March 2025.

Masako YOKOYAMA (MORIISHI)
Division of Chemical Engineering Science
Department of Materials Engineering Science
Graduate School of Engineering Science, Osaka University

CONTENTS

GENERAL INTRODUCTION

1. Nonlinear Optics

Nonlinear optics (NLO) is a research field that treats strong light-matter interaction where the polarization of matter shows nonlinear responses to the electromagnetic field of light. Since the magnetic field strength is much smaller than the electronic field strength from Maxwell's equations, it is usually enough to consider the interaction between electric fields and materials. When the applied light intensity is weak, the dielectric polarization $\boldsymbol{P}$ induced in the substance is proportional to the electric field $\boldsymbol{E}$:

$$\boldsymbol{P} = \varepsilon_0 \chi^{(1)} \boldsymbol{E} \tag{1}$$

Here, ε_0 is the dielectric constant of the vacuum, and $\chi^{(1)}$ is the linear (electric) susceptibility. When the applied light intensity becomes stronger, $\boldsymbol{P}$ responds to $\boldsymbol{E}$ nonlinearly due to the strong light-matter interaction. The relationship between $\boldsymbol{P}$ and $\boldsymbol{E}$ cannot be described well by the above expression and should be expressed by the power series as follows[1]:

$$\begin{aligned} \boldsymbol{P} &= \boldsymbol{P}^{(1)} + \boldsymbol{P}^{(2)} + \boldsymbol{P}^{(3)} + \cdots \\ &= \varepsilon_0 \left(\chi^{(1)} \boldsymbol{E} + \chi^{(2)} \boldsymbol{E}\boldsymbol{E} + \chi^{(3)} \boldsymbol{E}\boldsymbol{E}\boldsymbol{E} + \cdots \right) \end{aligned} \tag{2}$$

Here, $\boldsymbol{P}^{(n)}$ represents the nth-order polarization. $\chi^{(2)}$ and $\chi^{(3)}$ are the second and third-order nonlinear susceptibilities that characterize the magnitudes of the second and third-order NLO effects.

The electrical response of such macroscopic materials can be derived from the polarization of materials at the microscopic level, such as atoms and molecules. A similar expression describes the microscopic polarization p as Eq. (2), although we should expand it in terms of the local electric field $\boldsymbol{F}$ (different from the external electric field $\boldsymbol{E}$) of the radiation field at the point where the molecule is located[1]:

$$\boldsymbol{p} = \alpha \boldsymbol{F} + \beta \boldsymbol{F}\boldsymbol{F} + \gamma \boldsymbol{F}\boldsymbol{F}\boldsymbol{F} + \cdots \tag{3}$$

Here, the polarizability α, first hyperpolarizability β, and second hyperpolarizability γ are the microscopic origins of linear optical, second-order NLO, and third-order NLO effects, respectively.

Several second-order NLO effects, including three-wave mixing [second harmonic generation (SHG), sum frequency generation (SFG), and difference frequency generation (DFG)] and nonlinear refractive index (Pockels effect, a first-order electro-optic effect), can occur typically in ferroelectrics and piezoelectrics. SHG is a typical example of second-order NLO: When the input light frequency is ω, an output light with doubled frequency 2ω can be emitted. This phenomenon is utilized for constructing wavelength conversion devices. Third-order NLO effects can occur in any kind of material. There are various third-order NLO effects concerning four-wave mixing [third harmonic generation (THG) and degenerated four-wave mixing (DFWM)], nonlinear refractive index (second-order electro-optic effect, the optical Kerr effect), two-photon absorption, and induced scattering. Hereafter, we focus on the two-photon absorption phenomenon of molecular materials.

2. Two-Photon Absorption

Two-Photon Absorption Process

Two-photon absorption (TPA) is a third-order NLO effect where a molecule absorbs two photons to become its excited state. In this dissertation, we only discuss the simultaneous TPA process in which two photons are absorbed by a molecule simultaneously. Most photochemical reactions caused by UV or visible light irradiation are typically initiated by the one-photon absorption (OPA) process in which a molecule absorbs a single photon to become an excited state. Figure 1 schematically shows transitions of one-photon, non-resonant two-photon and three-photon absorption processes. In the OPA process, the excitation can occur when the incident photon energy $h\nu$ matches the energy difference between the excited and ground states ΔE (one-photon resonance condition, $\Delta E - h\nu = 0$). In the non-resonant TPA processes, the excitation can occur even if the incident photon energy $h\nu'$ does not meet the one-photon resonance condition but satisfies the two-photon resonance condition $\Delta E - 2h\nu' = 0$, which means that $h\nu'$ is half the excitation energy value. This transition appears to occur via a virtual state at the position where $\Delta E' = h\nu'$ (dashed line). Similarly, the excitation can occur in the three-photon absorption process when $\Delta E - 3h\nu'' = 0$ is satisfied. Owing to these features of multiphoton absorption processes, we can create electronic excitations of molecules (typical organic molecules tend to exhibit the first OPA band around the UV-Vis region) with light of longer wavelengths, such as the near-infrared (NIR) light. The non-resonant TPA process occurs when two photons simultaneously collide with the molecule. High photon density is necessary to increase the probability of such a process.

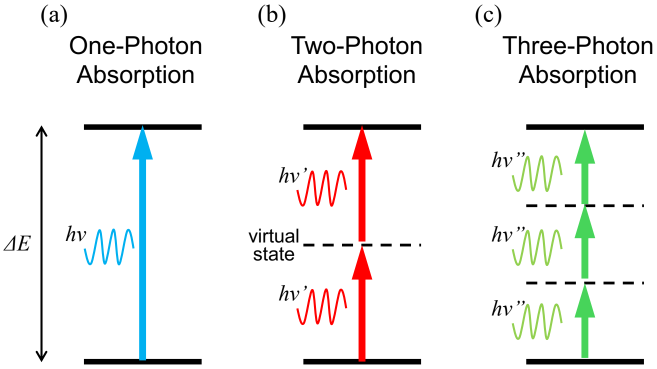

Figure 1. Schemes of (a) one-photon, (b) two-photon, and (c) three-photon absorption processes. Dashed lines represent virtual levels.

Another essential aspect of TPA is the selection rule for optical transition. Consider a centrosymmetric molecule to which the Laporte rule applies. Parity-preserving electronic transitions are forbidden in OPA and allowed in TPA. Transitions between the states with different parities (*gerade* and *ungerade*) are allowed in OPA but forbidden in TPA. Gerade and *ungerade* states have symmetric and antisymmetric wavefunctions concerning the inversion center. In contrast, transitions between the states with the same parities (*gerade* and *gerade* or *ungerade* and *ungerade*) are forbidden in OPA but allowed in TPA (Figure 2). In other words, OPA and TPA follow opposite selection rules. Namely, there are excited states that OPA cannot access, but TPA can. Such excited states are sometimes called "dark states" because they are "invisible" electronic states with conventional spectrophotometers. Forbidden transitions become allowed for non-centrosymmetric molecules, and both OPA and TPA can access the same excited state[1].

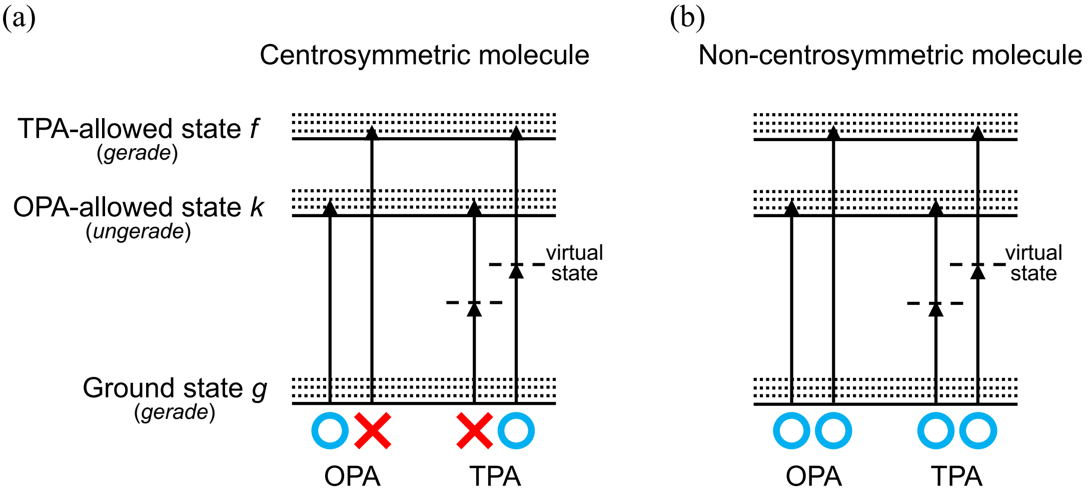

Figure 2. Allowed and forbidden transitions for OPA and TPA in (a) centrosymmetric and (b) non-centrosymmetric molecules.

A Brief History of Two-Photon Absorption

TPA is the first NLO effect for which the process was theoretically predicted by Maria Göppert (Maria Göppert-Mayer) in 1931[2]. With the invention of the Ruby laser by Maiman in 1960, TPA was first observed experimentally by Kaiser and Garrett in 1961[3]. For a while, fundamental research for TPA was conducted mainly using continuous-wave (CW) lasers and nanosecond pulsed lasers as a means of spectroscopic measurement. As laser technology has evolved, many applications utilizing TPA have been proposed. For example, two-photon laser scanning fluorescence microscopy was developed and applied to the biological field[4]. In the 1990s, a Ti:Sapphire laser capable of generating intense ultrashort pulses of about 20 femtoseconds (1 fs = 10^{-15} sec) became commercially available. After that, developing highly efficient TPA materials began attracting significant attention.

Efficiency of Two-Photon Absorption (Two-Photon Absorption Cross-Section)

Suppose a laser beam of intensity I is irradiated onto and passes through a sample along the z-axis. The decrease in the light intensity -dI (Figure 3(a)) after transmission through the area with a sufficiently small thickness dz is generally expressed as:

$$-\frac{dI}{dz} = \alpha^{(1)}I + \alpha^{(2)}I^2 + +\alpha^{(3)}I^3 \dots + \alpha^{(n)}I^n + \cdots \tag{4}$$

Here, $\alpha^{(1)}$ is the linear absorption coefficient (cm^{-1}), $\alpha^{(2)}$ is the two-photon absorption coefficient (cm/W), and $\alpha^{(n)}$ is the n-photon absorption coefficient, representing the absorption efficiencies of a sample. Each absorption coefficient is proportional to the imaginary part of the odd-order nonlinear susceptibility:

One-Photon Absorption: $\alpha^{(1)} \propto \mathrm{Im}\left[\chi^{(1)}\right]$

Two-Photon Absorption: $\alpha^{(2)} \propto \mathrm{Im}\left[\chi^{(3)}\right]$

Three-Photon Absorption: $\alpha^{(3)} \propto \mathrm{Im}\left[\chi^{(5)}\right]$

The linear absorption coefficient $\alpha^{(1)}$ corresponds to the absorption coefficient α defined by the Lambert-Beer law shown in Eq. (5):

$$A = -\log_{10}\left(\frac{I_1}{I_0}\right) = \alpha L = \varepsilon c L \tag{5}$$

I_0 and I_1 are the input and transmitted light intensities through a sample. The dimensionless quantity A is absorbance, defined by the ratio of I_0 and I_1. It characterizes the degree of light absorption after passing through a unit length L of the sample (the optical path length: generally, 1 cm). ε is the molar absorption coefficient [(mol/L)$^{-1}$ cm^{-1}], and c is the molar concentration of the sample as a medium (mol/L). ε characterizes the degree of light absorption per mole of material for the optical path length of 1 cm.

The relationships between the intensity I and light absorption of OPA and TPA processes given in Eq. (4) are illustrated in Figure 3(b). The light absorption of the OPA process is proportional to I and more significant than that of the TPA process in the weak I region. The light absorption of the OPA process increases nonlinearly with increasing I. For the intensities of I up to 10^4 W/cm^2, almost only the OPA process contributes to light absorption. When I becomes strong enough (typically, > 10^4 W/cm^2), the light absorption by the TPA process exceeds that by OPA. Figure 3(c) shows an example of laser light focused with a convex lens, and a high-intensity region can be prepared around the focal point. OPA can occur at any position the light passes, whereas TPA occurs only near the focal point. This property is useful for achieving spatially selective excitation.

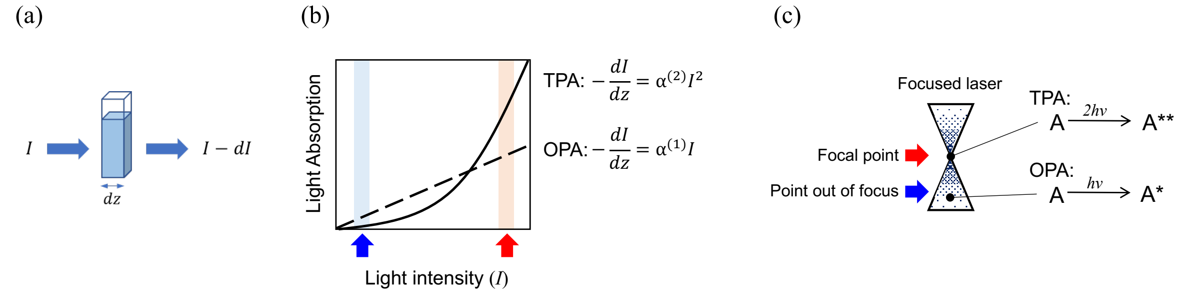

Figure 3. (a) Input light (*I*) and transmitted light (*I* – *dI*) passing through a sample with a sufficiently small thickness *dz*, (b) the light absorption of OPA and TPA processes as a function of light intensity *I*, (c) laser light focused with a convex lens. The red and blue arrows in (b) correspond to the intensities at the positions indicated in (c).

The absorption efficiency per molecule is expressed in a measure called cross-section. The photon flux Φ corresponds to the number of flowing photons per unit time and unit area (photon cm^{-2} s^{-1}). The light intensity *I* is expressed as $I = \hbar\omega\Phi$ using Φ and the photon energy $\hbar\omega$ (J). When the photon flux Φ passes through a sample with a number density of molecules *N* (molecules cm^{-3}), the decrease in photon flux $-d\Phi$ after transmission through the area with a thickness *dz* is expressed as:

$$-\frac{d\Phi}{dz} = N\sigma^{(1)}\Phi + N\sigma^{(2)}\Phi^2 + \cdots + N\sigma^{(n)}\Phi^n + \cdots \tag{6}$$

Here, $\sigma^{(1)}$ is the linear absorption cross-section (cm^2 molecule^{-1}), $\sigma^{(2)}$ is the two-photon absorption cross-section (cm^4 s photon^{-1} molecule^{-1}), $\sigma^{(n)}$ is the *n*-photon absorption cross-section (cm^{2n} s^{n-1} photon$^{-(n-1)}$ molecule^{-1}).

The relationship between $\sigma^{(1)}$ and $\alpha^{(1)}$, and that between $\sigma^{(2)}$ and $\alpha^{(2)}$ are expressed as follows:

$$\alpha^{(1)} = \sigma^{(1)}N \tag{7}$$

$$\alpha^{(2)} = \frac{\sigma^{(2)}}{\hbar\omega} \tag{8}$$

The growth rate of the magnitude of $\sigma^{(n)}$ with *n* is approximately expressed as follows[1]:

$\frac{\sigma^{(n+1)}}{\sigma^{(n)}} \sim 10^{-34}$ cm^2 s photon^{-1}

If $\sigma^{(1)} = 10^{-16}$ cm^2 molecule^{-1}, the magnitudes of $\sigma^{(2)}$ and $\sigma^{(3)}$ are approximately ~10^{-50} cm^4 s photon^{-1}. The value of $\sigma^{(2)}$ (TPA cross-section) is usually expressed in units of GM (1 GM = $1.0\times10^{-}$

^{50} cm^4 s photon^{-1} molecule^{-1}), an acronym for the last name of Maria Göppert-Mayer, who first predicted the existence of the TPA process.

3. Applications of Two-Photon Absorption Materials

Here, we briefly introduce various applications of TPA through spatially selective photoexcitation.

Three-Dimensional Optical Storage

A three-dimensional (3D) optical storage technique utilizing the TPA process was first proposed in 1989 by Parthenopoulos et al[5]. TPA occurs only near the laser focus. This property can be used for high-density recording in 3D space with sub-μm order resolution. This technique attracted great attention because of its potential for enormous recording capacities of 1012 bits/cm^3 or more. In this first proposal, a photochromic dye, spirobenzo-pyran, was used in the recording layer (Figure 4(a)). TPA excites the dye molecule, and the subsequent structural change corresponds to the data-writing process. Fluorescence detection from the recorded mark corresponds to the readout process. In 2000, Kawata et al. reported a readout image of bits written in 26 consecutive layers, validating the concept of multilayer optical storage utilizing TPA (Figure 4(b))[6]. Materials with large TPA cross-section is required for practical use: To date, various new TPA dyes have been proposed to meet the requirements for practical use.

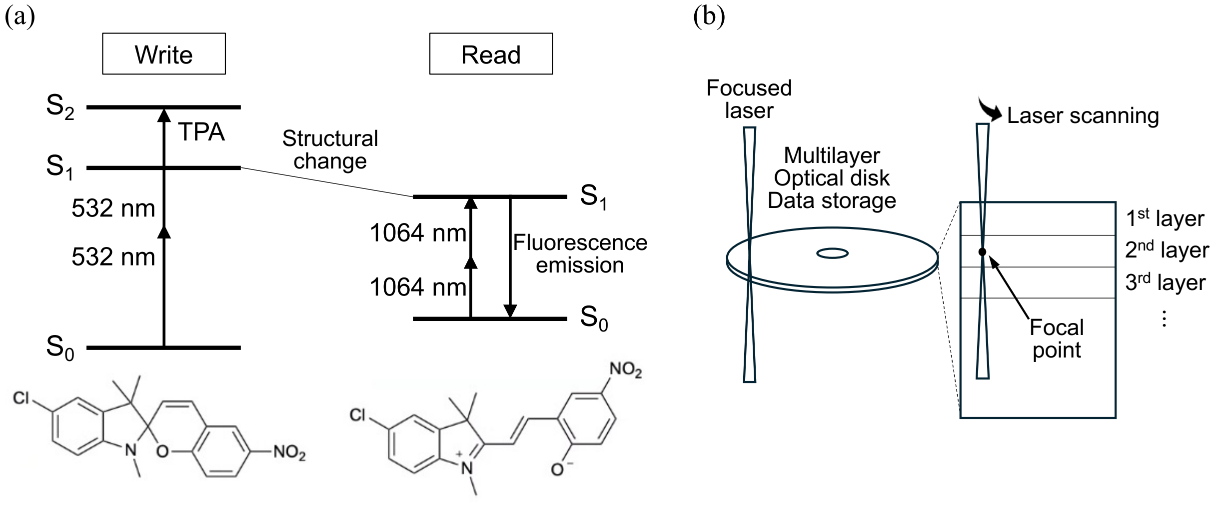

Figure 4. (a) Scheme of structural change and fluorescence emission of spirobenzo-pyrancorresponding to “white” and “read”, (b) Conceptual image of multilayer optical disk data storage feasible by TPA.

Three-Dimensional Microfabrication

The optical fabrication utilizing TPA pioneered by Kawata et al. in 1997 has attracted significant attention. Kawata reported on micro-scale 3D models created by localized curing inside a photo-curable resin realized with a TPA initiator using a femtosecond laser and 3D scanning optics techniques (Figure

5)[7]. materials with TPA cross-section are essential for high sensitivity and precision in modeling in this application. In 1999, the modeling resolution was greatly improved. An extended π-conjugation system exhibiting a large TPA cross-section value (1,250 GM) achieved a length scale of ~1 μm[8]. In 2010, it was reported that line-shaped structures with widths of 65 nm could be created[9]. The TPP (two-photon polymerization) based direct laser writing technology is one of the micro-nano photocurable 3D printing technologies that have reached a high degree of commercialization to date and is called PμSL surface projection micro stereolithography. 3D printers based on TPP technology have been commercialized in Germany and Lithuania and are being applied in various fields, such as photonic material fabrication, microfluidic manufacturing, and metamaterials development.

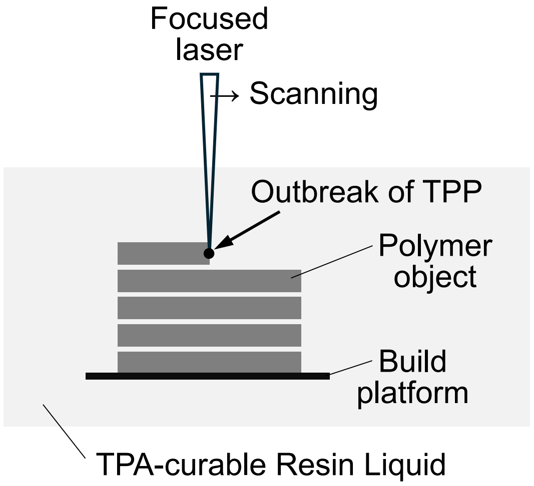

Figure 5. Conceptual image of TPA-based 3D microfabrication.

Three-Dimensional Fluorescence Imaging

Fluorescence imaging techniques combined with the TPA process were first reported in 1990 by Denk et al[4]. Cells labeled with cellular DNA stained with a UV excitation fluorescent stain solution are irradiated with a femtosecond laser, and the emitted fluorescence is detected. This two-photon excitation (TPE) fluorescence microscopy technique allows localized excitation compared to conventional confocal microscopy (Figure 6). With TPA, we can create electronic excited states with long wavelength excitation light, such as in the near-infrared region, which is easily transmitted deep into the tissue, has low scattering, and causes little photodamage, thus offering the advantages of less fading and phototoxicity. Since the publication of this paper, TPE microscopy has been widely adopted in various fields, such as neuroscience, developmental biology, and immunology. It has become a powerful tool for observing molecular and cellular dynamics in vivo. In recent years, in collaboration with the development of highly photostable and low-toxicity fluorescent dyes, which have developed remarkably, techniques for observing molecular and cellular dynamics in living tissues continue to evolve[10]. Intravital imaging, which allows noninvasive, real-time observation of biological tissues, contributes greatly to elucidating the mechanisms of unexplained life events. Suppose fluorescent dyes with high TPA cross-section are developed. In that case, general-purpose lasers with lower output power will be able to be used for observation, and TPE microscopy will be more widely used.

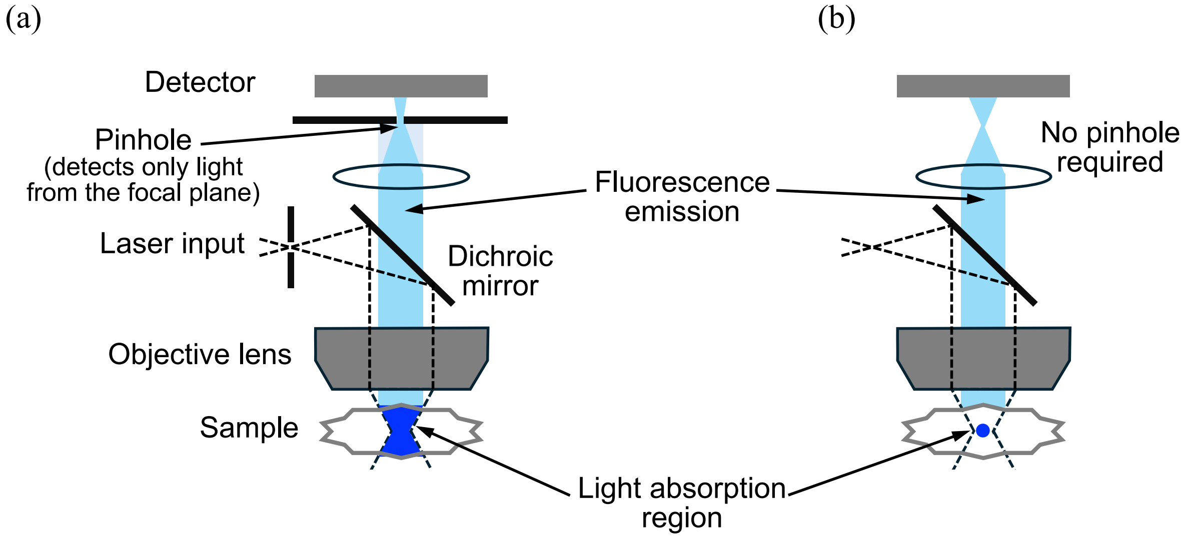

Figure 6. Mechanism images of (a) confocal microscopy and (b) two-photon excitation microscopy.

4. Measurement of Two-Photon Absorption Cross-Section

Measurement Techniques

As described in section 2, TPA is a light intensity-dependent process. Therefore, the spatial and temporal distribution of the incident light must be considered in the measurement. Although intense pulsed lasers are used for the measurement, their stability also affects the measurement results. Unlike commercially available spectrophotometers for OPA spectra in the UV-visible region, no general-purpose measurement devices exist. Therefore, the reported values of TPA cross-sections may vary among methods and research groups even when measuring the same compound.

There are three commonly used methods for measuring TPA: two-photon-induced fluorescence (TPIF), intensity-dependent transmittance measurement (IDTM), and open aperture Z-scan. TPIF is a method to determine TPA cross-section indirectly from the intensity of fluorescence emission followed by TPA and its fluorescence quantum yield. Although this method allows measurements with relatively high sensitivity, it is necessary to assume that the fluorescence quantum yield is constant regardless of the sample's state or surrounding environment. In addition, this method does not apply to non-fluorescent samples. IDPM and Z-scan methods are classified as "direct" measurements because they measure changes in transmittance (absorption). IDPM measures nonlinear absorption by fixing the sample position and changing the incident light intensity. In the Z-scan, the sample is scanned along the direction of light propagation (z-axis) near the focal point of the focused incident light, thereby changing the intensity of the light irradiating the sample[11]. In other words, the laser output is constant, but the intensity of light irradiating the sample varies as a function of position *z*. Since it is necessary to assume that the light intensity irradiating the sample is constant over the *z* direction, the sample thickness must be sufficiently thin for the measurement. The following explains the flow up to TPA cross-section derivation, using Z-scan measurement as an example. An example of the optical system for Z-scan measurement is shown in Figure 7.

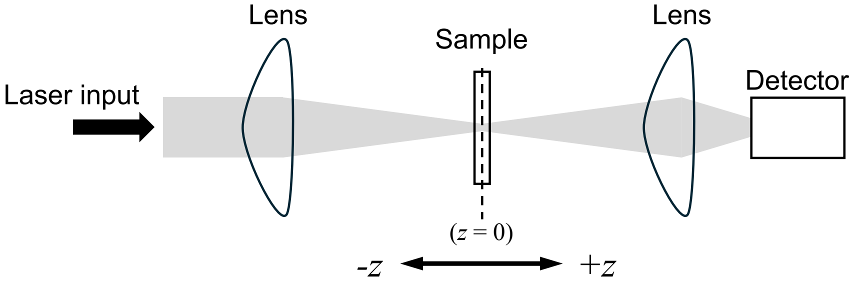

Figure 7. Schematic of optical experiment system for Z-scan measurement.

If the sample is liquid, a quartz cell with a 1 to 2 mm thickness is often used. For example, the light source is a laser beam with a pulse width of ~100 femtoseconds output from a Ti:Sapphire laser. Since these lasers have a single wavelength, they cannot be scanned automatically like commercially available UV-vis spectrophotometers. Thus, when evaluating the characteristics as a TPA spectrum, it is necessary to perform a point-by-point measurement by converting the wavelength of the light each time using a wavelength-tunable optical parametric amplifier or the like.

Furthermore, it should be noted that the change in transmittance obtained from the Z-scan measurement may include nonlinear absorption processes other than TPA [e.g., three-photon absorption, excited-state absorption (ESA), absorption saturation (SA), etc.]. This can be confirmed by performing measurements varying the laser power. The data and analysis image of the transmittance change with sample position *z* obtained from the open aperture Z-scan measurement are shown in Figure 8.

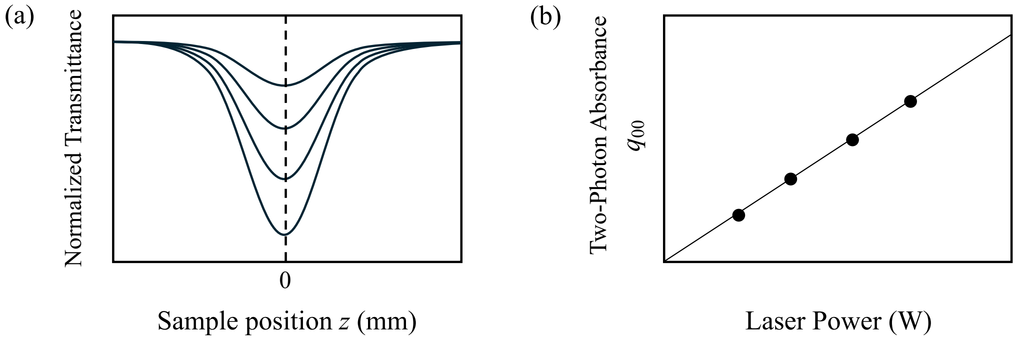

Figure 8. (a) Image of Z-scan trace and (b) two-photon absorbance for varying light intensity.

The example shown in Figure 8 is an image of a four-step change in laser power. The two-photon absorbance shown in Figure 8(b) was obtained by fitting the Z-scan trace in Figure 8(a) with the transmittance change formula described next. If the transmittance change is caused solely by TPA, q_{00} increases linearly with the laser power. If other nonlinear absorption processes are included, the change becomes nonlinear[12].

Experimental Evaluation of Two-Photon Absorption Cross-Section

First, the TPA coefficient $\alpha^{(2)}$ is derived from the slope of the plot shown in Figure 8(b). If the femtosecond laser pulse shape has a Gaussian shape in space and time, the intensity distribution $I(r,t)$ can be expressed as follows:

$$I(r,t) = I_0 \exp\left(-\frac{2r^2}{{w_0}^2} - \frac{t^2}{{t_0}^2}\right) \tag{9}$$

I_0 represents the peak power at the beam center. The relative position of sample ζ concerning the focal position z_0 normalized by Rayleigh length z_R is:

$$\zeta = \frac{z - z_0}{z_R} \tag{10}$$

z_R, which describes the degree of focusing, is the distance from the focal point to the position where the cross-section of the beam is twice that at the focal point. The transmittance at position ζ can be expressed as:

$$T(\zeta) = \frac{1}{\sqrt{\pi} q_0(\zeta)} \int_{-\infty}^{\infty} \ln\left[1 + q_0(\zeta) e^{-x^2}\right] dx \tag{11}$$

$q_0(\zeta)$ is the two-photon absorbance at position ζ. If the effect of the Fresnel reflection coefficient R (reflection on the sample surface) is also considered, $q_0(\zeta)$ is expressed as:

$$\begin{aligned} q_0(\zeta) &= \alpha^{(2)}(1-R) I_0(\zeta) L_{\mathrm{eff}} \\ &= \frac{\alpha^{(2)}(1-R) I_{00} L_{\mathrm{eff}}}{1+\zeta^2} = \frac{q_{00}}{1+\zeta^2} \end{aligned} \tag{12}$$

The numerator $q_{00} = \alpha^{(2)}(1-R) I_{00} L_{\mathrm{eff}}$ is the two-photon absorbance at the focal point ($\zeta = 0$). L_{eff} is the effective sample length ($L_{\mathrm{eff}} = (1 - e^{-\alpha^{(1)} L})/\alpha^{(1)}$). I_{00} is the peak power of the laser at the focus and is expressed by the following equation:

$$I_{00} = 4\sqrt{\frac{\ln 2}{\pi}}\frac{E_p}{\lambda z_R t_{FWHM}} \tag{13}$$

λ is the wavelength of the beam, E_p is the pulse energy, and t_{FWHM} is the temporal full width at half maximum of the pulse. From $\alpha^{(2)}$ and Eq. (8), we finally obtain TPA cross-section $\sigma^{(2)}$.

Measuring TPA cross-section value requires constructing an extensive experimental system and careful analysis of the results. Both experimental approach and theoretical analysis are indispensable for efficiently exploring materials exhibiting large TPA cross-sections. As the size and complexity of TPA dye molecules increase, the role of theory and computations has become more critical.

5. Analytic Expression for Two-Photon Absorption Cross-Section

The frequency dependence of TPA cross-section, $\sigma^{(2)}(\omega)$, relates to the imaginary part of γ for the DFWM process, $\mathrm{Im}\langle\gamma(-\omega;\omega,\omega,-\omega)\rangle$ by the following equation[13,14]:

$$\sigma^{(2)}(\omega) = \frac{24\pi^2\hbar\omega^2}{c^2n^2}L^4\mathrm{Im}\langle\gamma(-\omega;\omega,\omega,-\omega)\rangle \tag{14}$$

where $\hbar$ is Planck's constant divided by 2π, ω is the angular frequency of incident light, c is the speed of light, n is the refractive index, and L is the local field factor (equal to 1 for vacuum). $\langle\gamma\rangle$ indicates the orientationally averaged value for the hyperpolarizability tensor γ_{ijkl} based on the molecular axes $\{i, j, k, l\}$. $\mathrm{Im}\gamma_{ijkl}(-\omega;\omega,\omega,-\omega)$ characterizes the third-order nonlinear optical response of molecule. For example, based on the time-dependent perturbation theory, we can obtain the following sum-over-states (SOS) expression for $\mathrm{Im}\gamma_{iiii}(-\omega;\omega,\omega,-\omega)$[15]:

$$\mathrm{Im}\gamma_{iiii}(-\omega;\omega,\omega,-\omega) = \mathrm{Im}P\left[\begin{array}{c}\dfrac{{M_{gk}}^2{\Delta\mu_{gk}^i}^2}{(E_{gk}-\hbar\omega-i\Gamma_{gk})(E_{gk}-2\hbar\omega-i\Gamma_{gk})(E_{gk}-\hbar\omega-i\Gamma_{gk})}\\ +\displaystyle\sum_{k'}\dfrac{{M_{gk}^i}^2{M_{kk'}^i}^2}{(E_{gk}-\hbar\omega-i\Gamma_{gk})(E_{gk}-2\hbar\omega-i\Gamma_{gk'})(E_{gk}-\hbar\omega-i\Gamma_{gk})}\\ -\dfrac{{M_{gk}^i}^4}{(E_{gk}-\hbar\omega-i\Gamma_{gk})(E_{gk}+\hbar\omega+i\Gamma_{gk})(E_{gk}-\hbar\omega-i\Gamma_{gk})}\end{array}\right] \tag{15}$$

Here, P corresponds to a permutation operator over the optical frequencies. M^i_{gk} is the i-component of transition dipole moment (TDM) between the ground state $|\mathrm{g}\rangle$ and the excited state $|\mathrm{k}\rangle$, and $M^i_{\mathrm{kk'}}$ is the TDM between the excited states $|\mathrm{k}\rangle$ and $|\mathrm{k'}\rangle$. $\Delta^i\mu_{\mathrm{gk}}$ is the difference in the dipole moments between the states $|\mathrm{g}\rangle$ and $|\mathrm{k}\rangle$. E_{gk} is the excitation energy to $|\mathrm{k}\rangle$. $\hbar\omega$ is the photon energy, and Γ_{gk} is the damping parameter, typically 0.1 ~ 0.2 eV. The first term in Eq. (15) is called the dipolar term and the second term is called the three-state term. The third term gives a negative contribution but can be ignored for most TPA peaks, since it has a value when OPA occurs: Spectral shapes at such photon energy regions are out of the scope of analysis.

First, let us explain the dipolar term. To increase the contribution from this term, it is necessary to increase M_{gk} and $\Delta\mu_{\mathrm{gk}}$ in the numerator. In the case of a centrosymmetric molecule, if the state $|\mathrm{k}\rangle$ is OPA-allowed, TPA to this state is symmetry forbidden by the selection rule. In addition, $\Delta\mu_{\mathrm{gk}}$ becomes zero for such systems. Therefore, the dipolar term contributes to non-centrosymmetric molecules. The magnitude of M_{gk} becomes large when the spatial overlap between the wavefunctions of states $|\mathrm{g}\rangle$ and $|\mathrm{k}\rangle$ is large. In addition, M_{gk} corresponds to the moment of electronic dipole induced by the external electric field (field-induced electronic polarization). The length of electronic polarization upon excitation is important. On the other hand, $\Delta\mu_{\mathrm{gk}}$ corresponds to the difference in the permanent dipole moment. To increase the magnitude of $\Delta\mu_{\mathrm{gk}}$, the change density distributions in the ground and excited state should be different. For example, in molecules with a donor (D) and an acceptor (A) at the terminals, the directions of the permanent dipole moments in the states $|\mathrm{g}\rangle$ and $|\mathrm{k}\rangle$ are usually opposed. However, the M_{gk} and $\Delta\mu_{\mathrm{gk}}$ usually shows reversed trends, i.e., introducing D/A groups to increase $\Delta\mu_{\mathrm{gk}}$ sometimes cause the decrease in M_{gk} because of the reduction in the wavefunction overlap between $|\mathrm{g}\rangle$ and $|\mathrm{k}\rangle$. Balancing these effects is crucial. Lowering the excitation energy E_{gk} contributes to enhancing the magnitude of this term. Introduction of π-conjugated systems and D/A groups are considered to as efficient strategies to balance these contributions.

Next, the three-state term is explained. To increase the magnitude of the term, it is necessary to increase $M_{\mathrm{kk'}}$ in addition to M_{gk}. Similarly, it is necessary increase the overlap of the wavefunctions of the state $|\mathrm{k}\rangle$ (intermediate state: OPA state) and state $|\mathrm{k}'\rangle$ (final state: TPA state): Although introducing a π-conjugation system is an efficient strategy, the situation is not so simple because we must consider the balance of the overlaps between the states $|\mathrm{g}\rangle$, $|\mathrm{k}\rangle$, and $|\mathrm{k}'\rangle$. Sometimes, $M_{\mathrm{kk'}}$ shows an opposite trend to M_{gk} by chemical modifications. The denominator is important to determine the spectral shapes (peak positions). When the photon energy $\hbar\omega$ of the incident light approaches E_{gk}, the magnitude of this term increases. At the resonance condition, $\hbar\omega = E_{\mathrm{gk}}$, the spectrum exhibit a peak. The difference between $\hbar\omega$ (the energy for the virtual state of TPA) and E_{gk} is called the detuning energy ΔE. Reducing ΔE is also known as a point for designing molecules with large TPA cross-sections.

We must note that there is another approach to define the TPA cross-section, based on Fermi's golden rule for the two-photon transitions from the initial state $|\mathrm{g}\rangle$ to the final state $|\mathrm{k}'\rangle$[16–19]. In this dissertation, we employed this formulation to simulate the TPA spectra, because the SOS-based formalism based on the $\mathrm{Im}\gamma(-\omega;\omega,\omega,-\omega)$ is known to ill-behave around the photon energy region where OPA and TPA spectra overlap (i.e., ΔE is close to zero)[20,21]. We introduce the formalism of TPA cross-section based on Fermi's golden rule in Chapter 3 of PART I.

6. Design of Highly Efficient Two-Photon Absorption Materials

Various molecular design strategies have been proposed to increase TPA cross-sections. In this section, we introduce several key strategies.

Conjugation Length and Substituent Effects

As mentioned in the previous section, introducing π-conjugated systems and D/A groups is an effective strategy for increasing the TPA cross-sections. Albota et al. reported the TPA measurements of several π-conjugated molecules with D-π-A, D-π-D, and A-π-A structures based on a series of phenylene-vinylene derivatives[13]. Trans-stilbene derivative introducing the NBu_2 groups at the both ends showed a 15-fold increase in the TPA cross-section compared to the unsubstituted form Bis(styryl)benzene with an extended π-conjugated system showed a further enhancement of the TPA cross-sections close to 1,000 GM (Table 1(a)-(c)) owing to the D/A effect. Further extensions of the π-conjugated system were also considered (Table 1(d)). However, since the TPA cross-section is a quantity per molecule (molecule^{-1}), it is natural that the TPA cross-section increases to some extent with increasing molecular size, and comparisons of the TPA properties between the molecule should be done with a normalized quantity by, e.g., the molecular weight.

It can also be seen that the TPA peak position (TPA λ_{max}) was red-shifted by extending the π-conjugated system and introducing the D/A groups. It is important to obtain a large TPA cross-section value at a wavelength region suitable for a specific applications. Establishing molecular design strategies for tuning the TPA λ_{max} is therefore crucial.

Table 1. Effects of extension of π-conjugation and introduction of donor/acceptor groups on TPA cross-section (TPACS) values.

Compound	TPA λ_{max} (nm)	TPACS (GM)
(a) 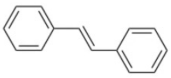	514	12
(b) 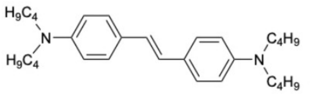	605	210
(c) 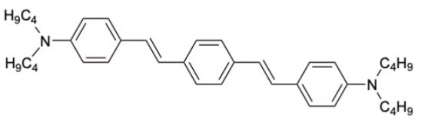	730	995
(d) 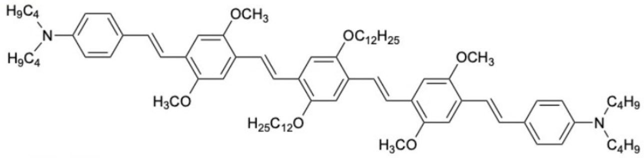	840	1420

Branched Structures

In addition to the linearly π-conjugated molecules shown in Table 1, molecules with branched structures have also been investigated as candidates for TPA dyes[22–31]. Several star-shaped and dendritic macromolecules have been synthesized, and their TPA properties were evaluated considering their solubility in solvents. As mentioned before, TPA cross-section values (per molecule) tend to increase with the number of dye units. If the interactions between the units are weak and simple, the rate of increase in the TPA cross-section is expected to be linear with the number of units. However, Chung et al. reported that the TPA cross-section of a three-branched structure (Figure 9(c)) is about seven times larger than that of the linear unit structure (Figure 9(a))[22]. This result suggests excitonic interaction effects between the branches. In addition, the red shift of absorption wavelength was suppressed despite the increase in the molecular size. This is due to decoupling the π-conjugation network at the branching point where the triphenylamine part has a non-planar twisted structure. The relationship between the strength of exciton coupling in the branched molecules and TPA cross-sections has also been examined theoretically using DFT simulations[32].

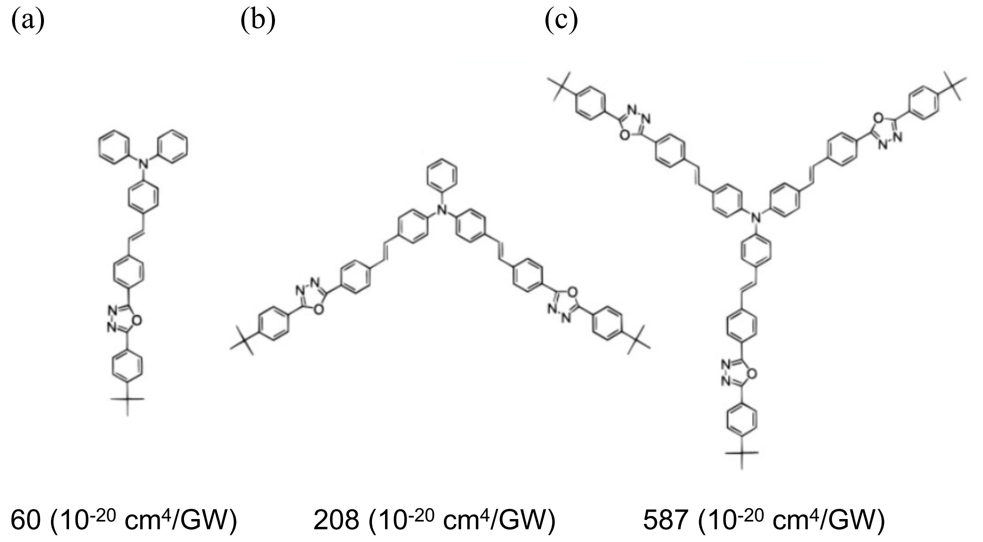

Figure 9. TPA cross-section values of (a) linear unit conjugated molecule and, (b) two-branched, and (c) three-branched conjugated molecules.

Molecular Planarity

Maintaining the structural planarity of extended π-conjugated molecules is crucial for efficient π-electron delocalization. Many studies have been conducted for ideally planar cyclic π-conjugated molecules such as porphyrins and phthalocyanines[33–38]. In addition, materials consisting of highly transparent multilayered clay were reported in which TPA molecules were inserted between the layers to suppress the rotation of aromatic rings. Their TPA cross-sections were increased more than two-fold compared to those measured in solvent[39,40]. These results showed that molecular planarity is a crucial molecular design for increasing TPA cross-sections and opened up the possibility of hybrid TPA materials with inorganic polymer compounds.

Resonance Enhancement Effect

According to the approximate three-state expression for the TPA cross-section, the TPA cross-section increases as the difference between the incident photon energy $\hbar\omega$ (the excitation energy for the virtual state) and E_{gk} (the excitation energy for the OPA-allowed state), called the detuning energy ΔE, is small. This type of enhancement is called the (double) resonance enhancement effect, where both one-photon and two-photon resonance conditions are (nearly) satisfied. The image of the resonance enhancement effect in TPA is shown in Figure 10. Enhancement of TPA cross-section has been observed in many molecules[41,42], although the measurement results are affected significantly by the OPA process: At the wavelength region where the OPA and TPA bands significantly overlap, the absorption nonlinearity is reduced and may not be possible to take advantage of attractive features of TPA such as spatial selective excitation.

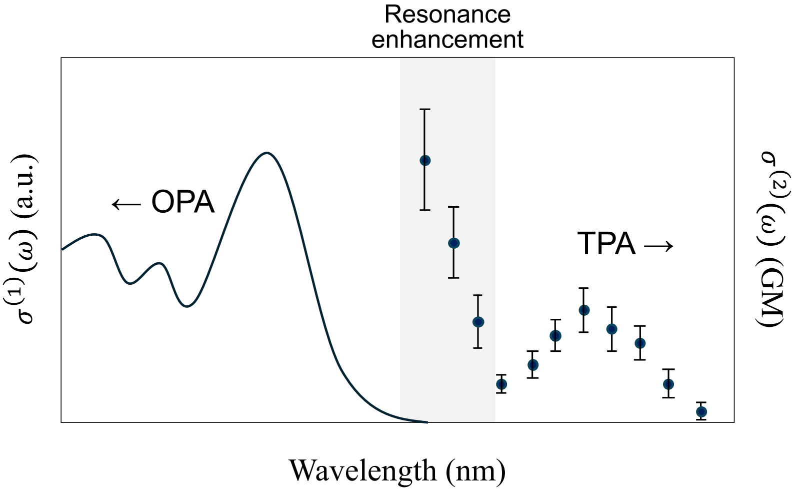

Figure 10. Image of the resonance enhancement effect in TPA. When TPA is measured while approaching the OPA wavelength region, the TPA cross-section rapidly increases even when approaching the foot of the OPA distribution.

Open-Shell Characters

So far, the design strategies have focused mainly on stable closed-shell molecular systems. Nakano, Kubo, Kamada, and their coworkers theoretically predicted and experimentally confirmed the possibility of dramatically improved NLO properties in designed open-shell singlet molecules[43–50]. Drastic changes in static ($\omega = 0$) (hyper)polarizabilities (α and γ) during the bond dissociation process were reported from several theoretical investigations[51,52]. Third-order NLO property, γ, was shown to depend on the degree of bonding or open-shell character and increase remarkably in the intermediate bonding/open-shell region.

Such intermediate open-shell systems have been challenging to synthesize and isolate. However, recent advances in structural organic chemistry have made it possible to realize such intermediate open-shell molecules. Phenalenyl (PLY; Figure 11(a)) is a neutral π-radical compound exhibiting high thermodynamic stability owing to the delocalized nature of the radical electron (characterized by the spatial distribution of singly occupied molecular orbital [SOMO]). PLYs have been used as a building block to design stable open-shell molecular materials[53–58]. In particular, syntheses and measurements and theoretical analyses for *s*-indaceno[1,2,3-*cd*;5,6,7-*c'd'*]diphenalene (IDPL), which consists of two phenalenyl groups connected by an aromatic ring and its extension dicyclopenta[*b*;*g*]naphthalene[1,2,3-*cd*;6,7,8-*c'd'*]diphenalene (NDPL) have pioneered a new direction for TPA materials[59–63]. These compounds are singlet diradicaloids (diradical-like molecules) with two interacting radical moieties but exhibit sufficient thermodynamic stabilities due to delocalized and stabilized radical electrons in the π-conjugated systems. Structures of IDPL and NDPL derivatives are shown in Figure 11(b) and their OPA and TPA spectra are shown in Figures 1 and 2 of Ref.[60,64] The measured maximum TPA cross-section for NDPL (8300 ± 1900 GM at 1050 nm, including resonance enhancement effect) is among the largest in pure hydrocarbon systems without hetero elements and D/A groups. Such open-shell singlet molecules usually have lower excitation energies for both OPA and TPA states than closed-shell molecules of similar molecular size. Even relatively small open-shell singlet molecules often show OPA and TPA band wavelengths in the NIR region. Designing open-shell molecules with tunable open-shell characters has been a new and attractive strategy to achieve giant TPA cross-sections. Still, open-shell singlet molecules are difficult to handle, and thus, their synthesis and isolation are challenging. To efficiently explore novel open-shell TPA systems, theoretical and computational approaches are essential to predict and analyze TPA properties and to elucidate the mechanism of large TPA cross-sections.

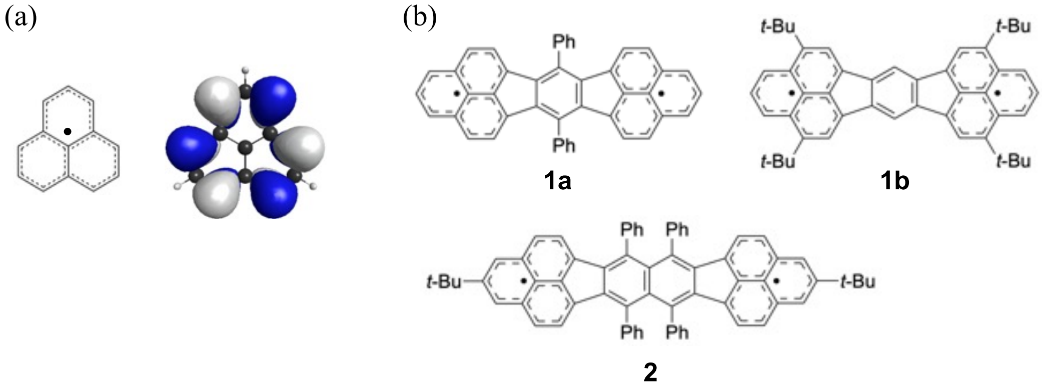

Figure 11. (a) Structures and SOMO of PLY. (b) Structures of IDPL and NDPL derivatives.

7. Design Principle of Efficient Open-Shell NLO Molecules

Mechanisms of large static γ and TPA cross-section values of intermediate open-shell systems have been clarified based on the electronic structures based on the model Hamiltonian involving parameters and model and realistic open-shell molecular systems. The advantages of using the model Hamiltonian are that we can focus on the fundamental relationship between the physically and chemically meaningful parameters and extract its governing factors. For model open-shell molecular systems, various open-shell electronic structures are artificially prepared by manually changing geometrical parameters (bond lengths, dihedral angles) for H_2 molecule, methyl radical and 1,3-dipole systems, and *p*-quinodimethane (PQM) molecule[65,66]. For realistic open-shell molecular systems, electronic structures and properties of (simplified or modified) synthesized molecules are investigated by quantum chemical calculations. Examples of actual open-shell molecules for which TPA measurements are reported include diphenalenyl radical molecules, such as IDPL and NDPL, zethrene derivatives[67–73], perylene derivatives[74–81], polyacenes[82], thienoacenes[83,84], and fluorenyls[85–87].

Open-shell characters of these systems can be quantified with a theoretical index, diradical character y. y is a measure of chemical bond instability taking a value from 0 to 1[88]. $y = 0$ corresponds to the closed-shell situation, and $y = 1$ to the fully open-shell limit. The intermediate open-shell situation exists between these situations ($0 < y < 1$). Consider the dissociation process of H_2, shown in Figure 12, as an example. A covalent bond is formed when the distance between two H atoms is small enough. The energy gap between the highest occupied molecular orbital and the lowest unoccupied molecular orbital (HOMO-LUMO gap) is sufficiently large in this state. Therefore, the ground state wavefunction is described well by a single electron configuration where two electrons occupy HOMO (called the ground configuration), which corresponds to the closed-shell electronic structure. When the distance between two H atoms is sufficiently large (at the dissociation limit), the HOMO-LUMO gap becomes ideally zero. In this situation, the wavefunction should be described by the superposition of two-electron configurations: the ground configuration and the double excitation configuration where two electrons occupy LUMO. This is the fully open-shell state. Upon dissociation, the covalent bond between the two H atoms gradually weakens, and an intermediate open-shell state appears. y is defined as twice the weight of the double excitation configuration in the ground state wavefunction.

The SOS expressions of static and frequency-dependent γ involve excitation energies and TDMs between the electronic states. As the y (weight of double excitation) increases, the excitation energies and TDMs change. Based on the two-site diradical model, Nakano et al. derived analytic expressions of excitation energies and TDMs in terms of y. By substituting them into the SOS expressions of γ and TPA cross-section based on the three-state approximation, they derived analytic expressions of γ and TPA cross-section in terms of y. They found that these quantities enhance significantly in the intermediate y region.

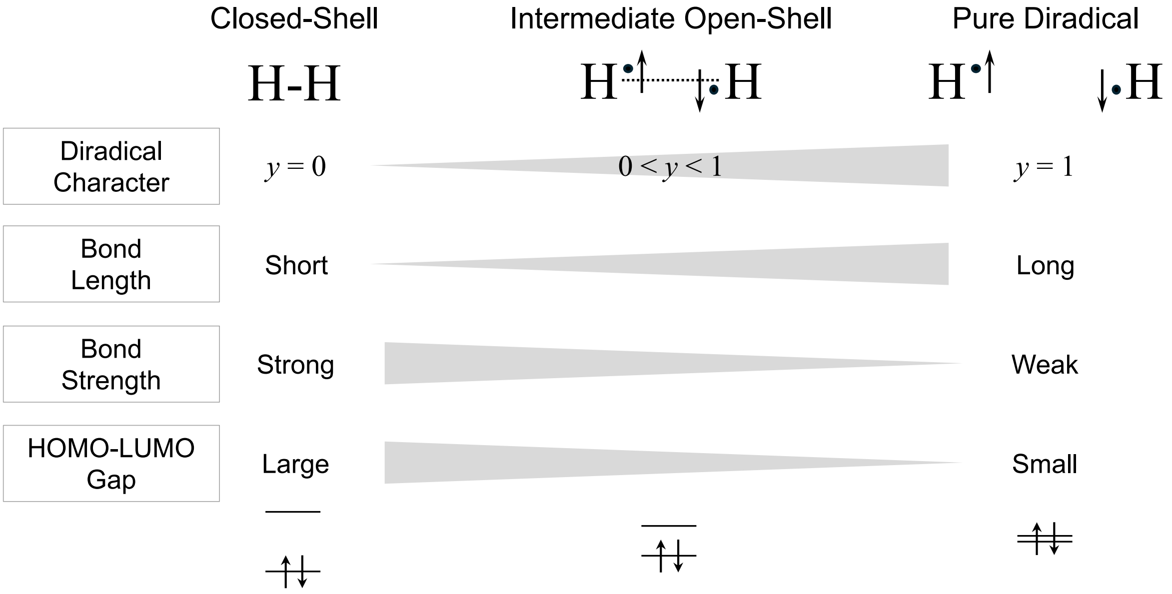

Figure 12. Dissociation process of an H_2 molecule.

After that, static γ values of several model open-shell molecules were examined using quantum chemical calculations. The relationships between the bond distance r (Å), y, and static γ for the H_2 dissociation model are shown in Figure 13[47,65]. Static γ increases significantly in the intermediate y region (0.5 ~ 0.7). This result was obtained based on the full configuration interaction (CI) method in quantum chemistry which gives the exact solution for a given basis function. However, its computational effort explosively increases with the system size (numbers of atoms and electrons), making it inapplicable to most systems of interest. In general, we must be careful when applying approximate solutions of the Schrödinger equation to evaluate static γ.

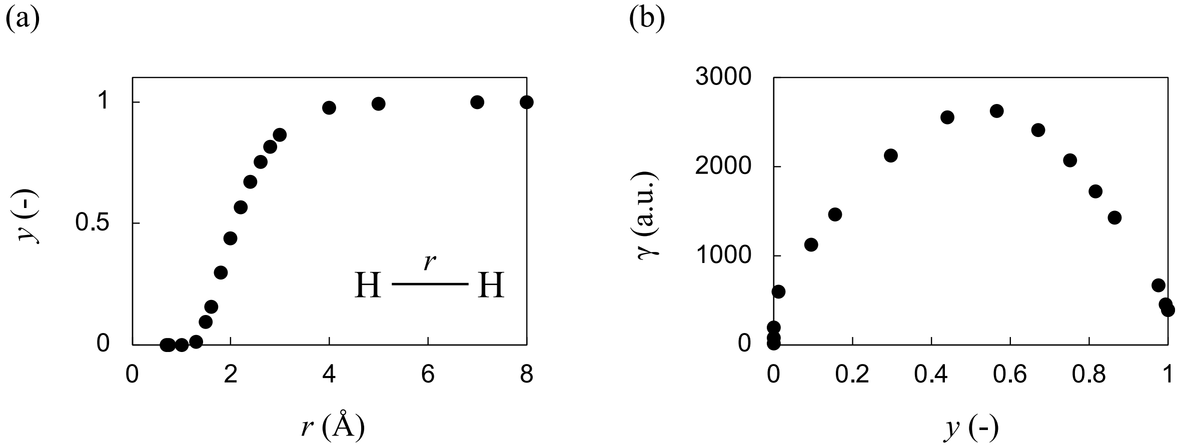

Figure 13. (a) r–y, (b) y-γ correlations for the H_2 dissociation model. These plots were reconstructed from the data in Table I of the paper by Nakano et al[47].

The PQM is a key structure in designing open-shell singlet molecules with tunable *y*. For example, IDPL contains two PLY units and a PQM structure. A previous study investigated the static γ of this system. By changing the terminal C=C bonds, R_1, the calculation results can be compared for the same molecule differing in *y*. The relationships between R_1, *y*, and γ in the bond-stretched PQM model are shown in Figure 14[65,89]. The results at the CCSD(T) (coupled cluster singles and doubles substitutions with the perturbative treatment of triples excitation: one of the most sophisticated approximation methods of quantum chemistry applicable to small- and medium-size systems) is considered to give the best result among the employed approximate calculation methods. Similar to the result of the H_2 dissociation model, the static γ increases significantly in the intermediate *y* region, although the peak position seems different between the systems.

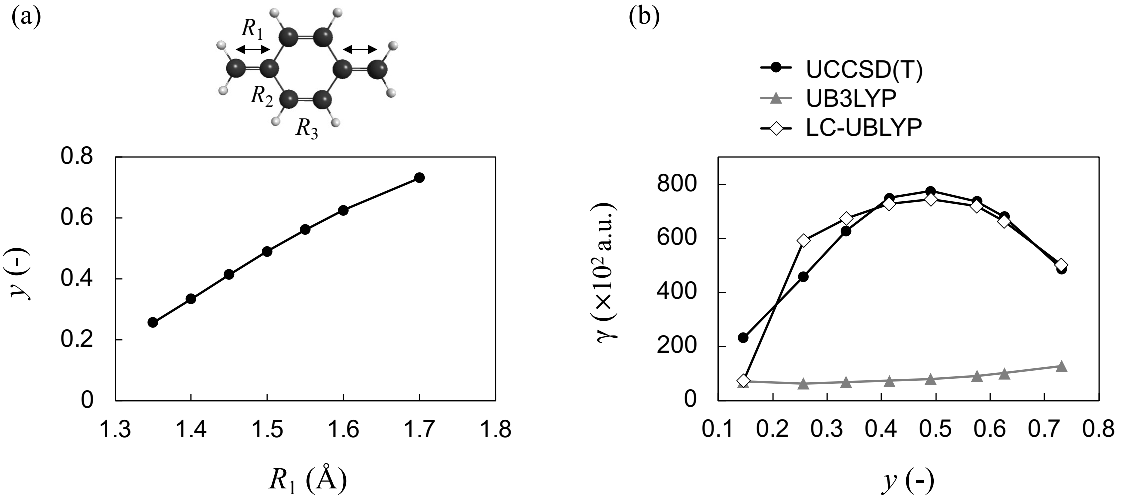

Figure 14. (a) R_1–*y*, (b) *y*-γ correlations for the PQM model. These plots were reconstructed from the data provided by the authors in the paper reported by Kishi et al[90].

We often employ the Kohn-Sham density functional theory (DFT) method for calculations of medium- and large-size systems. The B3LYP functional, the most used exchange-correlation functional for electronic structure calculations of molecules, is reported to give poor results for predicting the *y*-γ correlation. The long-range corrected functional (LC-UBLYP) reproduced the most reliable UCCSD(T) results well.

8. Open-Shell Molecular Aggregates as Candidate for Novel Open-Shell NLO Systems

Several derivatives of PLY have been reported to form stacked π-dimers and multimers in solution and crystalline phases[91–94]. The stacking distance (d) and the stacking configuration between PLY molecules in π-dimers can be modulated by substituents (-R) at the 2-, 5-, and 8-positions[95–98]. For instance, derivatives with R = t-Bu and R = C_6H_5 are known to form anti-type π-dimers in the solid state, with d ~ 3.31 Å[91] and ~ 3.02 Å[93], respectively (Figure 15(a), (b)). These experimental findings highlight the presence of a multicenter two-electron covalent-like bonding interaction between the PLY units, commonly referred to as pancake bonding[54].

Additionally, the formation of one-dimensional (1D) molecular aggregates composed of open-shell molecules has been observed (Figure 15(c))[99]. For example, the derivative with R = C_6F_5 forms eclipsed-type 1D π-stacks in the solid state, with a stacking distance of approximately 3.50 Å[99]. In multiradical systems, where the number of radical moieties (N) exceeds two ($N = 2n$, $n = 2, 3, \ldots$), multiple diradical characters (y_i) can be defined. Several theoretical and computational studies have investigated the open-shell characters and third-order nonlinear optical (NLO) properties of such 1D chains of monoradicals.

Nakano et al. employed the simplest 1D chain model of hydrogen atoms and averaged y (y_{av}) values to characterize their open-shell characters[48]. They found that γ per unit in the 1D chains (multiradical) takes a maximum in a smaller y_{av} region compared with the diradical systems. Yoneda et al. conducted density functional theory (DFT) calculations on eclipsed- and anti-type π-dimer and π-tetramer of PLY (PLY_2 and PLY_4, respectively) with varying d in the singlet state[100]. They found that y of the PLY_2 decreases as decreasing d, and γ per monomer takes the maximum around $d = 2.9$ Å, at which y is in the intermediate region (Figure 16). Salustro et al. performed the first direct computation of γ_∞ for 1D chains of PLY[101], employing the coupled-perturbed Kohn-Sham (CPKS) analytic derivative method under periodic boundary conditions, as implemented in the CRYSTAL package[102–106]. Matsui et al. extended these investigations by examining the effect of increasing the number of monomers (N) on γ per unit in 1D chains of hydrogen atoms and cyclic thiazyl radicals[107]. They extrapolated their results to estimate the γ per unit in the limit $N \rightarrow \infty$ (γ_∞). These studies collectively suggest that the third-order NLO properties of closely stacked 1D chains of π-radicals are comparable to those of π-conjugated polymers, emphasizing the importance of through-space (TS) conjugation in such systems. Figure 16(a) and (b) compare the results of static γ per monomer of PLY_2 and PLY_4 as a function of d. The peak value of static γ per monomer of PLY_4 is about five times higher than that of PLY_2. In the same study, the d-dependence of static γ for π-stack aggregates of closed-shell coronene was also investigated for comparison. The static γ per monomer was about 1/8 of that of PLY_2, regardless of the stacking distance. This result indicates that the π-stack aggregates of open-shell molecules are expected to show a remarkable change in electronic structure due to covalent intermolecular interactions, which is not expected in the closed-shell aggregates.

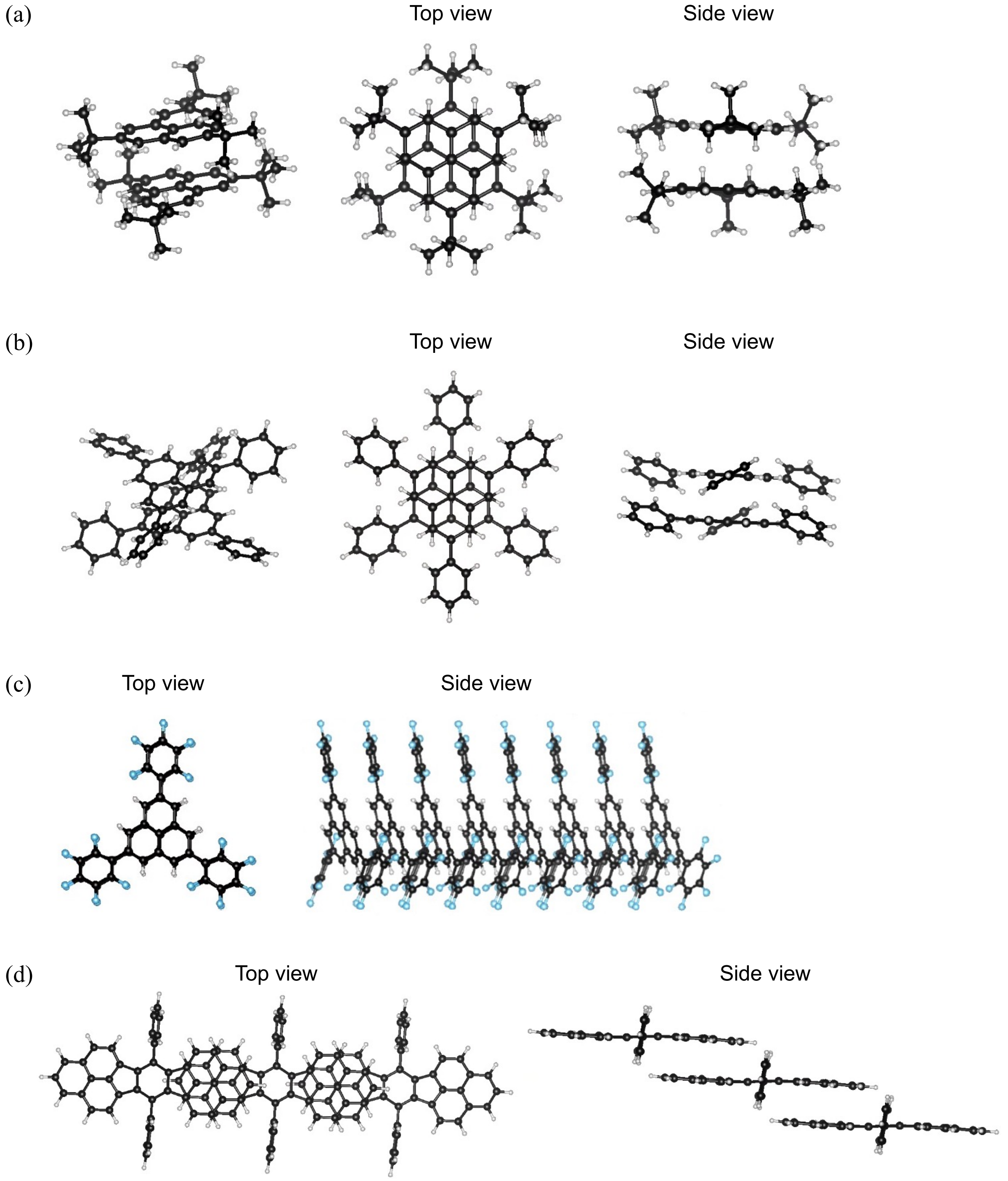

Figure 15. Examples of one-dimensional (1D) molecular aggregates composed of open-shell molecules. Molecular structures of anti-type π-dimers of PLY derivatives with (a) R = *t*-Bu, (b) R = C_6H_5. (c) Eclipsed-type 1D π-stacks of PLY derivatives with R = C_6F_5. (d) Slip-stack structures obtained from IDPL derivatives by recrystallization in chlorobenzene. Image of (a) and (b) was reconstructed from the structural data in supporting information of the paper by Mou et al[93], (c) was by Uchida et al[99], (d) was by Shimizu et al[62].

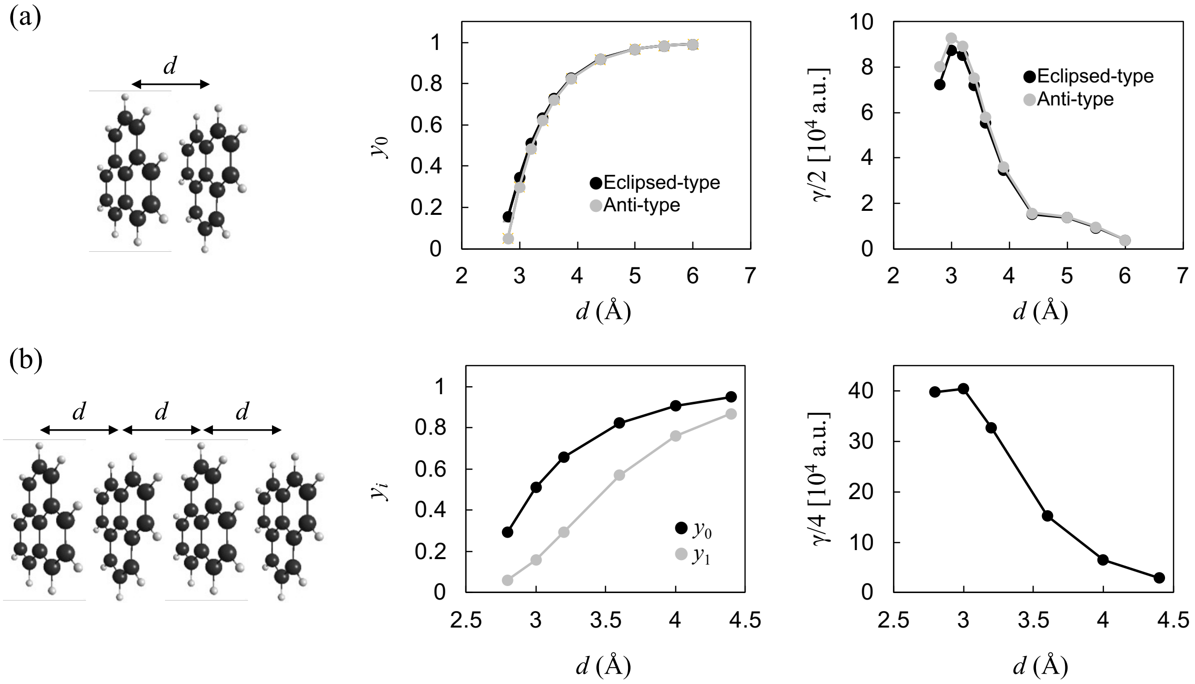

Figure 16. *d*-*y* and *d*-γ correlations for the (a) PLY$_2$, (b) PLY$_4$ model. These plots were reconstructed from the data in Table 1S and 3S of the paper by Yoneda et al[100].

Design and synthesis of single molecules exhibiting multiradical characters are generally difficult. Therefore, such multiradical-based novel third-order NLO materials (including TPA materials) are potentially realized by molecular aggregate systems in a solid state, such as molecular crystals. Indeed, solid-state physical properties of slip-stack structures have been investigated for IDPL derivatives that contain PLYs in their structure (Figure 15(d))[62].

9. Outline of This Dissertation

The general objective of this dissertation is to theoretically elucidate the structure-property relationship of TPA in open-shell molecular systems, which are attracting attention as candidates for NLO materials. Among the open-shell molecular systems, we have focused on open-shell π-conjugated molecules and their aggregates in the singlet state. The goals of this dissertation work are (i) elucidation of the key factors of structures and electronic states that govern the TPA phenomena in open-shell systems and (ii) construction of design guidelines for novel open-shell NLO materials.

(i) Elucidation of the key factors of structures and electronic states that govern the TPA phenomena in open-shell systems

Since the experimental assessment of TPA properties is generally difficult and complex, developing theoretical and computational analysis methods with accuracy is strongly desired for exploring efficient materials and promising applications. Theoretical treatment of the electronic states open-shell molecular systems is extremely complicated for the ground, lower-lying, and higher-lying excited states that contribute to the TPA transition. Both experimental and theoretical analyses for such electronic states have not been established sufficiently for the open-shell systems. Experimental results of TPA properties of open-shell molecular systems have been discussed so far, but there may be a kind of overinterpretation of the y-γ and y-TPA correlations, which are derived from the minimal two-site model. The applicability of y-based discussion to the analysis of spectral shapes of TPA cross-sections of real open-shell molecules is still unclear. Recent advances in the electronic structure theory and computational methods have made it possible to analyze these issues, although it is still challenging. In this study, we aim to elucidate the TPA properties in open-shell molecular systems and their aggregates in detail by utilizing the theoretical analysis methods accumulated by our group.

(ii) Construction of design guidelines for novel open-shell NLO materials

Aggregates systems consisting of open-shell molecules have attracted much attention in recent years. Due to their electronic structures easily fluctuating by external stimuli, these systems exhibit more interesting and unique properties than the closed-shell molecular systems. For the applications in NLO, several theoretical studies have been carried out, aiming to establish molecular design guidelines. For example, tuning the interactions between open-shell molecular units in the aggregates is an efficient strategy. These previous theoretical studies have focused mainly on the static γ. Still, efficient strategies for controlling the positions and intensities of TPA peaks in the aggregates of open-shell molecules have not been established sufficiently. The potentials of finite-size stacking systems, such as dimers and tetramers, and the infinite systems (e.g., assuming real organic crystals) have not yet been explored. In molecular aggregates where monomers interact with each other strongly, nonlinear enhancement of TPA properties for the number of molecules (N) can be expected.

This dissertation covers topics (i) and (ii), focusing on the y-dependence of TPA properties of molecular aggregate systems consisting of π-conjugated monoradicals. It is important for future development to understand whether the TPA cross-sections in real molecular systems can be increased through the control of y. Also, it is necessary to examine whether the molecular design guidelines established for controlling the static γ can also be used for the TPA properties. We assign several TPA peaks and then discuss the correlation with y in realistic open-shell molecular aggregates for the first time. In addition, we discuss the validity and applicability of quantum chemical methods for treating the ground and excited states of open-shell molecular aggregates, which is indispensable for the comparison of theoretical results with experiments. Based on these analyses, we will extract optimal conditions and structural parameter regions for enhancing the TPA cross-section, and then, we will propose design guidelines for novel NLO materials based on open-shell molecular aggregates.

This dissertation will also bridge the present gap between the theoretical and experimental analyses for the static γ and TPA of open-shell molecular systems. In the theoretical analyses, there are several assumptions, hypothetical conditions, and calculation conditions, depending on the size and characters of the system. It is necessary to pay attention to whether the theoretical results reproduce the actual measurement results both qualitatively and quantitatively. From the experimental side, a wide range of factors can influence the quality of the results, such as the measurement conditions and the surrounding environment. It is not always easy to identify the parameters that contribute to the observed phenomena. To essentially connect both the analysis results together, not only the technical development but also a willingness to mutual understanding and collaboration is important. In practice, many steps are still needed. Still, organic NLO materials that can be used practically have not yet been created. To establish theory-experiment joint research, it is essential to elucidate the mechanism and principle describing the physico-chemical phenomena and then obtain materials design guidelines that can be incorporated into synthesizable and realistic candidate materials.

This dissertation is organized as follows:

PART I. Electronic structure theory, theory of nonlinear optics, and theory of TPA of open-shell systems

PART II. Discussion of the N-dependence of static γ, which is fundamental to the discussion of TPA of multiradical systems

PART III. Detailed theoretical analysis of TPA from dimers to multimers of radicals

This dissertation is expected to connect theory and experiment on TPA properties of open-shell molecular aggregates systems, to provide a basis for the theoretical materials design in accordance with actual phenomena, and to contribute to the creation of novel optical functional materials.

References

[1] Y. R. Shen, *The Principles of Nonlinear Optics*, John Wiley & Sons, Inc, **2002**.

[2] M. Göppert, *Naturwissenschaften*, **1929**, *17*, 932.

[3] W. Kaiser and C. G. B. Garrett, *Phys. Rev. Lett.*, **1961**, *7*, 229–231.

[4] W. Denk, J. H. Strickler and W. W. Webb, *Science (80-.).*, **1990**, *248*, 73–76.

[5] D. A. P. A. P. M. RENTZEPIS, *Science (80-.).*, **1989**, *245*, 843–845.

[6] S. Kawata and Y. Kawata, *Chem. Rev.*, **2000**, *100*, 1777–1788.

[7] S. Maruo, O. Nakamura and S. Kawata, *Opt. Lett.*, **1997**, *22*, 132–134.

[8] B. H. Cumpston, S. P. Ananthavel, S. Barlow, D. L. Dyer, J. E. Ehrlich, L. L. Erskine, A. A. Heikal, S. M. Kuebler, I. S. Lee, D. Mccord-maughon, J. Qin, M. Rumi, X. Wu, S. R. Marder and J. W. Perry, *Nature*, **1999**, *398*, 51–54.

[9] J. Fischer, G. Von Freymann and M. Wegener, *Adv. Mater.*, **2010**, *22*, 3578–3582.

[10] X. J. Feng, P. L. Wu, F. Bolze, H. W. C. Leung, K. F. Li, N. K. Mak, D. W. J. Kwong, J. F. Nicoud, K. W. Cheah and M. S. Wong, *Org. Lett.*, **2010**, *12*, 2194–2197.

[11] M. Sheik-Bahae, A. A. Said, T. H. Wei, D. J. Hagan and E. W. Van Stryland, *IEEE J. Quantum Electron.*, **1990**, *26*, 760–769.

[12] R. R. Tykwinski, K. Kamada, D. Bykowski, F. A. Hegmann and R. J. Hinkle, *J. Opt. A Pure Appl. Opt.*, **2002**, *4*, S202–S206.

[13] M. Albota, D. Beljonne, J. L. Brédas, J. E. Ehrlich, J. Y. Fu, A. A. Heikal, S. E. Hess, T. Kogej, M. D. Levin, S. R. Marder, D. McCord-Maughon, J. W. Perry, H. Röckel, M. Rumi, G. Subramaniam, W. W. Webb, X. L. Wu and C. Xu, *Science (80-.).*, **1998**, *281*, 1653–1656.

[14] F. Terenziani, C. Katan, E. Badaeva, S. Tretiak and M. Blanchara-Desce, *Enhanced two-photon absorption of organic chromophores: Theoretical and experimental assessments*, **2008**, vol. 20.

[15] T. Kogej, D. Beljonne, F. Meyers, J. W. Perry, S. R. Marder and J. L. Brédas, *Chem. Phys. Lett.*, **1998**, *298*, 1–6.

[16] K. Ohta and K. Kamada, *J. Chem. Phys.*, **2006**, *124*, 124303.

[17] K. Ohta, S. Yamada, K. Kamada, A. D. Slepkov, F. A. Hegmann, R. R. Tykwinski, L. D. Shirtcliff, M. M. Haley, P. Sałek, F. Gel'mukhanov and H. Ågren, *J. Phys. Chem. A*, **2011**, *115*, 105–117.

[18] M. Nakano, K. Yoneda, R. Kishi, H. Takahashi, T. Kubo, K. Kamada, K. Ohta, B. Champagne and E. Botek, in *AIP Conference Proceedings*, **2012**, vol. 1504, pp. 136–142.

[19] M. T. P. Beerepoot, D. H. Friese, N. H. List, J. Kongsted and K. Ruud, *Phys. Chem. Chem. Phys.*, **2015**, *17*, 19306–19314.

[20] V. Shakin and S. Abe, *Phys. Rev. B - Condens. Matter Mater. Phys.*, **1996**, *53*, 10656–10666.

[21] R. Kishi, M. Nakano, S. Yamada, K. Kamada, K. Ohta, T. Nitta and K. Yamaguchi, *Chem. Phys. Lett.*, **2004**, *393*, 437–441.

[22] S. J. Chung, K. S. Kim, T. C. Lin, G. S. He, J. Swiatkiewicz and P. N. Prasad, *J. Phys. Chem. B*, **1999**, *103*, 10741–10745.

[23] O. Mongin, L. Porrès, C. Katan, T. Pons, J. Mertz and M. Blanchard-Desce, *Tetrahedron Lett.*, **2003**, *44*, 9065.

[24] M. Drobizhev, A. Karotki, Z. Suo, C. Spangler and A. Rebane, *OSA Trends Opt. Photonics Ser.*, **2003**, *88*, 290–292.

[25] H. J. Lee, J. Sohn, J. Hwang and S. Y. Park, *Chem. Mater.*, **2004**, *16*, 456–465.

[26] R. Kannan, G. S. He, T. C. Lin, P. N. Prasad, R. A. Vaia and L. S. Tan, *Chem. Mater.*, **2004**, *16*, 185–194.

[27] Y. Z. Cui, Q. Fang, G. Xue, G. B. Xu, L. Yin and W. T. Yu, *Chem. Lett.*, **2005**, *34*, 644–645.

[28] J. Li, F. Meng, H. Tian, J. Mi and W. Ji, *Chem. Lett.*, **2005**, *34*, 922–923.

[29] A. Bhaskar, R. Guda, M. M. Haley and T. Goodson, *J. Am. Chem. Soc.*, **2006**, *128*, 13972–13973.

[30] S. I. Kato, T. Matsumoto, M. Shigeiwa, H. Gorohmaru, S. Maeda, T. Ishi-i and S. Mataka, *Chem. - A Eur. J.*, **2006**, *12*, 2303–2317.

[31] J. Wu, Y. Zhao, X. Li, M. Shi, F. Wu and X. Fang, *New J. Chem.*, **2006**, *30*, 1098–1103.

[32] E. Michail, M. H. Schreck, M. Holzapfel and C. Lambert, *Phys. Chem. Chem. Phys.*, **2020**, *22*, 18340–18350.

[33] K. Ogawa, A. Ohashi, Y. Kobuke, K. Kamada and K. Ohta, *J. Am. Chem. Soc.*, **2003**, *125*, 13356–13357.

[34] H. Rath, J. Sankar, V. PrabhuRaja, T. K. Chandrashekar, A. Nag and D. Goswami, *J. Am. Chem. Soc.*, **2005**, *127*, 11608–11609.

[35] K. Ogawa, A. Ohashi, Y. Kobuke, K. Kamada and K. Ohta, *J. Phys. Chem. B*, **2005**, *109*, 22003–22012.

[36] M. Drobizhev, Y. Stepanenko, A. Rebane, C. J. Wilson, T. E. O. Screen and H. L. Anderson, *J. Am. Chem. Soc.*, **2006**, *128*, 12432–12433.

[37] Y. Tanaka, S. Saito, S. Mori, N. Aratani, H. Shinokubo, N. Shibata, Y. Higuchi, Z. S. Yoon, K. S. Kim, S. B. Noh, J. K. Park, D. Kim and A. Osuka, *Angew. Chemie*, **2008**, *120*, 693–696.

[38] J. Dy, K. Ogawa, K. Kamada, K. Ohta and Y. Kobuke, *Chem. Commun.*, **2008**, 3411–3413.

[39] K. Kamada, Y. Tanamura, K. Ueno, K. Ohta and H. Misawa, *J. Phys. Chem. C*, **2007**, *111*, 11193–11198.

[40] Y. Suzuki, Y. Tenma, Y. Nishioka, K. Kamada, K. Ohta and J. Kawamata, *J. Phys. Chem. C*, **2011**, *115*, 20653–20661.

[41] K. Kamada, K. Ohta, Y. Iwase and K. Kondo, *Chem. Phys. Lett.*, **2003**, *372*, 386–393.

[42] M. Drobizhev, N. S. Makarov, T. Hughes and A. Rebane, *J. Phys. Chem. B*, **2007**, *111*, 14051–14054.

[43] M. Nakano, R. Kishi, T. Nitta, T. Kubo, K. Nakasuji, K. Kamada, K. Ohta, B. Champagne, E. Botek and K. Yamaguchi, *J. Phys. Chem. A*, **2005**, *109*, 885–891.

[44] M. Nakano, R. Kishi, N. Nakagawa, S. Ohta, H. Takahashi, S. I. Furukawa, K. Kamada, K. Ohta, B. Champagne, E. Botek, S. Yamada and K. Yamaguchi, *J. Phys. Chem. A*, **2006**, *110*, 4238–4243.

[45] M. Nakano, T. Kubo, K. Kamada, K. Ohta, R. Kishi, S. Ohta, N. Nakagawa, H. Takahashi, S. I. Furukawa, Y. Morita, K. Nakasuji and K. Yamaguchi, *Chem. Phys. Lett.*, **2006**, *418*, 142–147.

[46] S. Ohta, M. Nakano, T. Kubo, K. Kamada, K. Ohta, R. Kishi, N. Nakagawa, B. Champagne, E. Botek, S. Y. Umezaki, A. Takebe, H. Takahashi, S. I. Furukawa, Y. Morita, K. Nakasuji and K. Yamaguchi, *Chem. Phys. Lett.*, **2006**, *420*, 432–437.

[47] M. Nakano, R. Kishi, S. Ohta, A. Takebe, H. Takahashi, S. I. Furukawa, T. Kubo, Y. Morita, K. Nakasuji, K. Yamaguchi, K. Kamada, K. Ohta, B. Champagne and E. Botek, *J. Chem. Phys.*, **2006**, *125*, 074113.

[48] M. Nakano, A. Takebe, R. Kishi, S. Ohta, M. Nate, T. Kubo, K. Kamada, K. Ohta, B. Champagne, E. Botek, H. Takahashi, S. ichi Furukawa, Y. Morita and K. Nakasuji, *Chem. Phys. Lett.*, **2006**, *432*, 473–479.

[49] M. Nakano, R. Kishi, S. Ohta, H. Takahashi, T. Kubo, K. Kamada, K. Ohta, E. Botek and B. Champagne, *Phys. Rev. Lett.*, **2007**, *99*, 033001.

[50] M. Nakano, K. Yoneda, R. Kishi, H. Takahashi, T. Kubo, K. Kamada, K. Ohta, E. Botek and B. Champagne, *J. Chem. Phys.*, **2009**, *131*, 114316.

[51] B. Champagne, V. Deguelle and J. M. André, *J. Mol. Struct. THEOCHEM*, **1995**, *332*, 93–104.

[52] M. Nakano, H. Nagao and K. Yamaguchi, *Phys. Rev. A - At. Mol. Opt. Phys.*, **1997**, *55*, 1503–1513.

[53] S. K. Mandal, S. Samanta, M. E. Itkis, D. W. Jensen, R. W. Reed, R. T. Oakley, F. S. Tham, B. Donnadieu and R. C. Haddon, *J. Am. Chem. Soc.*, **2006**, *128*, 1982–1994.

[54] M. Kertesz, *Chem. - A Eur. J.*, **2019**, *25*, 400–416.

[55] S. K. Pal, M. E. Itkis, F. S. Tham, R. W. Reed, R. T. Oakley and R. C. Haddon, *Science (80-.).*, **2005**, *309*, 281–284.

[56] M. E. Itkis, X. Chi, A. W. Cordes and R. C. Haddon, *Science (80-.).*, **2002**, *296*, 1443–1445.

[57] X. Chi, M. E. Itkis, K. Kirschbaum, A. A. Pinkerton, R. T. Oakley, A. W. Cordes and R. C. Haddon, *J. Am. Chem. Soc.*, **2001**, *123*, 4041–4048.

[58] S. K. Pal, M. E. Itkis, F. S. Tham, R. W. Reed, R. T. Oakley, B. Donnadieu and R. C. Haddon, *J. Am. Chem. Soc.*, **2007**, *129*, 7163–7174.

[59] T. Kubo, A. Shimizu, M. Sakamoto, M. Uruichi, K. Yakushi, M. Nakano, D. Shiomi, K. Sato, T. Takui, Y. Morita and K. Nakasuji, *Angew. Chemie - Int. Ed.*, **2005**, *44*, 6564–6568.

[60] K. Kamada, K. Ohta, T. Kubo, A. Shimizu, Y. Morita, K. Nakasuji, R. Kishi, S. Ohta, S. I. Furukawa, H. Takahashi and M. Nakano, *Angew. Chemie - Int. Ed.*, **2007**, *46*, 3544–3546.

[61] | Presto-Jst ; Berson, J. A. Matsuda, K. Iwamura, H. Mcmasters, D. R. Wirz, J. Abe, M. Kawakami, T. Ohata, S. Nozaki and K. Nojima, *Org. Lett.*, **2007**, *9*, 81–84.

[62] A. Shimizu, M. Uruichi, K. Yakushi, H. Matsuzaki, H. Okamoto, M. Nakano, Y. Hirao, K. Matsumoto, H. Kurata and T. Kubo, *Angew. Chemie - Int. Ed.*, **2009**, *48*, 5482–5486.

[63] A. Shimizu, T. Kubo, M. Uruichi, K. Yakushi, M. Nakano, D. Shiomi, K. Sato, T. Takui, Y. Hirao, K. Matsumoto, H. Kurata, Y. Morita and K. Nakasuji, *J. AM. CHEM. SOC*, **2010**, *132*, 14421–14428.

[64] K. Kamada, K. Ohta, A. Shimizu, T. Kubo, R. Kishi, H. Takahashi, E. Botek, B. Champagne and M. Nakano, *J. Phys. Chem. Lett.*, **2010**, *1*, 937–940.

[65] R. Kishi, S. Bonness, K. Yoneda, H. Takahashi, M. Nakano, E. Botek, B. Champagne, T. Kubo, K. Kamada, K. Ohta and T. Tsuneda, *J. Chem. Phys.*, **2010**, *132*, 094017.

[66] M. Nakano, T. Minami, H. Fukui, R. Kishi, Y. Shigeta and B. Champagne, *J. Chem. Phys.*, **2012**, *136*, 024315.

[67] Y. Li, W. K. Heng, B. S. Lee, N. Aratani, J. L. Zafra, N. Bao, R. Lee, Y. M. Sung, Z. Sun, K. W. Huang, R. D. Webster, J. T. López Navarrete, D. Kim, A. Osuka, J. Casado, J. Ding and J. Wu, *J. Am. Chem. Soc.*, **2012**, *134*, 14913–14922.

[68] Z. Sun, S. Lee, K. H. Park, X. Zhu, W. Zhang, B. Zheng, P. Hu, Z. Zeng, S. Das, Y. Li, C. Chi, R. W. Li, K. W. Huang, J. Ding, D. Kim and J. Wu, *J. Am. Chem. Soc.*, **2013**, *135*, 18229–18236.

[69] Z. Sun and J. Wu, *Pure Appl. Chem.*, **2014**, *86*, 529–537.

[70] Z. Sun, Z. Zeng and J. Wu, *Acc. Chem. Res.*, **2014**, *47*, 2582–2591.

[71] Y. C. Hsieh, H. Y. Fang, Y. T. Chen, R. Yang, C. I. Yang, P. T. Chou, M. Y. Kuo and Y. T. Wu, *Angew. Chemie - Int. Ed.*, **2015**, *54*, 3069–3073.

[72] Y. Ni, S. Lee, M. Son, N. Aratani, M. Ishida, A. Samanta, H. Yamada, Y. T. Chang, H. Furuta, D. Kim and J. Wu, *Angew. Chemie - Int. Ed.*, **2016**, *55*, 2815–2819.

[73] P. Hu, S. Lee, K. H. Park, S. Das, T. S. Herng, T. P. Gonçalves, K. W. Huang, J. Ding, D. Kim and J. Wu, *J. Org. Chem.*, **2016**, *81*, 2911–2919.

[74] Z. Zeng, M. Ishida, J. L. Zafra, X. Zhu, Y. M. Sung, N. Bao, R. D. Webster, B. S. Lee, R. W. Li, W. Zeng, Y. Li, C. Chi, J. T. L. Navarrete, J. Ding, J. Casado, D. Kim and J. Wu, *J. Am. Chem. Soc.*, **2013**, *135*, 6363–6371.

[75] Z. Zeng, S. Lee, J. L. Zafra, M. Ishida, X. Zhu, Z. Sun, Y. Ni, R. D. Webster, R. W. Li, J. T. López Navarrete, C. Chi, J. Ding, J. Casado, D. Kim and J. Wu, *Angew. Chemie - Int. Ed.*, **2013**, *52*, 8561–8565.

[76] Z. Zeng, S. Lee, J. L. Zafra, M. Ishida, N. Bao, R. D. Webster, J. T. López Navarrete, J. Ding, J. Casado, D. Kim and J. Wu, *Chem. Sci.*, **2014**, *5*, 3072–3080.

[77] S. Das, S. Lee, M. Son, X. Zhu, W. Zhang, B. Zheng, P. Hu, Z. Zeng, Z. Sun, W. Zeng, R. W. Li, K. W. Huang, J. Ding, D. Kim and J. Wu, *Chem. - A Eur. J.*, **2014**, *20*, 11410–11420.

[78] Z. Zeng, S. Lee, M. Son, K. Fukuda, P. M. Burrezo, X. Zhu, Q. Qi, R. W. Li, J. T. L. Navarrete, J. Ding, J. Casado, M. Nakano, D. Kim and J. Wu, *J. Am. Chem. Soc.*, **2015**, *137*, 8572–8583.

[79] Z. Zeng and J. Wu, *Chem. Rec.*, **2015**, *15*, 322–328.

[80] D. Schmidt, M. Son, J. M. Lim, M. J. Lin, I. Krummenacher, H. Braunschweig, D. Kim and F. Würthner, *Angew. Chemie - Int. Ed.*, **2015**, *54*, 13980–13984.

[81] W. Zeng, Y. Hong, S. Medina Rivero, J. Kim, J. L. Zafra, H. Phan, T. Y. Gopalakrishna, T. S. Herng, J. Ding, J. Casado, D. Kim and J. Wu, *Chem. - A Eur. J.*, **2018**, *24*, 4944–4951.

[82] E. Garoni, J. Zirzlmeier, B. S. Basel, C. Hetzer, K. Kamada, D. M. Guldi and R. R. Tykwinski, *J. Am. Chem. Soc.*, **2017**, *139*, 14017–14020.

[83] X. Shi, S. Lee, M. Son, B. Zheng, J. Chang, L. Jing, K. W. Huang, D. Kim and C. Chi, *Chem. Commun.*, **2015**, *51*, 13178–13180.

[84] X. Shi, E. Quintero, S. Lee, L. Jing, T. S. Herng, B. Zheng, K. W. Huang, J. T. López Navarrete, J. Ding, D. Kim, J. Casado and C. Chi, *Chem. Sci.*, **2016**, *7*, 3036–3046.

[85] X. Lu, S. Lee, J. O. Kim, T. Y. Gopalakrishna, H. Phan, T. S. Herng, Z. Lim, Z. Zeng, J. Ding, D. Kim and J. Wu, *J. Am. Chem. Soc.*, **2016**, *138*, 13048–13058.

[86] X. Lu, S. Lee, Y. Hong, H. Phan, T. Y. Gopalakrishna, T. S. Herng, T. Tanaka, M. E. Sandoval-Salinas, W. Zeng, J. Ding, D. Casanova, A. Osuka, D. Kim and J. Wu, *J. Am. Chem. Soc.*, **2017**, *139*, 13173–13183.

[87] J. Wang, G. Kim, M. E. Sandoval-Salinas, H. Phan, T. Y. Gopalakrishna, X. Lu, D. Casanova, D. Kim and J. Wu, *Chem. Sci.*, **2018**, *9*, 3395–3400.

[88] K. Yamaguchi, in *Self-Consistent Field: Theory and Applications*, Elsevier, Amsterdam, The Netherlands, **1990**.

[89] M. Nakano and B. Champagne, *Wiley Interdiscip. Rev. Comput. Mol. Sci.*, **2016**, *6*, 198–210.

[90] R. Kishi, S. Bonness, K. Yoneda, H. Takahashi, M. Nakano, E. Botek, B. Champagne, T. Kubo, K. Kamada, K. Ohta and T. Tsuneda, *J. Chem. Phys.*, **2010**, *132*, 094107.

[91] K. Goto, T. Kubo, K. Yamamoto, K. Nakasuji, K. Sato, D. Shiomi, T. Takui, M. Kubota and T. Kobayashi, *J. Am. Chem. Soc.*, **1999**, *121*, 1619–1620.

[92] S. Suzuki, Y. Morita, K. Fukui, K. Sato, D. Shiomi, T. Takui and K. Nakasuji, *J. Am. Chem. Soc.*, **2006**, *128*, 2530–2531.

[93] Z. Mou, K. Uchida, T. Kubo and M. Kertesz, *J. Am. Chem. Soc.*, **2014**, *136*, 18009–18022.

[94] T. Kubo, *Bull. Chem. Soc. Jpn.*, **2021**, *94*, 2235–2244.

[95] Y. Takano, T. Taniguchi, H. Isobe, T. Kubo, Y. Morita, K. Yamamoto, K. Nakasuji, T. Takui and K. Yamaguchi, *Chem. Phys. Lett.*, **2002**, *358*, 17–23.

[96] V. Zaitsev, S. V. Rosokha, M. Head-Gordon and J. K. Kochi, *J. Org. Chem.*, **2006**, *71*, 520–526.

[97] Z. H. Cui, H. Lischka, H. Z. Beneberu and M. Kertesz, *J. Am. Chem. Soc.*, **2014**, *136*, 5539–5542.

[98] Z. Tang, Z. Jiang, H. Chen, P. Su and W. Wu, *J. Chem. Phys.*, **2019**, *151*, 244106.

[99] K. Uchida, Y. Hirao, H. Kurata, T. Kubo, S. Hatano and K. Inoue, *Chem. - An Asian J.*, **2014**, *9*, 1823–1829.

[100] K. Yoneda, M. Nakano, K. Fukuda, H. Matsui, S. Takamuku, Y. Hirosaki, T. Kubo, K. Kamada and B. Champagne, *Chem. - A Eur. J.*, **2014**, *20*, 11129–11136.

[101] S. Salustro, L. Maschio, B. Kirtman, M. Rérat and R. Dovesi, *J. Phys. Chem. C*, **2016**, *120*, 6756–6761.

[102] R. Dovesi, R. Orlando, A. Erba, C. M. Zicovich-Wilson, B. Civalleri, S. Casassa, L. Maschio, M. Ferrabone, M. De La Pierre, P. D'Arco, Y. Noël, M. Causà, M. Rérat and B. Kirtman, *Int. J. Quantum Chem.*, **2014**, *114*, 1287–1317.

[103] R. Dovesi, A. Erba, R. Orlando, C. M. Zicovich-Wilson, B. Civalleri, L. Maschio, M. Rérat, S. Casassa, J. Baima, S. Salustro and B. Kirtman, *WIREs Comput. Mol. Sci.*, **2018**, *8:e1360*, 1–36.

[104] W. Yoshida, H. Matsui, H. Miyamoto, T. Tonami, R. Sugimori, K. Yoneda, R. Kishi and M. Nakano, *ACS Omega*, **2021**, *6*, 3046–3059.

[105] K. Yamaguchi, *Chem. Phys. Lett.*, **1975**, *33*, 330–335.

[106] Y. Tawada, T. Tsuneda, S. Yanagisawa, T. Yanai and K. Hirao, *J. Chem. Phys.*, **2004**, *120*, 8425–8433.

[107] H. Matsui, M. Yamane, T. Tonami, M. Nakano, M. De Wergifosse, T. Seidler and B. Champagne, *J. Phys. Chem. C*, **2018**, *122*, 6779–6785.

PART I

General Theory

Chapter 1.

Electronic Structures of Open-Shell Singlet Molecules

This chapter introduces the fundamentals of the electronic structure theory of open-shell molecules. First, an analytical expression for open-shell character, a quantitative index of instability of chemical bonding, is derived using the valence configuration interaction (VCI) approach. Based on this expression, we explain the relationship between electronic properties, including excitation energies, and open-shell characteristics. Next, we describe a quantitative evaluation method for the open-shell character of diradical systems using a two-site model consisting of two-electrons and two-orbitals. The process of extending this method to multiradical systems is also described. Finally, we present practical methods for evaluating open-shell characteristics by quantum chemical calculations using the spin-unrestricted method.

1.1. Electronic Structures of Open-Shell Singlet Molecules Based on Valence Configuration Interaction Theory

In this section, we use the valence configuration interaction (VCI) method to describe the electronic structure of the symmetric two-electron, two-orbital model, which is the simplest model of an open-shell singlet molecule[1–3]. This two-site model consists of two atomic sites A and B, with atomic orbitals (AOs) $\chi_A(\boldsymbol{r})$ and $\chi_B(\boldsymbol{r})$, respectively (Figure I.1.1).

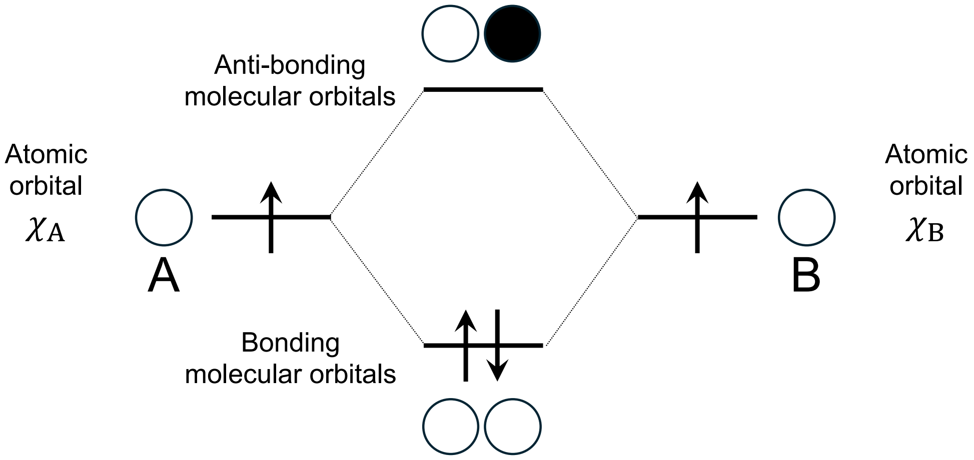

Figure I.1.1. Orbital correlation diagram for symmetric two-electron and two-orbital model with diatomic molecule.

The bonding and anti-bonding symmetry-adopted molecular orbitals (SA-MOs), $g(\boldsymbol{r})$ and $u(\boldsymbol{r})$, are represented by a linear combination of these AOs as follows:

$$g(\boldsymbol{r}) = \frac{1}{\sqrt{2(1+S_{AB})}}\left(\chi_A(\boldsymbol{r}) + \chi_B(\boldsymbol{r})\right),$$
$$u(\boldsymbol{r}) = \frac{1}{\sqrt{2(1-S_{AB})}}\left(\chi_A(\boldsymbol{r}) - \chi_B(\boldsymbol{r})\right) \qquad (\mathrm{I}.1.1)$$

Here, S_{AB} is overlap integral between $\chi_A(\boldsymbol{r})$ and $\chi_B(\boldsymbol{r})$ ($S = \langle\chi_A|\chi_B\rangle$). MOs in the singlet state of open-shell molecules are given by the unrestricted Hartree-Fock (UHF) method with a mixed parameter θ ($0 \le \theta \le \pi/4$) of bonding and anti-bonding orbitals.

$$\psi^{\alpha}(\boldsymbol{r}) = cos\theta g(\boldsymbol{r}) + sin\theta u(\boldsymbol{r}),$$
$$\psi^{\beta}(\boldsymbol{r}) = cos\theta g(\boldsymbol{r}) - sin\theta u(\boldsymbol{r}) \qquad (\mathrm{I}.1.2)$$

In the case of $\theta = 0$, these MOs are given by the restricted Hartree-Fock (RHF) method. On the other hand, in the case of $\theta = \pi/4$, the MOs are fully localized UHF MOs. The MOs in these cases are expressed using localized natural orbitals (LNOs) as follows[1]:

$$\begin{aligned} \psi^{\alpha}(\boldsymbol{r}) &= cos\omega a(\boldsymbol{r}) + sin\omega b(\boldsymbol{r}), \\ \psi^{\beta}(\boldsymbol{r}) &= cos\omega b(\boldsymbol{r}) + sin\omega a(\boldsymbol{r}) \end{aligned} \tag{I.1.3}$$

where, the LNOs, $a(\boldsymbol{r})$ and $b(\boldsymbol{r})$, are obtained by the unitary transformations from the delocalized MOs, $g(\boldsymbol{r})$ and $u(\boldsymbol{r})$:

$$\begin{aligned} a(\boldsymbol{r}) &= \frac{1}{\sqrt{2}}\big(g(\boldsymbol{r}) + u(\boldsymbol{r})\big), \\ b(\boldsymbol{r}) &= \frac{1}{\sqrt{2}}(g(\boldsymbol{r}) - u(\boldsymbol{r})) \end{aligned} \tag{I.1.4}$$

The LNOs are similar to the AOs χ_{A} and χ_{B} but fulfill the orthogonal condition $\langle a|b\rangle = 0$ unlike AOs.

Consider frontier MOs that can be described by a linear combination of LNO $a(\boldsymbol{r})$ and $b(\boldsymbol{r})$. Considering the two active electrons, in two valence orbitals and other closed-shell frozen core orbitals, there are two neutral determinants (Eq. (I.1.5)) and two ionic determinants (Eq. (I.1.6)) for spin angular momentum quantum number $M_S = 0$:

$$\begin{aligned} |a\bar{b}\rangle &\equiv |\mathrm{core}\ a\bar{b}\rangle, \\ |b\bar{a}\rangle &\equiv |\mathrm{core}\ b\bar{a}\rangle \end{aligned} \tag{I.1.5}$$

$$\begin{aligned} |a\bar{a}\rangle &\equiv |\mathrm{core}\ a\bar{a}\rangle, \\ |b\bar{b}\rangle &\equiv |\mathrm{core}\ b\bar{b}\rangle \end{aligned} \tag{I.1.6}$$

where "core" represents an inactive orbital (frozen core orbital), the upper bar represents down spin (β spin), and the non-bar represents up spin (α spin). These four determinants are shown in Figure I.1.2.

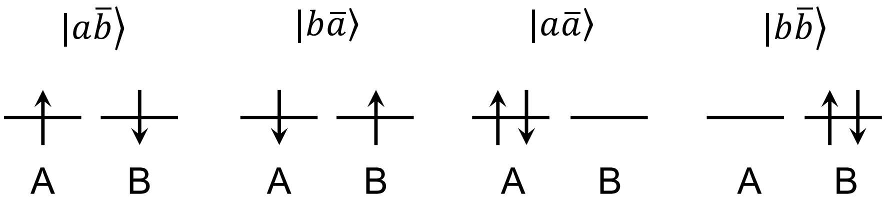

Figure I.1.2. Four types of NLO determinants.

The configuration interaction (CI) matrix $\boldsymbol{H}$ based on Eqs. (1.1.5) and (1.1.6) is expressed as:

$$\boldsymbol{H} = \begin{pmatrix} \langle a\bar{b}|\hat{H}|a\bar{b}\rangle & \langle a\bar{b}|\hat{H}|b\bar{a}\rangle & \langle a\bar{b}|\hat{H}|a\bar{a}\rangle & \langle a\bar{b}|\hat{H}|b\bar{b}\rangle \\ \langle b\bar{a}|\hat{H}|a\bar{b}\rangle & \langle b\bar{a}|\hat{H}|b\bar{a}\rangle & \langle b\bar{a}|\hat{H}|a\bar{a}\rangle & \langle b\bar{a}|\hat{H}|b\bar{b}\rangle \\ \langle a\bar{a}|\hat{H}|a\bar{b}\rangle & \langle a\bar{a}|\hat{H}|b\bar{a}\rangle & \langle a\bar{a}|\hat{H}|a\bar{a}\rangle & \langle a\bar{a}|\hat{H}|b\bar{b}\rangle \\ \langle b\bar{b}|\hat{H}|a\bar{b}\rangle & \langle b\bar{b}|\hat{H}|b\bar{a}\rangle & \langle b\bar{b}|\hat{H}|a\bar{a}\rangle & \langle b\bar{b}|\hat{H}|b\bar{b}\rangle \end{pmatrix} \tag{I.1.7}$$

To simplify $\boldsymbol{H}$, it can be rewritten as follows:

$$\langle a\bar{b}|\hat{H}|a\bar{b}\rangle = \langle a\bar{b}|\hat{H}|b\bar{a}\rangle = 0, \tag{I.1.8}$$

$$\langle a\bar{a}|\hat{H}|a\bar{a}\rangle = \langle b\bar{b}|\hat{H}|b\bar{b}\rangle = U_{aa} - U_{ab} \equiv U, \tag{I.1.9}$$

$$\langle a\bar{b}|\hat{H}|b\bar{a}\rangle = \langle b\bar{a}|\hat{H}|a\bar{b}\rangle = \langle a\bar{a}|\hat{H}|b\bar{b}\rangle = \langle b\bar{b}|\hat{H}|a\bar{a}\rangle = K_{ab} \tag{I.1.10}$$

$$\begin{aligned} &\langle a\bar{a}|\hat{H}|a\bar{b}\rangle = \langle a\bar{a}|\hat{H}|b\bar{a}\rangle = \langle a\bar{a}|\hat{H}|b\bar{a}\rangle = \langle b\bar{b}|\hat{H}|b\bar{a}\rangle \\ &= \langle a\bar{b}|\hat{H}|a\bar{a}\rangle = \langle a\bar{b}|\hat{H}|b\bar{b}\rangle = \langle b\bar{a}|\hat{H}|a\bar{a}\rangle = \langle b\bar{a}|\hat{H}|b\bar{b}\rangle = t_{ab} \end{aligned} \tag{I.1.11}$$

U is the on-site coulomb repulsion, K_{ab} is the exchange integral, and t_{ab} is the transfer integral. From the above, CI matrix in $\boldsymbol{H}$ can be written in simplified form as follows:

$$\boldsymbol{H} = \begin{pmatrix} 0 & K_{ab} & t_{ab} & t_{ab} \\ K_{ab} & 0 & t_{ab} & t_{ab} \\ t_{ab} & t_{ab} & U & K_{ab} \\ t_{ab} & t_{ab} & K_{ab} & U \end{pmatrix} \tag{I.1.12}$$

Furthermore, the dimensionless CI matrix of the $\boldsymbol{H}_{DL}$ by dividing $\boldsymbol{H}$ by U, is expressed using the dimensionless parameters r_t and r_K as follows:

$$\boldsymbol{H}_{DL} = \begin{pmatrix} 0 & r_K/2 & r_t & r_t \\ r_K/2 & 0 & r_t & r_t \\ r_t & r_t & 1 & r_K/2 \\ r_t & r_t & r_K/2 & 1 \end{pmatrix} \tag{I.1.13}$$

r_t and r_K are the following:

$$r_t \equiv \frac{|t_{ab}|}{U}, \text{ and } r_K \equiv \frac{2K_{ab}}{U} \tag{I.1.14}$$

The diagonalization of the CI and dimensionless CI matrix shown in Eqs. (I.1.12) and (I.1.13) gives the analytical expressions for the eigenvalues [E(S_{1g}), E(S_{2g}), E(S_{1u}), E(T_{1u})] of the four eigenstates [S_{1g}, S_{2g}, S_{1u}, T_{1u}]. S_{1g} is the singlet state with *g* (*gerade*) symmetry and lower energy, S_{2g} is the singlet state with *g* symmetry and higher energy, S_{1u} is the ionic singlet state with *u* (*ungerade*) symmetry, and T_{1u} is the neutral triplet state with u symmetry. These wave functions and energies (and dimensionless energies, $E_{\mathrm{DL}} \equiv E/U$) are each expressed as follows:

(1) S_{1g} state

$$|S_{1g}\rangle = \kappa\left(|a\bar{b}\rangle + |b\bar{a}\rangle\right) + \eta\left(|a\bar{a}\rangle + |b\bar{b}\rangle\right) \tag{I. 1.15}$$

$$E\left(S_{1g}\right) = K_{ab} + \frac{U - \sqrt{U^2 + 16{t_{ab}}^2}}{2}, \quad E\left(S_{1g}\right)_{\mathrm{DL}} = r_K + \frac{1 - \sqrt{1 + 16{r_t}^2}}{2} \tag{I. 1.16}$$

(2) S_{2g} state

$$|S_{2g}\rangle = -\eta\left(|a\bar{b}\rangle + |b\bar{a}\rangle\right) + \kappa\left(|a\bar{a}\rangle + |b\bar{b}\rangle\right) \tag{I. 1.17}$$

$$E\left(S_{2g}\right) = K_{ab} + \frac{U + \sqrt{U^2 + 16{t_{ab}}^2}}{2}, \quad E\left(S_{2g}\right)_{\mathrm{DL}} = r_K + \frac{1 + \sqrt{1 + 16{r_t}^2}}{2} \tag{I. 1.18}$$

The coefficients κ and η are

$$\kappa = \frac{1}{2}\sqrt{1 + \frac{U}{\sqrt{U^2 + 16{t_{ab}}^2}}} = \frac{1}{2}\sqrt{1 + \frac{1}{\sqrt{1 + 16{r_t}^2}}} \tag{I. 1.19}$$

$$\eta = \frac{2|t_{ab}|}{\sqrt{\left(U + \sqrt{U^2 + 16{t_{ab}}^2}\right)\sqrt{U^2 + 16{t_{ab}}^2}}} = \frac{2r_t}{\sqrt{\left(1 + \sqrt{1 + 16{r_t}^2}\right)\sqrt{1 + 16{r_t}^2}}} \tag{I. 1.20}$$

with relationships

$$2(\kappa^2 + \eta^2) = 1, \text{ and } \kappa > \eta > 0 \tag{I. 1.21}$$

$2\kappa^2$ and $2\eta^2$ correspond to the weights of the covalent and ionic contributions, respectively. The introduction of dimensionless parameters r_t and r_K simplifies the expressions for κ and η and the properties of the diradicals.

(3) S_{1u} state

$$|S_{1u}\rangle = \frac{1}{\sqrt{2}}\left(|a\bar{a}\rangle - |b\bar{b}\rangle\right) \tag{I. 1.22}$$

$$E(S_{1u}) = U - K_{ab},\ E(S_{1u})_{\mathrm{DL}} = 1 - r_K \tag{I.1.23}$$

(4) T_{1u} state

$$|T_{1u}\rangle = \frac{1}{\sqrt{2}}\left(|a\bar{b}\rangle - |b\bar{a}\rangle\right) \tag{I.1.24}$$

$$E(T_{1u}) = -K_{ab},\ E(T_{1u})_{\mathrm{DL}} = -r_K \tag{I.1.25}$$

These equations provide a simple way to understand the relationship between the ground and excited states of the diradical system.

1.2. Diradical Character: a Quantitative Indicator of Open-Shell Characteristics

In this section, we describe a quantitative evaluation of the properties of open-shell molecules. Open-shell character can be paraphrased as bond instability, represented by the diradical character (y)[4]. y is the square of the weight of the double excitation configuration in the singlet ground state, defined as follows[5]:

$$|\psi\rangle = C_G|G\rangle + C_D|D\rangle, \qquad \text{and} \qquad y = 2|C_D|^2 \tag{I.1.26}$$

where $|G\rangle$ and $|D\rangle$ denote the ground and double excitation configurations respectively.

To obtain the analytical expression for y, rewrite the eigenstates obtained in Eqs. (I.1.15), (I.1.17), (I.1.22) and (I.1.24) using MO basis. The four electron configurations shown in Figure I.1.3 represent, respectively, $|g\bar{g}\rangle$ as the ground configuration, $|g\bar{u}\rangle$ and $|u\bar{g}\rangle$ as the singly excitation configurations from HOMO to LUMO, and $|u\bar{u}\rangle$ as the doubly excitation configuration from HOMO to LUMO.

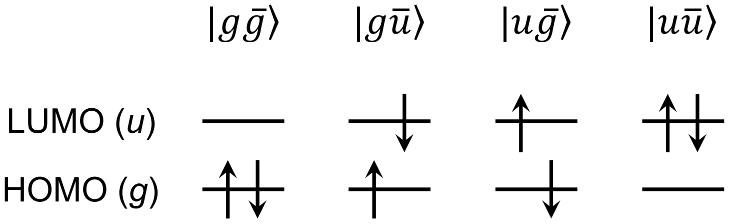

Figure I.1.3. Electron configurations on MO basis.

Using these configurations, eigenstates expressed in the LNO basis can be rewritten as follows:

$$|S_{1g}\rangle = \xi|g\bar{g}\rangle - \zeta|u\bar{u}\rangle \tag{I.1.27}$$

$$|S_{2g}\rangle = \zeta|g\bar{g}\rangle + \xi|u\bar{u}\rangle \tag{I.1.28}$$

$$|S_{1u}\rangle = \frac{1}{\sqrt{2}}(|g\bar{u}\rangle + |u\bar{g}\rangle) \tag{I.1.29}$$

$$|T_{1u}\rangle = \frac{1}{\sqrt{2}}(|g\bar{u}\rangle - |u\bar{g}\rangle) \tag{I.1.30}$$

where, $\xi^2 + \zeta^2 = 1$ and $\xi \geq \zeta$. Also, from Eqs. (I.1.15), (I.1.19), (I.1.20) and (1.1.27), the coefficients ξ and ζ can be derived as follows:

$$\xi = \kappa + \eta = \frac{1}{2}\sqrt{1 + \frac{1}{\sqrt{1+16{r_t}^2}} + \frac{4r_t}{\sqrt{\left(1+\sqrt{1+16{r_t}^2}\right)\sqrt{1+16{r_t}^2}}}} \tag{I.1.31}$$

$$\zeta = \kappa - \eta = \frac{1}{2}\sqrt{1 + \frac{1}{\sqrt{1+16{r_t}^2}} - \frac{4r_t}{\sqrt{\left(1+\sqrt{1+16{r_t}^2}\right)\sqrt{1+16{r_t}^2}}}} \tag{I.1.32}$$

As shown in Eq. (I.1.26), y is defined as twice the weight of the doubly excitation configuration in the S_{1g} state, which leads to the following analytical expression for y:

$$\begin{aligned} y &= 2\zeta^2 = 2(\kappa-\eta)^2 = 1 - 4\kappa\eta \quad (\because 2(\kappa^2+\eta^2) = 1 \ (\text{Eq.}\,(\text{I.}\,1.21))) \\ &= 1 - \frac{4r_t}{\sqrt{1+16{r_t}^2}} \end{aligned} \tag{I.1.33}$$

From the above, it can be seen that y can be expressed only by dimensionless parameter r_t and y decreases with increasing r_t (Figure I.1.4). r_t is the transfer integral between two sites (sites A and B) $|t_{ab}|$ divided by the coulomb repulsion U, as shown in Eq. (1.1.14), and represents the ease of electron transfer. In other words, a large r_t represents a system in which electrons are delocalized to sites A and B, and y is small. Conversely, a small r_t indicates a system in which electrons are localized to sites A and B, and y is large. In summary, y is related to the degree of electron localization or the strength of electron correlation (chemical bonding).

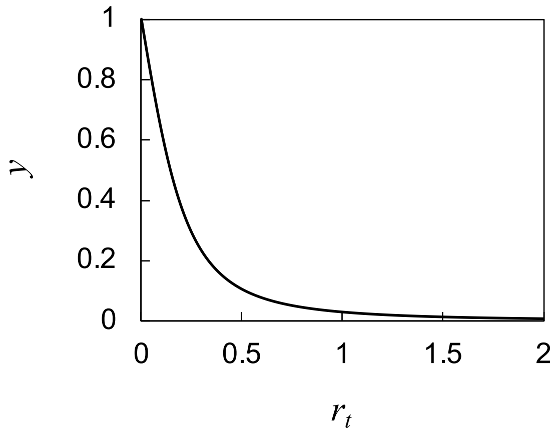

Figure I.1.4. r_t-dependence of diradical character *y*.

The electronic structure of a singlet open-shell molecule to obtain C_D must be obtained strictly on the basis of high-precision *ab initio* calculation methods such as multi-configurational self-consistent field (MC-SCF) theory. However, this may be impractical to apply to real molecular systems because of the extremely high computational cost. In practice, spin-unrestricted single determinant approach such as the spin-unrestricted HF (UHF) or density functional theory (UDFT), which are less computationally expensive, can be used, although it should be noted that they include spin-contamination errors[6,7]. In the spin-unrestricted single determinant approach, *y* is defined by the occupation number (*n*k, where k denotes the natural orbitals label) of the lowest unoccupied natural orbitals (LUNO)[8].

$$y \equiv n_{\mathrm{LUNO}} \tag{I.1.34}$$

The *k*-th NOs (Φ_k) and *n*k are obtained by diagonalizing the spin-less first-order reduced density matrix[9]:

$$\begin{aligned}\rho(\boldsymbol{r};\boldsymbol{r}') &= N\int \Psi^*(\boldsymbol{r},\boldsymbol{r}_2,\cdots,\boldsymbol{r}_N;\boldsymbol{\sigma})\Psi(\boldsymbol{r}',\boldsymbol{r}_2,\cdots,\boldsymbol{r}_N;\boldsymbol{\sigma})d\boldsymbol{r}_2\cdots d\boldsymbol{r}_N d\boldsymbol{\sigma} \\ &= \sum_k n_k \Phi^*{}_k(\boldsymbol{r})\,\Phi_k(\boldsymbol{r}')\end{aligned} \tag{I.1.35}$$

where *N* is the number of all electrons, and $\boldsymbol{r}_i$ and $\boldsymbol{\sigma}$ are the space variables for the *i*-th electron and spin variable of all electrons, respectively. For the two-site diradical model in the VCI method, the expression for *y* in Eq. (I.1.34) is equivalent to the originally defined Eq. (I.1.26). From Eq. (I.1.27), the wave function in the ground state can be expressed using $\boldsymbol{r}_i$ and $\boldsymbol{\sigma}$ as:

$$
\begin{aligned}
\Psi &= C_G|g\bar{g}\rangle + C_D|u\bar{u}\rangle \\
&= C_G\frac{1}{\sqrt{2}}\begin{vmatrix} g(\boldsymbol{r}_1)\alpha(\boldsymbol{\sigma}_1) & g(\boldsymbol{r}_1)\beta(\boldsymbol{\sigma}_1) \\ g(\boldsymbol{r}_2)\alpha(\boldsymbol{\sigma}_2) & g(\boldsymbol{r}_2)\beta(\boldsymbol{\sigma}_2) \end{vmatrix} + C_D\frac{1}{\sqrt{2}}\begin{vmatrix} u(\boldsymbol{r}_1)\alpha(\boldsymbol{\sigma}_1) & u(\boldsymbol{r}_1)\beta(\boldsymbol{\sigma}_1) \\ u(\boldsymbol{r}_2)\alpha(\boldsymbol{\sigma}_2) & u(\boldsymbol{r}_2)\beta(\boldsymbol{\sigma}_2) \end{vmatrix} \\
&= \frac{1}{\sqrt{2}}\{C_G g(\boldsymbol{r}_1)g(\boldsymbol{r}_2) + C_D u(\boldsymbol{r}_1)u(\boldsymbol{r}_2)\}\{\alpha(\boldsymbol{\sigma}_1)\beta(\boldsymbol{\sigma}_2) - \beta(\boldsymbol{\sigma}_1)\alpha(\boldsymbol{\sigma}_2)\}
\end{aligned} \tag{I.1.36}
$$

Substituting Eq. (I.1.36) into Eq. (I.1.35) yields the following equation:

$$
\begin{aligned}
\rho(\boldsymbol{r};\boldsymbol{r}') = {} & 2\int \Psi^*(\boldsymbol{r},\boldsymbol{r}_2;\boldsymbol{\sigma}_1,\boldsymbol{\sigma}_2)\Psi(\boldsymbol{r}',\boldsymbol{r}_2;\boldsymbol{\sigma}_1,\boldsymbol{\sigma}_2)d\boldsymbol{r}_2 d\boldsymbol{\sigma_1} d\boldsymbol{\sigma_2} \\
&= 2|C_G|^2 g^*(\boldsymbol{r})g(\boldsymbol{r}') + 2|C_D|^2 u^*(\boldsymbol{r})u(\boldsymbol{r}')
\end{aligned} \tag{I.1.37}
$$

To organize Eq. (I.1.37), the orthonormal orthogonality conditions $\langle g|u\rangle = 0$ and $\langle \alpha|\beta\rangle = 0$ for spatial orbitals and spin functions were applied. Here, $g(\boldsymbol{r})$ is HONO and $u(\boldsymbol{r})$ is LUNO, and the occupation numbers are expressed as follows:

$$
n_{\mathrm{HONO}} = 2|C_G|^2, \qquad \text{and} \qquad n_{\mathrm{LUNO}} = 2|C_D|^2 \tag{I.1.38}
$$

From this and Eq. (I.1.34):

$$
y = 2|C_D|^2 \tag{I.1.39}
$$

This formula is consistent with Eq. (I.1.26).

Broken symmetry (BS-)MOs in UHF and UDFT with α and β-spins are defined as linear combinations of SA-MOs ($\varphi(\boldsymbol{r})$).

$$
\begin{aligned}
\varphi_{\mathrm{H}}^{\alpha}(\boldsymbol{r}) &= \cos\theta\,\varphi_{\mathrm{H}}(\boldsymbol{r}) + \sin\theta\,\varphi_{\mathrm{L}}(\boldsymbol{r}), \\
\varphi_{\mathrm{H}}^{\beta}(\boldsymbol{r}) &= \cos\theta\,\varphi_{\mathrm{H}}(\boldsymbol{r}) - \sin\theta\,\varphi_{\mathrm{L}}(\boldsymbol{r}), \\
\varphi_{\mathrm{L}}^{\alpha}(\boldsymbol{r}) &= -\sin\theta\,\varphi_{\mathrm{H}}(\boldsymbol{r}) + \cos\theta\,\varphi_{\mathrm{L}}(\boldsymbol{r}), \\
\varphi_{\mathrm{L}}^{\beta}(\boldsymbol{r}) &= \sin\theta\,\varphi_{\mathrm{H}}(\boldsymbol{r}) + \cos\theta\,\varphi_{\mathrm{L}}(\boldsymbol{r})
\end{aligned} \tag{I.1.40}
$$

where the labels H and L mean HOMO and LUMO, respectively. H-i (HOMO-i) and L+i (LUMO+i) are defined similarly:

$$
\begin{aligned}
\varphi_{\mathrm{H}-i}^{\alpha}(\boldsymbol{r}) &= \cos\theta\,\varphi_{\mathrm{H}-i}(\boldsymbol{r}) + \sin\theta\,\varphi_{\mathrm{L}+i}(\boldsymbol{r}), \\
\varphi_{\mathrm{H}-i}^{\beta}(\boldsymbol{r}) &= \cos\theta\,\varphi_{\mathrm{H}-i}(\boldsymbol{r}) - \sin\theta\,\varphi_{\mathrm{L}+i}(\boldsymbol{r}), \\
\varphi_{\mathrm{L}+i}^{\alpha}(\boldsymbol{r}) &= -\sin\theta\,\varphi_{\mathrm{H}-i}(\boldsymbol{r}) + \cos\theta\,\varphi_{\mathrm{L}+i}(\boldsymbol{r}), \\
\varphi_{\mathrm{L}+i}^{\beta}(\boldsymbol{r}) &= \sin\theta\,\varphi_{\mathrm{H}-i}(\boldsymbol{r}) + \cos\theta\,\varphi_{\mathrm{L}+i}(\boldsymbol{r})
\end{aligned} \tag{I.1.41}
$$

These MOs can be transformed to the corresponding orbitals χ_i and η_i by unitary transformations[6].

$$\chi_i = \sum_s \varphi_s^\alpha U_{si},$$
$$\eta_i = \sum_s \varphi_s^\beta V_{si} \qquad (\mathrm{I.1.42})$$

The overlap matrix of these corresponding orbits χ_i and η_i is as follows:

$$T_{ij} = \langle \chi_i | \eta_j \rangle = T_i \delta_{ij} \qquad (\mathrm{I.1.43})$$

where $0 \leq T_i \leq 1$. As in Eq. (I.1.1), other orbitals are obtained by linear combination with the corresponding orbitals and orbital overlap T_i:

$$\lambda_i = \frac{1}{\sqrt{2(1+T_i)}} (\chi_i + \eta_i),$$
$$\nu_i = \frac{1}{\sqrt{2(1-T_i)}} (\chi_i - \eta_i) \qquad (\mathrm{I.1.44})$$

where these orbitals satisfy the orthogonal conditions of $\langle \lambda_i | \nu_j \rangle = 0$ and $\langle \lambda_i | \lambda_j \rangle = \langle \nu_i | \nu_j \rangle = \delta_{ij}$. The corresponding orbitals are given by

$$\chi_i = cos\omega_i \lambda_i + sin\omega_i \nu_i,$$
$$\eta_i = cos\omega_i \lambda_i - sin\omega_i \nu_i \qquad (\mathrm{I.1.45})$$

where denotes a mixing parameter, descrived by

$$cos\omega_i = \frac{\sqrt{2+2T_i}}{2},$$
$$sin\omega_i = \frac{\sqrt{2-2T_i}}{2} \qquad (\mathrm{I.1.46})$$

The overlap T_i is expressed by

$$T_i = cos^2\omega_i - sin^2\omega_i = cos2\omega_i \qquad (\mathrm{I.1.47})$$

$\rho(\boldsymbol{r}; \boldsymbol{r}')$ of the UHF wave function is invariant under the unitary transformation in Eq. (I.1.42). Thus, $\rho(\boldsymbol{r}; \boldsymbol{r}')$ is calculated as follows:

$$\begin{aligned}
\rho(\boldsymbol{r};\boldsymbol{r}') &= \sum_i \varphi_i^{\alpha*}(\boldsymbol{r})\varphi_i^{\alpha}(\boldsymbol{r}') + \sum_i \varphi_i^{\beta*}(\boldsymbol{r})\varphi_i^{\beta}(\boldsymbol{r}') \\
&= \sum_i \chi_i^*(\boldsymbol{r})\chi_i(\boldsymbol{r}') + \sum_i \eta_i^*(\boldsymbol{r})\eta_i(\boldsymbol{r}') \\
&= \sum_i 2cos^2\omega_i\lambda_i^*(\boldsymbol{r})\lambda_i(\boldsymbol{r}') + \sum_i 2sin^2\omega_i\nu_i^*(\boldsymbol{r})\nu_i(\boldsymbol{r}') \\
&= \sum_i (1+T_i)\lambda_i^*(\boldsymbol{r})\lambda_i(\boldsymbol{r}') + \sum_i (1-T_i)\nu_i^*(\boldsymbol{r})\nu_i(\boldsymbol{r}') \qquad \text{(I. 1.48)}
\end{aligned}$$

λ_i and ν_i in Eq. (I.1.48) are the natural orbitals (NOs) of HONO-i and LUNO+i, respectively, and T_i affects the occupation numbers of NOs as follows:

$$\begin{aligned}
n_{\lambda_i} &= n_{\mathrm{HONO}-i} = 1 + T_i, \\
n_{\nu_i} &= n_{\mathrm{LUNO}+i} = 1 - T_i \qquad \text{(I. 1.49)}
\end{aligned}$$

Diradical character y related to HONO and LUNO and y_i related to HONO-i and LUNO+i are expressed as follows:

$$\begin{aligned}
y &= n_{\mathrm{LUNO}} = 2 - n_{\mathrm{HONO}} = 1 - T_0, \\
y_i &= n_{\mathrm{LUNO}+i} = 2 - n_{\mathrm{HONO}-i} = 1 - T_i \qquad \text{(I. 1.50)}
\end{aligned}$$

The above equation allows us to quantitatively evaluate the open-shell nature of not only diradicals but also multiradicals.

1.3. Description of Singlet Open-Shell Characteristics Using Spin-Unrestricted Methods

In spin-unrestricted methods such as UHF and UDFT, higher spin states such as triplet can be mixed into the singlet wavefunctions, resulting in spin-contamination errors that lead to inaccurate wavefunctions. In this section, we describe the solution to this problem. The approximate spin projection (ASP) scheme can be used to solve this problem[10]. For simplicity, consider the UHF wave function of the diradical model with two electrons and two orbitals; the UHF ground state is expressed using the corresponding orbitals (χ_{H} and η_{H}) and NOs (λ_{H} and ν_{H}) as follows:

$$\begin{aligned}\Phi^{\mathrm{UHF}} &= |\chi_{\mathrm{H}}\bar{\eta}_{\mathrm{H}}\rangle \\ &= cos^2\omega|\lambda_{\mathrm{H}}\bar{\lambda}_{\mathrm{H}}\rangle - sin^2\omega|\nu_{\mathrm{L}}\bar{\nu}_{\mathrm{L}}\rangle - cos\omega sin\omega(|\lambda_{\mathrm{H}}\bar{\nu}_{\mathrm{L}}\rangle - |\nu_{\mathrm{L}}\bar{\lambda}_{\mathrm{H}}\rangle) \\ &= \frac{1+cos2\omega}{2}|\lambda_{\mathrm{H}}\bar{\lambda}_{\mathrm{H}}\rangle - \frac{1-cos2\omega}{2}|\lambda_{\mathrm{L}}\bar{\lambda}_{\mathrm{L}}\rangle - \sqrt{\frac{1-cos^2 2\omega}{2}}(|\lambda_{\mathrm{H}}\bar{\nu}_{\mathrm{L}}\rangle - |\nu_{\mathrm{L}}\bar{\lambda}_{\mathrm{H}}\rangle) \\ &= \frac{1+T}{2}|\lambda_{\mathrm{H}}\bar{\lambda}_{\mathrm{H}}\rangle - \frac{1-T}{2}|\lambda_{\mathrm{L}}\bar{\lambda}_{\mathrm{L}}\rangle - \sqrt{\frac{1-T^2}{2}}(|\lambda_{\mathrm{H}}\bar{\nu}_{\mathrm{L}}\rangle - |\nu_{\mathrm{L}}\bar{\lambda}_{\mathrm{H}}\rangle) \qquad (\mathrm{I}.1.51)\end{aligned}$$

The first term in Eq. (I.1.51) is the singlet ground configuration and the second term is the doubly excited configuration. $|\lambda_{\mathrm{H}}\bar{\nu}_{\mathrm{L}}\rangle - |\nu_{\mathrm{L}}\bar{\lambda}_{\mathrm{H}}\rangle$, in the third term, is the triplet component from Eq. (I.1.30). Rewritten as follows:

$$\Phi^{\mathrm{UHF}} = C_G|G\rangle + C_D|D\rangle + C_T|T\rangle \qquad (\mathrm{I}.1.52)$$

which satisfy the following normalized condition.

$$C_G{}^2 + C_D{}^2 + C_T{}^2 = 0 \qquad (\mathrm{I}.1.53)$$

Thus, the UHF wave function of the diradical model consisting of two-electrons and two-orbitals contains only the triplet component. This triplet configuration can be removed by the ASP scheme. The spin-projected UHF (PUHF) wave function obtained by renormalizing the wave function while preserving the ratio of the coefficient of the singlet ground configuration and the doubly excited configuration, C_G and C_D, is as follows:

$$\Phi^{\mathrm{PUHF}} = C'_G|G\rangle + C'_D|D\rangle \qquad (\mathrm{I}.1.54)$$

$$\begin{aligned} C'_G &= \frac{1+T}{\sqrt{2+2T^2}}, \\ C'_D &= -\frac{1-T}{\sqrt{2+2T^2}} \end{aligned} \qquad (\mathrm{I}.1.55)$$

Therefore, the spin-projected occupation numbers $n_{\mathrm{HONO}}^{\mathrm{ASP}}$ and $n_{\mathrm{LUNO}}^{\mathrm{ASP}}$ and y^{ASP} are as follows:

$$\begin{aligned} n_{\mathrm{HONO}}^{\mathrm{ASP}} &= 2|C'_G|^2 = 2\frac{(1+T)^2}{2+2T^2} = \frac{n_{\mathrm{HONO}}^2}{1+T^2} \\ &= 1 + \frac{2T}{1+T^2} = 2 - y^{\mathrm{ASP}}, \end{aligned} \qquad (\mathrm{I}.1.56)$$

$$
\begin{aligned}
n_{\mathrm{LUNO}}^{\mathrm{ASP}} &= 2\left|C'_{D}\right|^{2} = 2\frac{(1-T)^{2}}{2+2T^{2}} = \frac{n_{\mathrm{LUNO}}^{2}}{1+T^{2}} \\
&= 1-\frac{2T}{1+T^{2}} = y^{\mathrm{ASP}}
\end{aligned}
\tag{I. 1.57}
$$

These equations can be extended to any pair of HONO-*i* and LUNO+*i* and are applicable to multiradical systems.

$$
\begin{aligned}
n_{\mathrm{HONO}-i}^{\mathrm{ASP}} &= \frac{n_{\mathrm{HONO}-i}^{2}}{1+{T_i}^{2}} = 1+\frac{2T_i}{1+{T_i}^{2}} \\
&= 2-y_i^{\mathrm{ASP}}
\end{aligned}
\tag{I. 1.58}
$$

$$
\begin{aligned}
n_{\mathrm{LUNO}+i}^{\mathrm{ASP}} &= \frac{n_{\mathrm{LUNO}+i}^{2}}{1+{T_i}^{2}} = 1-\frac{2T_i}{1+{T_i}^{2}} \\
&= y_i^{\mathrm{ASP}}
\end{aligned}
\tag{I. 1.59}
$$

References

[1] C. J. Calzado, J. Cabrero, J. P. Malrieu and R. Caballol, *J. Chem. Phys.*, **2002**, *116*, 2728–2747.

[2] M. Nakano, R. Kishi, S. Ohta, H. Takahashi, T. Kubo, K. Kamada, K. Ohta, E. Botek and B. Champagne, *Phys. Rev. Lett.*, **2007**, *99*, 033001.

[3] J. P. Malrieu, R. Caballol, C. J. Calzado, C. De Graaf and N. Guihéry, *Chem. Rev.*, **2014**, *114*, 429–492.

[4] K. Yamaguchi, in *Self-Consistent Field: Theory and Applications*, eds. R. Carbo and M. Klobukowski, Elsevier, **1990**, p. 727.

[5] Edward F. Hayes and A. K. Q. Siu, *J. Am. Chem. Soc.*, **1971**, *93*, 2090.

[6] A. T. Amos and G. G. Hall, *Proc. R. Soc. A*, **1961**, *263*, 483–493.

[7] H. Nakatsuji, H. Kato and T. Yonezawa, *J. Chem. Phys.*, **1969**, *51*, 3175–3180.

[8] M. Head-Gordon, *Chem. Phys. Lett.*, **2003**, *372*, 508–511.

[9] A. Szabo and N. L. Ostlund, in *Modern Quantum Chemistry: Introduction to Advanced Electronic Structure Theory*, Dover Publication, Inc., Mineola, New York, **1996**.

[10] K. Yamaguchi, *Chem. Phys. Lett.*, **1975**, *33*, 330–335.

Chapter 2.

Theory of Nonlinear Optics

In this chapter, we will discuss the general theory of the second hyperpolarizability γ, which is closely related to TPA. γ is the microscopic origin of the third-order NLO. γ can be computed in two main ways. One is the Sum-Over-States (SOS) method, which is a perturbative approach, and the other is the Finite-Field (FF) method, which is a variational approach. After a brief description of each method, the correlation between static γ and the diradical character y representing open-shell nature will be discussed.

2.1. Two Approaches to Derive the Second Hyperpolarizability γ: SOS and FF Methods

It was mentioned earlier that γ is the coefficient of the third-order term (*FFF*) in the expression (Eq. (3)) for the molecular polarization *p* due to the local electric field *F*. Eq. (3) can be expressed in component form as follows:

$$p_i = \sum_j \alpha_{ij} F_j + \sum_{jk} \beta_{ijk} F_j F_k + \sum_{jkl} \gamma_{ijkl} F_j F_k F_l + \cdots \tag{I.2.1}$$

As is clear from the above equations, these are tensor quantities. *i, j, k*, and *l* denote the components of the molecular coordinate system.

2.1.1. SOS method

The SOS method is calculated considering all excited states based on time-dependent perturbation theory[1,2]. The time-dependent Schrödinger equation for all Hamiltonians is shown below:

$$\widehat{H}(t)\Psi(t) = i\hbar \frac{\partial}{\partial t} \Psi(t) \tag{I.2.2}$$

The Hamiltonian can be expressed in terms of a time-dependent term and a time-independent term:

$$\widehat{H}(t) = \widehat{H}_0 + \widehat{H}'(t) \tag{I.2.3}$$

The time-independent Hamiltonian $\widehat{H}_0$ has been resolved:

$$\widehat{H}_0 |n\rangle = E_n |n\rangle = \hbar\omega_n |n\rangle \tag{I.2.4}$$

where E_n is the eigenvalue of $\widehat{H}_0$, $|n\rangle$ is the eigenstate, ω_n is the frequency. The time-dependent wave function is expressed as:

$$\Psi(t) = \sum_n C_n(t) |n\rangle e^{-i\omega_n t} \tag{I.2.5}$$

$C_n(t)$ is a time-dependent coefficient that can be extended as follows:

$$C_n(t) = \sum_l C_n^{(l)}(t) \tag{I.2.6}$$

Here, *l* is the order of perturbation expansion. From Eqs. (I.2.2), (I.2.5) and (I.2.6), we obtain the time differential equation for $C_n^{(l)}$:

$$\frac{dC_n^{(0)}(t)}{dt} = 0,$$

$$\frac{dC_n^{(l)}(t)}{dt} = \frac{1}{i\hbar}\sum_k C_k^{(l-1)}(t)\langle n|\hat{H}'(t)|k\rangle e^{-i\omega_n t} \quad (l \geq 1) \tag{I.2.7}$$

Solving Eq. (I.2.7) yields $C_n(t)$ under the following conditions:

$$C_n^{(0)}(t) = \delta_{n0}, \quad \text{and} \quad C_n^{(l)}(0) = 0 \quad (l \geq 1) \tag{I.2.8}$$

This condition indicates that the unperturbed molecule is in the ground state.

Next, we consider the second hyperpolarizability of the molecule using the time-dependent wave function and the perturbation Hamiltonian. In the dipole approximation, the perturbation Hamiltonian $\hat{H}'$, which is generated by the interaction between the molecule and the external electric field, is:

$$\hat{H}' = -\hat{\boldsymbol{\mu}}\boldsymbol{F}(t) \tag{I.2.9}$$

The expectation value of $\hat{\boldsymbol{\mu}}$ with $\Psi(\mathrm{t})$ is approximately expressed as:

$$\begin{aligned}\langle\Psi(t)|\hat{\boldsymbol{\mu}}|\Psi(\mathrm{t})\rangle &= \boldsymbol{\mu}(t)\\ &= \boldsymbol{\mu}_0 + \boldsymbol{p}(t)\\ &= \boldsymbol{\mu}_0 + \boldsymbol{p}^{(1)}(t) + \boldsymbol{p}^{(2)}(t) + \boldsymbol{p}^{(3)}(t) + \cdots\end{aligned} \tag{I.2.10}$$

$\boldsymbol{\mu}_0$ is the perturbation-less, and $\boldsymbol{p}(t)$ is the perturbation term. $\boldsymbol{p}^{(1)}(t)$, $\boldsymbol{p}^{(2)}(t)$, and $\boldsymbol{p}^{(3)}(t)$ are the linear, the second-order nonlinear, and the third-order nonlinear polarizations, respectively. The detailed expression for $\boldsymbol{\mu}(t)$ is obtained using Eq. (I.2.5):

$$\boldsymbol{\mu}(t) = \sum_{a,b} C_a^*(t)C_b(t)\langle a|\hat{\boldsymbol{\mu}}|b\rangle e^{i\omega_{ab}t} \tag{I.2.11}$$

where $\langle a|\hat{\boldsymbol{\mu}}|b\rangle$ is the transition dipole moment and ω_{ab} is the energy difference between states *a* and *b*. The *i*-axis component of $\boldsymbol{\mu}(t)$ is given by:

$$\boldsymbol{\mu}_i(t) = \sum_{a,b} C_a^*(t)C_b(t)\mu_{ab}^i e^{i\omega_{ab}t} \tag{I.2.12}$$

$\boldsymbol{\mu}_{ab}^{i}$ is the *i*-axis component of the transition dipole moment vector. Since the perturbation Hamiltonian is described by the first order of the electric field, the *n*th-order perturbation term is proportional to the *n*th-order of the electric field. Therefore, $\boldsymbol{\mu}_0$, $\boldsymbol{p}^{(1)}(t)$, $\boldsymbol{p}^{(2)}(t)$, and $\boldsymbol{p}^{(3)}(t)$ are obtained as follows:

$$\mu_{0,i} = \mu_{00}^{i}, \tag{I.2.13}$$

$$p_i^{(1)}(t) = \sum_{a} C_a^{(1)}(t)\mu_{0a}^{i} e^{i\omega_{0a}t} + \mathrm{c.c}, \tag{I.2.14}$$

$$p_i^{(2)}(t) = \sum_{ab} C_a^{(1)*} C_b^{(1)}(t)\mu_{ab}^{i} e^{i\omega_{ab}t} + \sum_{a} (C_a^{(2)*}(t)\mu_{0a}^{i} e^{i\omega_{0a}t} + \mathrm{c.c}), \tag{I.2.15}$$

$$p_i^{(3)}(t) = \sum_{ab} C_a^{(1)*} C_b^{(1)}(t)\mu_{ab}^{i} e^{i\omega_{ab}t} + \sum_{a} C_a^{(3)*}(t)\mu_{0a}^{i} e^{i\omega_{0a}t} + \mathrm{c.c} \tag{I.2.16}$$

The "c.c." refers to complex conjugate. Based on time-dependent perturbation theory, the primary coefficient $C_n^{(l)}(t)$ is expressed as:

$$C_n^{(1)}(t) = \begin{cases} 0 \quad (n \neq 0) \\ \dfrac{1}{\hbar}\displaystyle\sum_{j} \mu_{n0}^{j}(t)\left\{\dfrac{F_j e^{i(\omega_{n0}-\omega)t}}{\omega_{n0}-\omega} + \dfrac{F_j^{*} e^{i(\omega_{n0}+\omega)t}}{\omega_{n0}+\omega}\right\} \quad (n \neq 0) \end{cases} \tag{I.2.17}$$

Substituting Eq. (I.2.17) into Eq. (I.2.14), we obtain:

$$\begin{aligned} P_i^{(1)}(t) &= \frac{1}{\hbar}\sum_{a\neq 0}\sum_{j} \mu_{a0}^{j}\left\{\frac{F_j e^{i(\omega_{a0}-\omega)t}}{\omega_{a0}-\omega} + \frac{F_j^{*} e^{i(\omega_{a0}+\omega)t}}{\omega_{a0}+\omega}\right\}\mu_{0a}^{i} e^{i\omega_{0a}t} + \mathrm{c.c} \\ &= \frac{1}{\hbar}\sum_{a\neq 0}\sum_{j} \mu_{a0}^{j}\mu_{0a}^{i}\left\{\frac{F_j e^{-i\omega t}}{\omega_{a0}-\omega} + \frac{F_j^{*} e^{i\omega t}}{\omega_{a0}+\omega}\right\} + \mathrm{c.c} \\ &= \sum_{j}\frac{1}{\hbar}\sum_{a\neq 0}\left\{\frac{\mu_{0a}^{i}\mu_{a0}^{j}}{\omega_{a0}-\omega} + \frac{\mu_{0a}^{j}\mu_{a0}^{i}}{\omega_{a0}+\omega}\right\}F_j e^{-i\omega t} + \mathrm{c.c} \end{aligned} \tag{I.2.18}$$

By comparing the above equation with the first-order term in Eq. (I.2.1), the tensor of polarizability, α_{ij}, can be expressed as:

$$\alpha_{ij}(-\omega;\omega) = \frac{1}{\hbar}\sum_{a\neq 0}\left\{\frac{\mu_{j,a0}\mu_{i,0a}}{\omega_{a0}-\omega} + \frac{\mu_{i,a0}\mu_{j,0a}}{\omega_{a0}+\omega}\right\} \tag{I.2.19}$$

By a similar process, the tensors β_{ijk} and γ_{ijkl} for the first and second hyperpolarizabilities are expressed as follows:

$$\begin{aligned}\beta_{ijk}(-(\omega_1+\omega_2);\omega_1,\omega_2) &= \frac{1}{2\hbar^2}P(i,j,k;-(\omega_1+\omega_2);\omega_1,\omega_2) \\ &\times\sum_{n\neq 0}\sum_{m\neq 0}\frac{\mu_{0n}^{i}\mu_{nm}^{j}\mu_{m0}^{k}}{\{\omega_{n0}-(\omega_1+\omega_2)\}(\omega_{n0}-\omega_2)},\end{aligned} \qquad (\mathrm{I}.2.20)$$

$$\begin{aligned}\gamma_{ijkl}(-(\omega_1+\omega_2+\omega_3);\omega_1,\omega_2,\omega_3) &= \frac{1}{6\hbar^3}P(i,j,k,l;-(\omega_1+\omega_2+\omega_3);\omega_1,\omega_2,\omega_3) \\ \times\sum_{n\neq 0}\sum_{m\neq 0}\sum_{n'\neq 0}&\frac{\mu_{0n}^{i}\bar{\mu}_{nm}^{j}\bar{\mu}_{mn'}^{k}\mu_{n'0}^{l}}{\{\omega_{n0}-(\omega_1+\omega_2+\omega_3)\}(\omega_{m0}-\omega_2-\omega_3)(\omega_{n'0}-\omega_3)} \\ -\sum_{n\neq 0}\sum_{m\neq 0}&\frac{\mu_{0n}^{i}\mu_{n0}^{j}\mu_{0m}^{k}\mu_{m0}^{l}}{\{\omega_{n0}-(\omega_1+\omega_2+\omega_3)\}(\omega_{m0}-\omega_2-\omega_3)(\omega_{n'0}-\omega_3)}\end{aligned} \qquad (\mathrm{I}.2.21)$$

where P represents the permutation operator and $\bar{\mu}_{nm}\equiv\mu_{nm}-\mu_{00}\delta_{nm}$. These are the SOS expressions for the frequency-dependent hyperpolarizabilities; the limit values of $\omega_m \rightarrow 0$ (m = 1, 2, 3) are the static (hyper)polarizabilities. Discussing the NLO properties using the static γ, frequency-independent parameter, has the advantage of uniquely defining the values associated with the second hyperpolarizability of the molecule. In this way, the discussion can be simplified. The diagonal component of the static second hyperpolarizability γ_{iiii} is given by:

$$\begin{aligned}\gamma_{iiii}(0) &= 4\left(\sum_{n\neq 0}\sum_{m\neq 0}\sum_{n'\neq 0}\frac{\mu_{0n}^{i}\bar{\mu}_{nm}^{i}\bar{\mu}_{mn'}^{i}\mu_{n'0}^{i}}{E_{n0}E_{m0}E_{n'0}}-\sum_{n\neq 0}\sum_{m\neq 0}\frac{\left(\mu_{n0}^{i}\right)^2\left(\mu_{m0}^{i}\right)^2}{(E_{n0})^2E_{m0}}\right) \\ &= 4\left(\begin{array}{c}\displaystyle\sum_{n\neq 0}\frac{\left(\mu_{n0}^{i}\right)^2\left(\Delta\mu_{nn}^{i}\right)^2}{{E_{n0}}^3}-\sum_{n\neq 0}\sum_{m\neq 0}\frac{\left(\mu_{n0}^{i}\right)^2\left(\mu_{m0}^{i}\right)^2}{(E_{n0})^2E_{m0}} \\ \displaystyle +2\sum_{n\neq 0}\sum_{\substack{m\neq 0\\ m\neq n}}\frac{\mu_{0n}^{i}\Delta\mu_{mn}^{i}\mu_{nm}^{i}\mu_{m0}^{i}}{(E_{n0})^2E_{m0}}+\sum_{n\neq 0}\sum_{\substack{m\neq 0\\ m\neq n}}\sum_{\substack{n'\neq 0\\ n'\neq m}}\frac{\mu_{0n}^{i}\mu_{nm}^{i}\mu_{mn'}^{i}\mu_{n'0}^{i}}{E_{n0}E_{m0}E_{n'0}}\end{array}\right)\end{aligned} \qquad (\mathrm{I}.2.22)$$

where E_{n0} and $\Delta\mu_{aa}^{i}$ are the difference in excitation energy and transition dipole moment between the ground state and the *n*th excited state, respectively. $E_{n0}=\hbar\omega_{n0}$, and $\Delta\mu_{aa}=\mu_{aa}-\mu_{00}$. The four terms in Eq. (I.2.22) correspond to the unique virtual transition processes through the excited states that contribute to the third-order optical response, respectively, as shown in Figure I.2.1[3,4]. The first term corresponds to a transition process through the *n*th excited state only. Such transition paths are classified as type I (0-*n*-*n*-*n*-0), where the symbol "0" represents the ground state. Similarly, the other three terms are classified as type II (0-*n*-0-*m*-0), type III-1 (0-*n*-*m*-*m*-0), and type III-2 (0-*n*-*m*-*n'*-0) pathways. From Eq. (I.2.22), we see that the type I term gives a positive contribution, and the type II term gives a negative contribution to γ_{iiii}. The type III terms generally give positive contributions. The type I and type III-1 contributions disappear in centrosymmetric molecules because of the dipole moment difference between the states involved[4,5]. Type II is negative in the frequency range where there is no first one-photon resonance, but the contribution to the TPA cross-section is small because there is no two-photon resonance term[6,7]. In the case of TPA, the type III-2 contribution is dominant. As can be seen from Eq. (I.2.22), molecules with smaller excitation energies, larger transition dipole moments between states, and larger dipole moment differences tend to exhibit larger γ values. The total value of γ_{iiii} is determined by the relative balance of these terms.

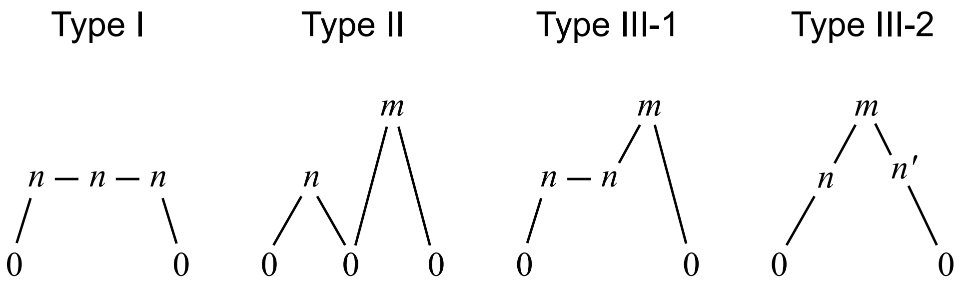

Figure I.2.1. Four types of virtual transition processes of the static γ.

2.1.2. FF method

In the case of the SOS method, it is necessary to obtain the transition dipole moments between the eigenstates of the system, which requires high-precision calculations, but in the FF method, the static γ can be obtained only by calculating the ground state[8]. From the Hellmann-Feynman theorem, the derivative of energy with respect to the electric field F is:

$$\frac{\partial E}{\partial F_i} = \left\langle \Psi \middle| \frac{\partial \hat{H}}{\partial F_i} \middle| \Psi \right\rangle \tag{I.2.23}$$

Substituting Eqs. (I.2.3) and (I.2.9) into the above equation, we obtain:

$$\begin{aligned} \frac{\partial E}{\partial F_i} &= \langle \Psi | -\hat{\mu}_i | \Psi \rangle = -\mu_i \\ &= -\mu_{0,i} - p_i \\ &= -\mu_{0,i} - \sum_j \alpha_{ij} F_j - \sum_{jk} \beta_{ijk} F_j F_k - \sum_{jkl} \gamma_{ijkl} F_j F_k F_l + \cdots \end{aligned} \tag{I.2.24}$$

Transposing yields the following equation:

$$\mu_i = \mu_{0,i} + \sum_j \alpha_{ij} F_j + \sum_{jk} \beta_{ijk} F_j F_k + \sum_{jkl} \gamma_{ijkl} F_j F_k F_l + \cdots \tag{I.2.25}$$

If the Hellmann-Feynman theorem is satisfied, the dipole moment is associated with the energy, so from Eq. (I.2.25):

$$E(\boldsymbol{F}) = E(0) - \sum_{i} \mu_{0,i} F_i - \frac{1}{2}\sum_{ij} \alpha_{ij} F_i F_j - \frac{1}{3}\sum_{ijk} \beta_{ijk} F_i F_j F_k - \frac{1}{4}\sum_{ijkl} \gamma_{ijkl} F_i F_j F_k F_l + \cdots \quad \text{(I. 2.26)}$$

Taylor expansion of the energy when an electric field is applied around $F = 0$ yields the following equation:

$$E(\boldsymbol{F}) = E(0) + \sum_{i} \left.\frac{\partial E(\boldsymbol{F})}{\partial F_i}\right|_{F=0} F_i + \frac{1}{2!}\sum_{ij} \left.\frac{\partial^2 E(\boldsymbol{F})}{\partial F_i \partial F_j}\right|_{F=0} F_i F_j$$

$$+ \frac{1}{3!}\sum_{ijk} \left.\frac{\partial^3 E(\boldsymbol{F})}{\partial F_i \partial F_j \partial F_k}\right|_{F=0} F_i F_j F_k + \frac{1}{4!}\sum_{ijkl} \left.\frac{\partial^4 E(\boldsymbol{F})}{\partial F_i \partial F_j \partial F_k \partial F_l}\right|_{F=0} F_i F_j F_k F_l \cdots \quad \text{(I. 2.27)}$$

Thus, the static (hyper)polarizabilities are obtained as follows:

$$\alpha_{ij} = -\left.\frac{\partial^2 E(\boldsymbol{F})}{\partial F_i \partial F_j}\right|_{F=0} \quad \text{(I. 2.28)}$$

$$\beta_{ijk} = -\frac{1}{2}\left.\frac{\partial^3 E(\boldsymbol{F})}{\partial F_i \partial F_j \partial F_k}\right|_{F=0} \quad \text{(I. 2.29)}$$

$$\gamma_{ijkl} = -\frac{1}{6}\left.\frac{\partial^4 E(\boldsymbol{F})}{\partial F_i \partial F_j \partial F_k \partial F_l}\right|_{F=0} \quad \text{(I. 2.30)}$$

The analytical expression for $E(\boldsymbol{F})$ is not implemented in the usual quantum chemical calculation program packages, but the static γ_{iiii} can be obtained by calculating the diagonal components using higher-order numerical derivatives:

$$\gamma_{iiii} = \frac{\{E(3F_i) + E(-3F_i)\} - 12\{E(2F_i) + E(-2F_i)\} + 39\{E(F_i) + E(-F_i)\} - 56E(0)}{36{F_i}^4} \quad \text{(I. 2.31)}$$

2.2. Dependence of the Static γ on Open-Shell Characteristics

In open-shell singlet systems, the second hyperpolarizability γ, the microscopic origin of NLO, strongly depends on the open-shell character (*y*). The value of the static γ increases markedly in the intermediate region of *y*. For increasing NLO properties, including TPA, theoretical studies using the static γ are very important for understanding phenomena and obtaining molecular design guidelines. In this section, we derive the relationship between the static γ and *y* in a two-site VCI diradical model.

It was explained in the previous section that for systems with symmetric centers, the terms for type I and type III-1 shown in Figure I.2.1 disappear from Eq. (I.2.22). Therefore, in the two-site diradical model, the system reduces to the three-state approximation shown in Figure I.2.2, and in the static limit, the diagonal γ_{iiii} components are expressed as follows:

$$\gamma = \gamma^{\mathrm{II}} + \gamma^{\mathrm{III-2}} = -4\sum_{n\neq 0}\sum_{m\neq 0}\frac{(\mu_{n0})^2(\mu_{m0})^2}{(E_{n0})^2E_{m0}} + 4\sum_{n\neq 0}\sum_{\substack{m\neq 0\\ m\neq n}}\sum_{\substack{n'\neq 0\\ n'\neq m}}\frac{\mu_{0n}\mu_{nm}\mu_{mn'}\mu_{n'0}}{E_{n0}E_{m0}E_{n'0}}$$

$$= -4\frac{\left(\mu_{S_{1\mathrm{g}},S_{1\mathrm{u}}}\right)^4}{\left(E_{S_{1\mathrm{u}},S_{1\mathrm{g}}}\right)^3} + 4\frac{\left(\mu_{S_{1\mathrm{g}},S_{1\mathrm{u}}}\right)^2\left(\mu_{S_{1\mathrm{u}},S_{2\mathrm{g}}}\right)^2}{\left(E_{S_{1\mathrm{u}},S_{1\mathrm{g}}}\right)^2 E_{S_{2\mathrm{g}},S_{1\mathrm{g}}}} \qquad (\mathrm{I}.2.32)$$

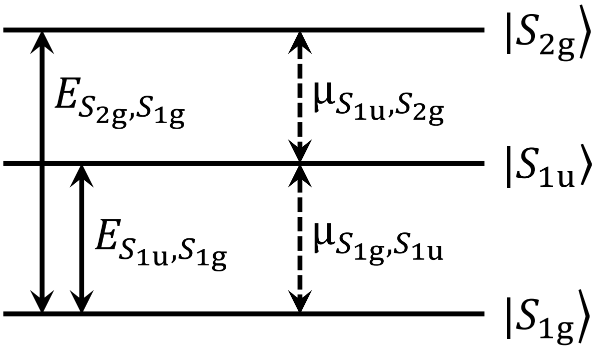

Figure I.2.2. Three singlet states $\{|S_{1g}\rangle,\ |S_{1u}\rangle,\ |S_{2g}\rangle\}$ of the two-site diradical model.

The dimensionless excitation energies $E_{\mathrm{DL}\,S_{1\mathrm{u}},S_{1\mathrm{g}}}$ and $E_{\mathrm{DL}\,S_{2\mathrm{g}},S_{1\mathrm{g}}}$ are derived using Eqs. (I.1.16), (I.1.18), (I.1.23) and (I.1.33) as follows[9]:

$$E_{\mathrm{DL}\,S_{1\mathrm{u}},S_{1\mathrm{g}}} = \frac{E(S_{1\mathrm{u}}) - E(S_{1\mathrm{g}})}{U} = \frac{1}{2}\left(1 - r_K - \frac{1-\sqrt{1+16{r_t}^2}}{2}\right)$$

$$= \frac{1}{2}\left(1 - 2r_K + \frac{1}{\sqrt{1-(1-y)^2}}\right) \qquad (\mathrm{I}.2.33)$$

$$\begin{aligned} E_{\mathrm{DL}\,S_{2\mathrm{g}},S_{1\mathrm{g}}} &= \frac{E\left(S_{2\mathrm{g}}\right) - E\left(S_{1\mathrm{g}}\right)}{U} = \sqrt{1 + 16{r_t}^2} \\ &= \frac{1}{\sqrt{1-(1-y)^2}} \end{aligned} \tag{I. 2.34}$$

The dipole moment operator is given by the following equation:

$$\hat{\mu} = -\sum_n \boldsymbol{r}_n \tag{I. 2.35}$$

where $\boldsymbol{r}_i$ is the position vector of the *n*th electron. The transition dipole moment between the $S_{1\mathrm{g}}$ and $S_{1\mathrm{u}}$ states is expressed as follows:

$$\begin{aligned} \mu_{S_{1\mathrm{g}},S_{1\mathrm{u}}} &= -\left\langle S_{1\mathrm{g}}\right| \textstyle\sum_n \boldsymbol{r}_n \left|S_{1\mathrm{u}}\right\rangle = -\left\langle S_{1\mathrm{g}}\right|(r_1 + r_2)\left|S_{1\mathrm{u}}\right\rangle \\ &= -\frac{1}{\sqrt{2}}\left\{\kappa\left(\left\langle a\bar{b}\right| + \left\langle b\bar{a}\right|\right) + \eta\left(\left\langle a\bar{a}\right| + \left\langle b\bar{b}\right|\right)\right\}(r_1 + r_2)\left(\left|a\bar{a}\right\rangle - \left|b\bar{b}\right\rangle\right) \\ &= -\frac{1}{\sqrt{2}}\kappa\left(\left\langle\bar{b}\middle|r\middle|\bar{a}\right\rangle + \langle a|r|b\rangle - \langle b|r|a\rangle + \left\langle\bar{a}\middle|r\middle|\bar{b}\right\rangle\right) \\ &\quad -\frac{1}{\sqrt{2}}\eta\left(\langle a|r|a\rangle + \langle\bar{a}|r|\bar{a}\rangle - \langle b|r|b\rangle - \left\langle\bar{b}\middle|r\middle|\bar{b}\right\rangle\right) \\ &= -\sqrt{2}\eta\{\langle a|r|a\rangle - \langle b|r|b\rangle\} \\ &= \sqrt{2}\eta R_{\mathrm{BA}} \end{aligned} \tag{I. 2.36}$$

where $R_{\mathrm{BA}} = (b|r|b) - (a|r|a)$ represents the effective distance between unpaired electrons, thus multiplying by the electron charge results in a dipole. The transition dipole moment between the $S_{1\mathrm{u}}$ and $S_{2\mathrm{g}}$ states is then expressed as:

$$\begin{aligned} \mu_{S_{1\mathrm{u}},S_{2\mathrm{g}}} &= -\left\langle S_{1\mathrm{u}}\right|(r_1 + r_2)\left|S_{2\mathrm{g}}\right\rangle \\ &= \sqrt{2}\kappa\{\langle b|r|b\rangle - \langle a|r|a\rangle\} \\ &= \sqrt{2}\kappa R_{\mathrm{BA}} \end{aligned} \tag{I. 2.37}$$

Dimensionless transition dipole moments ($\mu_{\mathrm{DL}} \equiv \mu/R_{\mathrm{BA}}$) are respectively:

$$\mu_{\mathrm{DL}\,S_{1\mathrm{g}},S_{1\mathrm{u}}} = \sqrt{2}\eta,$$

$$\mu_{\mathrm{DL}\,S_{1\mathrm{u}},S_{2\mathrm{g}}} = \sqrt{2}\kappa \tag{I. 2.38}$$

Thus, the transition probability is expressed using the diradical character y as follows:

$$\left(\mu_{\mathrm{DL}\,S_{1\mathrm{g}},S_{1\mathrm{u}}}\right)^2 = 2\eta^2 = \frac{8{r_t}^2}{\left(1+\sqrt{1+16{r_t}^2}\right)\sqrt{1+16{r_t}^2}}$$

$$= \frac{1-\sqrt{1-(1-y)^2}}{2} \qquad (\mathrm{I.}\,2.39)$$

$$\left(\mu_{\mathrm{DL}\,S_{1\mathrm{u}},S_{2\mathrm{g}}}\right)^2 = 2\kappa^2 = \frac{1}{2}\left(1+\frac{1}{\sqrt{1+16{r_t}^2}}\right)$$

$$= \frac{1+\sqrt{1-(1-y)^2}}{2} \qquad (\mathrm{I.}\,2.40)$$

The y-dependence of the dimensionless excitation energies and transition moments for $r_K = 0$ is shown in Figure I.2.3 both $E_{\mathrm{DL}\,S_{1\mathrm{u}},S_{1\mathrm{g}}}$ and $E_{\mathrm{DL}\,S_{2\mathrm{g}},S_{1\mathrm{g}}}$ decrease rapidly with increasing y in the small y region, but the decrease rate is found to be greater for $E_{\mathrm{DL}\,S_{1\mathrm{u}},S_{1\mathrm{g}}}$. In addition, both of them hardly change in the region of large y. It can also be seen that $(\mu_{\mathrm{DL}\,S_{1\mathrm{u}},S_{2\mathrm{g}}})^2$ increases with increasing y, approaching 1, and $(\mu_{\mathrm{DL}\,S_{1\mathrm{g}},S_{1\mathrm{u}}})^2$ decreases with increasing y, approaching 0.

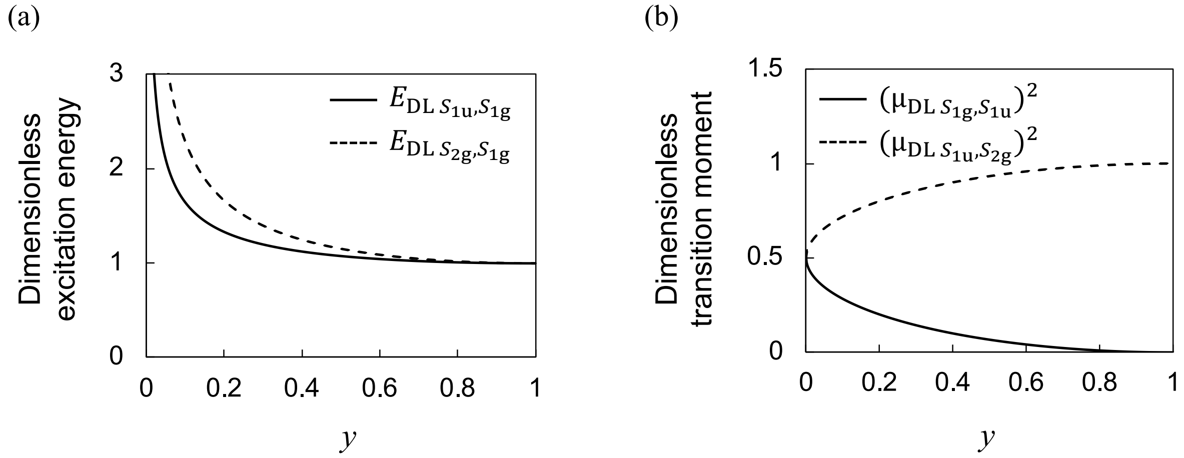

Figure I.2.3. Diradical character dependence of the dimensionless (a) excitation energies (b) transition moments for $r_K = 0$.

To consider the *y*-dependence of γ_{DL}, we consider $\gamma_{\mathrm{DL}}^{\mathrm{II}}$ and $\gamma_{\mathrm{DL}}^{\mathrm{III-2}}$, which from Eqs. (I.2.33), (I.2.34), (I.2.39) and (I.2.40), respectively, are expressed as follows:

$$\gamma_{\mathrm{DL}}^{\mathrm{II}} = -4\frac{\left(\mu_{\mathrm{DL}\,S_{1\mathrm{g}},S_{1\mathrm{u}}}\right)^4}{\left(E_{\mathrm{DL}\,S_{1\mathrm{u}},S_{1\mathrm{g}}}\right)^3} = -\frac{8(1-y)^4}{\left(1+\sqrt{1-(1-y)^2}\right)^2\left(1-2r_K+\frac{1}{\sqrt{1-(1-y)^2}}\right)^3} \qquad \text{(I.2.41)}$$

$$\gamma_{\mathrm{DL}}^{\mathrm{III-2}} = 4\frac{\left(\mu_{\mathrm{DL}\,S_{1\mathrm{g}},S_{1\mathrm{u}}}\right)^2\left(\mu_{\mathrm{DL}\,S_{1\mathrm{u}},S_{2\mathrm{g}}}\right)^2}{\left(E_{\mathrm{DL}\,S_{1\mathrm{u}},S_{1\mathrm{g}}}\right)^2 E_{\mathrm{DL}\,S_{2\mathrm{g}},S_{1\mathrm{g}}}} = \frac{4(1-y)^2}{\frac{1}{\sqrt{1-(1-y)^2}}\left(1-2r_K+\frac{1}{\sqrt{1-(1-y)^2}}\right)^2} \qquad \text{(I.2.42)}$$

The *y*-dependence of $(E_{\mathrm{DL}\,S_{1\mathrm{u}},S_{1\mathrm{g}}})^3$ and $(\mu_{\mathrm{DL}\,S_{1\mathrm{g}},S_{1\mathrm{u}}})^4$, the components of $\gamma_{\mathrm{DL}}^{\mathrm{II}}$ in Eq. (I.2.41), and $\gamma_{\mathrm{DL}}^{\mathrm{II}}$ are shown in Figure I.2.4(a), (b), respectively. The *y*-dependence of $(E_{\mathrm{DL}\,S_{1\mathrm{u}},S_{1\mathrm{g}}})^3 E_{\mathrm{DL}\,S_{2\mathrm{g}},S_{1\mathrm{g}}}$ and $(\mu_{\mathrm{DL}\,S_{1\mathrm{g}},S_{1\mathrm{u}}})^2(\mu_{\mathrm{DL}\,S_{1\mathrm{u}},S_{2\mathrm{g}}})^2$, the components of $\gamma_{\mathrm{DL}}^{\mathrm{III-2}}$ in Eq. (I.2.42), and $\gamma_{\mathrm{DL}}^{\mathrm{III-2}}$ are shown in Figure I.2.4(c), (d), respectively. Both are for the case $r_K = 0$. The components related to the dimensionless excitation energies and transition moments both tend to decrease with increasing *y*, with $(E_{\mathrm{DL}\,S_{1\mathrm{u}},S_{1\mathrm{g}}})^3$, $(\mu_{\mathrm{DL}\,S_{1\mathrm{g}},S_{1\mathrm{u}}})^4$ and $(E_{\mathrm{DL}\,S_{1\mathrm{u}},S_{1\mathrm{g}}})^3 E_{\mathrm{DL}\,S_{2\mathrm{g}},S_{1\mathrm{g}}}$ decreases steeply in the region of small *y* ($y < 0.2$). $\gamma_{\mathrm{DL}}^{\mathrm{II}}$ shows a negative maximum at $y = 0.134$, and $\gamma_{\mathrm{DL}}^{\mathrm{III-2}}$ shows a positive maximum at $y = 0.307$.

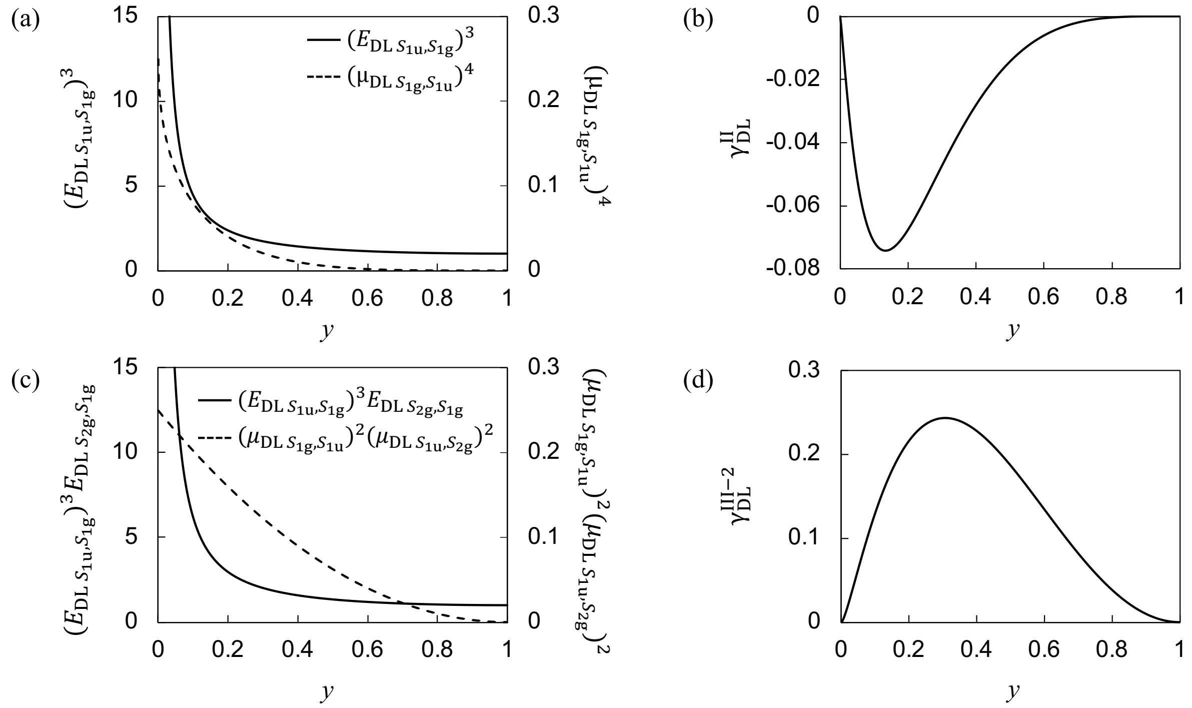

Figure I.2.4. Diradical character dependence of (a) components of $\gamma_{\mathrm{DL}}^{\mathrm{II}}$, (b) $\gamma_{\mathrm{DL}}^{\mathrm{II}}$, (c) components of $\gamma_{\mathrm{DL}}^{\mathrm{III-2}}$, (d) $\gamma_{\mathrm{DL}}^{\mathrm{III-2}}$ for $r_K = 0$.

Eqs. (I.2.32), (I.2.41) and (I.2.42), the dimensionless γ in the two-site VCI diradical model is expressed as:

$$\gamma_{\mathrm{DL}} = -\frac{8(1-y)^4}{\left(1+\sqrt{1-(1-y)^2}\right)^2\left(1-2r_K+\frac{1}{\sqrt{1-(1-y)^2}}\right)^3} + \frac{4(1-y)^2}{\frac{1}{\sqrt{1-(1-y)^2}}\left(1-2r_K+\frac{1}{\sqrt{1-(1-y)^2}}\right)^2} \qquad (\mathrm{I.2.43})$$

The y-dependence of γ_{DL} for $r_K = 0$ is shown in Figure I.2.5. γ_{DL} shows a positive maximum at y = 0.359, reflecting the character of $\gamma_{\mathrm{DL}}^{\mathrm{III-2}}$. Thus, the second hyperpolarizability γ and the diradical character y show a strong correlation, which is called the "y-γ correlation"; a system with intermediate y between 0 and 1 will have a closed shell (y = 0) and pure diradicals (y = 1) of similar size, which is the source of the giant NLO property.

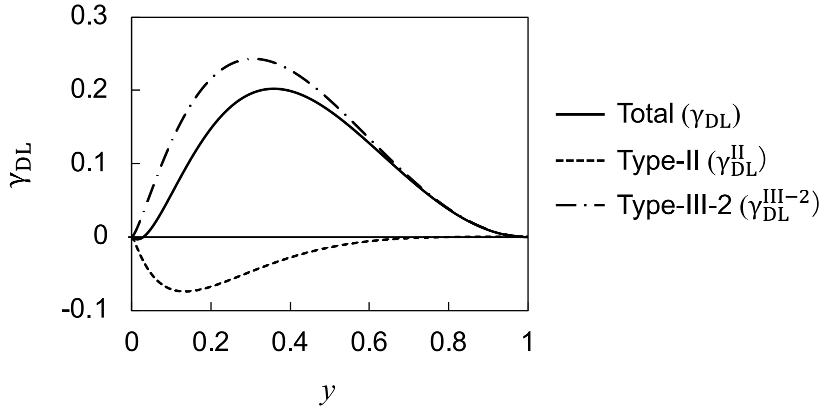

Figure I.2.5. Diradical character dependence of γ_{DL}, $\gamma_{\mathrm{DL}}^{\mathrm{II}}$ and $\gamma_{\mathrm{DL}}^{\mathrm{III-2}}$ for $r_K = 0$.

References

[1] B. J. Orr and J. F. Ward, *Mol. Phys.*, **1971**, *20*, 513–526.

[2] A. Willetts, J. E. Rice, D. M. Burland and D. P. Shelton, *J. Chem. Phys.*, **1992**, *97*, 7590–7599.

[3] M. Nakano, M. Okumura, K. Yamaguchi and T. Fueno, *Mol. Cryst. Liq. Cryst. Inc. Nonlinear Opt.*, **1990**, *182*, 1–15.

[4] M. Nakano and K. Yamaguchi, *Chem. Phys. Lett.*, **1993**, *206*, 285–292.

[5] M. Nakano, I. Shigemoto, S. Yamada and K. Yamaguchi, *J. Chem. Phys.*, **1995**, *103*, 4175–4191.

[6] H. Fujita, M. Nakano, M. Takahata and K. Yamaguchi, *Chem. Phys. Lett.*, **2002**, *358*, 435–441.

[7] M. Nakano, H. Fujita, M. Takahata and K. Yamaguchi, *Chem. Phys. Lett.*, **2002**, *356*, 462–468.

[8] H. D. Cohen and C. C. J. Roothaan, *J. Chem. Phys.*, **1965**, *43*, S34–S39.

[9] M. Nakano, R. Kishi, S. Ohta, H. Takahashi, T. Kubo, K. Kamada, K. Ohta, E. Botek and B. Champagne, *Phys. Rev. Lett.*, **2007**, *99*, 033001.

Chapter 3.

Theory of Two-Photon Absorption

In this chapter, the theoretical equation for two-photon absorption will be explained. There are two main ways to obtain the frequency-dependent two-photon absorption (TPA) cross-section $\sigma^{(2)}(\omega)$ by calculation. One is to obtain Imγ (see Chapter 2), as mentioned earlier (Eq. (14)) that $\sigma^{(2)}(\omega)$ is correlated with the imaginary part of the second hyperpolarizability (Imγ) in degenerate four-wave mixing (DFWM). However, previous studies that have used Imγ to calculate the spectrum of $\sigma^{(2)}(\omega)$ have shown that it does not exhibit the correct dispersion behavior in the frequency region near the one-photon resonance[1,2]. Another method is to calculate two-photon transition matrix elements from Fermi's golden rule. After a brief discussion of this method in comparison with the theoretical equation for one-photon absorption cross-section, we derive an equation relating the TPA cross-section, simplified to a three-state model, to the open-shell character (y).

3.1. Theoretical Formula for Light Absorption

The change from the steady state due to light absorption is a transition between levels in quantum theory. The probability $w_{a \to b}$ of a transition from an unperturbed state *a* to an unperturbed state *b* is expressed from Fermi's golden rule as follows:

$$w_{a \to b} = \frac{2\pi}{\hbar} \langle b | \hat{H}'(t) | a \rangle^2 \delta(E_b - E_a - \hbar\omega) \qquad (\mathrm{I.3.1})$$

Here, $\hbar$ is the Dirac's constant ($\hbar = h/2\pi$, where h is Planck's constant), *E* is the eigenenergy of the unperturbed Hamiltonian, and $\hbar\omega$ is the photon energy.

3.1.1. Theoretical formula for one-photon absorption

From Eq. (I.3.1), the strength of the one-photon absorption (OPA) transition from the ground state *g* to the excited state *f* (oscillator strength; f_{fg}) is defined as[3]:

$$f_{\mathrm{fg}} = \frac{2m_e\omega_{\mathrm{fg}}}{3n^2\hbar e^2} \langle |\boldsymbol{\mu}_{fg}|^2 \rangle \qquad (\mathrm{I.3.2})$$

where m_e is the electron mass, n is the refractive index of the medium, and e is the charge elementary quantity. $\boldsymbol{\mu}_{fg}$ is the transition dipole moment that gives the probability of OPA. The frequency-dependent molar absorption coefficient $\varepsilon(\omega)$ of OPA is expressed using f_{fg} as:

$$\varepsilon(\omega) = \frac{10^{-3}}{\ln 10} N_A \frac{2\pi^2 n e^2}{mc} f_{\mathrm{fg}} g(\omega) \qquad (\mathrm{I.3.3})$$

N_A is Avogadro's number, c is the speed of light in vacuum, and $g(\omega)$ is the normalized spectral shape function. Eqs. (I.3.2) and (I.3.3) show that the spectral of OPA cross-section $\sigma^{(1)}(\omega)$ is given by[4,5]:

$$\sigma^{(1)}(\omega) = \frac{4\pi^2\omega}{cn\hbar} \langle |\boldsymbol{\mu}_{fg}|^2 \rangle \, g(\omega) \qquad (\mathrm{I.3.4})$$

Here, ω is the angular frequency of the incident light, $\boldsymbol{\mu}_{fg}$ is the transition dipole moment between the states *g* and *f*. $|\boldsymbol{\mu}_{fg}|$ is expressed using the polarization vector $\boldsymbol{e}$ of the incident light as follows:

$$|\boldsymbol{\mu}_{fg}| = \langle f | \boldsymbol{e} \cdot \boldsymbol{\mu} | g \rangle \qquad (\mathrm{I.3.5})$$

$\langle \cdots \rangle$ means the orientational average, i.e.,

$$\langle |\boldsymbol{\mu}_{fg}|^2 \rangle = \sum_{\alpha}^{x,y,z} \langle f|\mu_\alpha|g\rangle^2 = \frac{\left\{ \left(\mu_{fg}^X\right)^2 + \left(\mu_{fg}^Y\right)^2 + \left(\mu_{fg}^Z\right)^2 \right\}}{3} \qquad (\mathrm{I}.3.6)$$

where μ_{fg}^{α} represents the α-axis component of the transition dipole moment $\boldsymbol{\mu}_{fg}$. In addition, the following Lorenz function is used as $g(\omega)$ in this doctoral thesis:

$$g(\omega) = \frac{1}{\pi} \frac{\Gamma_{fg}}{\left(\omega_{fg} - \omega\right)^2 + {\Gamma_{fg}}^2} \qquad (\mathrm{I}.3.7)$$

where $E_{fg} = \hbar\omega_{fg}$, and Γ_{fg} is damping constant from state *g* to *f*.

3.1.2. Theoretical formula for two-photon absorption

The spectrum of the TPA cross-section $\sigma^{(2)}(\omega)$ is given by[4,6]:

$$\sigma^{(2)}(\omega) = \frac{4\pi^3\omega^2}{c^2n^2} \langle \left| \boldsymbol{M}_{fg}^{(2)} \right|^2 \rangle \, g(2\omega) \qquad (\mathrm{I}.3.8)$$

where, $\boldsymbol{M}_{fg}^{(2)}$ is two-photon transition matrix element tensor, having the same dimension as the dipole polarizability, expressed as:

$$\boldsymbol{M}_{fg}^{(2)} = \frac{1}{\hbar} \sum_{k} \frac{\langle f|\boldsymbol{e}\cdot\boldsymbol{\mu}|k\rangle\langle k|\boldsymbol{e}\cdot\boldsymbol{\mu}|g\rangle}{\omega_{kg} - \omega} \qquad (\mathrm{I}.3.9)$$

The transition dipole moment of OPA shown in Eq. (I.3.5) relates to the transition from the initial state *g* to the final state *f*, whereas the two-photon transition matrix element of TPA shown in Eq. (I.3.9) is the transition through the intermediate state *k*. The denominator, $\omega_{kg} - \omega$, is the difference between the energy of the intermediate state *k* and the energy of the incident photon and is called the detuning energy. Figure I.3.1(a) shows an image of the sum-over-states (SOS) expression for adding up all intermediate states *k*. According to Feynman path integral, the actual process can be represented by the SOS expression that adds all possible routes together, taking into account their weights. This means that an expression equivalent to the transition of TPA via the virtual state, as shown in Figure I.3.1(b), is also possible.

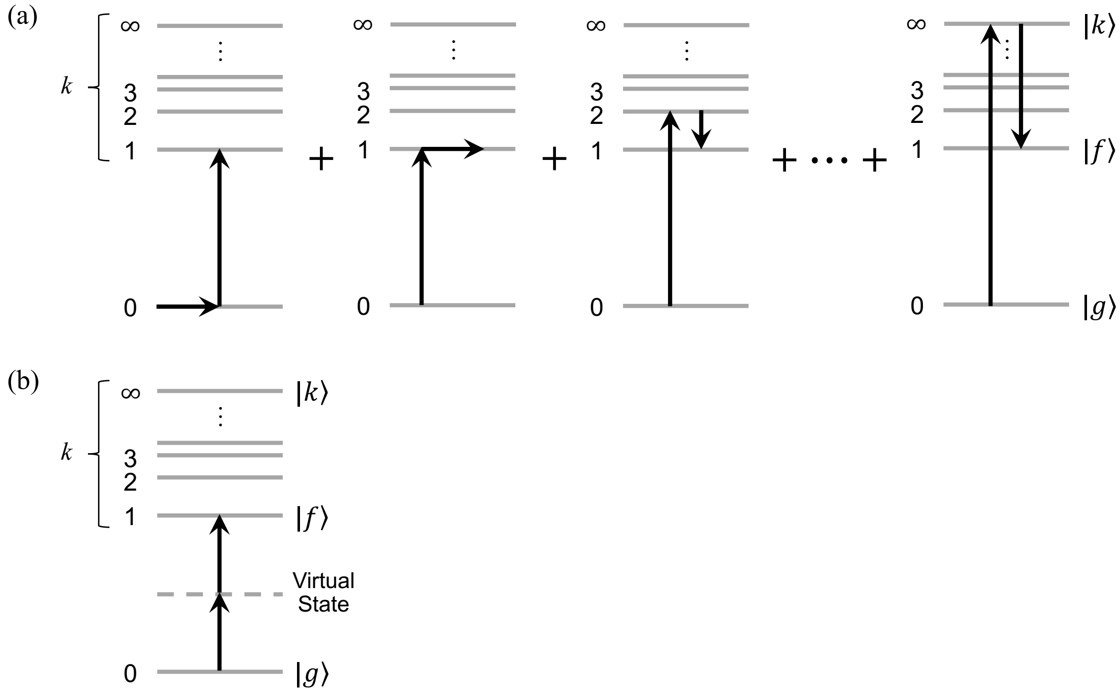

Figure I.3.1. Image of the representation of TPA transitions: (a) SOS expression, (b) via the virtual state.

$\langle |\boldsymbol{M}_{fg}^{(2)}|^2 \rangle$ in Eq. (I.3.8) is orientationally averaged TPA probability. $\langle |\boldsymbol{M}_{fg}^{(2)}|^2 \rangle$ can be expressed for the linearly polarized incident light using each component of the two-photon transition matrix element $M_{\alpha\beta}$ as follows:

$$\left\langle \left|\boldsymbol{M}_{fg}^{(2)}\right|^2 \right\rangle = \frac{1}{15} \sum_{\beta}^{x,y,z} \sum_{\alpha}^{x,y,z} \left(M_{\alpha\alpha} M_{\beta\beta}^{*} + 2 M_{\alpha\beta} M_{\alpha\beta}^{*} \right) \tag{I.3.10}$$

$M_{\alpha\beta}$ is expressed using transition dipole moments as follows:

$$M_{\alpha\beta} = \frac{1}{2\hbar} \sum_{k} \left[\frac{\langle f|\mu_\alpha|k\rangle\langle k|\mu_\beta|g\rangle}{\omega_{kg} - \omega - i\Gamma_{kg}} + \frac{\langle f|\mu_\beta|k\rangle\langle k|\mu_\alpha|g\rangle}{\omega_{kg} - \omega - i\Gamma_{kg}} \right] \quad (\alpha, \beta = X, Y, Z) \tag{I.3.11}$$

Γ_{kg} is damping constant from state g to k. We used the Lorentzian function for the normalized shape function $g(2\omega)$:

$$g(2\omega) = \frac{1}{\pi} \frac{\Gamma_{fg}}{\left(\omega_{fg} - 2\omega\right)^2 + {\Gamma_{fg}}^2} \tag{I.3.12}$$

Next, we discuss a simplification of the SOS expression, the idea of which is to take the sum of all transitions to which the intermediate state *k* contributes, but it is not realistic to actually consider an infinite number of states. Therefore, one method that can be employed is the single intermediate state approximation. This method considers only one of the intermediate states with the largest contribution (in most cases, the lowest energy OPA state). In the case of TPA for centrosymmetric system, the minimum required are the initial, intermediate, and final states. For a simplified model that considers only these three singlet states, the initial state corresponds to state $|S_{1g}\rangle$, the intermediate state to state $|S_{1u}\rangle$, and the final state to state $|S_{2g}\rangle$ (see Figure I.2.2), the two-site diradical model can be applied.

3.2. Open-Shell Character Dependence of One- and Two-Photon Absorption Cross-Sections

3.2.1. Open-shell character dependence of one-photon absorption cross-section

From Eqs. (I.2.33), (I.2.39) and (I.3.4), the dimensionless OPA peak cross-section $\sigma_{\mathrm{DL}}^{(1)}(\omega_{fg})$ is expressed as[5]:

$$\sigma_{\mathrm{DL}}^{(1)}(\omega_{fg}) \equiv \frac{\sigma^{(1)}(\omega_{fg})}{\left(\frac{4\pi}{3\hbar cn}\right)(eR_{\mathrm{BA}})^2} = \frac{1-\sqrt{1-(1-y)^2}}{2C_{fg}} \qquad (\mathrm{I}.3.13)$$

R_{BA} depicts the effective distance between A and B (see Eq. (I.2.36)). C_{fg} is the coefficient defined to represent the energy dependence of Γ_{fg} and is expressed by the following equation:

$$\Gamma_{fg} = C_{fg}E_{fg} \ (0 \le C_{fg} \le 1) \qquad (\mathrm{I}.3.14)$$

Eq. (I.3.13) shows that $\sigma_{\mathrm{DL}}^{(1)}(\omega_{fg})$ decreases inversely with C_{fg}. Figure I.3.2 shows the *y*-dependence of $\sigma_{\mathrm{DL}}^{(1)}(\omega_{fg})$ with C_{fg} as a fixed constant ($C_{fg} = 0.1$). $\sigma_{\mathrm{DL}}^{(1)}(\omega_{fg})$ is found to decrease with increasing *y*.

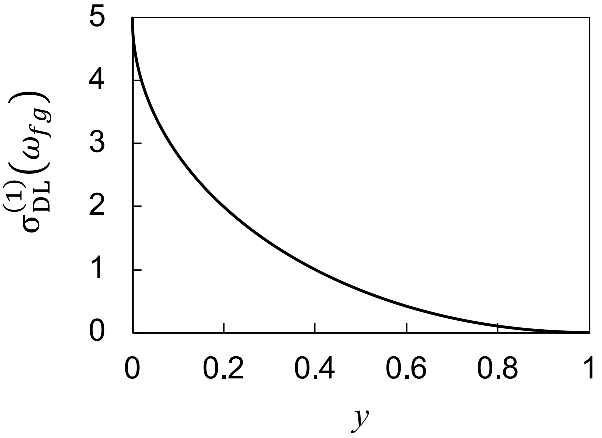

Figure I.3.2. Diradical character dependence of dimensionless OPA peak intensity $\sigma_{\mathrm{DL}}^{(1)}(\omega_{fg})$

3.2.2. Open-shell character dependence of two-photon absorption cross-section

From Eqs. (I.2.33), (I.2.34), (I.2.39), (I.2.40) and (I.3.8), the dimensionless TPA peak cross-section $\sigma_{\mathrm{DL}}^{(2)}(\omega_{fg})$ is expressed as[7]:

$$\begin{aligned}\sigma_{\mathrm{DL}}^{(2)}(\omega_{fg}) &\equiv \frac{\sigma^{(2)}(\omega)}{\left(\frac{16\pi^2}{5\hbar c^2 n^2}\right)\frac{(eR_{\mathrm{BA}})^4}{U}} \\ &= \frac{(1-y)^2}{4C_{fg}\sqrt{1-(1-y)^2}\left\{(1-2r_K)^2+p^2C_{fg}^2\left(1-2r_K+\frac{1}{\sqrt{1-(1-y)^2}}\right)^2\right\}}\end{aligned} \qquad (\mathrm{I}.3.15)$$

where p is the coefficient ratio that satisfies the following equation:

$$\begin{aligned}p &= C_{kg}/C_{fg} \quad (0 \le p \le 1), \\ \Gamma_{kg} &= C_{kg}E_{kg} \quad (0 \le C_{kg} \le 1)\end{aligned} \qquad (\mathrm{I}.3.16)$$

As C_{fg} is decreased, the value of y increases when $\sigma_{\mathrm{DL}}^{(2)}(\omega_{fg})$ is maximized, and its y-value increases rapidly as r_K is moved closer to 0.5[7]. In case of $r_K = 0.5$, $\sigma_{\mathrm{DL}}^{(2)}(\omega_{fg})$ follows from Eq. (I.3.15):

$$\sigma_{\mathrm{DL}}^{(2)}(\omega_{fg}) = \frac{1}{4p^2C_{fg}^3}(1-y)^2\sqrt{1-(1-y)^2} \qquad (\mathrm{I}.3.17)$$

Eq. (I.3.17) shows that an increase in C_{kg} or C_{fg} decreases $\sigma_{\mathrm{DL}}^{(2)}(\omega_{fg})$, but y-dependence is unchanged by these coefficients. y-dependence of $\sigma_{\mathrm{DL}}^{(2)}(\omega_{fg})$ is shown in Figure I.3.3 when C_{fg} is a fixed constant ($C_{fg} = 0.1$) and p is varied in the range 1.0 ~ 0.6 with interval = 0.1. It can be seen that

$\sigma_{\mathrm{DL}}^{(2)}(\omega_{fg})$ peaks at $y = 0.184$, independent of p. As described above, it is theoretically possible to derive that the TPA cross-section increases in systems that exhibit intermediate open-shell character.

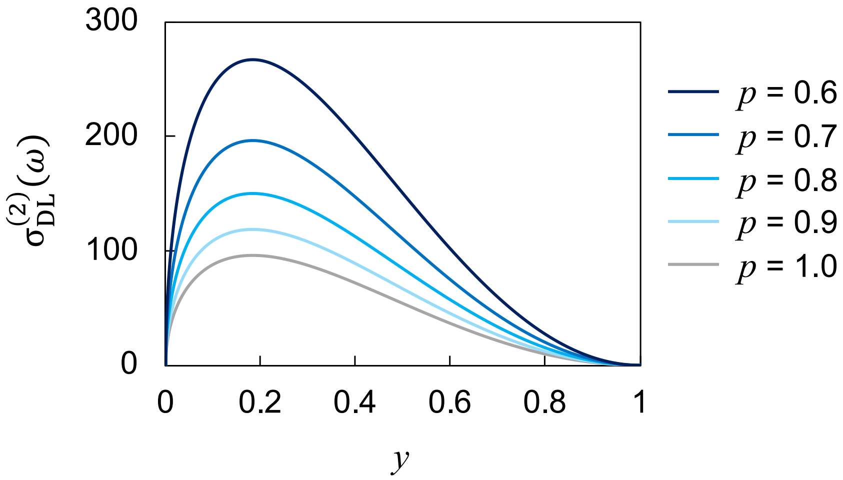

Figure I.3.3. Diradical character dependence of dimensionless TPA peak intensity $\sigma_{\mathrm{DL}}^{(2)}(\omega_{fg})$ for p = 1.0 ~ 0.6 under the condition of $C_{fg} = 0.1$ and $r_K = 0.5$.

References

[1] V. Shakin and S. Abe, *Phys. Rev. B - Condens. Matter Mater. Phys.*, **1996**, *53*, 10656–10666.

[2] R. Kishi, M. Nakano, S. Yamada, K. Kamada, K. Ohta, T. Nitta and K. Yamaguchi, *Chem. Phys. Lett.*, **2004**, *393*, 437–441.

[3] K. Ohta and K. Kamada, *J. Chem. Phys.*, **2006**, *124*, 124303.

[4] K. Ohta, S. Yamada, K. Kamada, A. D. Slepkov, F. A. Hegmann, R. R. Tykwinski, L. D. Shirtcliff, M. M. Haley, P. Sałek, F. Gel'mukhanov and H. Ågren, *J. Phys. Chem. A*, **2011**, *115*, 105–117.

[5] M. Nakano, K. Yoneda, R. Kishi, H. Takahashi, T. Kubo, K. Kamada, K. Ohta, B. Champagne and E. Botek, in *AIP Conference Proceedings*, **2012**, vol. 1504, pp. 136–142.

[6] M. T. P. Beerepoot, D. H. Friese, N. H. List, J. Kongsted and K. Ruud, *Phys. Chem. Chem. Phys.*, **2015**, *17*, 19306–19314.

[7] M. Nakano, K. Yoneda, R. Kishi, H. Takahashi, T. Kubo, K. Kamada, K. Ohta, E. Botek and B. Champagne, *J. Chem. Phys.*, **2009**, *131*, 114316.

PART II

Correlation Between Open-Shell Electronic Structures and Third-Order Nonlinear Optical Properties in One-Dimensional Chains of π-Radicals

The correlation between open-shell electronic structure and third-order nonlinear optical (NLO) properties of one-dimensional (1D) stacked chains of π-radicals was investigated theoretically. By employing the finite N-mer models consisting of methyl or phenalenyl radicals with different stacking distances, the average and standard deviation of diradical characters y_i for N-mer models of π-radicals (y_{av} and y_{SD}) were evaluated. Then, these diradical characters were estimated at the limit $N \rightarrow \infty$. These y-based indices were helpful in discussing the correlation between the open-shell electronic structures and the second hyperpolarizability per dimer at the limit $N \rightarrow \infty$, γ_∞, for the 1D chains with stacking distance alternation (SDA). The calculated γ_∞ values and the polymer/dimer ratio $\gamma_\infty/\gamma(N = 2)$ were enhanced significantly when both the stacking distance and the SDA are small. It was also found that the spin-unrestricted long-range corrected (LC-)UBLYP method with the range-separating parameter $\mu = 0.47$ bohr^{-1} reproduced well the trend of γ_∞ of this type of 1D chains estimated at the spin-unrestricted coupled-cluster levels. The present study is expected to contribute to establishing the design guidelines for future high-performance open-shell molecular NLO materials.

1. Introduction

For the past two decades, molecular materials exhibiting large third-order nonlinear optical (NLO) responses have been actively explored because such materials are essential for establishing future photonic and optoelectronic devices[1]. Molecular third-order NLO materials have advantages in their fast response time and molecular design feasibility compared with inorganic crystals. Numerous theoretical and experimental studies have been carried out to clarify design guidelines for molecular third-order NLO materials[2–8]. In addition to the molecular materials based on the stable closed-shell molecules, open-shell systems[9–14], such as diradicals, multiradical systems, and high-spin species, have recently been focused on as candidates for novel third-order NLO materials. Nakano et al. theoretically clarified the relationship between the diradical character y (a theoretical index characterizing the degree of open-shell in the singlet state) and the molecular second hyperpolarizability γ (the third-order NLO property at the molecular scale)[13]. They found that singlet diradicals and diradical-like molecules with intermediate y exhibit enhanced γ compared to closed-shell and complete open-shell counterparts. Recent advances in synthesis and measurement techniques have contributed to establishing open-shell third-order NLO materials[15–19].

The (partially) unpaired electrons in the open-shell molecules are sensitive to external stimuli, leading to their significant NLO property and high chemical reactivity. These highly active unpaired electrons often contribute to σ-bond formation with other open-shell molecules, which results in reducing their high response properties. Therefore, practical design strategies are needed to suppress the formation of σ-bonds while maintaining the activity and sensitivity of the unpaired electrons. In such situations, these unpaired electrons can be utilized to achieve huge response properties in their molecular assembly that cannot be achieved with single molecules alone. Several π-dimers exhibiting open-shell electronic structures have been realized by tuning the balance between the attractive and repulsive interactions between the open-shell π-conjugated molecules[20]. Notably, derivatives of phenalenyl radicals[21–23] and cyclic thiazyl radical[24–27], typical neutral π-radicals with high thermodynamic stabilities, were reported to form one-dimensional (1D) π-stacked chains in the crystalline phase, in which each monomer interacts with each other via the pancake bonding interaction[28–32]. Their stacking distances and relative configurations can be controlled by chemical modifications while maintaining the high activity of the unpaired electrons[28–32].

Several theoretical and computational studies have evaluated the third-order NLO properties of such 1D chains of monoradicals. Nakano et al. employed the simplest 1D chain model of hydrogen atoms and averaged y (y_{av}) values to characterize their open-shell characters[33]. They found that γ per unit in the 1D chains (multiradical) takes a maximum in a smaller y_{av} region compared with the diradical systems. Yoneda et al. performed the density functional theory (DFT) calculations for π-dimers of phenalenyl radicals with different stacking distances d in the singlet state[29]. They found that y of the dimer decreases as decreasing d, and γ per monomer takes the maximum around $d = 2.9$ Å, at which y is in the intermediate region. Salustro et al. evaluated the γ_∞ of 1D chains of phenalenyl radicals[32] by extending the coupled-perturbed Kohn-Sham (CPKS) analytic derivative method under the periodic boundary condition implemented in the CRYSTAL package[34,35], which was the first direct computation of γ_∞ of this type of 1D chain. In a series of theoretical studies, Matsui et al. investigated the effects of increasing the number of monomers (N) on the γ per unit based on the 1D chains of hydrogens and cyclic thiazyl radicals[31]. They estimated the γ per unit in the limit $N \rightarrow \infty$ (γ_∞) by extrapolating the results of N-mers. These studies predicted that the third-order NLO properties of closely stacked 1D chains of π-radicals are comparable to those of π-conjugated polymers, suggesting through-space (TS) conjugation in such systems.

It is expected that y_{av} can fairly characterize the degree of open-shell in the 1D chains of π-radicals with the uniform stacking distance d. Of course, realizing 1D chains of π-radicals with a uniform stacking distance is challenging. Even if 1D chains are formed successfully in crystalline, alternations of the stacking distance often appear. In such a situation, y_{av} may not always uniquely characterize their open-shell electronic structures related to the third-order NLO responses. Here, another y-based index, y_{SD}, corresponding to the standard deviation of y, was introduced and examined how y_{av} and y_{SD} can help characterize the open-shell electronic structure of the stacked 1D chains of π-radicals where two types of stacking distance, d_1 and d_2, appear alternately. The dependence of stacking distance alternation (SDA) on y_{av}, y_{SD}, and γ_∞ in 1D chain models of π-radicals was then investigated based on quantum chemical calculations.

2. Methods

2.1. Model systems

The sp[2] methyl radical[36] and the phenalenyl radical were employed as monomer units (the 1D chains composed of each are shown in Figure II.1(a) and (b), respectively). Figure II.1(c) illustrates their dimer's frontier orbital energy levels ($N = 2$) and tetramers ($N = 4$). It is known that there is a good negative correlation between y and the energy gap between the highest occupied and lowest unoccupied molecular orbitals (HOMO and LUMO) for diradicaloids. The HOMO and LUMO are constructed by bonding and anti-bonding interactions of the singly occupied MOs (SOMOs) of the monomers. Thus, the HOMO-LUMO gap of the dimer tends to increase with decreasing the stacking distance d_1 in the dimer unit.

For the multiradicaloids ($N \geq 4$), plural diradical characters y_i can be defined from the occupation numbers of the i-th pair of natural orbitals (NOs), i.e., HONO-i and LUNO+i. Roughly, y_i ($i = 0, 1, \ldots N/2-1$) is negatively correlated with the energy gap between the HOMO-i and LUMO+i. When the tetramer is composed of two almost non-interacting dimers with $d_2 >> d_1$, the orbital interaction between the HOMOs (LUMOs) of the dimer can be negligible. As a result, the HOMO and HOMO-1 (LUMO and LUMO+1) of the tetramer with $d_2 >> d_1$ are nearly degenerated. Thus, $y_0 \sim y_1$ will be obtained in such a situation. When $d_2 \sim d_1$ (and they are sufficiently small), the orbital interaction between the HOMOs (LUMOs) of the dimer becomes considerable, resulting in $y_0 >> y_1$. Since y_{av} is defined by the arithmetic average of $\{y_{\mathrm{i}}\}$, situations can be found where y_0 and y_1 are different but y_{av} is similar. Thus, in addition to y_{av}, another y-based index, the standard deviation of y_{i}, denoted as y_{SD}, is introduced here. It can be expected that, for example, $y_{\mathrm{SD}} \sim 0$ for the non-interacting dimers, but $y_{\mathrm{SD}} > 0$ for the interacting dimers. For $N \rightarrow \infty$, if the conduction and valence bands are constructed primarily from the SOMOs of the monomers, these indices can be considered at $N \rightarrow \infty$, i.e., $y_{\mathrm{av}}(N \rightarrow \infty)$ and $y_{\mathrm{SD}}(N \rightarrow \infty)$. These indices are related to the averaged band gap and widths. Generally, the band gap and widths are essential for characterizing the optical response properties.

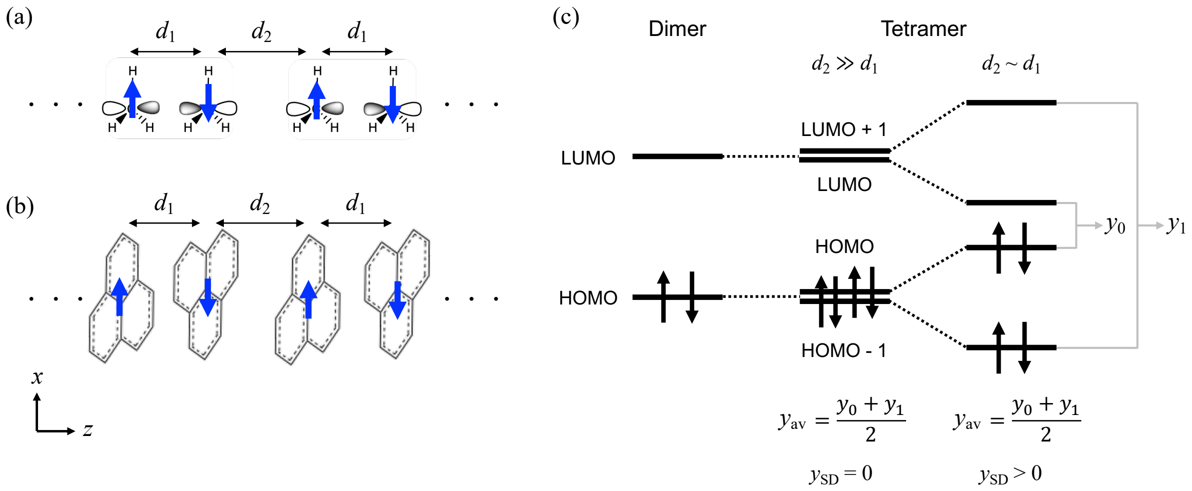

Figure II.1. Structures of 1D chain models consisting of (a) methyl radicals, and (b) phenalenyl radicals, and (c) orbital interaction diagram for the tetramers with different staking distance alternations.

2.2. Computational details

The molecular geometry of methyl radical optimized at the UCCSD(T)/aug-cc-pVDZ level under the D_{3h} symmetry constraint was employed[36]. Then, eclipsed-stacking 1D N-mer models [$(\mathrm{CH_3})_N$] were constructed, keeping the intramolecular geometries fixed.

The y_{i} values for the N-mer were calculated at the projected unrestricted Hartree-Fock (PUHF) level using Yamaguchi's equation [Eq. (II.1)][37],

$$y_i = 1 - \frac{2T_i}{1 + T_i^{\,2}} \tag{II.1}$$

Here T_i is calculated from the occupation numbers n of NOs at the UHF level

$$T_i = \frac{n_{\mathrm{HONO}-i} - n_{\mathrm{LUNO}+i}}{2} \tag{II.2}$$

The y_{av} for the N-mer is defined by the following equation.

$$y_{\mathrm{av}}(N) = \sum_{i=0}^{N/2-1} y_i(N) \qquad \mathrm{(II.3)}$$

Note that there are $N/2$ radical pairs in the N-mer. Then, the standard deviation y_{SD} is defined by the following equation.

$$y_{\mathrm{SD}}(N) = \sqrt{\frac{1}{N/2}\sum_{i=0}^{N/2-1}\left(y_i(N) - y_{\mathrm{av}}(N)\right)^2} \qquad \mathrm{(II.4)}$$

For $N = 4$, y_{av} and y_{SD} are expressed by the following equations,

$$y_{\mathrm{av}}(N = 4) = \frac{y_0 + y_1}{2} \qquad \mathrm{(II.5)}$$

$$y_{\mathrm{SD}}(N = 4) = \frac{y_0 - y_1}{2} \qquad \mathrm{(II.6)}$$

The stacking direction component of the static γ values of N-mer $\gamma(N) = \gamma_{zzzz}(N)$ was then computed. The $\gamma(N)$ values were evaluated using the finite-field method. The fourth-order numerical derivative of total energy under the static electric field in the range from 5.0×10^{-4} a.u. to 6.0×10^{-3} a.u. was employed, which gives the relative errors of about 1 % for γ.

The total energies in the presence of an electric field were evaluated at the spin-unrestricted coupled-cluster singles and doubles with triples corrections [UCCSD(T)] and the long-range corrected (LC-)UBLYP[38,39] levels. Previous studies usually evaluated the γ values at the LC-UBLYP level with $\mu = 0.33$ bohr^{-1}. This range-separating parameter μ is known to reproduce the results based on the highly correlated UCCSD(T) for several intramolecular diradicaloids and dimers of π-radicals[40]. In this study, the calculation results of LC-UBLYP using $\mu = 0.33$ bohr^{-1} and 0.47 bohr^{-1} were compared with the UCCSD(T) results for N-mers. During the calculations, an initial guess for the singlet state with the all-antiparallel spin alignment was prepared. The 6-31+G basis set used in the previous studies for 1D stacked systems consisting of a methyl radical model was employed. All these calculations were conducted by Gaussian 09 rev. D.[41]

After that, an attempt was made to estimate y_{av}, y_{SD}, and γ at the limit of $N \rightarrow \infty$. The calculation results of

$$\Delta\gamma(N) = \frac{\gamma(N+2) - \gamma(N)}{2} \tag{II.7}$$

were fitted with the form of

$$\Delta\gamma(N) = \gamma_{\infty} - b\exp(-cN) \tag{II.8}$$

and then estimated γ_{∞}[31]. The results of $y_{\mathrm{av}}(N)$ and $y_{\mathrm{SD}}(N)$ were fitted using the same exponential form as Eq. (II.8) to calculate these values at the limit of $N \rightarrow \infty$, $y_{\mathrm{av},\infty}$ and $y_{\mathrm{SD},\infty}$.

The 1D stacked chains of phenalenyl radicals were also considered. The geometry optimization for the phenalenyl monomer was performed at the UB3LYP/6-31G* level. Then, π-stacked N-mer models (PLY)$_N$ in the anti-parallel configuration (see Figure II.1(a)) were constructed to evaluate y_i of the N-mers at the PUHF level. γ_{∞} of the infinite 1D chain was directly computed at the LC-UBLYP($\mu = 0.47$ bohr^{-1})/6-31G* level using the CRYSTAL 17 package. Details of the DFT calculations under the periodic boundary condition for 1D chains of phenalenyl radicals are discussed in the later section.

3. Results and Discussion

3.1. 1D chains of methyl radicals

Figure II.2 shows the stacking distance (d_1) dependences of y_0 and $\gamma(N = 2)$ for the methyl radical π-dimer calculated at the PUHF/6-31+G and UCCSD(T)/6-31+G levels, respectively. y_0 decreased monotonically with decreasing d_1. $\gamma(N = 2)$ showed a bell-shaped dependence on d_1 with a maximum [$\gamma(N = 2) = 31 \times 10^3$ a.u.] around d_1 = 2.8-2.9 Å where y is in the intermediate region ($y_0 = 0.45$ at d_1 = 2.8 Å, and $y_0 = 0.51$ at d_1 = 2.9 Å).

1D N-mer models of methyl radicals with different d_1 and d_2 were constructed: **A1**(2.5 Å, 2.5 Å), **B1**(3.0 Å, 3.0 Å), **C1**(3.5 Å, 3.5 Å), **A2**(2.5 Å, 3.0 Å), **B2**(3.0 Å, 3.5 Å), and **C2**(3.5 Å, 4.0 Å). Note that, for the dimer, $y_0 = 0.27$ and $\gamma(N = 2) = 21 \times 10^3$ a.u. at d_1 = 2.5 Å, $y_0 = 0.56$ and $\gamma(N = 2) = 29 \times 10^3$ a.u. at d_1 = 3.0 Å, and $y_0 = 0.75$ and $\gamma(N = 2) = 16 \times 10^3$ a.u. at d_1 = 3.5 Å, respectively. **A1**-**C1** are the SDA-less ($d_2 = d_1$) models whereas **A2-C2** exhibit the SDA pattern with $d_2 = d_1 + 0.5$ Å. Figure II.3 shows the $y_{\mathrm{av}}(N)$ and $y_{\mathrm{SD}}(N)$ variations for these models with increasing N calculated at the PUHF/6-31+G level. The convergence behavior of $y_{\mathrm{SD}}(N)$ is relatively slow compared to $y_{\mathrm{av}}(N)$. Table II.1 shows the results of $y_{\mathrm{av},\infty}$ and $y_{\mathrm{SD},\infty}$ estimated by the fitting scheme. $y_{\mathrm{av},\infty}$ was almost determined by d_1. Namely, the $y_{\mathrm{av},\infty}$ values of **A*n*** were almost the same. On the other hand, $y_{\mathrm{SD},\infty}$ was in the order of **A1** > **B1** > (**A2**,

C1, **B2**) > **C2**. From this result, $y_{\mathrm{SD},\infty}$ depends on the ratio d_2/d_1 as well as d_1 itself. **A1** and **A2** exhibited similar $y_{\mathrm{av},\infty}$ but different $y_{\mathrm{SD},\infty}$.

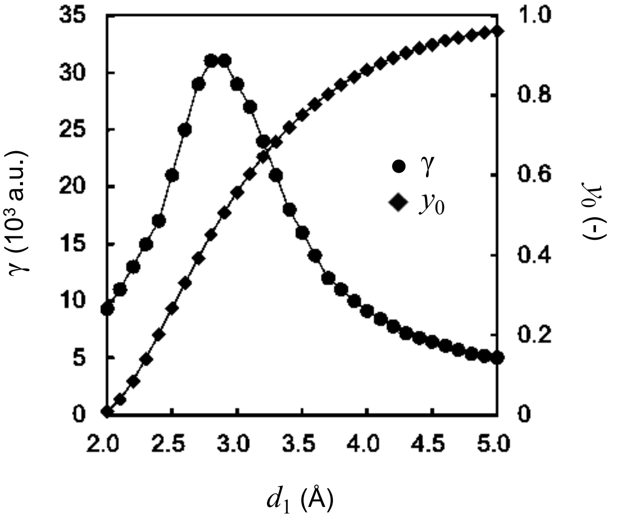

Figure II.2. Stacking distance [d_1 (= d_2)] dependences of y_0 and static $\gamma(N = 2)$ for the methyl radical π-dimer calculated at the PUHF and UCCSD(T) levels, respectively, using the 6-31+G basis set.

In Figure II.3(c) shows the convergence behaviors of $\Delta\gamma(N)$ with increasing N for these models. **A1** showed a slow convergence behavior of with N. **A2** also showed a relatively slow convergence behavior compared with other systems. These features reflected that the intermolecular interactions become significant when the stacking distances are small. Table II.1 also summarizes the results of γ_∞ and the ratio of γ_∞ from the γ of the dimer with the same d_1, i.e., $\gamma_\infty/\gamma(N = 2)$. The "polymer/dimer" ratio $\gamma_\infty/\gamma(N = 2)$ was in the order of **A1** > **A2** > **B1** > (**C1**, **B2**) > **C2**. From these results, the polymer/dimer ratio $\gamma_\infty/\gamma(N = 2)$ tends to be enhanced significantly when i) $y_{\mathrm{av},\infty}$ is in the small-medium region and then ii) $y_{\mathrm{SD},\infty}$ is large. The condition i) was already discussed in the previous paper[33]. For the condition ii), effect of the SDA ratio d_2/d_1 was usually discussed[33]. However, different situations, such as the relative orientations of monomers in 1D chains, can influence the tendency of $y_{\mathrm{SD},\infty}$.

The exchange-correlation (xc-)functional dependence of γ_∞ was next examined when the Kohn-Sham DFT method is employed to calculate γ_∞. The applications of the UCCSD(T) method to the 1D chains of phenalenyl radicals and other realistic systems are usually infeasible. Among the xc-functionals, the LC-UBLYP with the range-separating parameter μ = 0.33 bohr^{-1} [denoted as LC-UBLYP(0.33)] is known to reproduce well the γ values at the UCCSD(T) level for several diradical(oid)s with medium-large y[40]. However, it was also suggested that the LC-UBLYP(0.33) tends to overestimate the UCCSD(T) results for systems with small y, where γ_∞ is expected to increase significantly in the 1D chains (multiradicals). LC-UBLYP calculations with different μ values (0.33 bohr^{-1} and 0.47 bohr^{-1}) were performed for the 1D chain models of methyl radicals and compared the results with those of UCCSD(T).

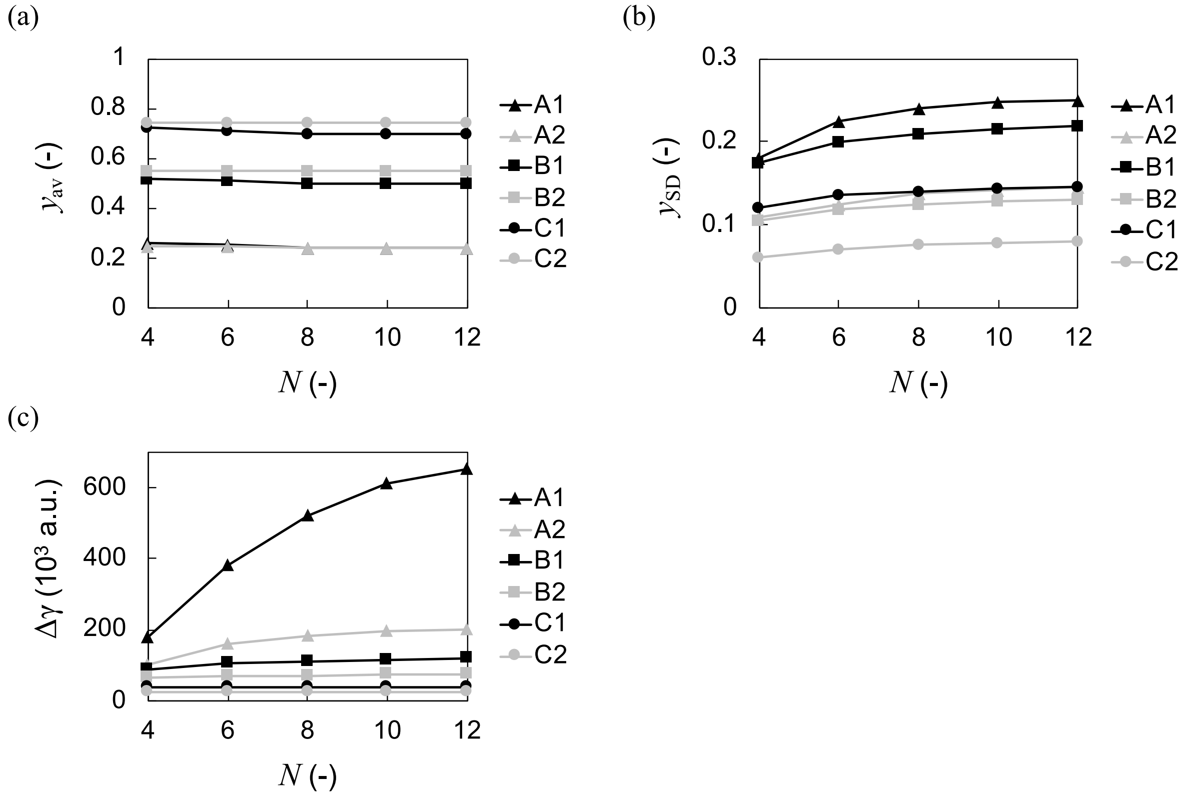

Figure II.3. N dependence of (a) y_{av} and (b) y_{SD} calculated at the PUHF/6-31+G level, and (c) $\Delta\gamma$ calculated at the UCCSD(T)/6-31+G level.

Table II.1. Results of $y_{av\infty}$, $y_{SD,\infty}$ and γ_∞ were obtained by fitting the results in Figure II.3.

Model (d_1, d_2)	$y_{av,\infty}$	$y_{SD,\infty}$	γ_∞ [10^3 a.u.]	$\gamma_\infty/\gamma(N = 2)$ [-]
A1 (2.5Å, 2.5Å)	0.26	0.25	740	36.0
A2 (2.5Å, 3.0Å)	0.27	0.15	200	9.6
B1 (3.0Å, 3.0Å)	0.48	0.22	128	4.4
B2 (3.0Å, 3.5Å)	0.54	0.13	72	2.4
C1 (3.5Å, 3.5Å)	0.69	0.14	42	2.7
C2 (3.5Å, 4.0Å)	0.73	0.08	28	1.8

Figure II.4 presents a comparison of the results of $\Delta\gamma(N)$ of **B1** calculated at the UCCSD(T), LC-UBLYP(0.47), and LC-UBLYP(0.33) levels with the 6-31+G basis set. In this model, the LC-UBLYP(0.33) overestimated the $\Delta\gamma(N)$ values of UCCSD(T) significantly for $N \geq 4$, although the result was close to the reference value for $N = 2$ [39.9 × 10^3 a.u. at the UCCSD(T), 35.3 × 10^3 a.u. at the LC-UBLYP(0.33), and 19.2 × 10^3 a.u. at the LC-UBLYP(0.47), respectively]. The LC-UBLYP(0.47) underestimated the $\Delta\gamma(N)$ values of UCCSD(T) to some extent, but their convergence behaviors look similar. Since the $\Delta\gamma(N)$ values and their convergence behaviors depend on the model, Table II.2 provides a summary of the results of γ_∞ and the polymer/dimer ratio $\gamma_\infty/\gamma(N = 2)$ for all the models. The γ_∞ values and the polymer/dimer ratio $\gamma_\infty/\gamma(N = 2)$ at the LC-UBLYP(0.33) level were more than twice as large as those at the UCCSD(T) level for all these models. Overestimations of the LC-UBLYP(0.33) became especially significant when d_1 was small. On the other hand, the LC-UBLYP(0.47) results reproduced better the UCCSD(T) results for both the γ_∞ and $\gamma_\infty/\gamma(N = 2)$ compared with the LC-UBLYP(0.33).

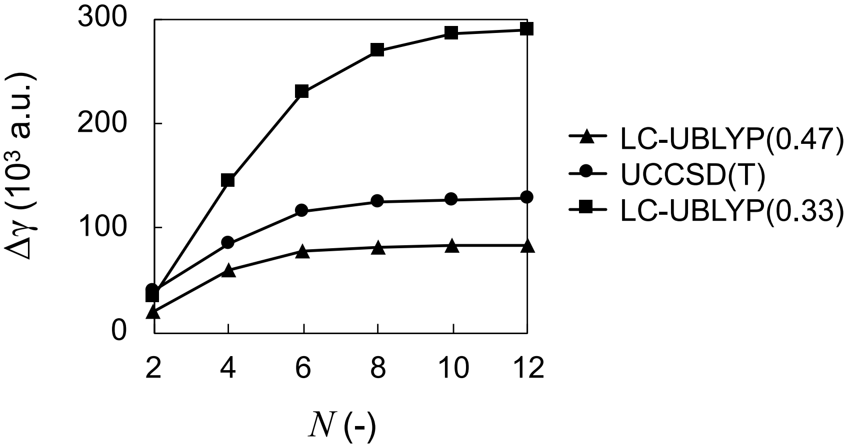

Figure II.4. N dependence of $\Delta\gamma$ [10^3 a.u.] of **B1** calculated at the UCCSD(T), LC-UBLYP(0.33) and LC-UBLYP(0.47) levels with the 6-31+G basis set.

Table II.2. Results of γ_∞ [10^3 a.u.] calculated at the UCCSD(T), LC-UBLYP(0.47) and LC-UBLYP(0.33) levels with the 6-31+G basis set. Values in round parenthesis are the polymer/dimer ratio $\gamma_\infty/\gamma(N = 2)$ [-] where $\gamma(N = 2)$ was calculated at d_1 at the same level of approximation.

Model (d_1, d_2)	UCCSD(T)	LC-UBLYP(0.33)	LC-UBLYP(0.47)
A1 (2.5Å, 2.5Å)	740 (36)	3200 (110)	550 (23)
A2 (2.5Å, 3.0Å)	200 (9.6)	590 (21)	180 (7.4)
B1 (3.0Å, 3.0Å)	130 (4.4)	300 (8.4)	84 (4.4)
B2 (3.0Å, 3.5Å)	72 (2.5)	140 (4.1)	49 (2.6)
C1 (3.5Å, 3.5Å)	42 (2.7)	84 (3.2)	30 (2.5)
C2 (3.5Å, 4.0Å)	28 (1.8)	55 (2.1)	22 (1.8)

The hyperpolarizability (γ-)density analysis[42] was conducted to examine the third-order electronic polarizations at these DFT levels. The γ-density, $\rho_{zzz}^{(3)}(\boldsymbol{r})$, is defined as the third-order field-induced response of charge density:

$$\rho_{zzz}^{(3)}(\boldsymbol{r}) = \left.\frac{\partial^3 \rho(\boldsymbol{r}, F_z)}{\partial F_z^3}\right|_{F_z=0} \qquad (\mathrm{II}.9)$$

where $\rho(\boldsymbol{r}, F_z)$ is the electron density at the position $\boldsymbol{r}$ in the presence of static electric field along the z-axis, F_z. $\rho^{(3)}_{zzz}(\boldsymbol{r})$ relates to γ_{zzzz} by the following spatial integration.

$$\gamma_{zzzz} = -\frac{1}{3!}\int z\rho^{(3)}_{zzz}(\boldsymbol{r})d\boldsymbol{r}^3 \tag{II.10}$$

Thus, the γ-density represents the spatial contributions of γ. Unfortunately, the electron density at the UCCSD(T) level is not available from the Gaussian program package, and the γ-density analysis was instead performed at the UCCSD level. Table II.A1 summarizes the results of γ_∞ at the UCCSD/6-31+G level and the ratio γ_∞(UCCSD)/γ_∞(UCCSD(T)). The UCCSD (with the 6-31+G) underestimated the UCCSD(T) results when d_1 was small, and their results were close to the LC-UBLYP(0.47) ones.

Figure II.5 shows the γ-density maps of **A2** with $N = 2$ and 4 calculated at the UCCSD, LC-UBLYP(0.33), and LC-UBLYP(0.47) (Figure II.A2 also includes the plotted results for $N = 12$). Yellow and blue surfaces represent the increase and decrease of electron density when the static electric field F_z is applied to the system toward the direction illustrated in Figure II.5. Thus, a pair of positive (yellow) and negative (blue) γ-densities represents the field-induced third-order electronic polarization (dipole moment). When the direction of the dipole moment vector of the pair is the same as that of the external field F_z, it contributes positively to the total γ (see the relation between $\rho^{(3)}_{zzz}(\boldsymbol{r})$ and γ_{zzzz}). For $N = 2$, although the amplitudes of positive and negative γ-densities on the carbon atoms were slightly more prominent in the LC-UBLYP(0.33) result than the other methods, the differences in the γ-density maps were very slight. For $N = 4$, positive and negative γ-densities are distributed alternately on each monomer. Similar alternation patterns of γ-densities were observed in tetramers of phenalenyl radicals[29]. The direction of the field-induced dipole moment of the inner monomers is opposite to that of the outer

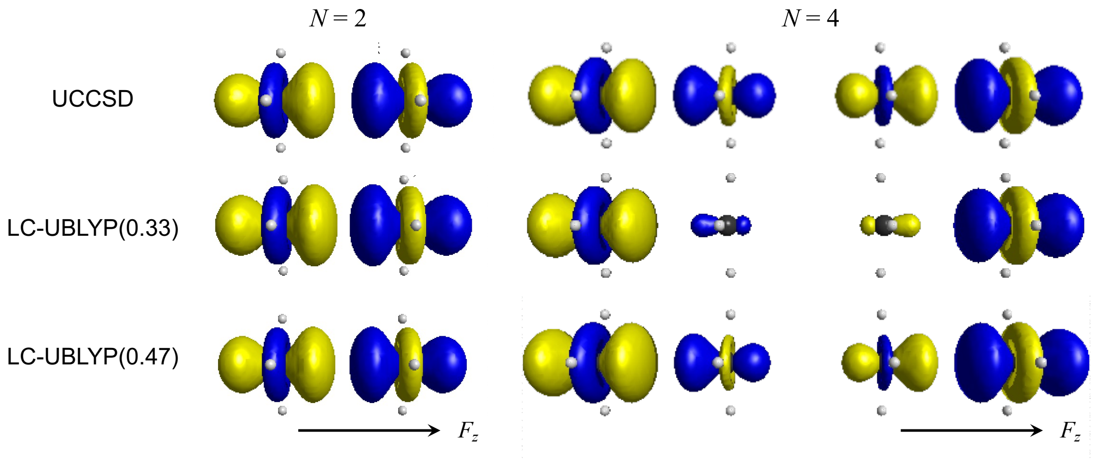

Figure II.5. γ-density maps of **A2** (N = 2 and 4) at the UCCSD, LC-UBLYP(0.33), and LC-UBLYP(0.47) levels. Yellow and blue surfaces represent the isosurfaces of $\rho^{(3)}_{zzz}(\boldsymbol{r})$ with the contour values of ± 100 a.u.

monomers. Thus, the total γ becomes significant when the amplitudes of γ-density on the inner monomers are reduced, the situation of which indicates the delocalization of electrons over the whole system. In the UCCSD and LC-UBLYP(0.47) results, the amplitudes of γ-density on the inner monomers were slightly reduced compared with those of the outer monomers. The reduction of γ-densities on the inner monomers were more apparent in the LC-UBLYP(0.33) result. These results indicated that the LC-UBLYP(0.33) overestimated the delocalization of electrons over the dimer pairs when the external field was applied. Thus, the optimal value of μ for the 1D chains of interacting π-radicals can be more significant than that for the dimers to suppress the over-delocalization.

3.2. 1D chains of phenalenyl radicals

The open-shell characters and third-order NLO properties of 1D chains of phenalenyl radicals were also investigated. Initially, y and $\gamma(N = 2)$ were calculated as a function of d_1 for the dimer (PLY)$_2$ (Figure II.6), even though their behaviors have already been discussed in several previous studies[29,32]. Like the case of $(CH_3)_2$, y decreased monotonically with decreasing d_1, and $\gamma(N = 2)$ showed a bell-shaped dependence on d_1. $\gamma(N = 2)$ attained a maximum around $d_1 = 2.8$ Å where y is in the intermediate region [at $d_1 = 2.8$ Å, $\gamma(N = 2) = 7.3 \times 10^4$ a.u. and $y_0 = 0.36$].

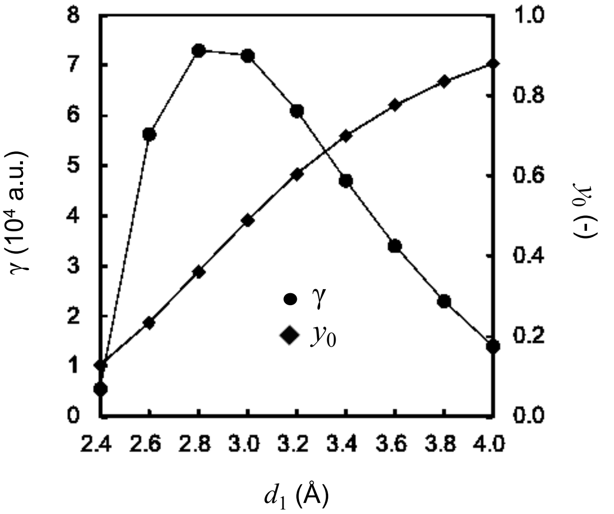

Figure II.6. Stacking distance (d_1) dependences of y_0 and static $\gamma(N = 2)$ for the phenalenyl radical π-dimer calculated at the PUHF and LC-UBLYP(0.47) levels, respectively, using the 6-31G* basis set.

The results at the limit $N \rightarrow \infty$ for models with different d_1 and d_2 were compared (Figure II.1(b)). Calculations of γ for the N-mers of phenalenyls with large N, needed for estimating γ_∞, were time-consuming and numerically complex even with the DFT. γ_∞ were directly calculated based on the band structure calculations. In CRYSTAL 17, the fourth-order analytic derivative of total energy can be calculated based on the coupled-perturbed Kohn Sham (CPKS) method under the parodic boundary condition[35,43–45]. Salustro et al. evaluated the γ_∞ of 1D chains of phenalenyl radicals using the LC-UBLYP(0.33) functional using a development version of CRYSTAL[32]. They also proposed a rough estimation of γ_∞ at the UCCSD level by combining the results of the dimer at the UCCSD level with the polymer/dimer ratio [i.e., $\gamma_\infty/\gamma(N = 2)$] estimated from the UHF and LC-UBLYP(0.33) calculations (15.0 ± 4.0). The LC-UBLYP(0.47) was employed to calculate γ_∞. In the CRYSTAL 17 package, the single particle crystalline orbitals are expressed as a linear combination of Bloch functions defined in terms of atomic orbital (AO) basis functions. The 6-31G* basis set, without the diffuse function, was used as the local AO basis. Salustro et al. employed a modified 6-31+(0.08)G* basis set (with a diffuse exponent of 0.08 upscaled from the original 0.04 value) to obtain the converged results of γ_∞ of the 1D chains of phenalenyl radicals[32]. Matsui et al. compared the LC-UBLYP(0.33) results with the 6-31+G* and 6-31G* basis sets for the 1D N-mer models of cyclic thiazyl radicals (DTDAs) with $d = 3.1$ Å and showed that the 6-31G* underestimated the 6-31+G* results less than 10 %[31]. They also mentioned that the basis set superposition error (BSSE) effects on γ were negligible. The LC-UBLYP(0.47) γ values for the dimer with different basis sets were compared (Figure II.A3), demonstrating that the 6-31G* is sufficient for our purpose. Parameter settings suitable for the band structure calculations using the CRYSTAL 17 package were also verified (see Appendix).

Figure II.7 shows calculated $y_{\mathrm{av},\infty}$, $y_{\mathrm{SD},\infty}$, and γ_∞ for the infinite 1D chains as a function of d_1 with different SDA ratios d_2/d_1 (= 1.0, 1.2, and 2.0). It should be noted the geometries of the infinite 1D chains were optimized by Salustro et al. at the RB3LYP-D/6-31G* level [$(d_1, d_2) = (3.05$Å, 3.19Å$)$; $d_2/d_1 \sim 1.05$] and UB3LYP-D/6-31G* [$(d_1, d_2) = (3.11$Å, 3.12Å$)$; $d_2/d_1 \sim 1.00$] levels. The results were plotted here for the range 2.8 Å $\leq d_1 \leq$ 4.0 Å[32]. $y_{\mathrm{av},\infty}$ of these models were almost independent of the ratio d_2/d_1, whereas $y_{\mathrm{SD},\infty}$ for $d_2/d_1 = 1.0$ is about twice as large as that for $d_2/d_1 = 1.2$. $y_{\mathrm{SD},\infty}$ for $d_2/d_1 = 2.0$ were almost zero. γ_∞ enhanced significantly when d_1 is small and d_2/d_1 approached 1.0. These tendencies were similar to those obtained in the 1D chains of methyl radicals.

So far, there have been several reports of the synthesis of 1D stacked chains of phenalenyl radicals. For example, Uchida et al. reported the formation of the uniform 1D chains of 2,5,8-tris(pentafluorophenyl) phenalenyl radicals in the parallel stacking with $d = 3.503$ Å[22]. The distance is, however, larger than the vdW contact distance of the carbon atom (3.4 Å), and $y_{\mathrm{av},\infty}$ at $d_1 = 3.5$ Å, is estimated to be more than 0.7. Although $d_2/d_1 = 1.0$ was achieved, this 1D chain may not drastically enhance γ. Designing and synthesizing such uniform 1D chains requires tuning the balance between the attractive and repulsive interactions acting on each monomer and considering the entropic effects, which is challenging. However, from the stacking distances realized in the π-dimers of several derivatives of phenalenyl radicals, it may be possible to achieve the 1D chains with distances of about 3.1-3.2 Å[20]. If d_1 can be reduced to about 3.2 Å without the SDA, γ can be enhanced by about one order of magnitude compared with the dimer as a unit. Even if the SDA patterns appear, an enhancement of γ can still be expected when the d_2/d_1 ratio is less than 1.2 [at $d_1 = 3.2$ Å, $\gamma_\infty/\gamma(N = 2) = 9.5$ for $d_2/d_1 = 1.0$ and $\gamma_\infty/\gamma(N = 2) = 3.5$ for $d_2/d_1 = 1.2$]. The obtained polymer/dimer ratio around $d_1 = 3.2$ Å is consistent with that predicted by Salustro et al. Regarding diradical characters, $y_{\mathrm{av},\infty} \leq 0.6$ and $y_{\mathrm{SD},\infty} \geq 0.1$ would be the target region for achieving severalfold enhancement of γ as a rough estimation from these results.

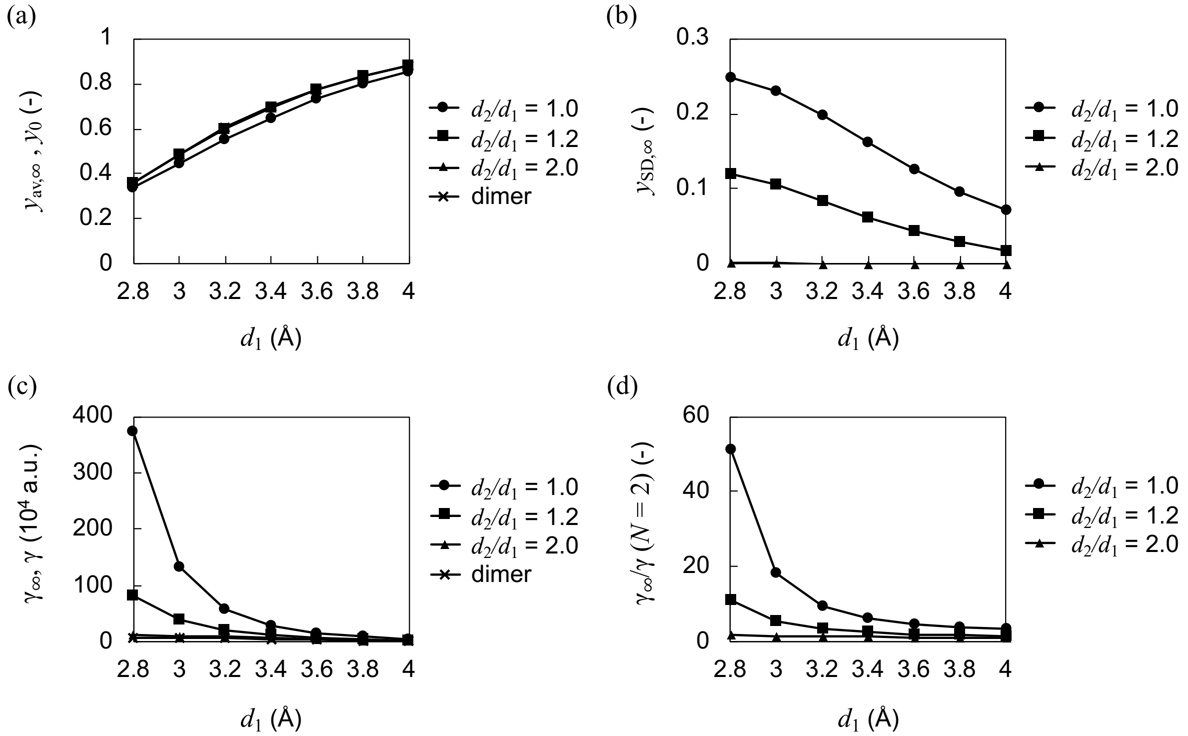

Figure II.7. Stacking distance (d_1) dependences of (a) $y_{\mathrm{av},\infty}$, (b) $y_{\mathrm{SD},\infty}$, (c) γ_∞ and (d) $\gamma_\infty/\gamma(N = 2)$ for the phenalenyl radical π-dimer calculated at the PUHF (for y) and LC-UBLYP(0.47) (for γ) levels, respectively, using the 6-31G* basis set.

On the other hand, although the present study focused on the dependence on the ratio of distances, the orbital interactions between the monomers tend to become smaller when the monomers are relatively slipped or rotated. Calculations and analysis based on y_{av} and y_{SD} are expected to work for such cases. As an example, in Figure II.8, 1D chain models introducing alternating misalignment (Δd_y) in the y-direction and calculated $y_{\mathrm{av},\infty}$, $y_{\mathrm{SD},\infty}$, and the polymer/dimer ratio $\gamma_\infty/\gamma(N = 2)$ were calculated with fixed d_1 = 3.2 Å and d_2/d_1 = 1.0. When Δd_y was increased, the orbital interactions between the monomers became weak, and as a result, $y_{\mathrm{av},\infty}$ increased while $y_{\mathrm{SD},\infty}$ decreased. In this case, $\gamma_\infty/\gamma(N = 2)$ was kept high when $y_{\mathrm{av},\infty} \leq 0.6$ and $y_{\mathrm{SD},\infty} \geq 0.1$. Thus, the combination of $y_{\mathrm{av},\infty}$ and $y_{\mathrm{SD},\infty}$ is expected to help characterize the open-shell electronic structures in 1D chains with several different configurations.

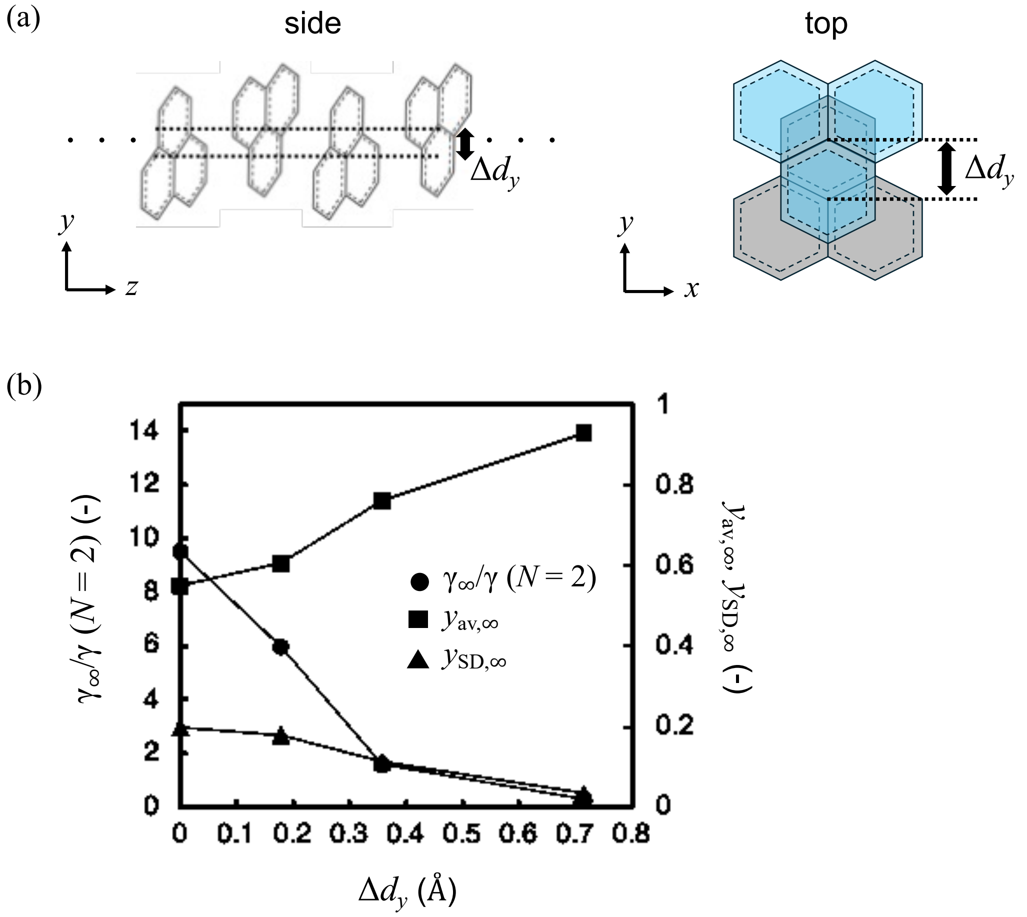

Figure II.8. (a) Side and top views of 1D chain models with alternating misalignment (Δd_y) in the y-direction and calculation results of $y_{\mathrm{av},\infty}$, $y_{\mathrm{SD},\infty}$, and (b) the polymer/dimer ratio $\gamma_\infty/\gamma(N = 2)$ with fixed $d_1 = 3.2$ Å and $d_2/d_1 = 1.0$.

4. Conclusion

In this paper, the correlation between the open-shell electronic structure and third-order nonlinear optical (NLO) properties of 1D chains of π-radicals was theoretically investigated. The calculations of 1D chain models consisting of methyl radicals revealed that considering both $y_{\mathrm{av},\infty}$ and $y_{\mathrm{SD},\infty}$ was essential for characterizing their open-shell electronic structures and discussing the γ_∞ values in relation to the stacking distance alternation (SDA). Additionally, the exchange-correlation (xc-) functional dependence of γ_∞ was examined, and it was found that LC-UBLYP(0.47) reproduced the γ_∞ values and their polymer/dimer ratio predicted at the UCCSD(T) level with good accuracy. By employing the LC-UBLYP(0.47) method, the γ_∞ values of 1D chains of phenalenyl radicals were also evaluated. The results indicated that 1D chains with $y_{\mathrm{av},\infty} \leq 0.6$ and $y_{\mathrm{SD},\infty} \geq 0.1$ are promising candidates for novel third-order NLO materials with enhanced properties. These conditions are satisfied when the primary stacking distance is $d_1 \leq 3.2$ Å with a small SDA (d_2/d_1) ratio. The SDA and the relative configurations between monomers significantly influence γ_∞ through variations in y. Consequently, the combined use of $y_{\mathrm{av},\infty}$ and $y_{\mathrm{SD},\infty}$ proves to be a valuable tool in elucidating the relationship between open-shell electronic structures and third-order NLO properties in 1D chains of π-radicals.

On the other hand, the estimation of $y_{\mathrm{av},\infty}$ and $y_{\mathrm{SD},\infty}$ at the PUHF level requires careful preparation of the initial guess for large N, along with a thorough examination of the convergence behaviors of total energy and wavefunction to ensure the acquisition of physically meaningful calculation results. Alternatively, it is suggested that $y_{\mathrm{av},\infty}$ and $y_{\mathrm{SD},\infty}$ can be roughly estimated from the $y_{\mathrm{av},\infty}$ and $y_{\mathrm{SD},\infty}$ values of $N = 4$ using Eqs. (II.5)-(II.6), as demonstrated by the convergence behaviors of $y_{\mathrm{av}}(N)$ and $y_{\mathrm{SD}}(N)$ in Figure II.3. It would, of course, be advantageous to compute $y_{\mathrm{av},\infty}$ and $y_{\mathrm{SD},\infty}$ (or their equivalents) directly from quantum chemical calculations under periodic boundary conditions[46], ensuring consistency with the band gap and width results. The y-based indices introduced in this study are expected to further contribute to the advancement of data-driven approaches in the search for novel open-shell functional materials[47].

Additionally, the present results suggest that enhanced third-order NLO properties can be expected for 1D chains of phenalenyl radicals with $d_1 \leq 3.2$ Å while maintaining a small SDA. The exploration of appropriate substituent groups that facilitate the stabilization of the uniform π-stacking configuration in the crystal phase is highly desirable. In this context, a comprehensive investigation of the stabilization mechanisms of 1D chains with substituents is necessary, utilizing a variety of analysis methods for intermolecular interactions, similar to those conducted for the dimers of phenalenyl radicals[48–52].

Appendix

Basis set dependence of γ at the UCCSD(T) for the methyl radical dimer.

The basis set dependence of γ for the π-stacked multimer models of methyl radicals was investigated. Figure II.A1 compared the static γ (γ_{zzzz}) results for the methyl radical π-dimer calculated at the UCCSD(T) level using the aug-cc-pVDZ and 6-31+G basis sets. Even though the results with the 6-31+G tend to overestimate those with the aug-cc-pVDZ basis set, it can reproduce the stacking distance (d_1) dependencies calculated with the aug-cc-pVDZ basis set. Consequently, the 6-31+G basis set was employed for the evaluation of γ and *y* in the 1D chains of methyl radicals.

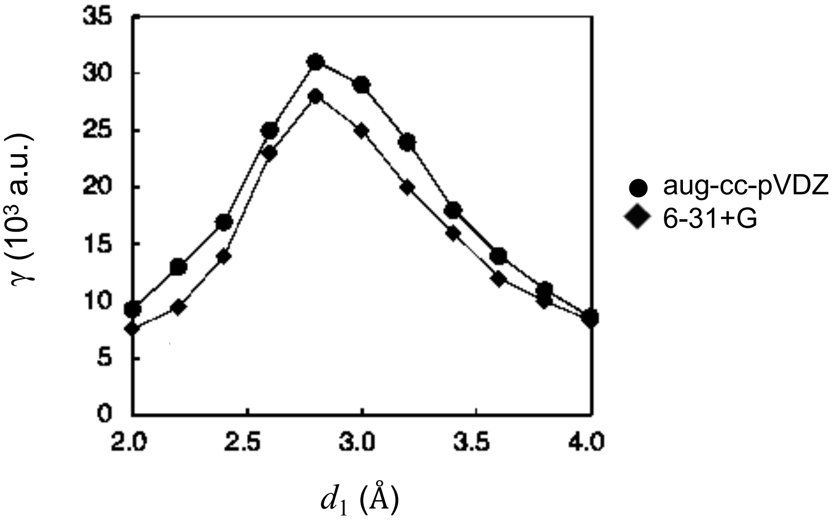

Figure II.A1. Stacking distance (d_1) dependences of static γ (γ_{zzzz}) for the methyl radical π-dimer calculated at the UCCSD(T) level using the aug-cc-pVDZ and 6-31+G basis sets.

γ values at the UCCSD level for the 1D chain models of methyl radicals.

Table II. A1. Results of γ_∞ [10^3 a.u.] at the UCCSD/6-31+G level and the ratio γ_∞(UCCSD)/ γ_∞(UCCSD(T)) for the 1D chain models of methyl radicals.

	γ_∞	γ_∞(UCCSD) / γ_∞(UCCSD(T)) [-]
A1	506	0.66
A2	152	0.77
B1	98	0.76
B2	60	0.83
C1	42	1.00
C2	24	0.86

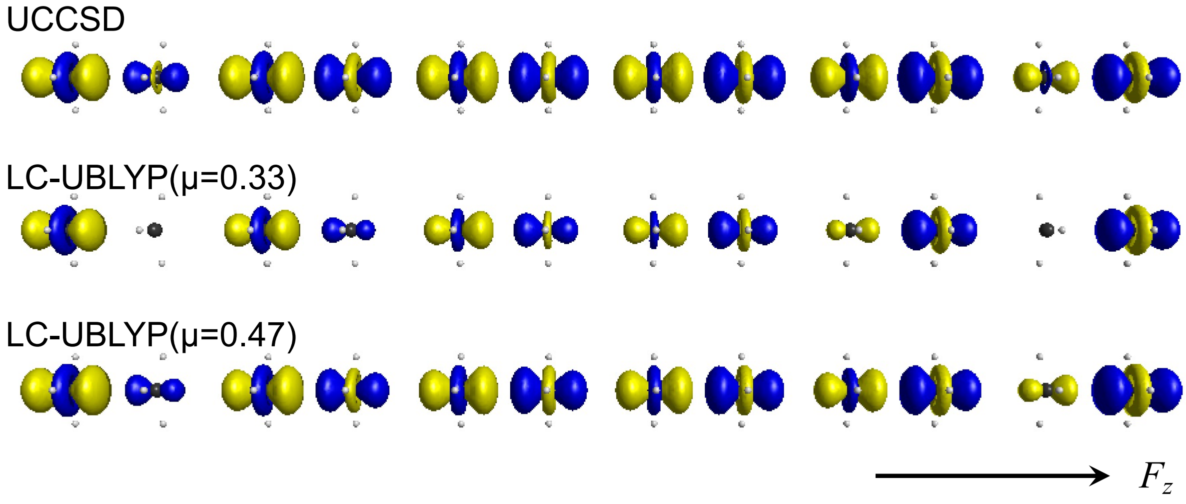

Figure II.A2. γ-density maps of **A2** (N = 12) at the UCCSD, LC-UBLYP(0.33), and LC-UBLYP(0.47). Yellow and blue surfaces represent the isosurfaces of $\rho_{zzz}^{(3)}(\boldsymbol{r})$ with the contour values of ± 100 a.u.

Parameter settings suitable for the CPKS analytic derivative calculations of 1D chains of phenalenyl radicals using CRYSTAL 17 program package.

Several parameters must be set in the CRYSTAL 17 program package during the calculations of γ_∞. The most important ones are the five cut-off parameters T_i (i = 1-5) for the Coulomb and exchange series (details of T_i are given in the user's manual of CRYSTAL[1]). In the paper by Salustro et al., they set:

$$T_1 = T_2 = T_3 = T_4 = \frac{1}{2}T_5 \tag{II.A1}$$

with T_1 = 8. The convergence behaviors of γ_∞ with T_1 under the condition Eq. (II.A1) at the LC-UBLYP(0.47) level were checked using the 1D chain models of ***methyl radicals***. However, using the 6-31+G basis set, including the diffuse function, SCF convergence was not achieved in some cases due to the linear dependency in this basis set. Consequently, the T_i dependences of γ_∞ for 1D chains of methyl radicals were examined using the 6-31G basis set instead. Table II.A2 compared the results of Δγ at the LC-UBLYP(0.47) with the 6-31+G and 6-31G basis sets. The XXLGRID option was employed for grid option, the bielectronic integrals were computed exactly with the NOBIPOLA option, IS = 12 was used for **k**-point sampling. From these results, the 6-31G results gave ~70 % of the 6-31+G results for N = 4-12. The dimer unit was considered as the repeating unit structure.

Table II.A2. Results of $\Delta\gamma$ at the LC-UBLYP(0.47) with the 6-31+G and 6-31G basis sets for model **B1** of 1D chain of methyl radicals.

N	$\Delta\gamma$(6-31+G) [10^3 a.u.]	$\Delta\gamma$(6-31G) [10^3 a.u.]	$\Delta\gamma$(6-31G)/$\Delta\gamma$(6-31+G) [-]
4	78	52	0.67
6	107	73	0.69
8	117	80	0.68
10	121	83	0.69
12	122	83	0.68

Table II.A3 summarizes the T_1 dependences of γ_∞ for the 1D chain models of methyl radicals. The convergence of γ_∞ was slow in the case of **A1**, but it is found that $T_1 = 40$ seems sufficient to give the relative errors less than ~1 %. The results using these parameters were compared based on the fitting-extrapolation scheme and the band structure calculation (Table II.A4). Although the results of **A1** differed by ~2 %, these results agreed nicely with each other.

Table II.A3. T_1 dependences of γ_∞ under the constraint of Eq. (II.A1) calculated at the LC-UBLYP(0.47)/6-31G level

T_1	**A1**	**A2**	**B1**	**B2**	**C1**
10	393	55.2	15.3	117	28.4
20	434	57.1	15.3	125	28.8
30	465	57.1	15.4	127	28.8
40	471	57.6	15.4	129	28.9
50	472	57.6	15.4	129	28.9
60	472	57.6	15.4	129	28.9
70	476	57.6	15.4	129	28.9

Table II.A4. Calculation results of γ_∞ [10^3 a.u.] based on the fitting-extrapolation scheme (using Gaussian 09) and the band structure calculation (using CRYSTAL 17) at the LC-UBLYP(0.47)/6-31G level.

	A1	**A2**	**B1**	**B2**	**C1**
Fitting-extrapolation	460	57	15	127	29
Band structure	470	58	15	129	29

Following these analyses, the LC-UBLYP(0.47) with these parameters was employed for the band structure calculations of 1D chains of phenalenyl radicals. In this case, the 6-31G* basis set was used. The results for the phenalenyl radical π-dimers with different basis sets are compared in Figure II.A3. From this figure, the 6-31G* basis set reproduced well the results of aug-cc-pVDZ.

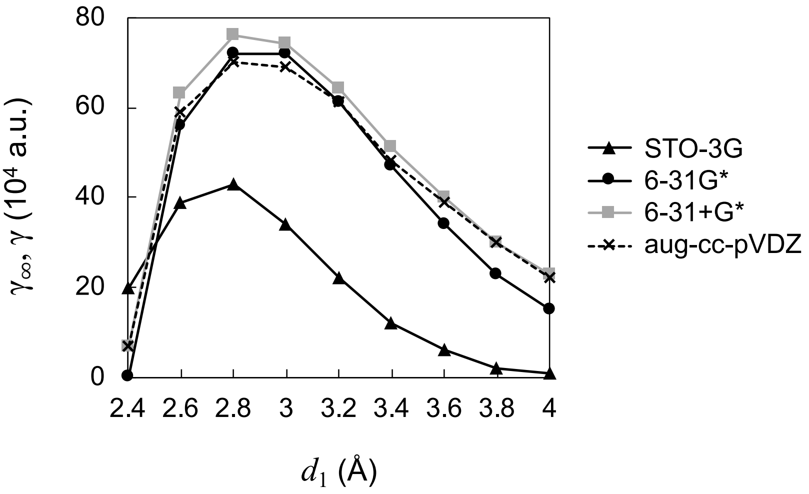

Figure II.A3. Stacking distance (d_1) dependences of static γ for the phenalenyl radical π-dimer (anti-parallel stacking) calculated at the LC-UBLYP(0.47) level using the 6-31+G*, 6-31G*, and aug-cc-pVDZ basis sets.

References

[1] H. S. Nalwa and S. Miyata, Eds., *Nonlinear Optics of Organic Molecules and Polymers, 1st ed*, CRC Press., **1996**.

[2] C. P. De Melo and R. Silbey, *J. Chem. Phys.*, **1988**, *88*, 2558–2566.

[3] N. J. Dawson, B. R. Anderson, J. L. Schei and M. G. Kuzyk, *Phys. Rev. A*, **2011**, *84*, 043407.

[4] N. J. Dawson, B. R. Anderson, J. L. Schei and M. G. Kuzyk, *Phys. Rev. A - At. Mol. Opt. Phys.*, **2011**, *84*, 043406.

[5] R. R. Tykwinski, U. Gubler, R. E. Martin, F. Diederich, C. Bosshard and P. Günter, *J. Phys. Chem. B*, **1998**, *102*, 4451–4465.

[6] F. Meyers, S. R. Marder, B. M. Pierce and J. L. Brédas, *J. Am. Chem. Soc.*, **1994**, *116*, 10703–10714.

[7] S. P. Karna, G. B. Talapatra, W. M. K. P. Wijekoon and P. N. Prasad, *Phys. Rev. A*, **1992**, *45*, 2763–2770.

[8] J. R. Heflin, K. Y. Wong, O. Zamani-Khamiri and A. F. Garito, *Phys. Rev. B*, **1988**, *38*, 1573–1576.

[9] M. Nakano and B. Champagne, *Wiley Interdiscip. Rev. Comput. Mol. Sci.*, **2016**, *6*, 198–210.

[10] H. Matsui, M. Nakano and B. Champagne, *Phys. Rev. A*, **2016**, *94*, 042515.

[11] M. Nakano, *Chem. Rec.*, **2017**, *17*, 27–62.

[12] H. Matsui, S. Ito and M. Nakano, *J. Phys. Chem. A*, **2018**, *122*, 3680–3687.

[13] M. Nakano, R. Kishi, S. Ohta, H. Takahashi, T. Kubo, K. Kamada, K. Ohta, E. Botek and B. Champagne, *Phys. Rev. Lett.*, **2007**, *99*, 033001.

[14] M. Nakano, H. Nagao and K. Yamaguchi, *Phys. Rev. A - At. Mol. Opt. Phys.*, **1997**, *55*, 1503–1513.

[15] J. Wu, *Diradicaloids, 1st ed.*, Jenny Stanford Publishing, New York, **2022**.

[16] A. Hinz, J. Bresien, F. Breher and A. Schulz, *Chem. Rev.*, **2023**, *123*, 10468–10526.

[17] C. Shu, Z. Yang and A. Rajca, *Chem. Rev.*, **2023**, *123*, 11954–12003.

[18] Y. Ishigaki, T. Harimoto, T. Shimajiri and T. Suzuki, *Chem. Rev.*, **2023**, *123*, 13952–13965.

[19] M. Abe, *Chem. Rev.*, **2013**, *113*, 7011–7088.

[20] M. Kertesz, *Chem. - A Eur. J.*, **2019**, *25*, 400–416.

[21] T. Kubo, A. Shimizu, M. Sakamoto, M. Uruichi, K. Yakushi, M. Nakano, D. Shiomi, K. Sato, T. Takui, Y. Morita and K. Nakasuji, *Angew. Chemie - Int. Ed.*, **2005**, *44*, 6564–6568.

[22] K. Uchida, Y. Hirao, H. Kurata, T. Kubo, S. Hatano and K. Inoue, *Chem. - An Asian J.*, **2014**, *9*, 1823–1829.

[23] P. A. Koutentis, Y. Chen, Y. Cao, T. P. Best, M. E. Itkis, L. Beer, R. T. Oakley, A. W. Cordes, C. P. Brock and R. C. Haddon, *J. Am. Chem. Soc.*, **2001**, *123*, 3864–3871.

[24] C. D. Bryan, A. W. Cordes, R. C. Haddon, T. T. M. Palstra, A. S. Perel, L. F. Schneemeyer, J. V. Waszczak, R. G. Hicks, D. K. Kennepohl, C. D. MacKinnon, R. T. Oakley and S. R. Scott, *J. Am. Chem. Soc.*, **1994**, *116*, 1205–1210.

[25] R. Suizu, A. Iwasaki, Y. Shuku and K. Awaga, *J. Mater. Chem. C*, **2015**, *3*, 7968–7977.

[26] A. W. Cordes, C. D. Bryan, W. M. Davis, R. H. De Laat, S. H. Glarum, J. D. Goddard, R. C. Haddon, R. G. Hicks, D. K. Kennepohl, R. T. Oakley, S. R. Scott and N. P. C. Westwood, *J. AM. CHEM. SOC*, **1993**, *115*, 7232–7239.

[27] S. Vela, F. Mota, M. Deumal, R. Suizu, Y. Shuku, A. Mizuno, K. Awaga, M. Shiga, J. J. Novoa and J. Ribas-Arino, *Nat. Commun.*, **2014**, *5:4411*, 1–9.

[28] H. Z. Beneberu, Y. H. Tian and M. Kertesz, *Phys. Chem. Chem. Phys.*, **2012**, *14*, 10713–10725.

[29] K. Yoneda, M. Nakano, K. Fukuda, H. Matsui, S. Takamuku, Y. Hirosaki, T. Kubo, K. Kamada and B. Champagne, *Chem. - A Eur. J.*, **2014**, *20*, 11129–11136.

[30] H. Matsui, M. Yamane, T. Tonami, T. Nagami, K. Watanabe, R. Kishi, Y. Kitagawa and M. Nakano, *Mater. Chem. Front.*, **2018**, *2*, 785–790.

[31] H. Matsui, M. Yamane, T. Tonami, M. Nakano, M. De Wergifosse, T. Seidler and B. Champagne, *J. Phys. Chem. C*, **2018**, *122*, 6779–6785.

[32] S. Salustro, L. Maschio, B. Kirtman, M. Rérat and R. Dovesi, *J. Phys. Chem. C*, **2016**, *120*, 6756–6761.

[33] M. Nakano, A. Takebe, R. Kishi, S. Ohta, M. Nate, T. Kubo, K. Kamada, K. Ohta, B. Champagne, E. Botek, H. Takahashi, S. ichi Furukawa, Y. Morita and K. Nakasuji, *Chem. Phys. Lett.*, **2006**, *432*, 473–479.

[34] R. Dovesi, R. Orlando, A. Erba, C. M. Zicovich-Wilson, B. Civalleri, S. Casassa, L. Maschio, M. Ferrabone, M. De La Pierre, P. D'Arco, Y. Noël, M. Causà, M. Rérat and B. Kirtman, *Int. J. Quantum Chem.*, **2014**, *114*, 1287–1317.

[35] R. Dovesi, A. Erba, R. Orlando, C. M. Zicovich-Wilson, B. Civalleri, L. Maschio, M. Rérat, S. Casassa, J. Baima, S. Salustro and B. Kirtman, *WIREs Comput. Mol. Sci.*, **2018**, *8:e1360*, 1–36.

[36] W. Yoshida, H. Matsui, H. Miyamoto, T. Tonami, R. Sugimori, K. Yoneda, R. Kishi and M. Nakano, *ACS Omega*, **2021**, *6*, 3046–3059.

[37] K. Yamaguchi, *Chem. Phys. Lett.*, **1975**, *33*, 330–335.

[38] Y. Tawada, T. Tsuneda, S. Yanagisawa, T. Yanai and K. Hirao, *J. Chem. Phys.*, **2004**, *120*, 8425–8433.

[39] H. Iikura, T. Tsuneda, T. Yanai and K. Hirao, *J. Chem. Phys.*, **2001**, *115*, 3540–3544.

[40] R. Kishi, S. Bonness, K. Yoneda, H. Takahashi, M. Nakano, E. Botek, B. Champagne, T. Kubo, K. Kamada, K. Ohta and T. Tsuneda, *J. Chem. Phys.*, **2010**, *132*, 094107.

[41] M. J. Frisch, G. W. Trucks, H. B. Schlegel, G. E. Scuseria, M. A. Robb, J. R. Cheeseman, G. Scalmani, V. Barone, B. Mennucci, G. A. Petersson, H. Nakatsuji, M. Caricato, H. P. H. X. Li, A. F. Izmaylov, G. Z. J. Bloino, J. L. Sonnenberg, M. Hada, M. Ehara, K. Toyota, R. Fukuda, J. Hasegawa, M. Ishida, T. Nakajima, Y. Honda, O. Kitao, H. Nakai, T. Vreven, J. J. A. Montgomery, J. E. Peralta, F. Ogliaro, M. Bearpark, J. J. Heyd, E. Brothers, K. N. Kudin, V. N. Staroverov, R. Kobayashi, J. Normand, K. Raghavachari, A. Rendell, J. C. Burant, S. S. Iyengar, J. Tomasi, M. Cossi, N. Rega, J. M. Millam, M. Klene, J. E. Knox, J. B. Cross, V. Bakken, C. Adamo, J. Jaramillo, R. Gomperts, R. E. Stratmann, O. Yazyev, A. J. Austin, R. Cammi, C. Pomelli, J. W. Ochterski, R. L. Martin, K. Morokuma, V. G. Zakrzewski, G. A. Voth, P. Salvador, J. J. Dannenberg, S. Dapprich, A. D. Daniels, Ö. Farkas, J. B. Foresman, J. V. Ortiz, J. Cioslowski and D. J. Fox, *Gaussian 09. Rev. D.01*, Gaussian Inc., Wallingford, CT, **2009**.

[42] M. Nakano, I. Shigemoto, S. Yamada and K. Yamaguchi, *J. Chem. Phys.*, **1995**, *103*, 4175–4191.

[43] R. Orlando, V. Lacivita, R. Bast and K. Ruud, *J. Chem. Phys.*, **2010**, *132*, 244106.

[44] M. Ferrero, B. Civalleri, M. Ŕrat, R. Orlando and R. Dovesi, *J. Chem. Phys.*, **2009**, *131*, 214704.

[45] R. Orlando, R. Bast, K. Ruud, U. Ekström, M. Ferrabone, B. Kirtman and R. Dovesi, *J. Phys. Chem. A*, **2011**, *115*, 12631–12637.

[46] K. Tada, Y. Kitagawa, T. Kawakami, M. Okumura and S. Tanaka, *Chem. Lett.*, **2021**, *50*, 392–396.

[47] Y. Hayashi and S. Kawauchi, *Polym. Chem.*, **2019**, *10*, 5584–5593.

[48] Y. Takano, T. Taniguchi, H. Isobe, T. Kubo, Y. Morita, K. Yamamoto, K. Nakasuji, T. Takui and K. Yamaguchi, *Chem. Phys. Lett.*, **2002**, *358*, 17–23.

[49] V. Zaitsev, S. V. Rosokha, M. Head-Gordon and J. K. Kochi, *J. Org. Chem.*, **2006**, *71*, 520–526.

[50] Z. H. Cui, H. Lischka, H. Z. Beneberu and M. Kertesz, *J. Am. Chem. Soc.*, **2014**, *136*, 5539–5542.

[51] Z. Tang, Z. Jiang, H. Chen, P. Su and W. Wu, *J. Chem. Phys.*, **2019**, *151*, 244106.

[52] Z. H. Cui, M. H. Wang, H. Lischka and M. Kertesz, *JACS Au*, **2021**, *1*, 1647–1655.

PART III

Two-Photon Absorption Properties of Open-Shell Molecular Aggregates

Chapter 1.

Stacking Distance Dependence of Two-Photon Absorption Properties of Phenalenyl π-Dimer Models

Stacking distance (*d*)-dependence of the peak positions and intensities of one-photon absorption (OPA) and two-photon absorption (TPA) spectra of phenalenyl π-dimer models was investigated theoretically. Calculations of excitation energies and transition dipole moments necessary for simulating the OPA and TPA spectra were performed using the extended multi-configurational quasi-degenerate second-order perturbation theory (XMC-QDPT2) approach. A two-order magnitude enhancement in the first TPA peak intensity was observed for the model with $d = 3.0$ Å, attributed to an electronic transition along the stacking direction, compared to the model with $d = 6.0$ Å. The diradical character (y) was found to influence the TPA properties of the first TPA peak of phenalenyl π-dimer models, as predicted by the valence-bond configuration interaction method based on a two-site model.

1.1. Introduction

As discussed in the section 3 of the General Introduction, two-photon absorption (TPA), a third-order nonlinear optical (NLO) process, holds significant potential for industrial applications across various fields[1–8]. The realization of such applications requires materials exhibiting a high TPA efficiency, characterized by the TPA cross section ($\sigma^{(2)}(\omega)$ expressed in units of GM (1 GM = 1 x 10^{-50} cm^4 s $photon^{-1}$), at a given input photon energy ($\hbar\omega$). According to time-dependent perturbation theory, $\sigma^{(2)}(\omega)$ for a centrosymmetric molecular system can be approximated by the following expression, referred to as the three-state approximation[9]:

$$\sigma^{(2)}(\omega) \propto \frac{\boldsymbol{\mu}_{gk}{}^2 \boldsymbol{\mu}_{kf}{}^2}{\left(E_{kg} - \frac{E_{fg}}{2}\right)^2 \Gamma_{kg}} \tag{III.1.1}$$

where the g is the ground state, k is a one-photon allowed excited state, and f is a two-photon allowed excited state. $\boldsymbol{\mu}_{gk}$ ($\boldsymbol{\mu}_{kf}$) denotes the transition dipole moment between the states. E_{kg} and Γ_{kg} represent the excitation energy and the damping factor for the state k. $\sigma^{(2)}(\omega)$ reaches a peak when the numerator $\boldsymbol{\mu}_{gk}{}^2\boldsymbol{\mu}_{kf}{}^2$ is non-zero and a two-photon resonant condition ($E_{fg}/2 = \hbar\omega$) is fulfilled. Optimizing the magnitudes of the transition dipole moments ($|\boldsymbol{\mu}_{gk}|$ and $|\boldsymbol{\mu}_{kf}|$) and minimizing the energy difference ($\left|E_{kg} - E_{fg}/2\right|$) are essential for enhancing the TPA peak intensity.

The design and synthesis of molecular systems exhibiting large $\sigma^{(2)}$ values have been variously reported for closed-shell molecular systems[9–13], but recently, open-shell singlet systems, which are novel third-order NLO materials, have attracted much attention[14–20]. As discussed in Chapter 1 of PART I, diradical character y is useful both as a theoretical index to characterize the degree of open-shell nature in the singlet ground (S_0) state and as a factor controlling the third-order NLO properties of the open-shell singlet system[14,21–23].

y assumes values between 0 and 1, reflecting bond instability, while $1 - y$ corresponds to an effective bond order. A value of $y = 0$ indicates a closed-shell configuration, whereas $y = 1$ represents a fully diradical state. As illustrated in Figures I.2.5 and I.3.3, the static second hyperpolarizability (γ) and the intensity of the lowest energy peak in TPA spectra (the cross-section of the first TPA peak) exhibit significant increases in the intermediate y based on the valence-bond configuration interaction (VBCI) method within the simplest symmetric two-site diradical model[14,20].

This chapter presents a theoretical analysis of the optical properties of the π-dimer of phenalenyl radicals, which demonstrates the potential for a significant enhancement in TPA cross-sections by modulating y through adjustments in the stacking distance (*d*). The structure of the unsubstituted phenalenyl radical (PLY) is illustrated in Figure III.1.1, **1a**. PLYs are the smallest units in polycyclic aromatic hydrocarbons (PAHs) that exhibit open-shell properties. Owing to its triangular framework and possession of 13 π-electrons, the PLY cannot achieve a fully closed-shell configuration based on the Hückel rule[24,25]. Consequently, its ground state contains a non-bonding orbital, the singly occupied molecular orbital (SOMO). The delocalization of the SOMO contributes to the high thermally stability of PLY, making it a versatile building block for open-shell molecular systems. Examples include IDPL and NDPL with *p*-quinodimethane linkers[26–28], as well as zethrene with an acene linker[29–35]. The open-shell nature of these systems can be fine-tuned through various chemical modifications.

The π-stacking aggregates (dimer-multimer) of PLY investigated in this study have also been synthesized in both solution and crystalline phases[36–38]. *d* of these systems can be tuned by introducing various substituent groups (-R) at 2-, 5-, and 8-positions of PLY. For instance, derivatives **1b** (R = *t*-Bu) and **1c** (R = C_6H_5) have been reported as anti-type π-dimers, with *d* values of approximately ~3.31 Å[36] and ~3.02 Å[38], respectively, as determined by X-ray crystal structure analysis. These results suggest the presence of the multi-center two-electron covalent-like bonding interaction between the PLYs, often referred to as pancake bonding[39]. These stabilization mechanisms have been investigated by analyzing the electronic structure and potential energy surface of the ground state (S_0)[40–43]. See section 8 of the General Introduction for additional details.

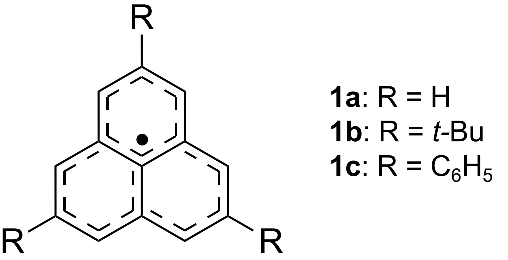

Figure III.1.1. Molecular structure of the unsubstituted phenalenyl molecule (**1a**) and examples of derivatives modified with substituent groups (-R) reported in actual synthesis and analysis (**1b**, **1c**)

Theoretical analyses of these open-shell molecular systems have primarily focused on the calculation of static γ, which serves as the microscopic origin of NLO properties. Yoneda et al. conducted a theoretical investigation into the relationship between *d*, *y*, and static γ for the π-dimer of **1a** model (**1a₂** in Figure III.1.2(a)) at the broken-symmetry density functional theory (DFT) approach[44]. Their findings revealed that *y* decreases monotonically as *d* decreases, while the static γ, as a function of *d*, reaches its maximum at approximately *d* = 2.9 Å with *y* attaining an intermediate value at this *d* (Figure 16). Large values of these static γ, when compared to those of closed-shell molecules, have led to the expectation of pronounced NLO properties, particularly in open-shell molecular systems exhibiting intermediate *y* (Yoneda et al. compared the static γ of the **1a₂** model with that of the closed-shell coronene dimer[44])[20]. However, the relationship between *y* and TPA properties remains insufficiently explored and has not been fully elucidated.

The theoretical prediction of TPA properties in open-shell singlet systems presents significant challenges due to the necessity of achieving a balanced description of both static and dynamic correlation effects. For instance, Nanda and Krylov developed computational and analytical frameworks for TPA spectra based on the spin-flip equation-of-motion coupled-cluster method with single and double substitutions (EOM-SF-CCSD)[45]. This approach has been successfully applied to several diradical molecules. Additionally, they introduced the natural transition orbital (NTO) analysis, which provides a visual representation of two-photon electronic transitions. This methodology is both sophisticated and reliable for investigating the TPA properties of small- to medium-sized diradical molecules where EOM-SF-CCSD calculations are computationally feasible. In contrast, multi-reference perturbation theory (MRPT) methods have been extensively employed to study the electronic structures of the ground and low-lying excited states in open-shell PAHs, provided that an appropriate active space can be defined. For example, the multi-configurational quasi-degenerate second-order perturbation theory (MC-QDPT2) method[46] has been applied to analyze the excited states of aromatic excimers, demonstrating its utility for systems requiring detailed multi-reference treatments[47].

To date, TPA properties of π-dimers and multimers of open-shell polycyclic aromatic hydrocarbons (PAHs) have not been thoroughly investigated, either theoretically or experimentally, despite their significant potential as promising candidates for novel open-shell nonlinear optical (NLO) materials. A comprehensive theoretical analysis of their TPA properties could provide valuable insights and serve as a foundation for developing design guidelines for innovative open-shell NLO materials.

1.2. Methods

1.2.1. Model systems

The *d*-dependence of the peak positions and intensities of the one-photon absorption (OPA) and TPA spectra of **1a**$_2$ was analyzed based on *ab initio* quantum chemical calculations. Geometry optimization for the monomer **1a** was performed at the UB3LYP/6-31G* level under the constraint of D_{3h} symmetry, resulting in the structure shown in Figure III.1.2(a). The anti-type π-dimer models **1a**$_2$ with different d (2.8 Å ≤ d ≤ 6.0 Å) were constructed, as illustrated in Figure III.1.2(b), with each monomer geometry kept fixed.

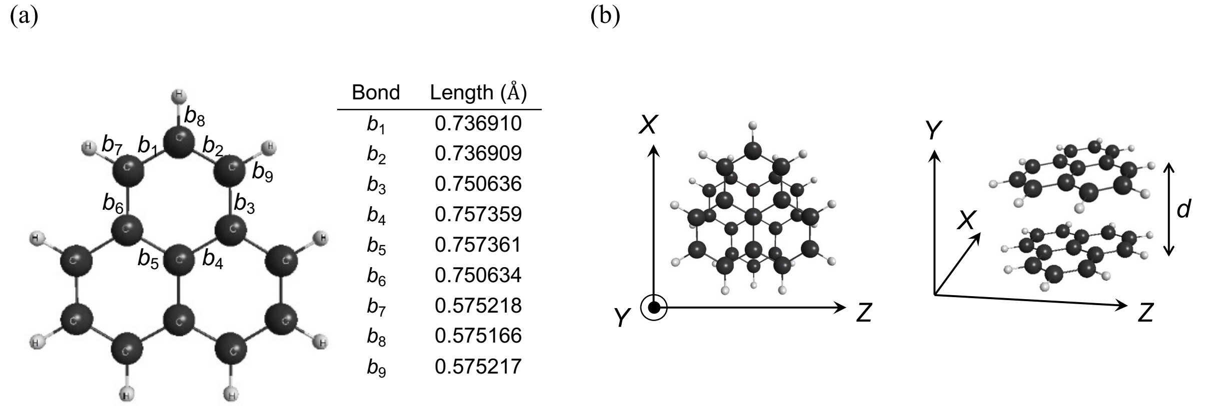

Bond	Length (Å)
b_1	0.736910
b_2	0.736909
b_3	0.750636
b_4	0.757359
b_5	0.757361
b_6	0.750634
b_7	0.575218
b_8	0.575166
b_9	0.575217

Figure III.1.2. Structures of (a) phenalenyl monomer **1a** optimized by UB3LYP/6-31G* level and (b) anti-type π-dimer model **1a**$_2$.

1.2.2. Quantum chemical calculations for the excitation energies and properties

Consequently, the dimer systems belong to C_{2h} symmetry regardless of d. For a given d, y was evaluated at the spin-projected (P)UHF/6-31G* level based on the following Yamaguchi's formula[22,23]:

$$y = 1 - \frac{2T}{1 + T^2} \tag{III.1.2}$$

$$T = \frac{n_{\mathrm{HONO}} - n_{\mathrm{LUNO}}}{2} \tag{III.1.3}$$

Here, n_{HONO} and n_{LUNO} are the occupation numbers of the highest occupied and lowest unoccupied natural orbitals (HONO and LUNO) derived from the UHF solutions. These calculations were performed using the Gaussian 09 program package[48].

The extended (X)MC-QDPT2 method[46,49], implemented in the GAMESS-US program package[50], was employed in this study to calculate the excitation energies and transition dipole moments of 1a2, despite reports indicating that (multi-reference) second-order perturbation theory methods may overestimate the binding energy of PLY π-dimers in the S_0 state[42].

To express the open-shell nature in the S_0 state of diradical systems, the two-electron and two-orbital complete active space [i.e., CAS(2,2)] is the minimal choice of the active space, which is consistent with the VBCI method within the two-site model developed by Nakano et al[14,20]. Expanding the active space is necessary to simulate the spectral shapes of OPA and TPA spectra over a wide range of wavelengths. However, the full π-valence space for **1a₂** is CAS(26,26), which is challenging to treat. State-averaged (SA-)CASSCF(10,10) calculations with the 6-31G* basis set were performed to solve for the twenty lowest singlet states. The 6-31G* basis set, without diffuse functions, is expected to provide sufficient accuracy in describing the vertical excitation energies of π-dimers of aromatic molecules when combined with MC-QDPT[47]. As the GMC-QDPT routine in GAMESS-US allows specification of up to three irreducible representations, calculations were limited to the A_g, B_u, and A_u states, which are essential for describing the OPA and TPA spectra. Excitation energies were evaluated at the XMC-QDPT2 level using an intruder state avoidance parameter of 0.02. Transition dipole moments between states were determined using the eigenvectors of the XMC-QDPT2 effective Hamiltonian.

1.2.3. Spectral simulations

The OPA cross-section, $\sigma^{(1)}(\omega)$, was evaluated by the following equation[51]:

$$\sigma^{(1)}(\omega) = \frac{4\pi^2\omega}{cn\hbar}\langle|\boldsymbol{\mu}_{fg}|^2\rangle\, g(\omega) \qquad (\mathrm{III}.1.4)$$

Here, c is the speed of light in vacuum, ω is the angular frequency of the incident light, n is the refractive index of the medium (set to 1.0 in this study). $\boldsymbol{\mu}_{fg}$ is the transition dipole moment between the states g and f. $\langle\cdots\rangle$ means the orientational average, i.e., $\langle|\boldsymbol{\mu}_{fg}|^2\rangle = \left\{(\mu_{fg}^X)^2 + (\mu_{fg}^Y)^2 + (\mu_{fg}^Z)^2\right\}/3$ where μ_{fg}^{α} represents the α-axis component of the transition dipole moment $\boldsymbol{\mu}_{fg}$. The following Lorentzian function was used for the normalized shape function $g(\omega)$:

$$g(\omega) = \frac{1}{\pi}\frac{\Gamma_{fg}}{(\omega_{fg}-\omega)^2 + {\Gamma_{fg}}^2} \qquad (\mathrm{III}.1.5)$$

where $E_{fg} = \hbar\omega_{fg}$ and Γ_{fg} is the damping parameter. This study employed $\hbar\Gamma$ = 0.1 eV for all the damping parameters.

The TPA cross-section, $\sigma^{(2)}(\omega)$, was evaluated by the following equation[51,52]:

$$\sigma^{(2)}(\omega) = \frac{4\pi^3\omega^2}{c^2n^2}\langle\left|\boldsymbol{M}_{fg}^{(2)}\right|^2\rangle\, g(2\omega) \qquad (\mathrm{III}.1.6)$$

Here, $\boldsymbol{M}_{fg}^{(2)}$ is the two-photon transition matrix element tensor with each component expressed as:

$$M_{fg,\alpha\beta}^{(2)} = \frac{1}{\hbar}\sum_k\left[\frac{\mu_{fk}^{\alpha}\mu_{kg}^{\beta}}{\omega_{kg}-\omega} + \frac{\mu_{fk}^{\beta}\mu_{kg}^{\alpha}}{\omega_{kg}-\omega}\right](\alpha,\beta = X,Y,Z) \qquad (\mathrm{III}.1.7)$$

The orientational average, $\langle|\boldsymbol{M}^{(2)}{}_{fg}|^2\rangle$, was calculated assuming linearly polarized incident light[51,52]. For the actual calculation, we replaced ω_{kg} in the denominator with $\omega_{kg} - i\Gamma_{kg}$. The Lorentzian function was again used for the normalized shape function $g(2\omega)$:

$$g(2\omega) = \frac{1}{\pi}\frac{\Gamma_{fg}}{(\omega_{fg}-2\omega)^2 + {\Gamma_{fg}}^2} \qquad (\mathrm{III}.1.8)$$

1.3. Results and Discussion

*1.3.1. Correlation between stacking distance (d) and diradical characters (y) for **1a₂***

Figure III.1.3 shows the calculation results of *y* at the PUHF/6-31G* level as a function of *d* for **1a**$_2$. The π-dimer **1a**$_2$ exhibited $y = 0.49$ (an intermediate open-shell nature) at $d = 3.0$ Å and $y = 1.00$ (an almost fully open shell nature) at $d = 6.0$ Å. In other words, the former situation corresponds to an intermediate covalent-bonded π-dimer, whereas the latter can be regarded as non-interacting monomers. Therefore, a comparison the OPA and TPA spectra was conducted for the models with $d = 3.0$ Å and 6.0 Å.

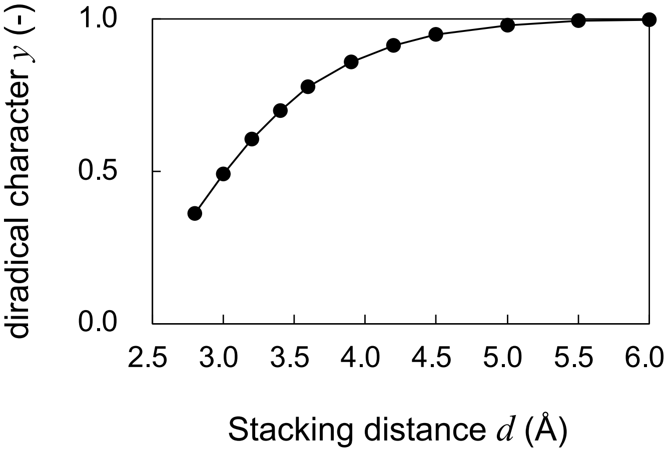

Figure II.1.3. Diradical character (*y*) as a function of the stacking distance (*d*) for the phenalenyl dimer model **1a**$_2$ calculated at the PUHF/6-31G* level.

*1.3.2. Comparison of OPA and TPA spectra between the **1a₂** models with d = 3.0 Å and d = 6.0 Å*

Figure III.1.4 presents the simulated OPA and TPA spectra, $\sigma^{(1)}(\omega)$ and $\sigma^{(2)}(\omega)$, for **1a**$_2$ with $d = 3.0$ Å and $d = 6.0$ Å. Each OPA spectrum was normalized to the peak intensity observed at approximately 5.1 eV for **1a**$_2$ with $d = 6.0$ Å. Additionally, the *X*-, *Y*-, and *Z*-axis components of OPA and TPA spectra, $\sigma^{(1),\alpha}(\omega)$ and $\sigma^{(2),\alpha\alpha}(\omega)$ ($\alpha = X, Y, Z$) are plotted to provide a detailed analysis of the directional contributions. For the molecular coordinate system employed in this study (see Figure III.1.2(b)), the *X*-, *Z*-axes and *Y*-axis directions correspond to the in-plane and stacking directions, respectively. For the OPA spectra, $\sigma^{(1)}(\omega) = \sigma^{(1),X}(\omega) + \sigma^{(1),Y}(\omega) + \sigma^{(1),Z}(\omega)$ is satisfied. However, the off-diagonal terms, like $M^{(2)}_{fg,XY}$ and $M^{(2)}_{fg,YX}$, contribute to the orientational averaged TPA spectra, $\sigma^{(2)}(\omega)$[52,53].

The discussion begins with the results of OPA spectra. As shown in Figure III.1.4(a) and (b), a peak is observed at approximately 5.1 eV for the model with $d = 6.0$ Å. This peak is characterized by significant contributions from the *X*-axis and *Z*-axis (in-plane) components, as the ($\sigma^{(1),X}(\omega)$ and $\sigma^{(1),Z}(\omega)$ components nearly overlap at this energy. These findings suggest that the peak originates from a local intramolecular π-π* transition within each monomer **1a**. For comparison, excited-state calculations for **1a** were performed at the time-dependent UCAM-B3LYP level (Table III.1.A1), yielding a first OPA peak at approximately 4.2 eV. Additionally, the SA-CASSCF(5,5) + XMC-QDPT2 calculations for **1a** were conducted to simulate the OPA and TPA spectra (Figure III.1.A4), predicting the first OPA peak position at approximately 3 eV. These results indicate that the excitation energy for the first OPA peak of **1a**$_2$ with $d = 6.0$ Å may be overestimated to some extent.

The OPA spectrum for **1a**$_2$ with $d = 6.0$ Å exhibited two peaks at ~2.47 eV (~502nm) and ~3.75 eV (~330nm). The higher energy peak was characterized by significant contributions from the *X*- and *Z*-axis (in-plane) components ($\sigma^{(1),X}(\omega)$ and $\sigma^{(1),Z}(\omega)$ components were overlapped almost completely at the peak). In contrast, the lower energy peak was primarily described by the *Y*-axis (stacking) component, $\sigma^{(1),Y}(\omega)$. These results suggest that the second OPA peak at ~3.75 eV originates from a local intramolecular π-π∗ transition, while the first OPA peak at ~2.47 eV arises from covalent-like intermolecular interactions.

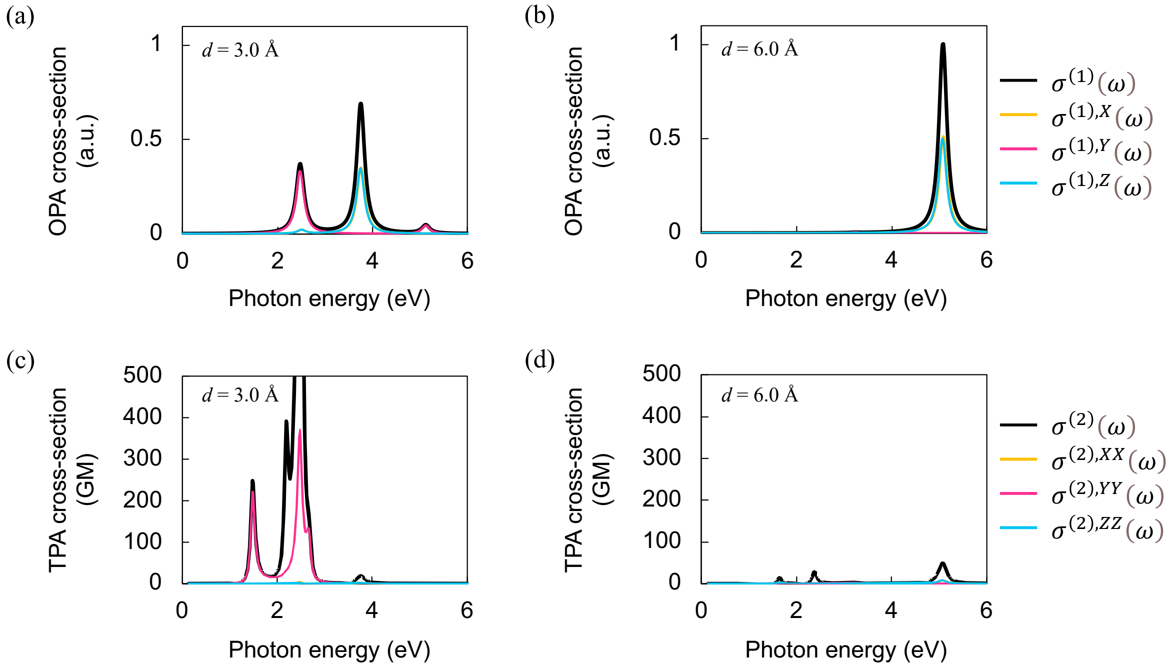

Figure III.1.4. Simulated OPA spectra of **1a**$_2$ with (a) $d = 3.0$ Å and (b) $d = 6.0$ Å and the TPA spectra of **1a**$_2$ with (c) $d = 3.0$ Å and (d) $d = 6.0$ Å. Spectra for the orientationally averaged $\sigma^{(1)}(\omega)$ and $\sigma^{(2)}(\omega)$ as well as their *X*-, *Y*-, and *Z*-axis direction components, $\sigma^{(1),\alpha}(\omega)$ and $\sigma^{(2),\alpha\alpha}(\omega)$ ($\alpha = X, Y, Z$), were presented.

The discussion now turns to the results of TPA spectra. For **1a**$_2$ with $d = 6.0$ Å, three peaks were observed at ~1.6 eV, ~2.4 eV, and ~5.1 eV (Figure III.1.4(d)), although their intensities were relatively weak. In contrast, **1a**$_2$ with $d = 3.0$ Å exhibited strong TPA bands at ~1.5 eV, ~2.2 eV, and ~2.5 eV (Figure III.1.4(c)). The higher energy TPA peaks for **1a**$_2$ with $d = 3.0$ Å overlapped substantially with the first OPA band. Such overlap leads to enhanced $\sigma^{(2)}(\omega)$ values, as both one-photon and two-photon resonance conditions are nearly satisfied[54,55]. It is called the resonance enhancement effect (for details, see Figure 10 and its description in the section 6 of the General Introduction). This phenomenon has been theoretically predicted, though experimental determination of $\sigma^{(2)}(\omega)$ values in the vicinity of OPA bands remains challenging. These TPA bands were primarily attributed to the *Y*-axis (stacking) direction component, $\sigma^{(2),YY}(\omega)$. However, the $\sigma^{(2),YY}(\omega)$ values around 2.2 eV were smaller than the total $\sigma^{(2)}(\omega)$, indicating significant contributions from off-diagonal terms to the second peak.

To analyze the spectral shapes of $\sigma^{(2)}(\omega)$, a comparison was conducted between the calculated excitation energies and transition dipole moments for **1a$_2$** with *d* = 3.0 Å and *d* = 6.0 Å. Figure III.1.5 and Table III.1.1 present the excitation energies and transition dipole moments of the excited states contributing to the first and second OPA and TPA peaks. Hereafter, the one-photon allowed excited states corresponding to the first and second OPA peaks are referred to as the **OPA1**, **OPA2**, and **OPA3** states. For **1a$_2$** with *d* = 6.0 Å, the excitation energies of the **OPA1**, **OPA2**, and **OPA3** states were calculated to be 3.23 eV, 5.06 eV, and 5.08 eV, respectively, with the **OPA2** and **OPA3** states were nearly degenerated. The transition dipole moment vectors for the **S$_0$-OPA2** and **S$_0$-OPA3** transitions were found to align predominantly with the *X*- and *Z*-axis (in-plane) directions, possessing magnitudes of approximately 5 D. In contrast, the transition dipole moment vector for the **S$_0$-OPA1** transition was oriented along the *Y*-axis (stacking) direction, but its magnitude was an order of magnitude smaller than those of the **S$_0$-OPA2** and **S$_0$-OPA3** transitions. Consequently, no distinct peak was observed around 3.23 eV in the OPA spectrum.

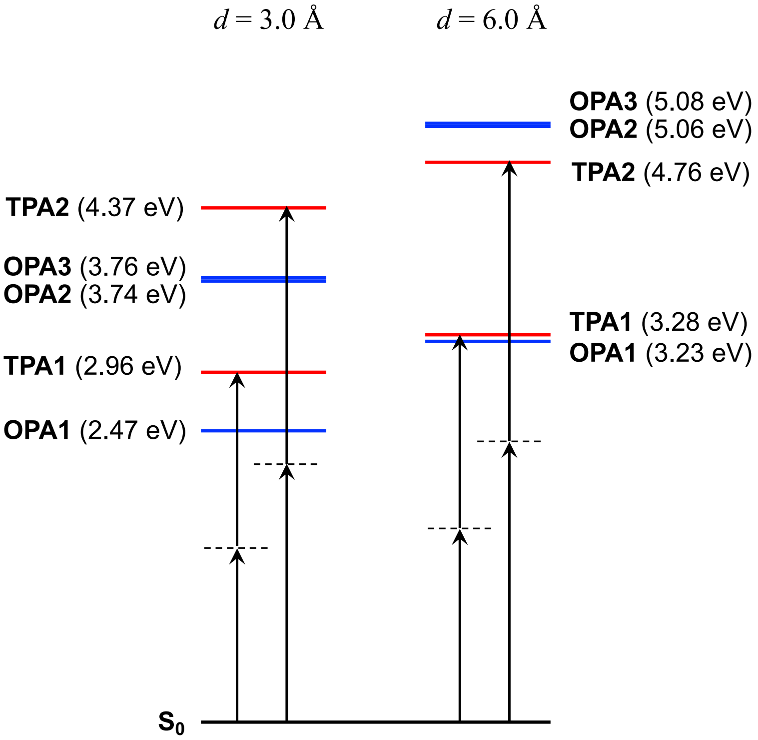

Figure III.1.5. Calculated excitation energies of the excited states (**OPA1-3** and **TPA1-3**) contributing to the OPA and TPA peaks for **1a$_2$** with *d* = 3.0 Å and *d* = 6.0 Å. Two upward arrows and a dashed line between them indicate the virtual state for the two-photon transition to the TPA target state.

Table III.1.1. Magnitudes of the *X*-, *Y*-, and *Z*-axis direction components of transition dipole moments [D] for **1a$_2$** with (a) $d = 3.0$ and (b) $d = 6.0$ Å.

(a) $d = 3.0$ Å

	$\lvert\mu_X\rvert$	$\lvert\mu_Y\rvert$	$\lvert\mu_Z\rvert$
S_0-OPA1	0.058	5.708	0.000
S_0-OPA2	0.000	0.000	4.736
S_0-OPA3	4.741	0.015	0.000
OPA1-TPA1	0.029	12.119	0.000
OPA1-TPA2	3.592	0.156	0.000
OPA1-TPA3	0.260	0.594	0.000
OPA2-TPA1	0.000	0.000	2.208
OPA2-TPA2	0.000	0.000	0.056
OPA2-TPA3	0.000	0.000	0.583
OPA3-TPA1	2.198	0.000	0.000
OPA3-TPA2	0.037	3.312	0.000
OPA3-TPA3	0.577	0.427	0.000

(b) $d = 6.0$ Å

	$\lvert\mu_X\rvert$	$\lvert\mu_Y\rvert$	$\lvert\mu_Z\rvert$
S_0-OPA1	0.034	0.353	0.000
S_0-OPA2	0.000	0.000	4.903
S_0-OPA3	4.944	0.040	0.000
OPA1-TPA1	0.013	27.777	0.000
OPA1-TPA2	6.210	0.231	0.000
OPA2-TPA1	0.000	0.000	5.432
OPA2-TPA2	0.000	0.000	0.165
OPA3-TPA1	5.441	0.057	0.000
OPA3-TPA2	0.064	13.679	0.000

For the **1a$_2$** model with $d = 3.0$ Å, the transition dipole moment vector for the **S_0-OPA2** and **S_0-OPA3** transitions were predominantly aligned with the *X*- and *Z*-axis (in-plane) directions exhibiting magnitudes of ~5 D, similar to the case of **1a$_2$** with $d = 6.0$ Å. Consequently, the second OPA peak in this model corresponds to the OPA peak observed at ~5.1 eV in the $d = 6.0$ Å model. However, the excitation energies for the **OPA2** and **OPA3** states decreased to 3.74 eV and 3.76 eV, respectively, resulting in a red-shift of the peak position. In contrast, the transition dipole moment vector for the **S_0-OPA1** transition in the $d = 3.0$ Å model was primarily oriented along the *Y*-axis (stacking) direction, with a magnitude of approximately 5D. This differs from the situation in the $d = 6.0$ Å model, where the **S_0-OPA1** transition exhibited a much smaller magnitude. The first OPA peak, observed at ~2.47 eV in the $d = 3.0$ Å model, originated from this **S_0-OPA1** transition.

To understand the trends in the TPA spectra, it is essential to examine the balance between $\boldsymbol{\mu}_{gk}$, $\boldsymbol{\mu}_{kf}$, and $\left|E_k - E_f/2\right|$. The two-photon allowed A$_g$ states corresponding to the first and second TPA peaks are denoted as the **TPA1** and **TPA2** states. For **1a$_2$** with $d = 6.0$ Å, the excitation energies of the **TPA1** and **TPA2** states were 3.28 eV and 4.76 eV, respectively. Weak TPA peaks were observed at ~1.6 eV and ~2.4 eV, corresponding to half of these excitation energies. The transition dipole moment vectors for the **S_0-OPA2-TPA1** and **S_0-OPA3-TPA1** transitions were almost parallel to the *Z*- and *X*-axis directions, respectively, with magnitudes of ~5 D. Consequently, the transition paths **S_0-OPA2-TPA1** and **S_0-OPA3-TPA1** can contribute to the TPA peak at ~1.6 eV. However, $\left|E_k - E_f/2\right|$ was large in this case (> 3 eV), resulting in a reduced peak intensity due to the large denominator in Eq. (III.1.1). Similarly, although the transition dipole moment for the **S_0-OPA3-TPA2** transition exhibited a considerable magnitude (~14 D), the transition path **S_0-OPA2-TPA2** contributed weakly to the TPA peak at ~2.4 eV because of the large $\left|E_k - E_f/2\right|$ (> 3 eV).

The excitation energies of the **TPA1**, **TPA2**, and **TPA3** states for **1a$_2$** with $d = 3.0$ Å were 2.96 eV, 4.37 eV, and 4.96 eV, respectively. The positions of the first, second, and third TPA peaks at ~1.5 eV, ~2.2 eV, and ~2.5 eV correspond to half of these excitation energies. The intensities of these peaks were significantly enhanced compared to those observed in the model with $d = 6.0$ Å, although the shifts in their peak positions were minimal. The transition dipole moment vector for the **OPA1-TPA1** transition was almost parallel to the *Y*-axis (stacking) direction with a magnitude of approximately 12 D. Additionally, $\left|E_k - E_f/2\right|$ decreased to a small value (0.99 eV) when the **TPA1** state was the target state f. Consequently, the transition path **S$_0$-OPA1-TPA1** became predominant in the TPA peak at ~1.5 eV, where both $\boldsymbol{\mu}_{gk}$ and $\boldsymbol{\mu}_{kf}$ were oriented along the *Y*-axis (stacking) direction.

For the second TPA peak at ~2.2 eV, three possible transition paths were identified: **S$_0$-OPA1-TPA2**, **S$_0$-OPA2-TPA2**, and **S$_0$-OPA3-TPA2**. The corresponding values of $\left|E_k - E_f/2\right|$ for these transitions were 0.285 eV, 1.555 eV, and 1.575 eV, respectively. Therefore, the **S$_0$-OPA1-TPA2** transition predominantly contributed to the second TPA peak at ~2.2 eV. The transition dipole moment vector for the **OPA1-TPA2** transition was almost parallel to the *X*-axis (in-plane) direction, with a magnitude of approximately 3.5 D. As a result, $\boldsymbol{\mu}_{gk}$ and $\boldsymbol{\mu}_{kf}$ were nearly perpendicular to each other, indicating that the off-diagonal terms, $M^{(2)}_{fg,XY}$ and $M^{(2)}_{fg,YX}$, contributed to this peak. For the prominent third TPA peak at ~2.5 eV, the transition path **S$_0$-OPA1-TPA3** made the dominant contribution. The peak intensity was strong due to the extremely small denominator $\left|E_k - E_f/2\right| = 0.01$ eV. However, the magnitudes of $\boldsymbol{\mu}_{gk}$ and $\boldsymbol{\mu}_{kf}$ for this transition were not particularly large. Consequently, the **TPA1** and **TPA2** states were considered as the key target states.

To elucidate the origin of the *d*-dependence in the OPA and TPA spectra, a further analysis of the wavefunctions of these electronic states was performed. Table III.1.2 summarizes the major electron configurations in both the ground and excited states that contribute to the first and second OPA and TPA peaks. Figure III.1.6 presents the energy diagrams and spatial distributions of the frontier molecular orbitals (MOs) for **1a$_2$** with $d = 3.0$ Å and $d = 6.0$ Å, as obtained from the SA-CASSCF calculations (i.e., the effective orbital energies derived from the state-averaged density matrix). In each model, the HOMO and LUMO were constructed as linear combinations of the SOMOs of the individual monomers. The **S$_0$**, **OPA1**, and **TPA1** states were primarily characterized by the configurations within the CAS(2,2) space, suggesting that the results obtained using the VBCI method based on the two-site model could qualitatively explain the excitation properties between the **S$_0$**, **OPA1**, and **TPA1** states. In other words, the positions and intensities of the first OPA and TPA peaks can be discussed based on their y-dependent expressions derived from the VBCI approach[14,20].

In contrast, the **OPA2**/**OPA3** and **TPA2** states were described by excitation configurations involving HOMO-2, HOMO-3, LUMO+2, LUMO+3, and LUMO+4, indicating that a clear y-dependence cannot be expected for the optical transition processes via **OPA2**/**OPA3** and **TPA2**. Therefore, the focus is placed solely on the **S$_0$-OPA1-TPA1** transition path, which corresponds to the first TPA peak.

Table III.1.2. Configurations of the electronic states describing the OPA and TPA peaks for the **1a₂** models with (a) *d* = 3.0 Å and (b) *d* = 6.0 Å, derived from the eigenvectors of the XMC-QDPT effective Hamiltonian. H and L represent for HOMO and LUMO, respectively.

(a) *d* = 3.0 Å

State	Configuration	Weight [%]
S_0	Ground conf. H,H → L,L	79.5 11.0
OPA1	H → L	92.5
OPA2	H → L+2 H–1 → L	59.7 17.4
OPA3	H → L+3 H–2 → L	60.7 16.8
TPA1	Ground conf. H,H → L,L	11.4 77.2
TPA2	H–2,H → L,L	85.8

(b) *d* = 6.0 Å

State	Configuration	Weight [%]
S_0	Ground conf. H,H → L,L	44.7 47.2
OPA1	H → L	94.1
OPA2	H-3 → L H → L+4	42.8 42.4
OPA3	H → L+3 H–2 → L	46.0 39.4
TPA1	Ground conf. H,H → L,L	46.5 44.7
TPA2	H–2,H → L,L H,H → L,L+3	48.6 41.7

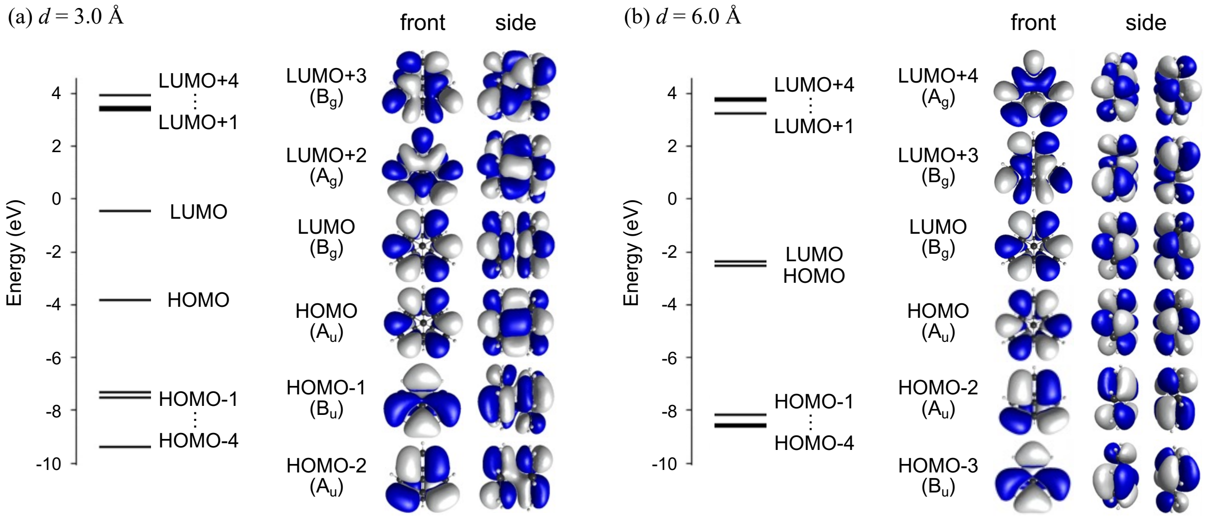

Figure III.1.6. Energies and spatial distributions of frontier MOs for the models **1a₂** with (a) *d* = 3.0 Å and (b) *d* = 6.0 Å.

Based on the weight of each configuration summarized in Table III.1.2, the wavefunctions of **S₀**, **OPA1**, and **TPA1** states can be expressed as follows[14,20]:

$$|\mathbf{S_0}\rangle = C_G|G\rangle + C_D|\mathrm{H,H \to L,L}\rangle + \cdots \tag{III.1.9}$$

$$|\mathbf{OPA1}\rangle = C_S|\mathrm{H \to L}\rangle + \cdots \tag{III.1.10}$$

$$|\mathbf{TPA1}\rangle = C_D'^{|\mathrm{H,H \to L,L}\rangle} + C_G'^{|G\rangle} + \cdots \tag{III.1.11}$$

Here, $|G\rangle$, $|\mathrm{H} \to \mathrm{L}\rangle$ and $|\mathrm{H}, \mathrm{H} \to \mathrm{L}, \mathrm{L}\rangle$ denote the ground configuration, HOMO-LUMO single and double excitation configurations, respectively. By applying the Slater-Condon rule[53], the transition dipole moment between these states can be approximately expressed as follows (for details, see Appendix):

$$\boldsymbol{\mu}_{\mathbf{S_0,OPA1}} \propto (C_G + C_D) C_S \boldsymbol{\mu}_{\mathrm{HL}} \tag{III.1.12}$$

$$\boldsymbol{\mu}_{\mathbf{OPA1,TPA1}} \propto (C_D' + C_G') C_S \boldsymbol{\mu}_{\mathrm{HL}} \tag{III.1.13}$$

where

$$\boldsymbol{\mu}_{\mathrm{HL}} = -e \int \boldsymbol{r} \rho_{\mathrm{HL}}(\boldsymbol{r}) d\boldsymbol{r} \tag{III.1.14}$$

$\rho_{\mathrm{HL}}(\boldsymbol{r}) \equiv \varphi_{\mathrm{H}}(\boldsymbol{r})\varphi_{\mathrm{L}}(\boldsymbol{r})$ is the one-electron transition density between the HOMO and LUMO at position $\boldsymbol{r}$[56]. Note that C_D has an opposite sign to C_G, whereas C_D' and C_G' have the same sign because of the configuration interaction between $|G\rangle$ and $\mathrm{H}, \mathrm{H} \to \mathrm{L}, \mathrm{L}\rangle$ (see Appendix[17–19]). In addition, $|C_G|^2 + |C_D|^2 \sim 1$, $|C_G'|^2 + |C_D'|^2 \sim 1$, and $|C_S| \sim 1$ for both the models[14,20]. Consequently, $|C_G + C_D| \sim 0$ for **1a₂** with *d* = 6.0 Å (see Table III.1.2), and the magnitude of the transition dipole moment for the **S₀-OPA1** transition became almost zero. In contrast, $|C_G + C_D| > 0$ for the model with *d* = 3.0 Å. The spatial distribution and phase of $\rho_{\mathrm{HL}}(\boldsymbol{r})$ determined the direction of the transition dipole moment. Positive (white) and negative (blue) regions of $\rho_{\mathrm{HL}}(\boldsymbol{r})$ are well-separated on each monomer **1a** (Figure III.1.7), resulting in the large transition dipole moment along the *Y*-axis (stacking) direction. Consequently, $|\mu_Y|$ for the transition **S₀-OPA1** increased with decreasing *d* because of an increase in $|C_G + C_D|$ from ~0.

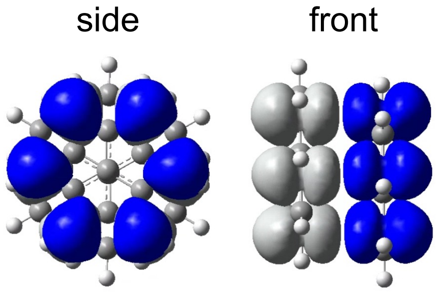

Figure III.1.7. One-electron transition density map for the HOMO and LUMO, $\rho_{\mathrm{HL}}(\boldsymbol{r}) = \varphi_{\mathrm{H}}(\boldsymbol{r})\varphi_{\mathrm{L}}(\boldsymbol{r})$, for the model with *d* = 3.0 Å. White and blue surfaces represent the positive and negative $\rho_{\mathrm{HL}}(\boldsymbol{r})$.

For the **OPA1-TPA1** transition [Eq. (III.1.13)], $|C_D' + C_G'|$ was expected almost unchanged regardless of *d* (see Figure III.1.A1). However, $|\boldsymbol{\mu}_{\mathrm{HL}}|$ depends on the distance between the positive and negative regions of $\rho_{\mathrm{HL}}(\boldsymbol{r})$, which is almost proportional to *d*. Thus, $|\mu_Y|$ of the model with *d* = 6.0 Å (~28 D) was almost twice as that of the model with *d* = 3.0 Å (~12 D).

1.3.3. d-dependence of the excitation properties

Figure III.1.8(a) presents the excitation energies of the **OPA1**, **OPA2**, **OPA3**, **TPA1**, and **TPA2** states as a function of *d*. Half of the excitation energies for the **TPA1** and **TPA2** states (corresponding to $E_f/2$) are also shown. The excitation energies of the **OPA1** and **TPA1** states decrease as *d* decreases from 6.0 Å, reaching a minimum around *d* ~ 3.5 Å, after which they increase. It should be noted that the experimental UV-vis absorption bands of **1b₂** were observed at ~610 nm (~2.0 eV) and ~340 nm (~3.6 eV) when *d* = 3.1-3.2 Å[20,54]. It has been reported that multi-reference second-order perturbation theory methods tend to overestimate the binding energy of PLY π-dimers in the S_0 state[42], which may result in an overestimated excitation energy for the first peak at ~2.5 eV. Despite this overestimation, it is expected that the condition $|E_{kg} - E_{fg}/2| \sim 0$ is nearly satisfied around *d* ~ 3.0 Å for the **TPA2** state as the final state f.

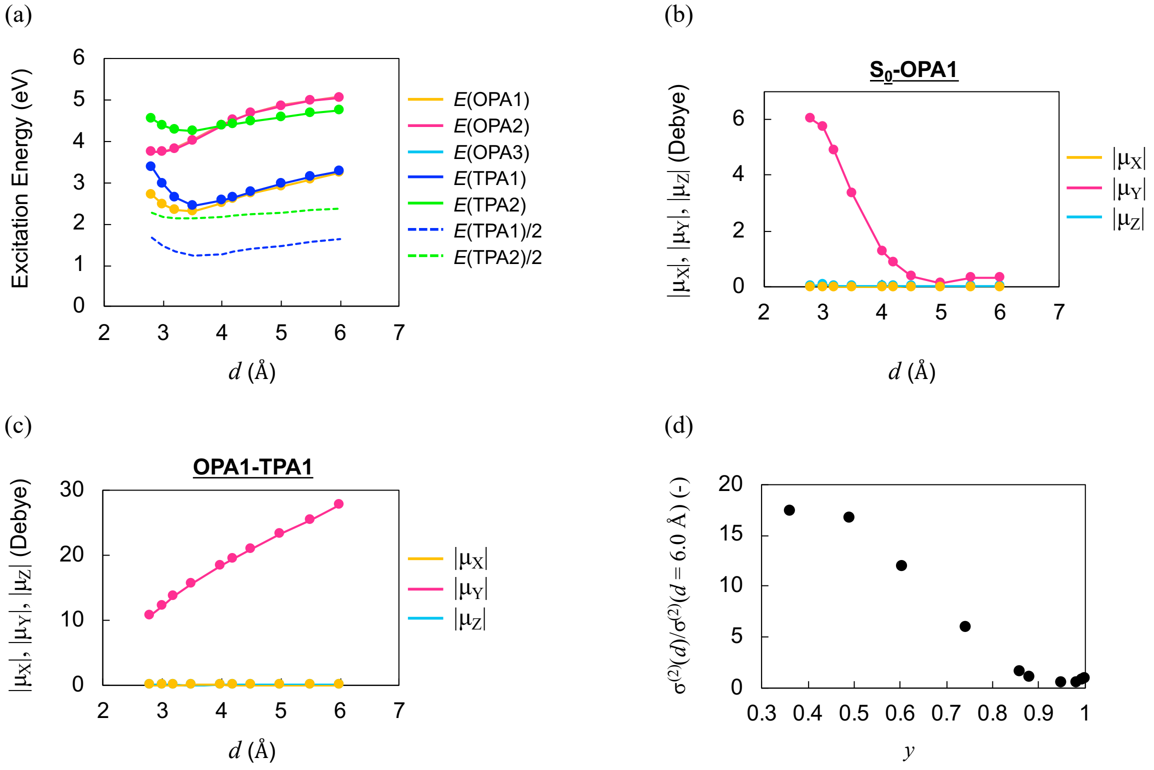

Figure III.1.8. *d*-dependence of (a) excitation energies, (b) $|\mu_X|$, $|\mu_Y|$ and $|\mu_Z|$ for the **S₀-OPA1** and (c) those for the **OPA1-TPA1** transition, and (d) *y*-dependence of the ratio of the increase $\sigma^{(2)}(d)/\sigma^{(2)}(d = 6.0\ \text{Å})$ for the first TPA peak targeted to the **TPA1** state.

Figure III.1.8(b) and (c) display the magnitudes of the transition dipole moments, $|\mu_X|$, $|\mu_Y|$ and $|\mu_Z|$, for the **S$_0$-OPA1** and **OPA1-TPA1** transitions. The magnitude of $|\mu_Y|$ for the **S$_0$-OPA1** transition increased with decreasing *d*, and $|\mu_Y|$ for the **OPA1-TPA1** transition decreased with decreasing *d*. These trends in the excitation energies and transition dipole moments were consistent with those obtained from the VBCI method based on the two-site model. Therefore, it is anticipated that the intensity of the first TPA peak exhibits a similar *y*-dependence as predicted by the VBCI method, as both an increase in $\boldsymbol{\mu}_{gk}{}^2\boldsymbol{\mu}_{kf}{}^2$ and a decrease in $\left|E_{kg} - E_{fg}/2\right|$ are expected in the intermediate *y* region[20]. These conditions are satisfied when $d \leq 3.4$ Å (i.e., $y < 0.7$, as shown in Figure III.1.3). Figure III.1.8(d) illustrates the *y*-dependence of the intensity enhancement ratio of the first TPA peak relative to that at $d = 6.0$ Å ($y = 1.00$). The peak intensity at $y = 0.49$ ($d = 3.0$ Å) was enhanced by approximately 15 times compared with that at $y = 1.00$ ($d = 6.0$ Å). The observed trend for the TPA peak was consistent with the prediction from the VBCI method based on the two-site model[20,44,57]. These results suggest that reducing *d* of **1a$_2$** can serve as an efficient strategy for modulating the TPA properties.

1.4. Conclusion

In summary, the effect of the stacking distance *d* in the PLY π-dimer models on the OPA and TPA properties was theoretically analyzed using the XMC-QDPT2 method. It was found that the first OPA and TPA peaks in the PLY π-dimer models correspond to electronic transitions along the stacking direction. The intensity of the first TPA peak was enhanced at small *d* (≤ 3.4 Å), where both an increase in $\boldsymbol{\mu}_{gk}{}^2\boldsymbol{\mu}_{kf}{}^2$ and a decrease in $\left|E_{kg} - E_{fg}/2\right|$ were observed. Additionally, it was found that the electronic states associated with the first TPA peak are described by configurations within the CAS(2,2) space, which aligns with the assumptions of the VBCI method based on the two-site model used to derive the *y*-dependent expressions for the TPA properties. A well-defined correlation between *y* and the first TPA peak is expected. However, such a correlation is not anticipated for the second (or higher) TPA peaks. In this chapter on the PLY π-dimer models, the first TPA peak was the most important, and the discussion focused consequently on the corresponding **S$_0$-OPA1-TPA1** transition pathway. The set of findings described in this chapter are expected to advance both theoretical and experimental analyses of the optical response properties of open-shell singlet systems with complex electronic structures and to contribute to the establishment of molecular design principles for novel open-shell NLO materials.

Appendix

Stacking distance (d-)dependence of the CI coefficients and transition dipole moments calculated with symmetry constraint for the excited states

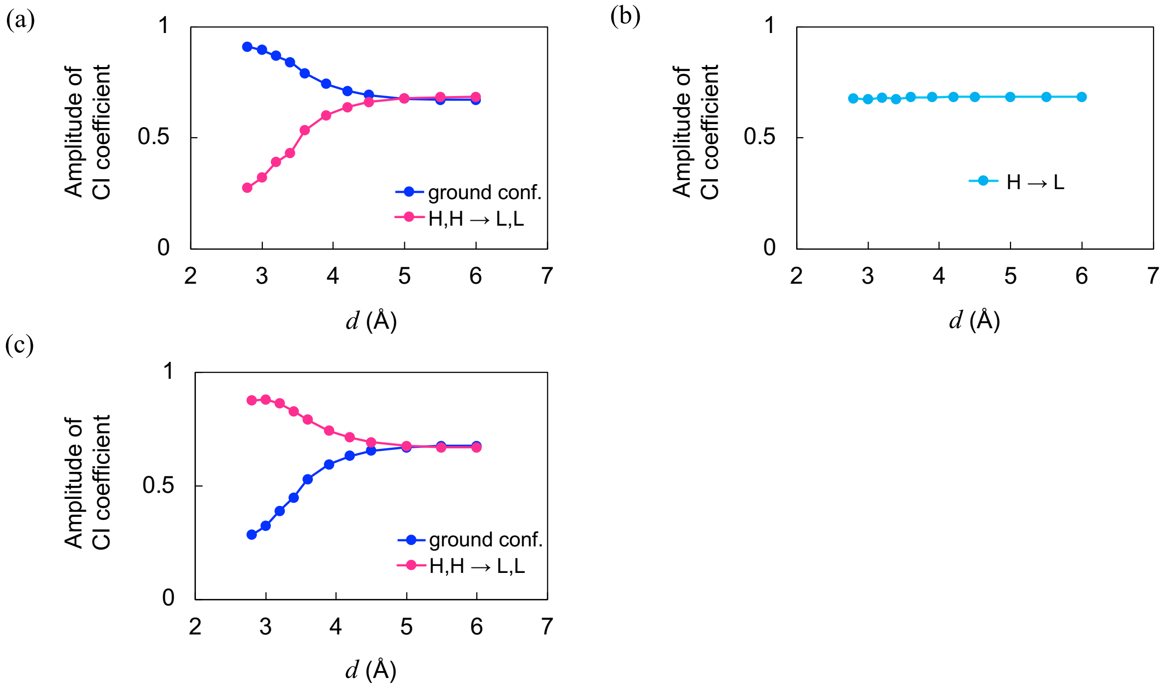

Figure III.1.A1. *d*-dependence of amplitude of CI coefficients for main configuration(s) in the (a) $\mathbf{S_0}$, (b) **OPA1**, (c) **TPA1** states for the phenalenyl dimer model $\mathbf{1a_2}$ with $d = 2.8 \sim 6.0$ Å with A_g, B_u, and A_u symmetries. H and L stand for HOMO and LUMO, respectively. Note that, the CI coefficients of the ground and H,H→L,L configurations in the $\mathbf{S_0}$ state have opposite sign whereas those in the **TPA1** state have the same sign.

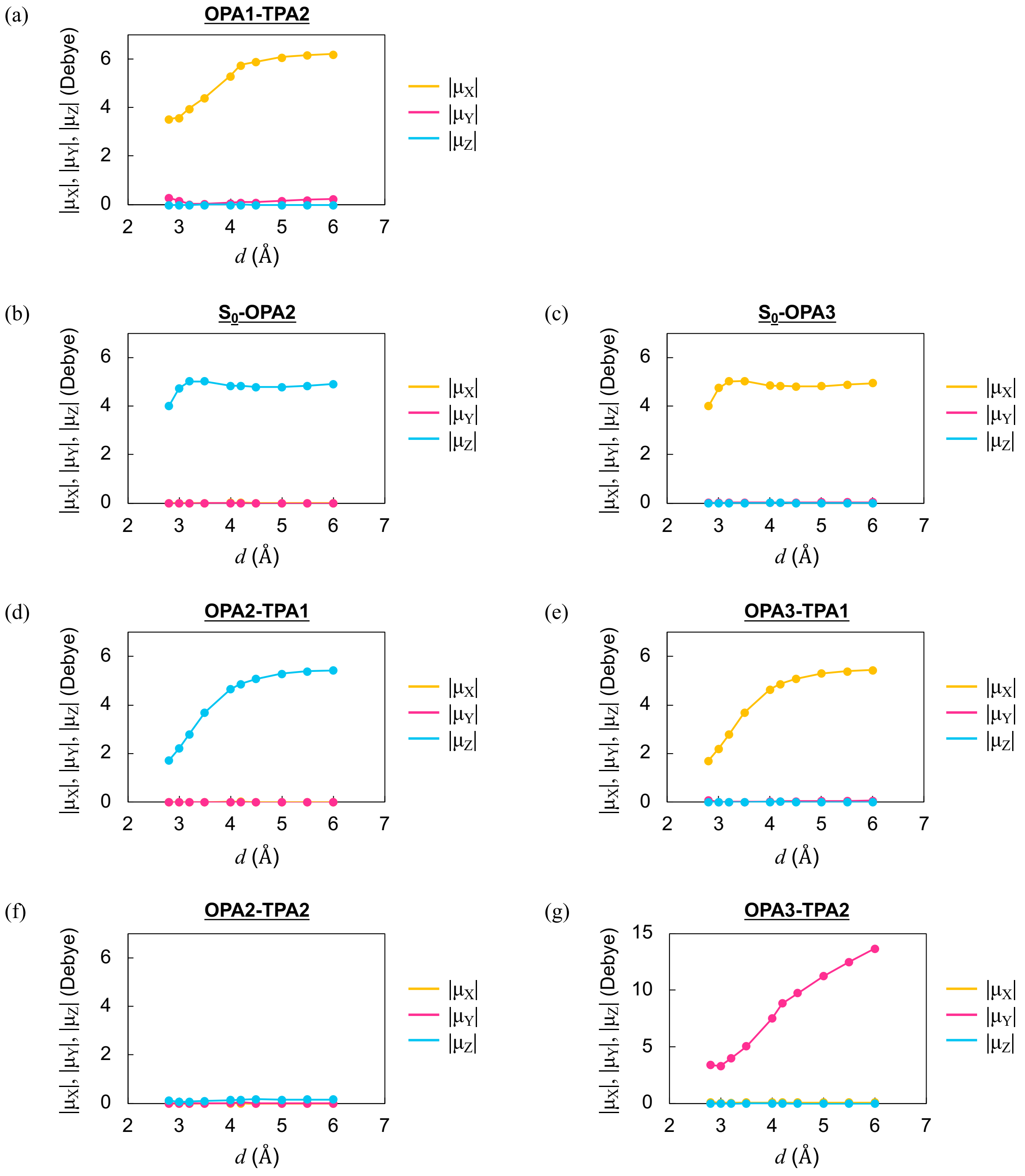

Figure III.1.A2. *d*-dependence of $|\mu_X|$, $|\mu_Y|$ and $|\mu_Z|$ for the (a) **OPA1-TPA2**, (b) **S$_0$-OPA2**, (c) **S$_0$-OPA3**, (d) **OPA2-TPA1**, (e) **OPA3-TPA1**, (f) **OPA2-TPA2**, and (g) **OPA3-TPA2** transitions for the phenalenyl dimer model **1a$_2$** with $d = 2.8 \sim 6.0$ Å with A$_g$, B$_u$, and A$_u$ symmetries.

Brief explanations for the relative signs of C_G, C_D C_G' *and* C_D'

For simplicity, the symmetric two-electron and two-site model is considered here. The configurations $|G\rangle$ and $|D\rangle$ are represented by the following Slater determinants:

$$|G\rangle = \frac{1}{\sqrt{2}}\psi_H(\boldsymbol{r}_1)\psi_H(\boldsymbol{r}_2)\{\alpha(1)\beta(2) - \alpha(2)\beta(1)\}$$

$$|D\rangle = \frac{1}{\sqrt{2}}\psi_L(\boldsymbol{r}_1)\psi_L(\boldsymbol{r}_2)\{\alpha(1)\beta(2) - \alpha(2)\beta(1)\}$$

Here, HOMO and LUMO are constructed by the linear combinations of (real) site-localized natural orbitals a and b (where a and b are defined such that $\int a(\boldsymbol{r})b(\boldsymbol{r})\,d\boldsymbol{r} = 0$, although the following discussion remains unchanged if the orbitals are defined with the non-zero overlap integral *S*):

$$\psi_H(\boldsymbol{r}) = \frac{1}{\sqrt{2}}\big(a(\boldsymbol{r}) + b(\boldsymbol{r})\big)$$

$$\psi_L(\boldsymbol{r}) = \frac{1}{\sqrt{2}}\big(a(\boldsymbol{r}) - b(\boldsymbol{r})\big)$$

Substituting them into the Slater determinants $|G\rangle$ and $|D\rangle$ gives the following formulae:

$$|G\rangle = \frac{1}{2\sqrt{2}}\big(a(\boldsymbol{r}_1)a(\boldsymbol{r}_2) + b(\boldsymbol{r}_1)b(\boldsymbol{r}_2) + a(\boldsymbol{r}_1)b(\boldsymbol{r}_2) + b(\boldsymbol{r}_1)a(\boldsymbol{r}_2)\big)\{\alpha(1)\beta(2) - \alpha(2)\beta(1)\}$$

$$|D\rangle = \frac{1}{2\sqrt{2}}\big(a(\boldsymbol{r}_1)a(\boldsymbol{r}_2) + b(\boldsymbol{r}_1)b(\boldsymbol{r}_2) - a(\boldsymbol{r}_1)b(\boldsymbol{r}_2) - b(\boldsymbol{r}_1)a(\boldsymbol{r}_2)\big)\{\alpha(1)\beta(2) - \alpha(2)\beta(1)\}$$

The first two terms correspond to the ionic configuration, in which both electrons occupy the same site (either *a* or *b*). The latter two terms correspond to the covalent (diradical) configuration, where the electrons occupy different sites (*a* and *b*).

$|G\rangle$ and $|D\rangle$ are the approximate wavefunctions for the ground and doubly excited states without considering the configuration interactions. Then, consider mixing of these configurations (note that $|\mathrm{H} \rightarrow \mathrm{L}\rangle = |S\rangle$ does not mix because it belongs to the different symmetry):

$$C_G|G\rangle + C_D|D\rangle$$

When C_G and C_D take opposite signs to each other, the ionic contribution is attenuated whereas the covalent (diradical) contribution is reinforced (see the signs of the ionic and covalent configurations in $|G\rangle$ and $|D\rangle$). As a result, this type of configuration mixing increases the covalent (diradical) contribution and reduces the (on-site) Coulomb repulsion energy in the ground state $|\boldsymbol{S_0}\rangle$. Thus, C_G

and C_D take opposite signs in $|\boldsymbol{S_0}\rangle$ due to the configuration interaction. The excited state $|\mathbf{TPA1}\rangle$ is orthogonal to $|\boldsymbol{S_0}\rangle$. Considering the configuration interaction (i.e., diagonalization of the CI Hamiltonian) within the vector space spanned by the bases $|G\rangle$ and $|D\rangle$ corresponds to the rotation of the basis vectors (unitary transformation) within the space, keeping the orthogonal relationship between them, and as illustrated in the following figure, C_G' and C_D' have the same sign.

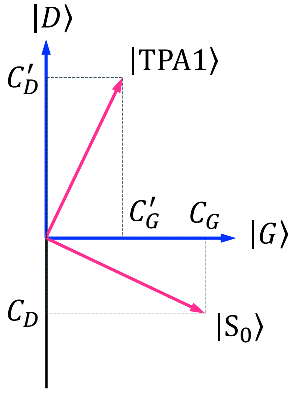

Figure III.1.A3. Illustration for understanding the configuration interaction between $|G\rangle$ and $|D\rangle$ in the ground and doubly excited state of symmetric diradical systems.

Brief explanations for Eqs. (III.1.12) and (III.1.13)

Based on the Eqs. (III.1.9)-(III.1.11), transition dipole moments between the **S₀** and **OPA1** states and between the **OPA1** and **TPA1** states are

$$\boldsymbol{\mu}_{\mathbf{S_0,OPA1}} = \langle \mathbf{S_0}|\hat{\boldsymbol{\mu}}|\mathbf{OPA1}\rangle = C_G C_S\langle G|\hat{\boldsymbol{\mu}}|\mathrm{H}\to\mathrm{L}\rangle + C_D C_S\langle \mathrm{H,H}\to\mathrm{L,L}|\hat{\boldsymbol{\mu}}|\mathrm{H}\to\mathrm{L}\rangle + \cdots$$

and

$$\boldsymbol{\mu}_{\mathbf{OPA1,TPA1}} = \langle \mathbf{OPA1}|\hat{\boldsymbol{\mu}}|\mathbf{TPA1}\rangle = C_D' C_S\langle \mathrm{H}\to\mathrm{L}|\hat{\boldsymbol{\mu}}|\mathrm{H,H}\to\mathrm{L,L}\rangle + C_G' C_S\langle \mathrm{H}\to\mathrm{L}|\hat{\boldsymbol{\mu}}|G\rangle + \cdots$$

Here, $\hat{\boldsymbol{\mu}} = -\sum_{i=1}^{N} e\hat{\boldsymbol{r}}_{\boldsymbol{i}} + \sum_{A=1}^{M} eZ_A\boldsymbol{R}_A$ is the dipole operator for the *N*-electron system ($\hat{\boldsymbol{r}}_{\boldsymbol{i}}$ is the position operator for the *i*-th electron. Z_A is the atomic number of nucleus *A* at $\boldsymbol{R}_A$, but the matrix element of the second term for the orthogonal wavefunctions will vanish). $\hat{\boldsymbol{\mu}}$ is expressed as the sum of one-electron operator. The Slater-Condon rules describe how integrals of one-electron operators over wavefunctions constructed as Slater determinants of orthonormal orbitals, like $\langle A|\sum_i \hat{o}_1(i)\,|B\rangle$, reduce to (the sum of) one-electron integrals. Applying the rules and then integrating the spin coordinates, the matrix element $\langle G|\hat{\boldsymbol{\mu}}|\mathrm{H}\to\mathrm{L}\rangle = \frac{1}{\sqrt{2}}\langle\cdots\varphi_{\mathrm{H}}\overline{\varphi_{\mathrm{H}}}|\hat{\boldsymbol{\mu}}|\cdots\varphi_{\mathrm{H}}\overline{\varphi_{\mathrm{L}}}\rangle + \frac{1}{\sqrt{2}}\langle\cdots\varphi_{\mathrm{H}}\overline{\varphi_{\mathrm{H}}}|\hat{\boldsymbol{\mu}}|\cdots\varphi_{\mathrm{L}}\overline{\varphi_{\mathrm{H}}}\rangle$ reduces to an one-electron integral of the HOMO and LUMO, $\sqrt{2}\times -e\int\varphi_{\mathrm{H}}(\boldsymbol{r})\boldsymbol{r}\varphi_{\mathrm{L}}(\boldsymbol{r})d\boldsymbol{r}$. The same rule can also be applied to the matrix element $\langle \mathrm{H}\to\mathrm{L}|\hat{\boldsymbol{\mu}}|\mathrm{H,H}\to\mathrm{L,L}\rangle = \frac{1}{\sqrt{2}}\langle\cdots\varphi_{\mathrm{H}}\overline{\varphi_{\mathrm{L}}}|\hat{\boldsymbol{\mu}}|\cdots\varphi_{\mathrm{L}}\overline{\varphi_{\mathrm{L}}}\rangle + \frac{1}{\sqrt{2}}\langle\cdots\varphi_{\mathrm{L}}\overline{\varphi_{\mathrm{H}}}|\hat{\boldsymbol{\mu}}|\cdots\varphi_{\mathrm{L}}\overline{\varphi_{\mathrm{L}}}\rangle$, leading to the same one-electron integral $\sqrt{2}\times -e\int\varphi_{\mathrm{H}}(\boldsymbol{r})\boldsymbol{r}\varphi_L(\boldsymbol{r})d\boldsymbol{r}$.

*Simulated OPA and TPA spectra of PLY monomer **1a***

State-averaged (SA-)CASSCF(5,5) calculations were conducted using 6-31G* basis set for the monomer **1a** to solved for the low-lying 20 singlet states within C1 point group (no symmetry) under the doublet spin multiplicity conditions. The excitation energies were subsequently evaluated at the XMC-QDPT2 level. However, direct comparison with the dimer calculations presented in Figure III.1.4 is not straightforward due to discrepancies in spin multiplicity, CAS space, and symmetry conditions.

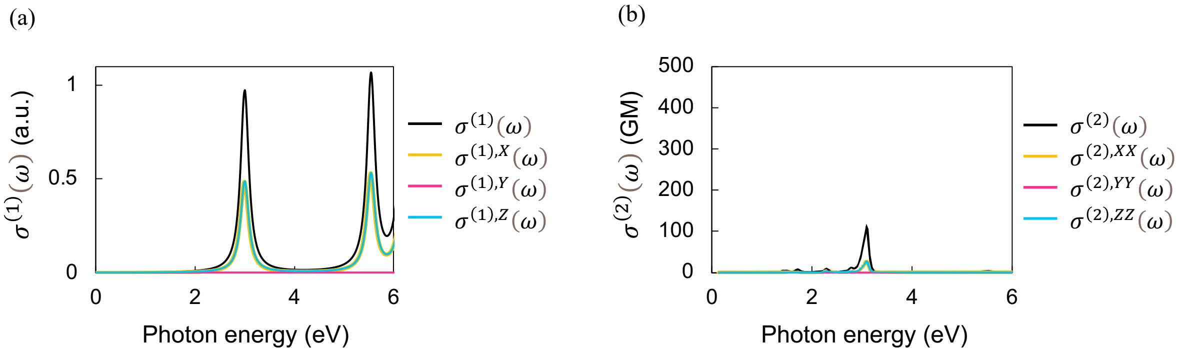

Figure III.1.A4. Simulated (a) OPA and (b) TPA spectra of **1a** for each orientationally averaged cross-sections ($\sigma^{(1)}(\omega)$ and $\sigma^{(2)}(\omega)$), *X*-axis (in-plane) direction components ($\sigma^{(1),X}(\omega)$ and $\sigma^{(2),XX}(\omega)$), *Y*-axis (stacking) direction components ($\sigma^{(1),Y}(\omega)$ and $\sigma^{(2),YY}(\omega)$), and *Z*-axis (stacking) direction components ($\sigma^{(1),Z}(\omega)$ and $\sigma^{(2),ZZ}(\omega)$). Each OPA spectrum was normalized to the peak intensity at ~3 eV.

Table III.1.A1. Excitation energies and transition dipole moments for the low-lying excited states of the monomer **1a** calculated at the time-dependent (TD-)UCAM-B3LYP/6-31G* level.

```
Excited State   1:   2.095-E       3.0169 eV   410.97 nm   f=0.0012   <S**2>=0.848
      44A -> 45A          0.65509
      43B -> 44B          0.73545

 Excited State   2:   2.095-E       3.0169 eV   410.97 nm   f=0.0012   <S**2>=0.848
      44A -> 46A          0.65509
      42B -> 44B          0.73545

 Excited State   3:   2.131-A2      3.3698 eV   367.93 nm   f=0.0000   <S**2>=0.886
      44A -> 47A          0.71233
      41B -> 44B         -0.67153

 Excited State   4:   2.183-A2      3.6183 eV   342.66 nm   f=0.0000   <S**2>=0.941
      41A -> 45A          0.10099
      42A -> 46A          0.10099
```

```
      44A -> 47A          0.66879
      41B -> 44B          0.70883
      42B -> 46B         -0.10838
      43B -> 47B         -0.10838

Excited State   5:   2.157-E      4.1563 eV   298.30 nm   f=0.2174   <S**2>=0.913
      43A -> 46A          0.17778
      44A -> 45A          0.71821
      42B -> 45B         -0.19595
      43B -> 44B         -0.63405

Excited State   6:   2.157-E      4.1563 eV   298.30 nm   f=0.2174   <S**2>=0.913
      43A -> 45A         -0.17778
      44A -> 46A          0.71821
      42B -> 44B         -0.63405
      43B -> 45B          0.19595
```

References

[1] A. S. Dvornikov, E. P. Walker and P. M. Rentzepis, *J. Phys. Chem. A*, **2009**, *113*, 13633–13644.

[2] A. Toriumi, S. Kawata and M. Gu, *Opt. Lett.*, **1998**, *23*, 1924–1926.

[3] B. H. Cumpston, S. P. Ananthavel, S. Barlow, D. L. Dyer, J. E. Ehrlich, L. L. Erskine, A. A. Heikal, S. M. Kuebler, I. S. Lee, D. Mccord-maughon, J. Qin, M. Rumi, X. Wu, S. R. Marder and J. W. Perry, *Nature*, **1999**, *398*, 51–54.

[4] S. Maruo, O. Nakamura and S. Kawata, **1997**, *22*, 132–134.

[5] W. Denk, J. H. Strickler and W. W. Webb, *Science (80-.).*, **1990**, *248*, 73–76.

[6] P. T. C. So, T. French, W. M. Yu, K. M. Berland and C. Y. Dong, *Bioimaging*, **1995**, *3*, 49–63.

[7] J. E. Ehrlich, X. L. Wu, I.-Y. S. Lee, Z.-Y. Hu, H. Röckel, S. R. Marder and J. W. Perry, *Opt. Lett.*, **1997**, *22*, 1843–1845.

[8] G. S. He, B. A. Reinhardt, J. C. Bhatt, A. G. Dillard, R. McKellar, C. Xu and P. N. Prasad, *Opt. Lett.*, **1995**, *20*, 1930.

[9] M. Albota, D. Beljonne, J. L. Brédas, J. E. Ehrlich, J. Y. Fu, A. A. Heikal, S. E. Hess, T. Kogej, M. D. Levin, S. R. Marder, D. McCord-Maughon, J. W. Perry, H. Röckel, M. Rumi, G. Subramaniam, W. W. Webb, X. L. Wu and C. Xu, *Science (80-.).*, **1998**, *281*, 1653–1656.

[10] B. A. Reinhardt, L. L. Brott, S. J. Clarson, A. G. Dillard, J. C. Bhatt, R. Kannan, L. Yuan, G. S. He and P. N. Prasad, *Chem. Mater.*, **1998**, *10*, 1863–1874.

[11] M. Pawlicki, H. A. Collins, R. G. Denning and H. L. Anderson, *Angew. Chemie - Int. Ed.*, **2009**, *48*, 3244–3266.

[12] F. Terenziani, C. Katan, E. Badaeva, S. Tretiak and M. Blanchara-Desce, *Enhanced two-photon absorption of organic chromophores: Theoretical and experimental assessments*, **2008**, vol. 20.

[13] M. Klausen and M. Blanchard-Desce, *J. Photochem. Photobiol. C Photochem. Rev.*, **2021**, *48*, 100423.

[14] M. Nakano, R. Kishi, S. Ohta, H. Takahashi, T. Kubo, K. Kamada, K. Ohta, E. Botek and B. Champagne, *Phys. Rev. Lett.*, **2007**, *99*, 033001.

[15] M. Nakano and B. Champagne, *J. Phys. Chem. Lett.*, **2015**, *6*, 3236–3256.

[16] M. Nakano and B. Champagne, *Wiley Interdiscip. Rev. Comput. Mol. Sci.*, **2016**, *6*, 198–210.

[17] M. Nakano, *Top. Curr. Chem.*, **2017**, *375*, 1–67.

[18] M. Nakano, *Chem. Rec.*, **2017**, *17*, 27–62.

[19] M. Nakano, R. Kishi, T. Nitta, T. Kubo, K. Nakasuji, K. Kamada, K. Ohta, B. Champagne, E. Botek and K. Yamaguchi, *J. Phys. Chem. A*, **2005**, *109*, 885–891.

[20] M. Nakano, T. Kubo, K. Kamada, K. Ohta, R. Kishi, S. Ohta, N. Nakagawa, H. Takahashi, S. I. Furukawa, Y. Morita, K. Nakasuji and K. Yamaguchi, *Chem. Phys. Lett.*, **2006**, *418*, 142–147.

[21] E. F. Hayes and A. K. Q. Siu, *J. Am. Chem. Soc.*, **1971**, *93*, 2090–2091.

[22] K. Yamaguchi, *Chem. Phys. Lett.*, **1975**, *33*, 330–335.

[23] K. Yamaguchi, in *Self-Consistent Field: Theory and Applications*, Elsevier, Amsterdam, The Netherlands, **1990**.

[24] D. H. Reid, *Q. Rev. Chem. Soc.*, **1965**, *19*, 274–302.

[25] I. Murata, in *Topics in Non-Benzenoid Aromatic Chemistry*, eds. T. Nozoe, R. Breslow, K. Hafner, S. Ito and I. Murata, John Wiley & Sons, Inc, New York, **1973**, vol. 1, pp. 159–190.

[26] T. Kubo, *Bull. Chem. Soc. Jpn.*, **2021**, *94*, 2235–2244.

[27] T. Kubo, A. Shimizu, M. Sakamoto, M. Uruichi, K. Yakushi, M. Nakano, D. Shiomi, K. Sato, T. Takui, Y. Morita and K. Nakasuji, *Angew. Chemie - Int. Ed.*, **2005**, *44*, 6564–6568.

[28] T. Kubo, A. Shimizu, M. Uruichi, K. Yakushi, M. Nakano, D. Shiomi, K. Sato, T. Takui, Y. Morita and K. Nakasuji, *Org. Lett.*, **2007**, *9*, 81–84.

[29] Y. Li, W. K. Heng, B. S. Lee, N. Aratani, J. L. Zafra, N. Bao, R. Lee, Y. M. Sung, Z. Sun, K. W. Huang, R. D. Webster, J. T. López Navarrete, D. Kim, A. Osuka, J. Casado, J. Ding and J. Wu, *J. Am. Chem. Soc.*, **2012**, *134*, 14913–14922.

[30] Z. Sun, S. Lee, K. H. Park, X. Zhu, W. Zhang, B. Zheng, P. Hu, Z. Zeng, S. Das, Y. Li, C. Chi, R. W. Li, K. W. Huang, J. Ding, D. Kim and J. Wu, *J. Am. Chem. Soc.*, **2013**, *135*, 18229–18236.

[31] Z. Sun and J. Wu, *Pure Appl. Chem.*, **2014**, *86*, 529–537.

[32] Z. Sun, Z. Zeng and J. Wu, *Acc. Chem. Res.*, **2014**, *47*, 2582–2591.

[33] Y. C. Hsieh, H. Y. Fang, Y. T. Chen, R. Yang, C. I. Yang, P. T. Chou, M. Y. Kuo and Y. T. Wu, *Angew. Chemie - Int. Ed.*, **2015**, *54*, 3069–3073.

[34] Y. Ni, S. Lee, M. Son, N. Aratani, M. Ishida, A. Samanta, H. Yamada, Y. T. Chang, H. Furuta, D. Kim and J. Wu, *Angew. Chemie - Int. Ed.*, **2016**, *55*, 2815–2819.

[35] P. Hu, S. Lee, K. H. Park, S. Das, T. S. Herng, T. P. Gonçalves, K. W. Huang, J. Ding, D. Kim and J. Wu, *J. Org. Chem.*, **2016**, *81*, 2911–2919.

[36] K. Goto, T. Kubo, K. Yamamoto, K. Nakasuji, K. Sato, D. Shiomi, T. Takui, M. Kubota and T. Kobayashi, *J. Am. Chem. Soc.*, **1999**, *121*, 1619–1620.

[37] S. Suzuki, Y. Morita, K. Fukui, K. Sato, D. Shiomi, T. Takui and K. Nakasuji, *J. Am. Chem. Soc.*, **2006**, *128*, 2530–2531.

[38] Z. Mou, K. Uchida, T. Kubo and M. Kertesz, *J. Am. Chem. Soc.*, **2014**, *136*, 18009–18022.

[39] M. Kertesz, *Chem. - A Eur. J.*, **2019**, *25*, 400–416.

[40] Y. Takano, T. Taniguchi, H. Isobe, T. Kubo, Y. Morita, K. Yamamoto, K. Nakasuji, T. Takui and K. Yamaguchi, *Chem. Phys. Lett.*, **2002**, *358*, 17–23.

[41] V. Zaitsev, S. V. Rosokha, M. Head-Gordon and J. K. Kochi, *J. Org. Chem.*, **2006**, *71*, 520–526.

[42] Z. H. Cui, H. Lischka, H. Z. Beneberu and M. Kertesz, *J. Am. Chem. Soc.*, **2014**, *136*, 5539–5542.

[43] Z. Tang, Z. Jiang, H. Chen, P. Su and W. Wu, *J. Chem. Phys.*, **2019**, *151*, 244106.

[44] K. Yoneda, M. Nakano, K. Fukuda, H. Matsui, S. Takamuku, Y. Hirosaki, T. Kubo, K. Kamada and B. Champagne, *Chem. - A Eur. J.*, **2014**, *20*, 11129–11136.

[45] K. D. Nanda and A. I. Krylov, *J. Chem. Phys.*, **2017**, *146*, 224103.

[46] H. Nakano, *J. Chem. Phys.*, **1993**, *99*, 7983–7992.

[47] S. Shirai, S. Iwata, T. Tani and S. Inagaki, *J. Phys. Chem. A*, **2011**, *115*, 7687–7699.

[48] M. J. Frisch, G. W. Trucks, H. B. Schlegel, G. E. Scuseria, M. A. Robb, J. R. Cheeseman, G. Scalmani, V. Barone, B. Mennucci, G. A. Petersson, H. Nakatsuji, M. Caricato, H. P. H. X. Li, A. F. Izmaylov, G. Z. J. Bloino, J. L. Sonnenberg, M. Hada, M. Ehara, K. Toyota, R. Fukuda, J. Hasegawa, M. Ishida, T. Nakajima, Y. Honda, O. Kitao, H. Nakai, T. Vreven, J. J. A. Montgomery, J. E. Peralta, F. Ogliaro, M. Bearpark, J. J. Heyd, E. Brothers, K. N. Kudin, V. N. Staroverov, R. Kobayashi, J. Normand, K. Raghavachari, A. Rendell, J. C. Burant, S. S. Iyengar, J. Tomasi, M. Cossi, N. Rega, J. M. Millam, M. Klene, J. E. Knox, J. B. Cross, V. Bakken, C. Adamo, J. Jaramillo, R. Gomperts, R. E. Stratmann, O. Yazyev, A. J. Austin, R. Cammi, C. Pomelli, J. W. Ochterski, R. L. Martin, K. Morokuma, V. G. Zakrzewski, G. A. Voth, P. Salvador, J. J. Dannenberg, S. Dapprich, A. D. Daniels, Ö. Farkas, J. B. Foresman, J. V. Ortiz, J. Cioslowski and D. J. Fox, *Gaussian 09. Rev. D.01*, Gaussian Inc., Wallingford, CT, **2009**.

[49] A. A. Granovsky, *J. Chem. Phys.*, **2011**, *134*, 214113.

[50] G. M. J. Barca, C. Bertoni, L. Carrington, D. Datta, N. De Silva, J. E. Deustua, D. G. Fedorov, J. R. Gour, A. O. Gunina, E. Guidez, T. Harville, S. Irle, J. Ivanic, K. Kowalski, S. S. Leang, H. Li, W. Li, J. J. Lutz, I. Magoulas, J. Mato, V. Mironov, H. Nakata, B. Q. Pham, P. Piecuch, D. Poole, S. R. Pruitt, A. P. Rendell, L. B. Roskop, K. Ruedenberg, T. Sattasathuchana, M. W. Schmidt, J. Shen, L. Slipchenko, M. Sosonkina, V. Sundriyal, A. Tiwari, J. L. Galvez Vallejo, B. Westheimer, M. Włoch, P. Xu, F. Zahariev and M. S. Gordon, *J. Chem. Phys.*, **2020**, *152*, 154102.

[51] K. Ohta, S. Yamada, K. Kamada, A. D. Slepkov, F. A. Hegmann, R. R. Tykwinski, L. D. Shirtcliff, M. M. Haley, P. Sałek, F. Gel'mukhanov and H. Ågren, *J. Phys. Chem. A*, **2011**, *115*, 105–117.

[52] M. T. P. Beerepoot, D. H. Friese, N. H. List, J. Kongsted and K. Ruud, *Phys. Chem. Chem. Phys.*, **2015**, *17*, 19306–19314.

[53] A. Szabo and N. L. Ostlund, *Modern Quantum Chemistry: IIntroduction to Advanced Electronic Structure Theory*, Dover Publication, Inc., New York, **1996**.

[54] K. Kamada, K. Ohta, T. Kubo, A. Shimizu, Y. Morita, K. Nakasuji, R. Kishi, S. Ohta, S. I. Furukawa, H. Takahashi and M. Nakano, *Angew. Chemie - Int. Ed.*, **2007**, *46*, 3544–3546.

[55] K. Kamada, K. Ohta, Y. Iwase and K. Kondo, *Chem. Phys. Lett.*, **2003**, *372*, 386–393.

[56] R. Kishi, M. Nakano, S. Yamada, K. Kamada, K. Ohta, T. Nitta and K. Yamaguchi, *Chem. Phys. Lett.*, **2004**, *393*, 437–441.

[57] M. Nakano, K. Yoneda, R. Kishi, H. Takahashi, T. Kubo, K. Kamada, K. Ohta, E. Botek and B. Champagne, *J. Chem. Phys.*, **2009**, *131*, 114316.

Chapter 2.

Two-Photon Absorption Properties of π-Stacked Multimer Models of Phenalenyl Radicals

The influence of the number of monomers (*N*) on the two-photon absorption (TPA) properties of π-stacked multimer models composed of phenalenyl radicals was investigated through theoretical analysis. Spectral simulations were performed for π-stacked *N*-mer models ($N = 2$, 4, and 6) with varying stacking distances (d_1) and alternation patterns (d_2/d_1). Excitation energies and transition dipole moments were calculated using extended multi-configurational quasi-degenerate second-order perturbation theory (XMC-QDPT2) based on complete active space self-consistent field (CASSCF) wavefunctions within the active space orbitals constructed from the singly occupied molecular orbitals (SOMOs) of the monomers. The TPA cross-section per dimer unit at the first peak, corresponding to the electronic transition along the stacking direction, was predicted to increase substantially as the d_2/d_1 ratio approached one, as d_1 decreased, and as *N* increased from 2 to 6. These trends closely align with the calculated results for static second hyperpolarizabilities (γ).

2.1. Introduction

In PART III, the investigation of the two-photon absorption (TPA) properties of open-shell one-dimensional (1D) π-aggregates systems composed of phenalenyl radicals (PLY), the smallest units of polycyclic aromatic hydrocarbons (PAHs) exhibiting open-shell characteristics, is presented in detail. An actual example of a synthesized 1D π-aggregates is a chain composed of TPFPPLYs (monomers functionalized with C_6F_5 groups at 2-, 5-, and 8- positions of PLYs)[1,2] illustrated in Figure 15(c). The 1D chain of TPFPPLYs was synthesized using a straightforward process: heating the σ-dimer of TPFPPLY to 572 K in a sealed, degassed tube, melting the material, and subsequently cooling it. The resulting dark-purple crystals were analyzed by X-ray crystallography and identified as an eclipsed-type π-stacked aggregates with a stacking distance (d) of approximately 3.50 Å. Previous studies on the π-dimer of PLY derivatives have demonstrated that the d can be modulated by the choice of substituents, highlighting variations in structural configurations[1–5]. While the crystalline π-stacked systems represent a promising subject for exploration, fewer examples of its synthesis and characterization exist compared to the well-studied π-dimer systems. Nevertheless, the potential applications of this crystalline systems in advanced material science continue to be an area of significant interest.

Theoretical investigations of open-shell 1D π-aggregates have advanced significantly, building on the foundational studies by Yoneda et al.[6], Salustro et al.[7], and Matsui et al.[8,9] Subsequent investigations by the authors demonstrated a substantial increase in the static γ value per monomer within the 1D chain of PLYs as the number of layers increased, establishing an evidence for the anticipated exceptional NLO properties (refer to PART II)[10]. Regarding TPA properties, the close proximity of two PLYs causes pancake bonding, which induces large electronic transitions along the molecular stacking direction. As detailed in the previous chapter, PLY π-dimers in such a state exhibit intermediate diradical character (y), leading to a pronounced increase in the cross-section of the first TPA peak within this region[11] (here, y is based on the valence-bond configuration interaction (VBCI) method within the simplest symmetric two-site diradical model[12,13]). Furthermore, the y-dependence of the TPA properties closely aligns with trends observed in static γ, suggesting that static γ may serve as a useful indicator for designing systems with enhanced TPA properties. The next critical step involves determining whether an increase in the number of monomer in the π-aggregates can effectively enhance TPA properties and identifying the structures of the systems that maximize this enhancement.

In contrast, theoretical investigations into TPA properties of open-shell π-aggregates remain scarce. A primary challenge lies in the accurate calculation of excitation energies and transition dipole moments between electronic states in open-shell singlet systems, owing to their inherently multiconfigurational character in the ground state. Moreover, the assignment and interpretation of spectral peaks in systems with complex interactions, such as π-aggregates, demand meticulous attention and a comprehensive accumulation of multifaceted analyses. The investigation of TPA properties, focusing on the effect of adding one additional pair of stacked PLY units (dimer), utilizing the y-based index proposed for describing the electronic structure of infinite 1D chains[10], provides a critical foundation for predicting the optical properties of multiradical systems.

2.2. Methods

2.2.1. Model systems

The effects of the number of monomers (N) on the TPA properties of π-stacked N-mer models consisting of **1a** with different primary stacking distances (**1a**$_N$; see Figure III.2.1) were investigated. Geometry optimization of monomer **1a** was performed at the UB3LYP/6-31G* level under the constraint of D_{3h} symmetry, consistent with previous studies (see Figure III.1.2(a) in this previous chapter)[6,10]. Anti-type π-stacked N-mer models ($N = 2$, 4, and 6) consisting of **1a** with different stacking distances d_1 (2.8 Å $\leq d_1 \leq$ 4.0 Å) were then constructed while maintaining each monomer geometry frozen. For tetramer ($N = 4$), the effects of stacking distance alternation between d_1 and d_2 were further examined by varying the ratio for SDA, d_2/d_1, from 1.0 to 2.0, as illustrated in Figure III.2.1(b). For simplicity, the N-mer model with the ratio d_2/d_1 is referred to as **1a**$_N$**(**$\boldsymbol{d_2/d_1}$**)**.

2.2.2. Quantum chemical calculations for the excitation energies and properties

The extended multi-configurational quasi-degenerate second-order perturbation theory (XMC-QDPT2) method[14,15] was applied to evaluate the excitation energies and transition dipole moments. Calculations were performed up to hexamer ($N = 6$) due to the high demands of computational resources in such calculations. However, the present study provides valuable information for experimental investigations on the TPA properties of open-shell molecular aggregates.

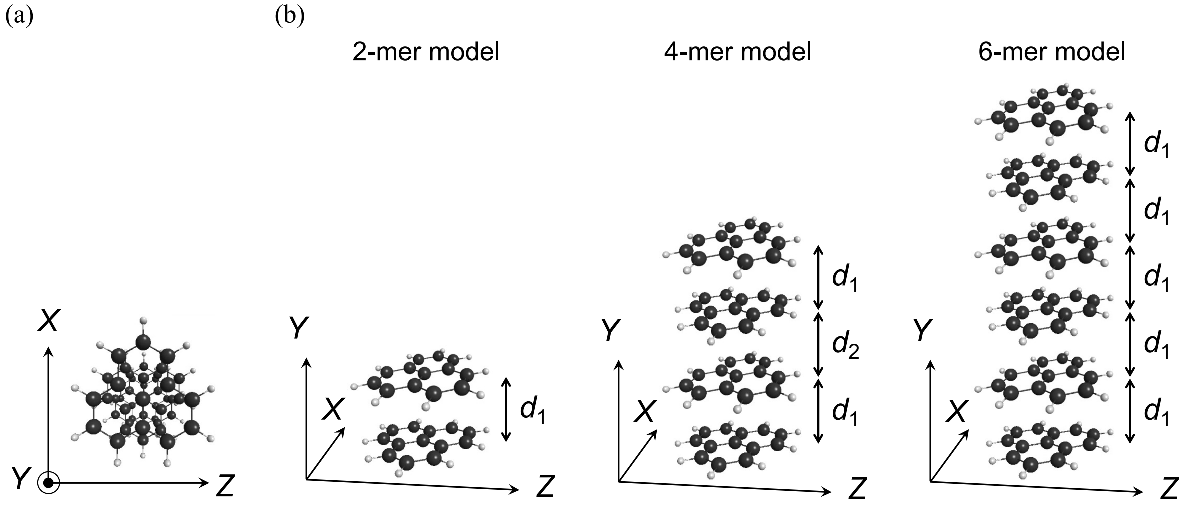

Figure III.2.1. (a) Top view of the molecular structure of **1a**$_4$ and (b) side views of anti-type dimer model **1a**$_2$, tetramer model **1a**$_4$**(**$\boldsymbol{d_2/d_1}$**)**, and hexamer model **1a**$_6$**(1.0)** ($d_2 = d_1$).

For a given N-mer system consisting of monoradicals ($N = 2m$; $m = 1, 2, \ldots$), $N/2$ diradical characters, y_i ($i = 0, 1, \ldots, N/2–1$; $1 \geq y_0 \geq y_1 \geq \ldots y_{N/2-1} \geq 0$) can be defined. The y_i values of each system were evaluated at the spin-projected (P)UHF/6-31G* level based on the following Yamaguchi's formula, which efficiently removes spin-contamination errors in the occupation numbers[16]:

$$y_i = 1 - \frac{2T_i}{1 + T_i^2}, \tag{III. 2.1}$$

$$T_i = \frac{n_{HONO-i} - n_{LUNO+i}}{2} \tag{III. 2.2}$$

Here, T_i is the orbital overlap between corresponding orbital pairs, and $n_{\mathrm{HONO}-i}$ and $n_{\mathrm{LUNO}+i}$ are the occupation numbers of UHF natural orbitals (UNOs). The averaged diradical character y_{av} was calculated using the following formula[17,18]:

$$y_{av}(N) = \sum_{i=0}^{\frac{N}{2}-1} y_i(N) \tag{III. 2.3}$$

Note that there are $N/2$ radical orbital pairs in the N-mer. The standard deviation, y_{SD}, was also computed, defined by the following equation[10]:

$$y_{SD}(N) = \sqrt{\frac{1}{N/2} \sum_{i=0}^{\frac{N}{2}-1} \{y_i(N) - y_{av}(N)\}^2} \tag{III. 2.4}$$

These y-based indices help characterize open-shell electronic structures of N-mers[10]. y_{av} is sensitive to the change in the primary stacking distance d_1 but insensitive to the change in the SDA ratio. y_{SD} can efficiently characterize the open-shell electronic structures of 1D chains of radicals with different SDA ratios. Note that $y_{\mathrm{av}}(4) = (y_0 + y_1)/2$ and $y_{\mathrm{SD}}(4) = (y_0 - y_1)/2$ for $N = 4$. The occupation numbers of UNOs were calculated using the Gaussian 09 program package[19].

2.2.3. Excited state calculations and spectrum simulations

Multi-reference methods should be used to examine the ground and excited states of diradical molecules and assemblies in principle for a balanced description of both the static and dynamical electron correlations. In this study, the extended (X)MC-QDPT2 method implemented in the GAMESS-US program package (ver. 2014)[20] was employed to calculate the excitation energies and transition dipole moments, although it is reported that the (multi-reference) second-order perturbation theory methods tend to overestimate the binding energy of PLY π-dimers in the S_0 state[21]. To express the open-shell nature in the S_0 state and two-photon transition of diradical systems, the two-electron and two-orbital complete active space [i.e., CAS(2,2)] is the minimal choice of the active space. For the dimer, the HOMO and LUMO constructed from the SOMOs of monomers are the minimal active orbitals. Accordingly, state-averaged (SA-)CASSCF calculations were performed based on the CAS(N, N) space, where the active orbitals are the frontier MOs constructed from the SOMOs of monomers. The low-lying three singlet states for $N = 2$ (all the electronic states derived from CAS(2,2) space) and for the low-lying ten singlet states with the A_g and B_u symmetries for N = 4 and 6 were solved for. This symmetry constraint is expected to efficiently describe the one-photon absorption (OPA) and TPA peaks of N-mers concerning the intermonomer electronic transitions.

Although the basis sets including diffuse functions can improve the description of excitation energies and binding energies of π-dimers, the 6-31G* basis set was used since it is reported to describe the vertical excitation energies of several π-dimers with sufficient accuracy in combination with the MC-QDPT[22]. The excitation energies were then evaluated at the XMC-QDPT2 level with the intruder state avoidance parameter of 0.02. It should be noted that the transition dipole moments between the states were evaluated using the eigenvectors of the XMC-QDPT2 effective Hamiltonian.

The OPA cross-section, $\sigma^{(1)}(\omega)$, was evaluated by the following equation[23]:

$$\sigma^{(1)}(\omega) = \frac{4\pi^2\omega}{cn\hbar}\langle\left|\boldsymbol{\mu}_{fg}\right|^2\rangle\, g(\omega) \qquad \text{(III. 2.5)}$$

Here, c is the speed of light in vacuum, ω is the angular frequency of the incident light, n is the refractive index of the medium (set to 1.0 in this study). $\boldsymbol{\mu}_{fg}$ is the transition dipole moment between the states g and f. $\langle\cdots\rangle$ means the orientational average, i.e., $\langle\left|\boldsymbol{\mu}_{fg}\right|^2\rangle = \left\{\left(\mu_{fg}^X\right)^2 + \left(\mu_{fg}^Y\right)^2 + \left(\mu_{fg}^Z\right)^2\right\}/3$ where μ_{fg}^{α} represents the α-axis component of the transition dipole moment $\boldsymbol{\mu}_{fg}$. Since only for the A_g and B_u states were solved for, the Z-axis component of $\boldsymbol{\mu}_{fg}$ is zero. The following Lorentzian function was used for the normalized shape function $g(\omega)$:

$$g(\omega) = \frac{1}{\pi}\frac{\Gamma_{fg}}{\left(\omega_{fg} - \omega\right)^2 + {\Gamma_{fg}}^2} \qquad \text{(III. 2.6)}$$

where $E_{fg} = \hbar\omega_{fg}$ and Γ_{fg} is the damping parameter. This study employed $\hbar\Gamma$ = 0.1 eV for all the damping parameters.

The TPA cross-section, $\sigma^{(2)}(\omega)$, was evaluated by the following equation[23,24]:

$$\sigma^{(2)}(\omega) = \frac{4\pi^3\omega^2}{c^2n^2}\langle\left|\boldsymbol{M}_{fg}^{(2)}\right|^2\rangle\, g(2\omega) \qquad \text{(III. 2.7)}$$

Here, $\boldsymbol{M}_{fg}^{(2)}$ is the two-photon transition matrix element tensor with each component expressed as follows:

$$M_{fg,\alpha\beta}^{(2)} = \frac{1}{\hbar}\sum_{k}\left[\frac{\mu_{fk}^{\alpha}\mu_{kg}^{\beta}}{\omega_{kg}-\omega}+\frac{\mu_{fk}^{\beta}\mu_{kg}^{\alpha}}{\omega_{kg}-\omega}\right] \qquad (\alpha,\beta = X,Y,Z) \qquad \text{(III.2.8)}$$

For the orientational average, $\langle\left|\boldsymbol{M}^{(2)}{}_{fg}\right|^{2}\rangle$, we assumed the linearly polarized incident light. For the actual calculation, we replaced ω_{kg} in the denominator with $\omega_{kg} - i\Gamma_{kg}$. Again, the Lorentzian function was used for the normalized shape function $g(2\omega)$:

$$g(2\omega) = \frac{1}{\pi}\frac{\Gamma_{fg}}{\left(\omega_{fg}-2\omega\right)^{2}+\Gamma_{fg}{}^{2}} \qquad \text{(III.2.9)}$$

2.3. Results and Discussion

2.3.1. Correlation between stacking distances and diradical characters

Figure III.2.2 shows the calculation results of y_{av} and y_{SD} as a function of d_1 (2.8 Å ≤ d_1 ≤ 4.0 Å) for each model. y_{av} decreased monotonically as the d_1 decreased, reaching intermediate values (~0.5) at d_1~3.0 Å. The ratio d_2/d_1 did not affect the results of y_{av} for **1a$_4$(d_2/d_1)** model. Furthermore, y_{av} values of **1a$_2$**, **1a$_4$(1.0)**, and **1a$_6$(1.0)** for the considered d_1 were almost the same, although their open-shell characters are different. y_{SD} can characterize such differences in the open-shell characters between the models at each d_1. The calculated y_{SD} values of **1a$_4$(2.0)** were almost zero regardless of d_1, whereas those of the other models increased monotonically with decreasing d_1. y_{SD} metric effectively characterized these orbital interaction between the dimer units. The value of y_i increases as the energy gap between the HOMO-i and LUMO+i decreases. The orbital interaction between the dimer units is weak for the tetramer when d_2 >> d_1. The HOMO and HOMO-1 (LUMO and LUMO+1) are nearly degenerated, resulting in y_0~y_1 (i.e., y_{SD}~0). As the d_2 approached d_1 (and as the d_1 became small), the orbital interaction between the dimer units resulted in the splitting of HOMO and HOMO-1 (LUMO and LUMO+1) and the increase in y_{SD}. y_{SD} of **1a$_6$(1.0)** was slightly larger than **1a$_4$(1.0)** at each d_1, but it is expected to converge to a certain value as increasing N[10].

2.3.2. One-photon and two-photon absorption properties of tetramers

Figure III.2.3 shows the simulated OPA spectra for the tetramer models **1a$_4$(d_2/d_1)** with d_1 = 3.0 Å. To compare the results with **1a$_2$**, $\sigma^{(1)}(\omega)$ and $\sigma^{(2)}(\omega)$ values per dimer unit were presented. The OPA spectra were normalized to that at the first peak of the model **1a$_4$(1.0)**.

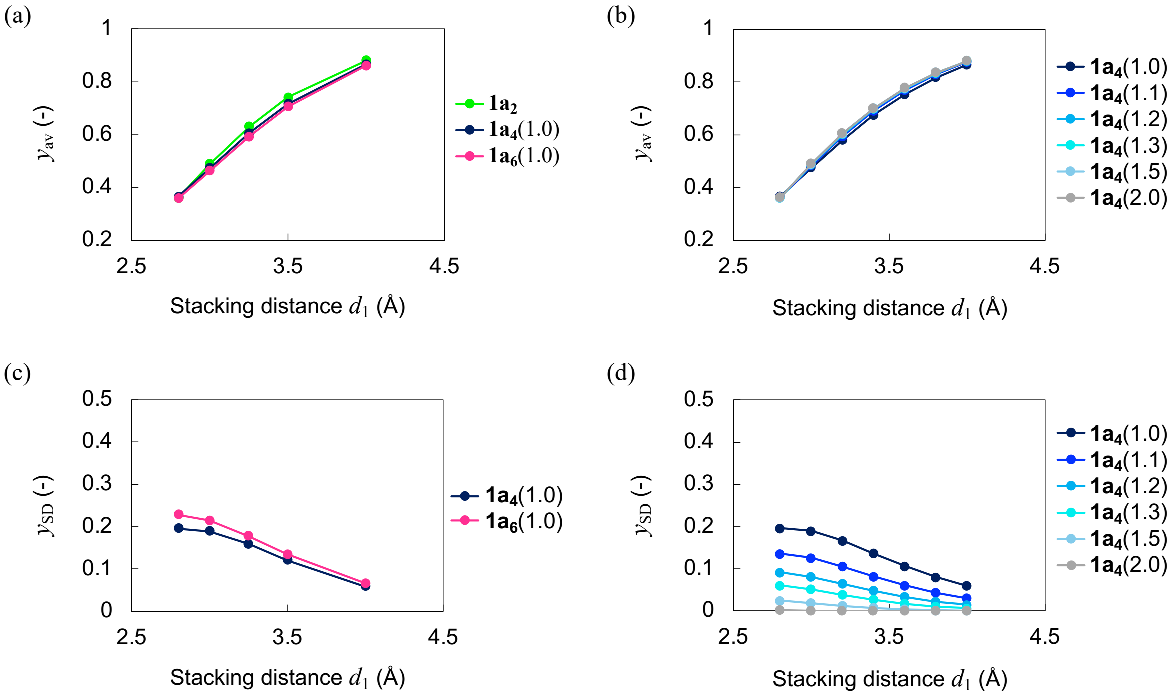

Figure III.2.2. Calculation results of y_{av} (a) for the models with the uniform stacking distance d_1 for **1a$_2$**, **1a$_4$(1.0)**, and **1a$_6$(1.0)**, (b) for **1a$_4$(d_2/d_1)** with different ratios $d_2/d_1 = 1.0$, 1.1, 1.2, 1.3, 1.5, and 2.0, results of y_{SD}, (c) for **1a$_4$(1.0)** and **1a$_6$(1.0)**, and (d) for **1a$_4$(d_2/d_1)**.

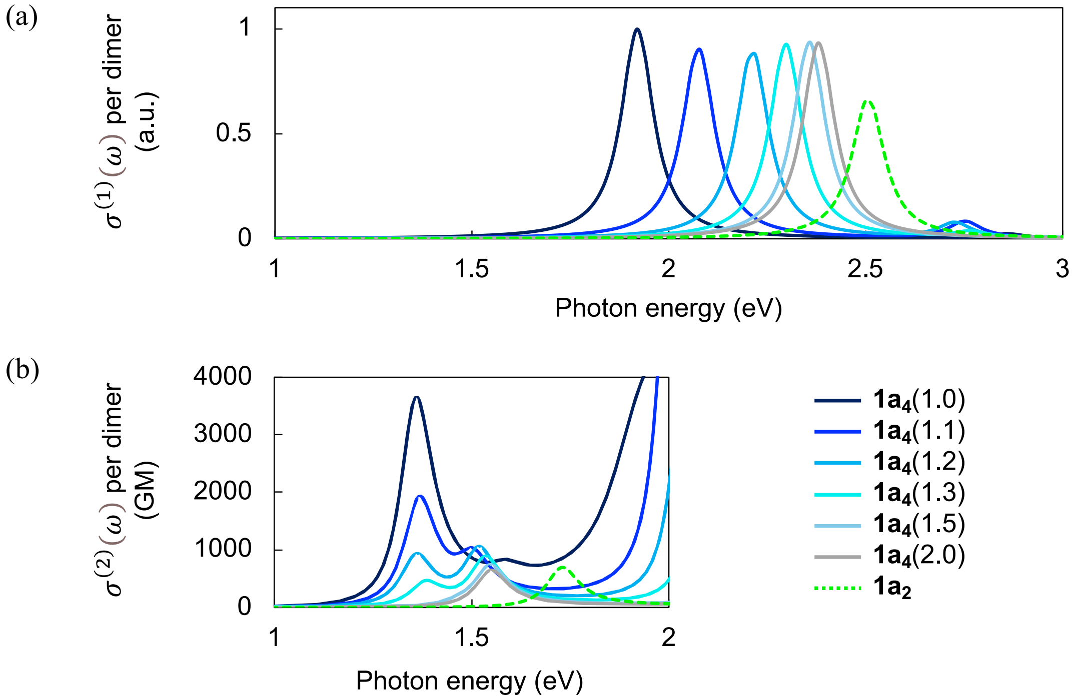

Figure III.2.3. Simulated (a) OPA and (b) TPA spectra of **1a$_2$** and **1a$_4$(d_2/d_1)** at d_1 = 3.0 Å with different ratios $d_2/d_1 = 1.0$, 1.1, 1.2, 1.3, 1.5, and 2.0. The OPA spectra were normalized to that at the first peak of the model **1a$_4$(1.0)**.

The first OPA and TPA peaks exhibited red-shifted as d_2/d_1 decreased (i.e., d_2 approached d_1) and d_1 decreased. For instance, the first OPA peak was observed at approximately 2.5 eV for **1a$_2$**, 2.4 eV for **1a$_4$(2.0)**, and 1.9 eV for **1a$_4$(1.0)**. The intensity of the first OPA peak remained nearly constant with changes in d_2/d_1. However, the peak intensities per dimer of **1a$_4$(d_2/d_1)** were stronger than those of **1a$_2$**, indicating the delocalization of wavefunction across dimers in the excited state.

For the TPA spectra, only a single peak appeared at ~1.7 eV for **1a$_2$**, attributed to the limited active space size [CAS(2,2)]. For the tetramer models **1a$_4$(d_2/d_1)**, increased TPA cross-section values (per dimer) were obtained as the incident photon energy approached the excitation energy of the OPA band. This enhancement can be attributed to the near-satisfaction of both one-photon and two-photon resonance conditions in this energy region[25,26]. However, the current level of approximation for the excited state calculations may inadequately describe the higher-lying excited states relevant to TPA transitions in this energy range. In the lower-energy region of incident photon energy (<1.7 eV), a single TPA peak identified at ~1.6 eV for **1a$_4$(2.0)** and **1a$_4$(1.5)**. As d_2/d_1 decreased, this peak position was red-shifted, and another peak appeared at ~1.4 eV. The intensity of the lower-energy peak at ~1.4 eV increased drastically as d_2/d_1 approached one.

Tables III.2.1 and III.2.2 present a summary of the excitation energies (E_{fg}) and the Y-axis components of the transition dipole moments ($|\mu_{ij}^{Y}|$), respectively, which are essential for characterizing the described OPA and TPA peaks. The 1A$_g$→1B$_u$ transition for all cases characterized the OPA peak. The $|\mu_{ij}^{Y}|$ value for the 1A$_g$→1B$_u$ transition of the tetramer models **1a$_4$(d_2/d_1)** slightly increased as the d_2/d_1 decreased, the feature of which was reflected in the OPA peak intensities. The TPA peak at ~1.6 eV was primarily described by the virtual transition via 1A$_g$→1B$_u$→5A$_g$. The $|\mu_{ij}^{Y}|$ value for the 1B$_u$→5A$_g$ transition decreased whereas the $|\mu_{ij}^{Y}|$ value for the 1B$_u$→4A$_g$ transition increased as the d_2/d_1 decreased. Therefore, the virtual transition via 1A$_g$→1B$_u$→4A$_g$ primarily described the lower-energy TPA peak at ~1.4 eV. The excitation energy of the 4A$_g$ state was almost unchanged in the range of $1.0 \leq d_2/d_1 \leq 1.3$, while the excitation energy of the 1B$_u$ state decreased, which led to a decrease in $|E_{kg} - E_{fg}/2|$ (k: 1B$_u$ state, f: 4A$_g$ state) as the d_2/d_1 approached to one. These tendencies were attributed to the enhancement of $\sigma^{(2)}(\omega)$ values per dimer at ~1.4 eV.

Table III.2.A1 summarizes the weights of electron configurations for these electronic states of **1a$_4$(1.0), 1a$_4$(1.2), 1a$_4$(1.5),** and **1a$_4$(2.0)** with d = 3.0 Å. In addition, Figure III.2.A1 illustrates the HOMO-1, HOMO, LUMO, and LUMO+1 of **1a$_4$(1.0)** with d = 3.0 Å. It is noteworthy that the bonding and anti-bonding characteristics of these frontier MOs remain unchanged across all considered d_1 and d_2 values. For all these models, the 1A$_g$ and 1B$_u$ states were primarily described by the ground electron configuration and the HOMO–LUMO single excitation configuration, respectively. However, the 1A$_g$ state of **1a$_4$(1.0)** exhibited a relatively large weight for the HOMO–LUMO double excitation configuration. For **1a$_4$(1.5)** and **1a$_4$(2.0)**, the 5A$_g$ state was described by the linear combination of HOMO-1–LUMO and HOMO–LUMO+1 single excitation configurations. In contrast, the 4A$_g$ state of these models was described by the linear combinations of the ground and several single and double excitation configurations. For **1a$_4$(1.2)**, the characters of 4A$_g$ and 5A$_g$ were reversed from those for

1a$_4$(1.5) and **1a$_4$(2.0)**. For **1a$_4$(1.0)**, the 4A$_g$ state was described primarily by the ground and HOMO–LUMO double excitation configurations.

Table III.2.1. Calculation results for excitation energies of **1a$_4$(d_2/d_1)**, E_{fg} (in eV), at d_1 = 3.0 Å with different ratios d_2/d_1 = 1.0, 1.1, 1.2, 1.3, 1.5, and 2.0. Results for the **1a$_2$** are also provided for reference.

System	y_{av}	y_{SD}	E_{fg}				
			1B$_u$	**2A$_g$**	**3A$_g$**	**4A$_g$**	**5A$_g$**
1a$_4$(1.0)	0.474	0.189	1.921	1.120	2.375	2.708	3.164
1a$_4$(1.1)	0.482	0.126	2.076	1.273	2.369	2.727	2.999
1a$_4$(1.2)	0.486	0.081	2.213	1.400	2.379	2.713	3.030
1a$_4$(1.3)	0.488	0.051	2.298	1.465	2.388	2.760	3.063
1a$_4$(1.5)	0.490	0.018	2.357	1.500	2.400	2.927	3.087
1a$_4$(2.0)	0.490	0.001	2.381	1.501	2.410	3.091	3.271
1a$_2$	0.490	–	2.573	3.452	–	–	–

Table III.2.2. Calculation results for the *Y*-axis (stacking direction) component of transition dipole moment between the states *i* and *j* $|\mu_{ij}^{Y}|$ (in Debye) for **1a$_4$(d_2/d_1)** at d_1 = 3.0 Å with different ratios d_2/d_1 = 1.0, 1.1, 1.2, 1.3, 1.5, and 2.0. Results for the **1a$_2$** are also provided for reference.

System	y_{av}	y_{SD}	$\lvert\mu_{ij}^{Y}\rvert$				
			1A$_g$→1B$_u$	**1B$_u$→2A$_g$**	**1B$_u$→3A$_g$**	**1B$_u$→4A$_g$**	**1B$_u$→5A$_g$**
1a$_4$(1.0)	0.474	0.189	11.6	1.0	1.1	21.2	2.3
1a$_4$(1.1)	0.482	0.126	10.6	2.7	0.1	19.2	7.4
1a$_4$(1.2)	0.486	0.081	10.2	2.1	0.4	14.8	12.1
1a$_4$(1.3)	0.488	0.051	10.2	0.9	1.0	10.4	13.2
1a$_4$(1.5)	0.490	0.018	10.1	0.1	1.4	4.1	13.7
1a$_4$(2.0)	0.490	0.001	10.0	0.0	1.0	0.1	13.5
1a$_2$	0.490	–	7.3	12.4	–	–	–

The effects of the primary stacking distance d_1 and the ratio d_2/d_1 on the intensity of the first TPA peak investigated. Figure III.2.4 shows the $\sigma^{(2)}(\omega)$ values per dimer for **1a$_4$(d_2/d_1)** with different d_1 (2.8 Å ≤ d_1 ≤ 4.0 Å) as a function of the ratio d_2/d_1. The intensity of the first TPA peak increased with decreasing d_1 and as d_2/d_1 approached 1. Similar trends were observed for the calculation results of static γ per unit of finite and infinite 1D stacks of **1a**[10]. The results indicate that both the static γ and $\sigma^{(2)}$ value of the first TPA peak are likely to be enhanced in uniform 1D stacks of PLYs. Such enhancements of the third-order NLO responses are expected when d_1 is less than the van der Waals contact distance for the carbon atoms (3.4 Å).

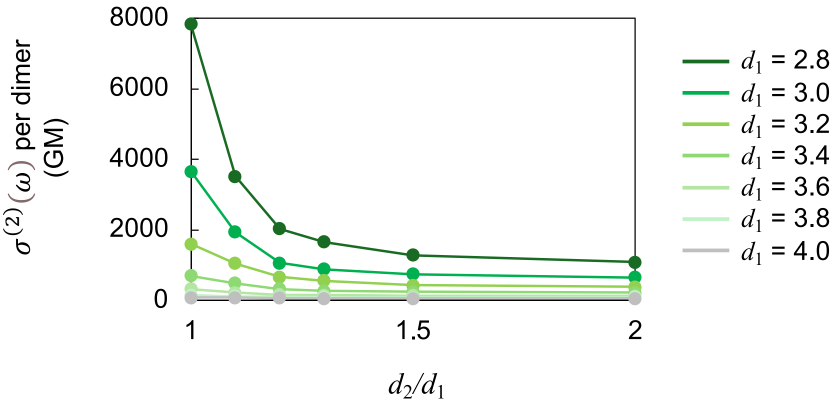

Figure III.2.4. Calculation results of $\sigma^{(2)}(\omega)$ values per dimer for **1a$_4$(d_2/d_1)** with different d_1 (2.8 Å ≤ d_1 ≤ 4.0 Å) as a function of the ratio d_2/d_1.

Figure III.2.A2 presents the variations in the excitation energies and transition dipole moments associated with key transitions in **1a$_4$(d_2/d_1)** models for different d_1 (2.8 Å ≤ d_1 ≤ 4.0 Å) as a function of the ratio d_2/d_1. As the d_1 decreased, the excitation energy for the TPA target (4A$_g$ or 5A$_g$) state increased more significantly than that for the OPA target (1B$_u$) state. As a result, the detuning energy, $|E_{kg} - E_{fg}/2|$, which inversely contributes to the $\sigma^{(2)}$ value at the peak, became small. The magnitude of the transition dipole moment for the 1A$_g$→1B$_u$ transition increased as the d_1 decreased, whereas that for the 1B$_u$→4A$_g$(5A$_g$) transition showed somewhat complicated behaviors because the characters of 4A$_g$ and 5A$_g$ states exchanged at d_2/d_1 = 1.2–1.3.

Finally, the TPA properties of the hexamer model **1a$_6$(1.0)** were calculated to investigate the effects of increasing N. Figure III.2.5 shows the calculation results of $\sigma^{(2)}$ value per dimer at the first TPA peak as a function of y_{av} for the **1a$_2$**, **1a$_4$(1.0)**, and **1a$_6$(1.0)** (for the relationship between d_1 and y_{av}, see Figure III.2.2(a)). The $\sigma^{(2)}$ values per dimer increased as the y_{av} decreased (i.e., as the d_1 decreased) for all the models. The enhancement of $\sigma^{(2)}$ values per dimer was more significant in N = 6 than in N = 4: At d_0 = 3.0 Å, $\sigma^{(2)}$ values per dimer of **1a$_4$(1.0)** and **1a$_6$(1.0)** were 5.1 and 8.4 times higher than that of **1a$_2$**. Further enhancement of the $\sigma^{(2)}$ values per dimer unit can be expected when N approaches to ∞ (i.e., for the infinite 1D π-stacks), although the value will converge to a specific value as was observed for the calculation results of static γ per unit[10]. Figure III.2.A3 compares the excitation energies and transition dipole moments of key transitions for **1a$_2$**, **1a$_4$(1.0)**, and **1a$_6$(1.0)** as a function of y_{av}. As N increased, the excitation energies for both the OPA and TPA target states decreased, and the detuning energy, $|E_{kg} - E_{fg}/2|$, became smaller, which is identified the primary factor contributing to the enhancement of $\sigma^{(2)}$ values at the first peak.

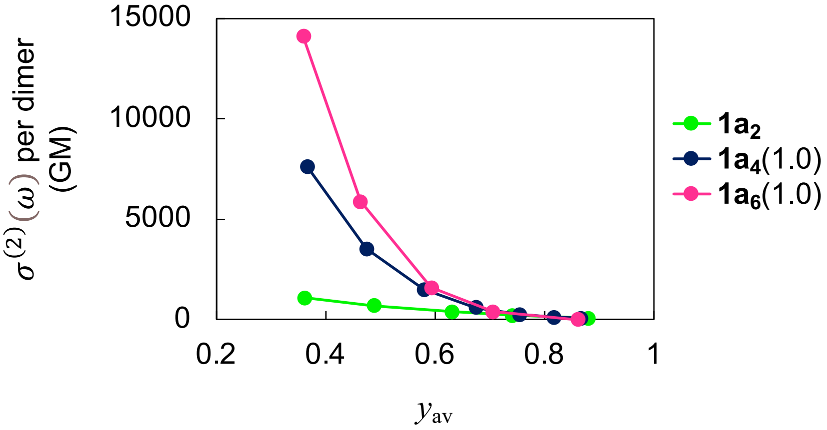

Figure III.2.5. Calculation results of $\sigma^{(2)}$ value per dimer at the first TPA peak as a function of y_{av} for the **1a$_2$**, **1a$_4$(1.0)**, and **1a$_6$(1.0)**.

2.4. Conclusion

In this study, the low-energy OPA and TPA properties of π-stacked *N*-mer models, **1a$_N$(d_2/d_1)** ($N = 2$, 4, and 6), composed of unsubstituted phenalenyl radicals with varying stacking distances d_1 and d_2, were theoretically examined. CASSCF(*N,N*) and XMC-QDPT2/6-31G* calculations were performed for the excitation energies and transition dipole moments, which were subsequently used to simulate the OPA and TPA spectra of these models. The $\sigma^{(2)}$ value per dimer unit at the first peak, originating from the electronic transition along the stacking direction, was predicted to increase significantly as d_2/d_1 approaches one, as d_1 decreases, and as N increases from 2 to 6. For the 1D chains of unsubstituted phenalenyl (**1a**), sufficiently enhanced TPA properties are anticipated when $d_1 \leq 3.2$ Å. The optimal d_1 value and d_2/d_1 ratio for achieving significantly enhanced TPA properties will depend on the specific monomer species.

The calculation of y-based indices, y_{av}, and y_{SD} will facilitate the identification of suitable regions for these parameters. However, it is generally challenging to fully characterize the electronic structures and excitation properties of 1D π-stacks using only a few indices. Accurate calculations and analyses are essential for predicting the OPA and TPA properties of more realistic models that incorporate substituent groups. Nonetheless, the present findings offer valuable insights into the relationship between the structural characteristics and linear/nonlinear optical responses of actual 1D π-stacked chains of open-shell molecular species.

Appendix

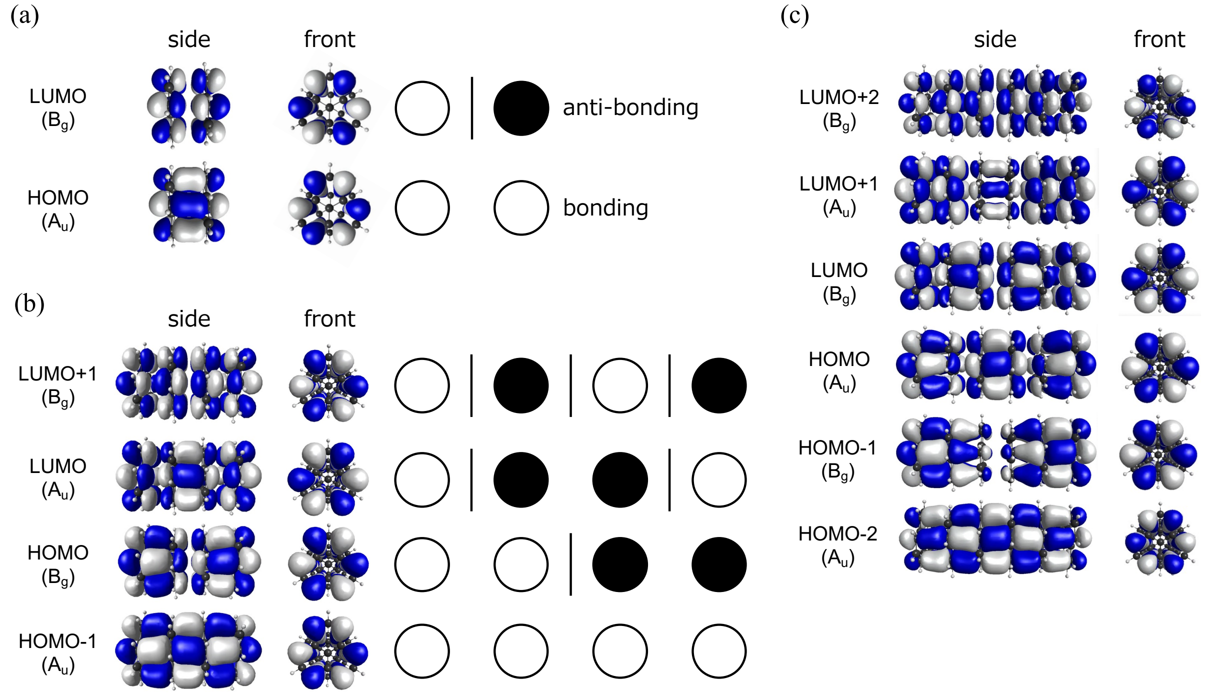

Figure III.2.A1. Frontier MOs involved in the active space of CASSCF calculations for (a) **1a$_2$**, (b) **1a$_4$(1.0)** and (c) **1a$_6$(1.0)** with d_1 = 3.0 Å.

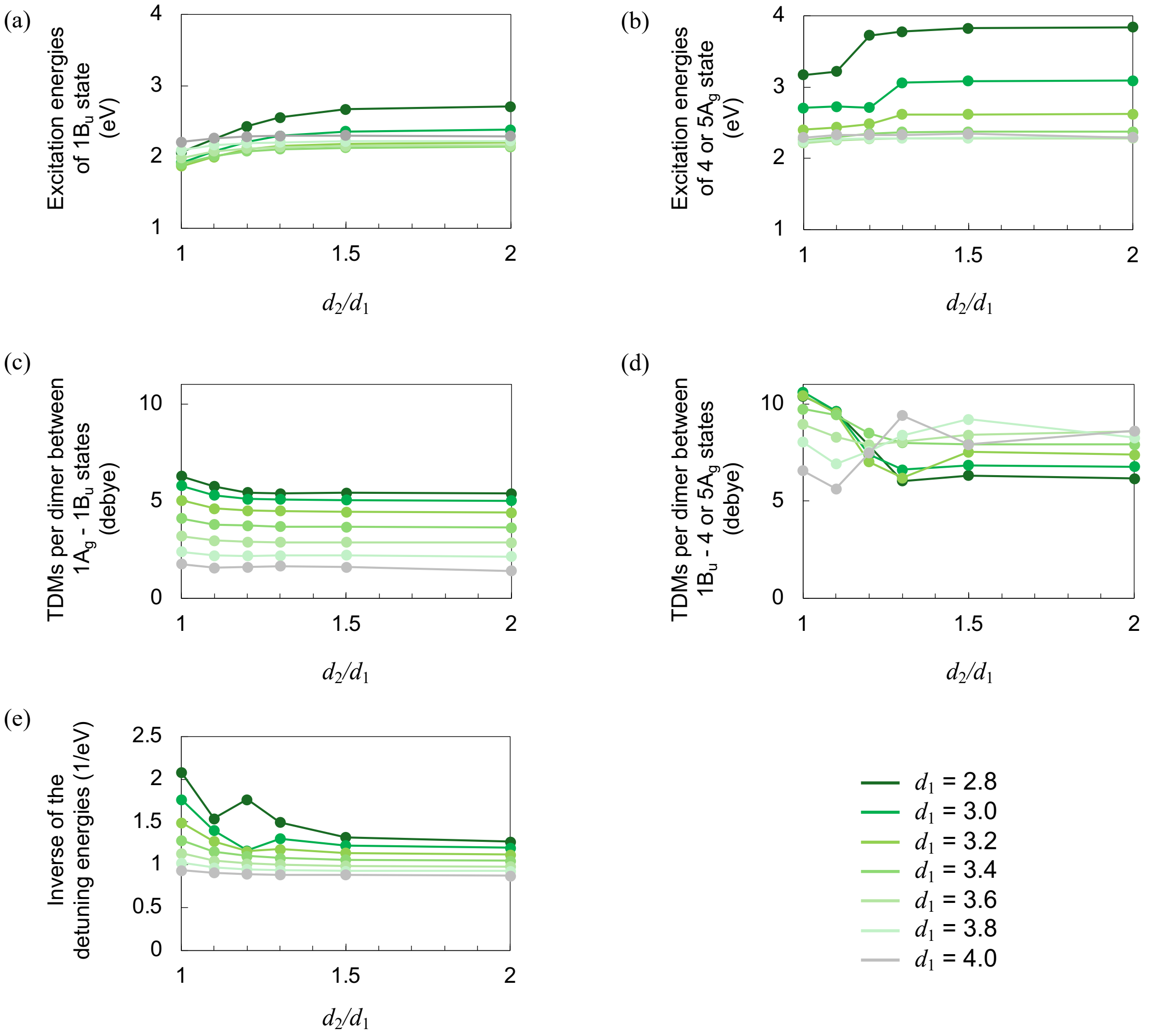

Figure III.2.A2. d_2/d_1 dependences of the excitation energies for (a) OPA target state, (b) first TPA target state, and magnitudes of the transition dipole moments (TDM)s (per dimer) for (c) $1A_g$-$1B_u$ transition, (d) $1B_u$-TPA target ($4A_g$ or $5A_g$) state, and (e) inverse of the detuning energy.

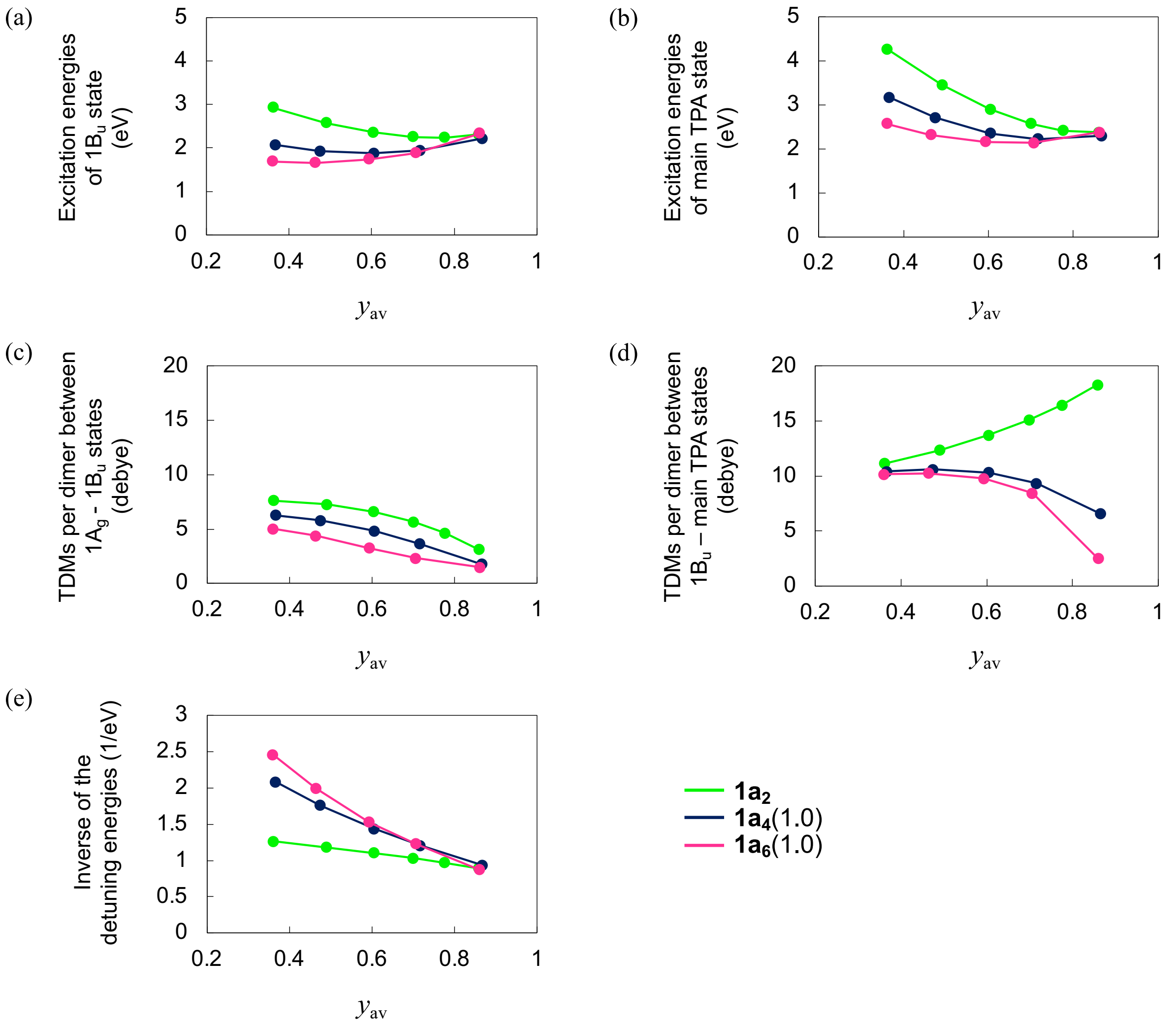

Figure III.2.A3. y_{av} dependences of the excitation energies for (a) OPA target state, (b) main TPA target state, and magnitudes of the transition dipole moments (TDM)s (per dimer) for (c) $1A_g$-$1B_u$ transition, (d) $1B_u$-TPA target state, and (e) inverse of the detuning energy.

Table III.2.A1. Electron configurations describing the crucial electronic states of **1a$_4$(1.0)**, **1a$_4$(1.2)**, **1a$_4$(1.5)** and **1a$_4$(2.0)** with d_1 = 3.0 Å.

	1a$_4$(1.0)		**1a$_4$(1.2)**		**1a$_4$(1.5)**		**1a$_4$(2.0)**	
	Conf.	Weight [%]	Conf.	Weight [%]	Conf.	Weight [%]	Conf.	Weight [%]
1A$_g$	2200	83	2200	85	2200	85	2200	85
	2020	8						
1B$_u$	2-+0	44	2-+0	44	2-+0	29	2-+0	24
	2+-0	44	2+-0	44	2+-0	29	2+-0	24
					-20+	19	-20+	23
					+20-	19	+20-	23
2A$_g$	2020	32	2020	28	2020	21	2020	19
	-2+0	11	0220	17	0220	19	0220	19
	+2-0	11	2002	14	2002	18	2002	19
	0220	10	0202	9	0202	17	0202	19
	2-0+	10	--++	6	--++	8	--++	8
	2+0-	10	++--	6	++--	8	++--	8
	2002	6						
3A$_g$	-2+0	24	-2+0	25	-2+0	23	-2+0	23
	2-0+	24	+2-0	25	+2-0	23	+2-0	23
	2-0+	21	2-0+	20	2-0+	22	2-0+	23
	2+0-	21	2+0-	20	2+0-	22	2+0-	23
4A$_g$	2200	14	2-0+	20	2200	13	2200	14
	2020	27	2+0-	20	2020	14	0022	13
	+--+	9	-2+0	17	0022	12	2020	10
	-++-	9	+2-0	17	-+-+	11	-+-+	10
	2-0+	7	0202	11	+-+-	11	+-+-	10
	2+0-	7			0220	9	0202	10
	-+-+	5			0202	8	0220	8
	+-+-	5			+--+	7	+--+	8
					-++-	7	-++-	8
					2002	7	2002	8
5A$_g$	0220	25	2200	12	2-0+	23	2-0+	24
	2002	9	2020	24	2+0-	23	2+0-	24
	0202	6	0220	12	-2+0	23	-2+0	24
	2-0+	6	-+-+	11	+2-0	23	+2-0	24
	2+0-	6	+-+-	11	0202	5		
	--++	6	0022	9				
	++--	6	2002	6				
	-+-+	5						
	+-+-	5						
	2020	5						
	-2+0	5						
	+2-0	5						

References

[1] K. Uchida, Y. Hirao, H. Kurata, T. Kubo, S. Hatano and K. Inoue, *Chem. - An Asian J.*, **2014**, *9*, 1823–1829.

[2] Z. Mou, K. Uchida, T. Kubo and M. Kertesz, *J. Am. Chem. Soc.*, **2014**, *136*, 18009–18022.

[3] K. Goto, T. Kubo, K. Yamamoto, K. Nakasuji, K. Sato, D. Shiomi, T. Takui, M. Kubota and T. Kobayashi, *J. Am. Chem. Soc.*, **1999**, *121*, 1619–1620.

[4] S. Suzuki, Y. Morita, K. Fukui, K. Sato, D. Shiomi, T. Takui and K. Nakasuji, *J. Am. Chem. Soc.*, **2006**, *128*, 2530–2531.

[5] M. Kertesz, *Chem. - A Eur. J.*, **2019**, *25*, 400–416.

[6] K. Yoneda, M. Nakano, K. Fukuda, H. Matsui, S. Takamuku, Y. Hirosaki, T. Kubo, K. Kamada and B. Champagne, *Chem. - A Eur. J.*, **2014**, *20*, 11129–11136.

[7] S. Salustro, L. Maschio, B. Kirtman, M. Rérat and R. Dovesi, *J. Phys. Chem. C*, **2016**, *120*, 6756–6761.

[8] H. Matsui, M. Nakano and B. Champagne, *Phys. Rev. A*, **2016**, *94*, 042515.

[9] H. Matsui, M. Yamane, T. Tonami, T. Nagami, K. Watanabe, R. Kishi, Y. Kitagawa and M. Nakano, *Mater. Chem. Front.*, **2018**, *2*, 785–790.

[10] J. Shoda, M. Yokoyama, W. Yoshida, H. Matsui, R. Sugimori, R. Kishi and Y. Kitagawa, *J. Phys. Chem. A*, **2024**, *128*, 8473–8482.

[11] M. Yokoyama, R. Kishi and Y. Kitagawa, *Bull. Chem. Soc. Jpn.*, **2024**, *97*, 1–9.

[12] M. Nakano, R. Kishi, S. Ohta, H. Takahashi, T. Kubo, K. Kamada, K. Ohta, E. Botek and B. Champagne, *Phys. Rev. Lett.*, **2007**, *99*, 033001.

[13] M. Nakano, T. Kubo, K. Kamada, K. Ohta, R. Kishi, S. Ohta, N. Nakagawa, H. Takahashi, S. I. Furukawa, Y. Morita, K. Nakasuji and K. Yamaguchi, *Chem. Phys. Lett.*, **2006**, *418*, 142–147.

[14] H. Nakano, *J. Chem. Phys.*, **1993**, *99*, 7983–7992.

[15] A. A. Granovsky, *J. Chem. Phys.*, **2011**, *134*, 214113.

[16] K. Yamaguchi, *Chem. Phys. Lett.*, **1975**, *33*, 330–335.

[17] M. Nakano, A. Takebe, R. Kishi, S. Ohta, M. Nate, T. Kubo, K. Kamada, K. Ohta, B. Champagne, E. Botek, H. Takahashi, S. ichi Furukawa, Y. Morita and K. Nakasuji, *Chem. Phys. Lett.*, **2006**, *432*, 473–479.

[18] M. Nakano, T. Minami, H. Fukui, R. Kishi, Y. Shigeta and B. Champagne, *J. Chem. Phys.*, **2012**, *136*, 024315.

[19] M. J. Frisch, G. W. Trucks, H. B. Schlegel, G. E. Scuseria, M. A. Robb, J. R. Cheeseman, G. Scalmani, V. Barone, B. Mennucci, G. A. Petersson, H. Nakatsuji, M. Caricato, H. P. H. X. Li, A. F. Izmaylov, G. Z. J. Bloino, J. L. Sonnenberg, M. Hada, M. Ehara, K. Toyota, R. Fukuda, J. Hasegawa, M. Ishida, T. Nakajima, Y. Honda, O. Kitao, H. Nakai, T. Vreven, J. J. A. Montgomery, J. E. Peralta, F. Ogliaro, M. Bearpark, J. J. Heyd, E. Brothers, K. N. Kudin, V. N. Staroverov, R. Kobayashi, J. Normand, K. Raghavachari, A. Rendell, J. C. Burant, S. S. Iyengar, J. Tomasi, M. Cossi, N. Rega, J. M. Millam, M. Klene, J. E. Knox, J. B. Cross, V. Bakken, C. Adamo, J. Jaramillo, R. Gomperts, R. E. Stratmann, O. Yazyev, A. J. Austin, R. Cammi, C. Pomelli, J. W. Ochterski, R. L. Martin, K. Morokuma, V. G.

Zakrzewski, G. A. Voth, P. Salvador, J. J. Dannenberg, S. Dapprich, A. D. Daniels, Ö. Farkas, J. B. Foresman, J. V. Ortiz, J. Cioslowski and D. J. Fox, *Gaussian 09. Rev. D.01*, Gaussian Inc., Wallingford, CT, **2009**.

[20] G. M. J. Barca, C. Bertoni, L. Carrington, D. Datta, N. De Silva, J. E. Deustua, D. G. Fedorov, J. R. Gour, A. O. Gunina, E. Guidez, T. Harville, S. Irle, J. Ivanic, K. Kowalski, S. S. Leang, H. Li, W. Li, J. J. Lutz, I. Magoulas, J. Mato, V. Mironov, H. Nakata, B. Q. Pham, P. Piecuch, D. Poole, S. R. Pruitt, A. P. Rendell, L. B. Roskop, K. Ruedenberg, T. Sattasathuchana, M. W. Schmidt, J. Shen, L. Slipchenko, M. Sosonkina, V. Sundriyal, A. Tiwari, J. L. Galvez Vallejo, B. Westheimer, M. Włoch, P. Xu, F. Zahariev and M. S. Gordon, *J. Chem. Phys.*, **2020**, *152*, 154102.

[21] Z. H. Cui, H. Lischka, H. Z. Beneberu and M. Kertesz, *J. Am. Chem. Soc.*, **2014**, *136*, 5539–5542.

[22] S. Shirai, S. Iwata, T. Tani and S. Inagaki, *J. Phys. Chem. A*, **2011**, *115*, 7687–7699.

[23] K. Ohta, S. Yamada, K. Kamada, A. D. Slepkov, F. A. Hegmann, R. R. Tykwinski, L. D. Shirtcliff, M. M. Haley, P. Sałek, F. Gel'mukhanov and H. Ågren, *J. Phys. Chem. A*, **2011**, *115*, 105–117.

[24] M. T. P. Beerepoot, D. H. Friese, N. H. List, J. Kongsted and K. Ruud, *Phys. Chem. Chem. Phys.*, **2015**, *17*, 19306–19314.

[25] K. Kamada, K. Ohta, T. Kubo, A. Shimizu, Y. Morita, K. Nakasuji, R. Kishi, S. Ohta, S. I. Furukawa, H. Takahashi and M. Nakano, *Angew. Chemie - Int. Ed.*, **2007**, *46*, 3544–3546.

[26] K. Kamada, K. Ohta, Y. Iwase and K. Kondo, *Chem. Phys. Lett.*, **2003**, *372*, 386–393.

GENERAL CONCLUSION

This dissertation theoretically investigated the structure-property correlations for TPA of open-shell π-conjugated molecules and their molecular aggregates to establish materials design guidelines for controlling the peak positions and intensities of TPA. PART II clarified the relationship between the static γ and open-shell character in the one-dimensional (1D) infinite stacks of π-radicals. PART III elucidated the correlation between the TPA properties, the structural parameters, and the number of molecules in the π-stacked aggregates of phenalenyl radicals. Here, the author summarizes the outcomes and conclude this dissertation.

Correlation between Open-shell Electronic Structures and Third-order Nonlinear Optical Properties in One-dimensional Chains of π-radicals

In PART II, the static γ values of one-dimensional (1D) molecular aggregates were thoroughly analyzed, focusing on their dependence on the stacking distance and the number of constituent molecules. The 1D chain composed of π-conjugated radicals, phenalenyls, was used as a model system. It was not easy to characterize the open-shell electronic structures of such aggregates only by a single index since multiple radical pairs exist in the *N*-mer systems. Therefore, the author employed two *y*-based indices: the average (y_{av}) and standard deviation (y_{SD}) of diradical characters y_i. y_{av} is known to help evaluate the "averaged" open-shell character. y_{SD}, which the authors introduced, is shown to help assess the "inter-dimer" interactions in the 1D molecular aggregates where the stacking distance alternation (SDA) is introduced. These *y*-based indices allow us to describe the open-shell electronic structure of realistic aggregate systems in which the stacking distance is not uniform.

Accurate theoretical prediction of the optical response properties of molecular aggregates and crystals is challenging. Conducting highly accurate quantum chemistry calculations to analyze aggregates of real π-conjugated molecules is still not feasible due to its explosive computational cost. Therefore, the author first compared the results of computationally less expensive density functional theory (DFT) methods with the highly accurate UCCSD(T) results for 1D aggregates of methyl radicals, the simplest model molecules of π-radicals. It is found that the long-range corrected (LC-)UBLYP functional with a range-separating parameter $\mu = 0.47$ bohr^{-1} reproduced well the results of γ_∞ (static γ at the limit of $N \rightarrow \infty$) and its polymer/dimer ratio at the UCCSD(T) level. The selected LC-UBLYP(0.47) method was used to estimate the γ_∞ value of the 1D chain of phenalenyl radicals. As a result, the author found that enhanced γ_∞ values were obtained when $y_{\mathrm{av},\infty} \leq 0.6$ and $y_{\mathrm{SD},\infty} \geq 0.1$. These open-shell character conditions can be obtained for systems with a uniform stacking distance of less than 3.2 Å. These results contribute to developing novel materials designed for open-shell molecular aggregates that exhibit remarkable third-order NLO effects.

Two-Photon Absorption Properties of Open-shell Molecular Aggregates

Chapter 1 of PART III analyzed the effect of the stacking distance on the OPA and TPA spectra for the π-dimers of phenalenyl radicals. To obtain the excitation energies and transition dipole moments required for the spectral simulations, the author applied the extended multiconfigurational quasi-degenerate second-order perturbation theory (XMC-QDPT2), a highly accurate electronic structure calculation method. The author assigned the lowest-energy TPA peak (the first TPA peak), which typically appears in a window region of the OPA spectrum, and the higher-energy TPA peaks. The OPA and TPA cross-sections were decomposed into the contributions from the stacking and in-plane directional components since the enhancement of the former contribution would reflect the degree of intermolecular electronic transition that can be increased upon the dimer formation. It is found that linear combinations of the SOMOs of phenalenyl monomers construct the HOMO and LUMO. The intensity of the first TPA peak is enhanced in the region of small stacking distance around 2.8-3.0 Å (intermediate open-shell nature: $y \sim 0.5$). The primary contribution to the first TPA peak was the stacking directional component. Namely, the enhanced TPA cross-section in the 1D aggregates of π-radicals at the low-energy region can signify strong intermolecular interactions and electron delocalizations in the low-lying excited states. This result confirms the plausibility of obtaining large TPA cross-sections by aggregating open-shell molecules. It suggests the feasibility of achieving large TPA cross-sections by appropriate molecular design of 1D aggregates.

Chapter 2 of PART III examined the position and intensity of the first TPA peak of multimers (up to hexamer) of phenalenyl radicals. The author discussed how the stacking distance and the number of molecules (N) affect the open-shell electronic structures, which were evaluated with y_{av} and y_{SD}, and TPA properties. It is found that the TPA cross-section at the first peak increased as the stacking distance decreased for multimers. This trend is similar to the static γ shown in PART II. In addition, the position of the first TPA peak shifted to the lower energy region as N increased. We have clarified the mechanism of peak shift. Furthermore, the TPA cross-section per dimer was 5.1 times higher for the tetramer and 8.4 times higher for the hexamer than for the dimer with a stacking distance of 3.0 Å. This is also consistent with the trend of static γ. The TPA cross-section value per dimer is considered to converge to a specific value when N approaches ∞. These results are the first detailed elucidation of TPA properties of aggregate systems of realistic open-shell π-conjugated molecules and contribute to creating novel open-shell TPA materials that outperform conventional systems.

In summary, this dissertation clarified the structure-property correlations in TPA properties of open-shell π-conjugated molecules and their molecular aggregates from the open-shell character viewpoint. Based on the results, several design guidelines are proposed for efficient TPA materials consisting of assemblies of open-shell molecules. The results and conclusions in this dissertation will contribute to accelerating the development and application of real open-shell TPA materials such as organic crystals and, at the same time, establishing the theoretical foundation for NLO material design.

FUTURE PROSPECTS

In this dissertation, we have investigated the structure-property correlations and the contribution of open-shell nature for TPA of open-shell π-conjugated molecule and their molecule aggregates through high-precision electronic structure computations and theoretical analysis. The analysis methods and the obtained results can be extended in several directions. We propose some topics as prospects.

Creation of new open-shell TPA molecular materials

In recent years, the usefulness of artificial intelligence (AI), machine learning (ML), and materials informatics (MI) in the screening and exploration of new materials that meet several conditions for applications has become widespread. Examples of the application of such data-driven research to the discovery of novel TPA materials and the prediction of TPA properties are beginning to be reported[1–3]. However, no mention of open-shell molecules has been made in such studies, even though many reports show huge TPA cross-sections in open-shell molecules: The targets of data-driven research on TPA materials have focused on closed-shell molecules. Plenty of data sets for structures and properties of closed-shell molecular systems have been available for data-driven research, the performance of which is generally improved as the data becomes rich. However, data describing the structures and properties of open-shell molecules and their aggregates is still poor in number and quality and has not been included sufficiently in the data sets. Descriptors that adequately represent the characters of open-shell molecular systems are essential in regression analysis and statistical modeling. The y-based indices, $y_{\mathrm{av,}}$ and y_{SD}, introduced in this dissertation, may be used as descriptors in the data-driven searches for open-shell functional molecular aggregates.

Toward realization of novel open-shell molecular systems through experimental synthesis

We have suggested that monomers be arranged with a uniform stacking distance to achieve large TPA cross-sections in open-shell 1D chains. In practice, it is still challenging to stabilize such uniform 1D chains of open-shell molecules by experimental synthesis. Introducing optimal substituents can help stabilize a specific arrangement by steric effects[4–8]. Bulky side chains have been reported to change the potential surface profile, stabilizing an energetically unfavorable geometry[9]. Another effective stabilization strategy is to introduce substituents that contribute to attractive interactions. For example, the perfluorophenyl-phenalenyl attractive interaction is stronger than the phenalenyl-phenalenyl one[10,11]. We must find optimal combinations of the open-shell core molecule and substituent groups to balance the attractive and repulsive interactions.

Applications utilizing TPA properties unique to open-shell 1D aggregates

The 1D aggregates studied in this dissertation consist of π-conjugated radicals. These open-shell 1D aggregates suggest the presence of through-space (TS) interactions between the open-shell monomers. This effect is predicted to result in NLO properties comparable to those of π-conjugated polymers[12]. The degree of electron delocalization in the TS-interacting systems is usually less than that in the through-bond (TB) conjugated systems, like π-conjugated polymers. The peak positions of the lowest allowed OPA and TPA bands in the open-shell aggregates are expected to appear in a relatively higher energy (shorter wavelength) region. In fact, for example, the wavelengths of the first TPA peaks of IDPL and NDPL derivatives are reported to be 1425 nm[13] and 1610 nm[14], while PLY_2 and PLY_4 with a uniform stacking distance of 3.0 Å were predicted to be 718 nm (3.452 eV as TPA state energy) and 916 nm (2.708 eV as TPA state energy) as described in PART III (see Figure III.2.3 and Table III.2.1). Since the wavelength of incident light contributes to the size of the irradiated spot, this characteristic can be an advantage in some applications. The minimum spot size (beam waist) w_0 of the laser is given by:

$$w_0 \propto \frac{\lambda}{NA} \tag{16}$$

Here, λ is the wavelength of the laser, and NA is the Numerical Aperture. From Eq. (16), a smaller w_0 can be achieved with a shorter λ for the same NA optical experimental system. There are a wide variety of applications where a small w_0 is required. For example, in TPA-based microfabrication, the small w_0 allows for a smaller minimum structure size (see Figure 5). In fluorescence imaging with TPE, a small w_0 can increase the resolution of the observation (see Figure 6). Even in TPA-based multilayer data storage (in the R&D stage), the small w_0 allows for increased recording density (see Figure 4(b)).

Structure-property correlation of open-shell π-conjugated polymers and the contribution of open-shell nature

The remaining issue in this dissertation is the incomplete analysis of TPA properties of open-shell singlet π-conjugated molecules, which have a different structure from that of open-shell π-stacking molecules. Consider open-shell systems involving two phenalenyl radicals as an example. The HOMO and LUMO of the π-stacked dimer are simply constructed by linear combinations of the SOMOs of the two monomers. This feature of TS-interacting systems validated the application of the two-site model to the analysis of the ground and low-lying excited states (Figure 17(a)). However, in open-shell π-conjugated molecules, radical moieties are directly connected with a bridging part. Therefore, the HOMO and LUMO are constructed from the SOMOs of the radical centers and the orbitals of the bridging part. This feature of TB-interacting systems may make it challenging to apply the two-site model to analyze the electronic structures (Figure 17(b)). The electronic structures of such open-shell π-conjugated molecules depend on the structures of radical species and bridging units. Detailed analysis of various open-shell π-conjugated molecules, such as IDPL and NDPL, should also be performed. Such analysis will contribute to extracting the control factors for the structure-property correlations of TPA properties of real open-shell molecules. Completing this research will contribute to creating innovative functional materials, whether the approach is experiment-driven or data-driven.

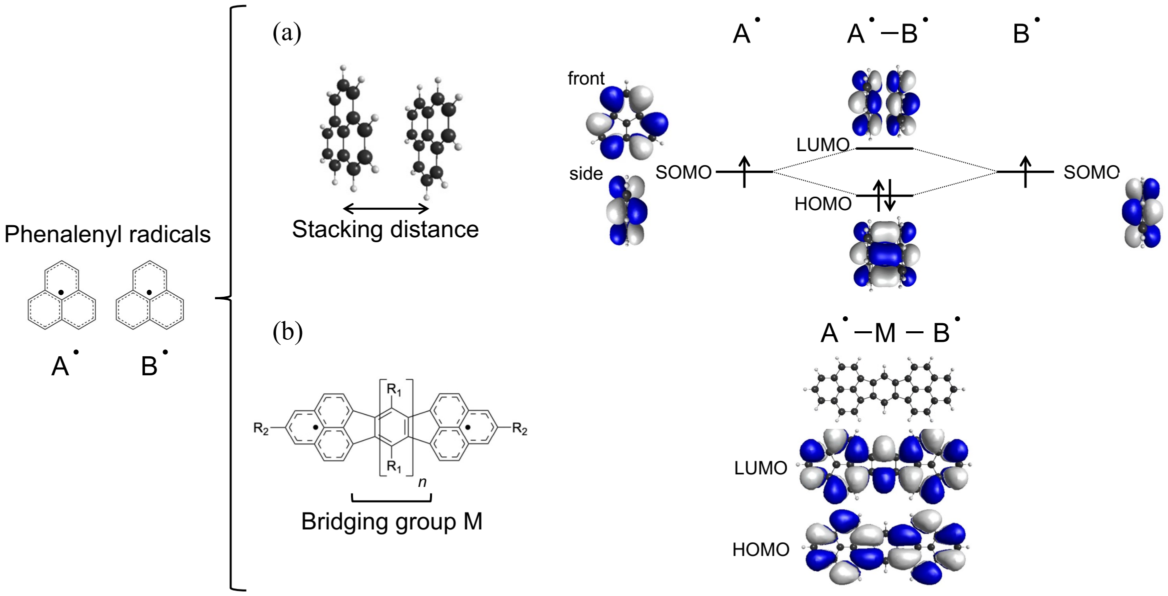

Figure 17. HOMO and LUMO of (a) π-conjugated, (b) π-stacking dimer by two phenalenyl radicals

References

[1] Y. Su, Y. Dai, Y. Zeng, C. Wei, Y. Chen, F. Ge, P. Zheng, D. Zhou, P. O. Dral and C. Wang, *Adv. Sci.*, **2023**, *10*, 2204902.

[2] H. Fu, M. Zhang, J. Leng, W. Hu, T. Zhu and Y. Zhang, *J. Phys. Chem. A*, **2024**, *128*, 431–438.

[3] Z. Garc, J. A. Arano-martinez, C. Mercado-z, C. Lizbeth and C. Torres-torres, *AI*, **2024**, *5*, 2203–2217.

[4] Y. Takano, T. Taniguchi, H. Isobe, T. Kubo, Y. Morita, K. Yamamoto, K. Nakasuji, T. Takui and K. Yamaguchi, *Chem. Phys. Lett.*, **2002**, *358*, 17–23.

[5] V. Zaitsev, S. V. Rosokha, M. Head-Gordon and J. K. Kochi, *J. Org. Chem.*, **2006**, *71*, 520–526.

[6] Z. H. Cui, H. Lischka, H. Z. Beneberu and M. Kertesz, *J. Am. Chem. Soc.*, **2014**, *136*, 5539–5542.

[7] Z. Tang, Z. Jiang, H. Chen, P. Su and W. Wu, *J. Chem. Phys.*, **2019**, *151*, 244106.

[8] Z. H. Cui, M. H. Wang, H. Lischka and M. Kertesz, *JACS Au*, **2021**, *1*, 1647–1655.

[9] P. R. Schreiner, L. V. Chernish, P. A. Gunchenko, E. Y. Tikhonchuk, H. Hausmann, M. Serafin, S. Schlecht, J. E. P. Dahl, R. M. K. Carlson and A. A. Fokin, *Nature*, **2011**, *477*, 308–311.

[10] G. W. Coates, A. R. Dunn, L. M. Henling, D. A. Dougherty and R. H. Grubbs, *Current*, **1997**, 248–251.

[11] G. W. Coates, A. R. Dunn, L. M. Henling, J. W. Ziller, E. B. Lobkovsky and R. H. Grubbs, *J. Am. Chem. Soc.*, **1998**, *120*, 3641–3649.

[12] H. Matsui, M. Yamane, T. Tonami, M. Nakano, M. De Wergifosse, T. Seidler and B. Champagne, *J. Phys. Chem. C*, **2018**, *122*, 6779–6785.

[13] K. Kamada, K. Ohta, T. Kubo, A. Shimizu, Y. Morita, K. Nakasuji, R. Kishi, S. Ohta, S. I. Furukawa, H. Takahashi and M. Nakano, *Angew. Chemie - Int. Ed.*, **2007**, *46*, 3544–3546.

[14] K. Kamada, K. Ohta, A. Shimizu, T. Kubo, R. Kishi, H. Takahashi, E. Botek, B. Champagne and M. Nakano, *J. Phys. Chem. Lett.*, **2010**, *1*, 937–940.

LIST OF PUBLICATIONS

Main Papers

[1] J. Shoda, M. Yokoyama, W. Yoshida, H. Matsui, R. Sugimori, R. Kishi, Y. Kitagawa, "Theoretical Study on the Correlation between Open-Shell Electronic Structures and Third-Order Nonlinear Optical Properties in One-Dimensional Chains of π-Radicals", *J. Phys. Chem. A,* **2024**, 128, 8473-8482.

[2] M. Yokoyama, R. Kishi, Y. Kitagawa, "Theoretical study on stacking distance dependence of one- and two-photon absorption properties of phenalenyl π -dimer models", *Bull. Chem. Soc. Jpn.*, **2024**, 97, uoae126 (9 pages).

[3] M. Yokoyama, R. Kishi, Y. Kitagawa, "Theoretical Study on One- and Two-Photon Absorption Properties of π-Stacked Multimer Models of Phenalenyl Radicals", *Chemistry*, **2024**, 6, 1427-1438.

International Conferences

[1] M. Yokoyama, R. Kishi, Y. Kitagawa, "Theoretical Study on Excitation Properties of Phenalenyl Dimer Models Based on Multi-Reference Perturbation Theory", 25th IUPAC Conference on Physical Organic Chemistry (ICPOC25), Hiroshima, Japan, July 10-15, 2022. (**Poster**)

ACKNOWLEDGEMENTS

This dissertation work was carried out under the supervision of Professor Dr. Yasutaka Kitagawa (2020.10-2025.3) and the late Professor Dr. Masayoshi Nakano (2020.10-2021.10) at Division of Chemical Engineering, Department of Materials Engineering Science, Graduate School of Engineering Science, Osaka University. Prof. Kitagawa always gave me numerous helpful, insightful, and challenging pieces of advice related to my study. I extend my profound gratitude to Prof. Nakano for his gracious support and understanding of my decision to take on the challenge of conduct research activities in his laboratory while concurrently fulfilling my responsibilities in the company's R&D division. I extend my boundless gratitude to Dr. Ryohei Kishi (Graduate School of Engineering Science, Osaka University) for imparting the fundamentals of research, revealing both the appeal and difficulties of theoretical chemistry, providing invaluable advice on my studies, and inspiring me to develop my philosophy through research endeavors.

I am deeply grateful to Prof. Dr. Yasutaka Kitagawa, Prof. Dr. Norikazu Nishiyama, Prof. Dr. Takayuki Hirai, and Dr. Ryohei Kishi for kindly accepting the referee of this dissertation.

I would like to express gratitude to Prof. Yasutaka Kitagawa, Dr. Ryohei Kishi and Dr. Kohei Tada for their insightful comments on this dissertation and for the instructions of quantum chemistry.

I extend my sincerely gratitude to Prof. Dr. Takashi Kubo (Graduate School of Science, Osaka University), Dr. Kenji Kamada (National Institute of Advanced Industrial Science and Technology), and the late Prof. Dr. Masayoshi Nakano for initiating and directing the theory-synthesis-measurement trinity approach for open-shell functional molecular design.

I also extend my heartfelt gratitude to Dr. Kenji Kamada for his meticulous and insightful guidance on two-photon absorption measurement experiments, his consistent willingness to address my questions with sincerity, his patience and support during our thorough discussions, and his invaluable encouragement that motivated me to pursue the doctoral course.

I would like to thank all the members I have shared time with in the Nakano and Kitagawa laboratories during the four and a half years of my Ph.D. course. Especially, I am deeply grateful to Mr. Jinki Shoda for his outstanding contributions to the theoretical aspects of static γ of multiradicals and his multidimensional analysis to achieving our common research goals.

I would like to thank my colleagues who collaborated with me at Panasonic Holdings Corporation. Especially, I will forever hold in high regard the days characterized by stimulating discussions and steadfast dedication as we worked together on the development of two-photon absorption materials through experimental methodologies. I wish to extend my deepest gratitude to Dr. Masa-aki Suzuki for his encouragement, which motivated me to delve into the study of theoretical chemistry, and to Dr. Nobuaki Nagao for his invaluable guidance in imparting the foundational knowledge of molecular simulation for optical properties. In addition, I am truly thankful to Dr. Teruhiko Saito, Mr. Yuki Ohara, and Mr. Kota Ando for their collaborative spirit and willingness to share their knowledge, which greatly enriched my research.

I would like to thank my current colleagues at Panasonic Housing Solutions Co., Ltd. for their understanding, encouragement and flexibility.

Finally, I particularly want to thank my family and lifelong friends who have been invaluable throughout my research journey. My parents, Masakatsu and Itsuko Moriishi, my sister, Mari, my parents-in-law, Hisanori and Chisato Yokoyama, and my grandparents believed and encouraged me for a long time. My friends Keika Yoshino and Akiko Sogawa always supported me emotionally, which was an indispensable pillar of strength, helping me navigate the challenges of my doctoral research.

At last but not least, my husband, Dr. Tomoyasu Yokoyama, always believed, encouraged and supported me. The intellectual support provided by him, a researcher whom I deeply admired and respected while also being a close and trusted presence, has been an essential part of my academic growth.

Masako YOKOYAMA (MORIISHI)
March 2025